Hybrid Monte Carlo/Deterministic Methods for Radiation Shielding Problems

by

Troy L. Becker

A dissertation submitted in partial fulfillment
of the requirements for the degree of
Doctor of Philosophy
(Nuclear Engineering and Radiological Sciences)
in the University of Michigan
2009

Doctoral Committee:

Professor Edward W. Larsen, Chair
Professor Michael I. Combi
Professor James P. Holloway
Professor William R. Martin
Robert E. Grove, Knolls Atomic Power Laboratory

To my family: my father Milton, my mother
Vicky, and my brother Weston

Acknowledgements

I wish to thank my advisor Prof. Edward Larsen. His breadth of knowledge, creativity, and enthusiasm were indispensable in the completion of this thesis. My understanding of radiation transport theory and my ability to carefully pursue a solution to a research problem have been greatly enhanced by working with Prof. Larsen. In addition, his constant patience, kindness, and humility have made my time working with him as a graduate student a truly joyful experience.

I would like to thank my parents Milton and Vicky Becker who have consistently been there throughout my entire life to encourage and enable me to pursue my ambitions. The values that they instilled in me and their enduring commitment to my educational advancement have allowed me to come this far. I am forever grateful.

I would also like to thank the myriad of friends who have walked with me through various parts of this journey. Their friendship has truly been a blessing. Since the list is much too long to include every person, I have chosen to mention those who have endured me the longest. From the NERS department, these include Peggy Gramer, Dave Griesheimer, Scott Kiff, Allan Wollaber, Jeremy Conlin, Haori Yang, Wei Ji, Yan Cao, Hao Jiang, Jean Peng, Greg Davidson, Jesse Cheatham, and Steve Anderson. From outside the department, these include Se Young Chun, Joshua Kang, James Escobar, Andrew Wong, Manoj Cheriyan, Erik Kim, Lulu Chen, Katie King, Beena Cheriyan, Mike Lee, Mitaire Ojaruege, Erika Kido, John Yim, and Julian Lim.

I also would like to thank Bob Grove, my lab advisor at KAPL, for his support throughout the process. His periodic phone calls were more encouraging than he could possibly know. I look forward to working with him upon graduating.

Finally, I would like to thank my fellowship for their invaluable support. This work was performed under appointment by the Admiral Hyman Rickover Graduate Fellowship Program in Nuclear Engineering.

Table of Contents

Dedication . . . . . **ii**

Acknowledgements . . . . . **iii**

List of Figures . . . . . **viii**

List of Tables . . . . . **xii**

List of Appendices . . . . . **xv**

Chapter

I. Introduction 1

II. Steady State Neutral-Particle Transport 8

2.1 The Steady-State Neutral-Particle Transport Equation 8
2.2 The Multigroup Approximation 11
2.3 The Forward Multigroup Diffusion Approximation 12
2.4 Transport-Corrected Multigroup Diffusion 14
2.5 The Adjoint Multigroup Diffusion Approximation 16
2.6 Analog Monte Carlo for Radiation Transport 17
2.6.1 Sampling for an Interior Source 18
2.6.2 Sampling the Distance-To-Next Collision 20
2.6.3 Sampling the Collision Type: Capture or Scatter . . 21
2.6.4 Sampling the Scattering Distribution 21
2.7 Particle Weight 22
2.8 Estimators 23
2.8.1 Path Length Estimator 23

2.8.2 Collision Estimator 24
2.9 Central Limit Theorem 25
2.10 Variance Reduction 26
2.10.1 Implicit Capture 26
2.10.2 Weight Windows 27

III. Spatially-Discretized Transport-Corrected Multigroup Diffusion Equations 29

3.1 The Cell-Edge Diffusion Discretization 29
3.2 Numerical Solution Technique 51
3.3 Grid-Adjusted Diffusion Coefficient 52
3.4 The Cell-Edge Adjoint Diffusion Discretization 55

IV. Theoretical Issues 56

4.1 The Monte Carlo Particle Flux 57
4.2 Weight Windows 58
4.2.1 The Monte Carlo Particle Flux 59
4.2.2 Weight Window Physics for Monte Carlo Sampling . 60
4.2.3 Estimators 68
4.3 The General Transform 72
4.3.1 The Monte Carlo Particle Flux 72
4.3.2 The Transformed Transport Equation 76
4.3.3 The "Transform" Function, $\hat{\mathcal{T}}(\mathbf{x}, \mathbf{\Omega}, E)$ 78
4.3.4 The Transform Parameters 80
4.3.5 Modified Physics for Monte Carlo Sampling 82
4.3.6 Estimators 96
4.4 Summary 100

V. Source-Detector Problems 102

5.1 The Contributon Flux 103
5.2 The Response Problem 110
5.3 The Flux Problem 110
5.4 The Transform Approach 111

5.5 Our Weight Window . . . 115
5.6 FW-CADIS . . . 116
5.7 Numerical Test Problem . . . 117
5.7.1 Problem Description . . . 117
5.7.2 Numerical Results . . . 121
5.8 Summary . . . 136

VI. Source-Region Problems . . . 137

6.1 The Response Problem . . . 138
6.2 The Flux Problem . . . 139
6.3 The Transform Approach . . . 139
6.4 Our Weight Window . . . 142
6.5 FW-CADIS . . . 144
6.6 Numerical Test Problem . . . 144
6.6.1 Problem Description . . . 144
6.6.2 Numerical Results . . . 148
6.7 Summary . . . 161

VII. Global Problems . . . 166

7.1 The Response Problem . . . 168
7.2 The Flux Problem . . . 169
7.3 The Transform Approach . . . 169
7.4 Our Weight Window . . . 171
7.5 FW-CADIS . . . 172
7.6 Numerical Test Problem . . . 172
7.6.1 Problem Description . . . 172
7.6.2 Numerical Results . . . 177
7.7 Summary . . . 192

VIII. Challenge Problems . . . 197

8.1 The Neutron Response Problem . . . 198
8.2 The Photon Response Problem . . . 199
8.3 Numerical Test Problem . . . 201

8.3.1 Problem Description 201
8.3.2 Numerical Results 206
8.4 Summary 220

IX. Conclusions 231

Appendices **235**

Bibliography **243**

List of Figures

Figure

3.1 Three-dimensional grid for the cell-edge diffusion discretization. . . 30

5.1 Problem Geometry and Material Properties 118

5.2 Scalar Flux along the plane $x = y$ 119

5.3 Group 2 FOM for Source-Detector (SD) Flux Problem 122

5.4 Group 2 Simulated MC Particle Flux for SD Flux Problem 123

5.5 Group 2 Predicted MC Particle Flux for SD Flux Problem 124

5.6 Group 2 FOM for SD Response Problem 125

5.7 Group 2 Simulated MC Particle Flux for SD Response Problem . . 126

5.8 Group 2 Predicted MC Particle Flux for SD Response Problem . . . 127

5.9 Total FOM for SD Flux Problem 128

5.10 Total Simulated MC Particle Flux for SD Flux Problem 129

5.11 Total Predicted MC Particle Flux for SD Flux Problem 130

5.12 Total FOM for SD Response Problem 131

5.13 Total Simulated MC Particle Flux for SD Response Problem 132

5.14 Total Predicted MC Particle Flux for SD Response Problem 133

6.1 Problem Geometry and Material Properties 145

6.2 Scalar Flux along the plane $x = y$ 146

6.3 Group-2 FOM for SR Flux Problem 151

6.4 Group-2 Simulated MC Particle Flux for SR Flux Problem 152

6.5 Group 2 Predicted MC Particle Flux for SR Flux Problem 153

6.6 Group-2 Region Statistics by Number of Voxels for SR Flux Problem 153

6.7 Group-2 FOM for SR Response Problem 154

6.8 Group-2 Simulated MC Particle Flux for SR Response Problem . . 155

6.9 Group-2 Predicted MC Particle Flux for SR Response Problem . . . 156

6.10 Group-2 Region Statistics by Number of Voxels for SR Response Problem 156

6.11 Total FOM for SR Flux Problem 157

6.12 Total Simulated MC Particle Flux for SR Flux Problem 158

6.13 Total Predicted MC Particle Flux for the Source-Region (SR) Flux Problem 162

6.14 Total Region Statistics by Number of Voxels for SR Flux Problem . 163

6.15 Total FOM for SR Response Problem 163

6.16 Total Simulated MC Particle Flux for SR Response Problem 164

6.17 Total Predicted MC Particle Flux for SR Response Problem 165

6.18 Total Region Statistics by Number of Voxels for SR Response Problem 165

7.1 Problem Geometry and Material Properties 173

7.2 Scalar Flux along the plane $x = y$ 174

7.3 Group-2 FOM for Global Flux Problem 181

7.4 Group-2 Simulated MC Particle Flux for Global Flux Problem . . . 182

7.5 Group 2 Predicted MC Particle Flux for Global Flux Problem . . . 183

7.6 Group-2 Global Statistics by Number of Voxels for Global Flux Problem . . . 183

7.7 Group-2 FOM for Global Response Problem . . . 184

7.8 Group-2 Simulated MC Particle Flux for Global Response Problem 185

7.9 Group-2 Predicted MC Particle Flux for Global Response Problem . 186

7.10 Group-2 Global Statistics by Number of Voxels for Global Response Problem . . . 186

7.11 Total FOM for Global Flux Problem . . . 187

7.12 Total Simulated MC Particle Flux for Global Flux Problem . . . 188

7.13 Total Predicted MC Particle Flux for Global Flux Problem . . . 193

7.14 Total Global Statistics by Number of Voxels for Global Flux Problem 193

7.15 Total FOM for Global Response Problem . . . 194

7.16 Total Simulated MC Particle Flux for Global Response Problem . . 195

7.17 Total Predicted MC Particle Flux for Global Response Problem . . 196

7.18 Total Global Statistics by Number of Voxels for Global Response Problem . . . 196

8.1 Problem Geometry . . . 202

8.2 Scalar Flux along the plane $x = y$ . . . 204

8.3 Total Flux FOM for Source-Detector (SD) Neutron Problem . . . 209

8.4 Total Simulated MC Particle Flux for SD Neutron Problem . . . 210

8.5 Total Predicted MC Particle Flux for SD Neutron Problem . . . 211

8.6 Total Flux FOM for Source-Region (SR) Neutron Problem . . . 212

8.7 Total Simulated MC Particle Flux for SR Neutron Problem . . . 213

8.8 Total Predicted MC Particle Flux for SR Neutron Problem . . . 214

8.9 Statistics by Number of Voxels for SR Neutron Problem 215

8.10 Total Flux FOM for Global Neutron Problem 216

8.11 Total Simulated MC Particle Flux for Global Neutron Problem . . . 217

8.12 Total Predicted MC Particle Flux for Global Neutron Problem . . . 218

8.13 Statistics by Number of Voxels for Global Neutron Problem 219

8.14 Total Flux FOM for Source-Detector (SD) Photon Problem 221

8.15 Total Simulated MC Particle Flux for SD Photon Problem 222

8.16 Total Predicted MC Particle Flux for SD Photon Problem 223

8.17 Total Flux FOM for Source-Region (SR) Photon Problem 224

8.18 Total Simulated MC Particle Flux for SR Photon Problem 225

8.19 Total Predicted MC Particle Flux for SR Photon Problem 226

8.20 Statistics by Number of Voxels for SR Photon Problem 227

8.21 Total Flux FOM for Global Photon Problem 228

8.22 Total Simulated MC Particle Flux for Global Photon Problem . . . 229

8.23 Total Predicted MC Particle Flux for Global Photon Problem . . . 230

8.24 Statistics by Number of Voxels for Global Photon Problem 230

List of Tables

Table

5.1 Detector FOM for all methods and all groups 121

5.2 Detector simulated MC particle flux for all methods and all groups 122

6.1 Region FOM statistics for group-1 flux 149

6.2 Region FOM statistics for group-2 flux 149

6.3 Region FOM statistics for the group-3 flux 149

6.4 Region FOM statistics for the total flux 149

6.5 Region simulated MC particle flux for the group-1 flux 150

6.6 Region simulated MC particle flux for the group-2 flux 150

6.7 Region simulated MC particle flux for the group-3 flux 150

6.8 Region simulated MC particle flux for the total flux 150

7.1 Global FOM statistics for group-1 flux 178

7.2 Global FOM statistics for group-2 flux 178

7.3 Global FOM statistics for the group-3 flux 179

7.4 Global FOM statistics for the total flux 179

7.5 Global simulated MC particle flux for the group-1 flux 179

7.6 Global simulated MC particle flux for the group-2 flux 179

7.7 Global simulated MC particle flux for the group-3 flux 180

7.8 Global simulated MC particle flux for the total flux 180
7.9 Detector vs global group-1 data 189
7.10 Detector vs global group-2 data 189
7.11 Detector vs global group-3 data 189
7.12 Detector vs global total flux data 190
8.1 Energy bounds for 10-group problem 204
8.2 FOM statistics for the total neutron flux 207
8.3 Monte Carlo particle flux statistics for the total neutron flux 207
8.4 FOM statistics for the total photon flux 208
8.5 Monte Carlo particle flux statistics for the total photon flux 208
8.6 Detector vs global total neutron and photon flux data 215
A.1 Composition of concrete 236
A.2 Composition of water 236
A.3 Composition of stainless steel 304 237
A.4 Composition of lead 237
A.5 Composition of uranium dioxide 237
B.1 Concrete cross-sections for groups 1-5 238
B.2 Concrete cross-sections for groups 6-10 239
B.3 Water cross-sections for groups 1-5 239
B.4 Water cross-sections for groups 6-10 239
B.5 Stainless steel 304 cross-sections for groups 1-5 240
B.6 Stainless steel 304 cross-sections for groups 6-10 240

B.7 Lead cross-sections for groups 1-5 240

B.8 Lead cross-sections for groups 6-10 241

B.9 Uranium dioxide cross-sections and fixed source for groups 1-5 . . . 241

B.10 Uranium dioxide cross-sections and fixed source for groups 6-10 . . 242

List of Appendices

Appendix

A. Atomic Composition of Materials 236

B. Multigroup Cross-Sections for Materials 238

Chapter I

Introduction

For most applications of nuclear technology, it is necessary to characterize the associated radiation to ensure that the technology performs as intended and that adequate shielding is provided to protect personnel and radiation-sensitive equipment. In many of these cases, it is desirable to optimize the shielding designs to minimize weight and size, and hence cost. An extreme example is in the design of space nuclear reactors, in which the weight and size of the accompanying radiation shield must be optimized to reduce both the payload cost and to protect equipment (and personnel for proposed manned missions). To optimize these conflicting demands, an accurate estimate of the radiation profile must be obtained.

Currently, two classes of techniques exist to solve these radiation shielding problems: *deterministic methods*, in which the integro-differential Boltzmann transport equation is discretized and the resulting large algebraic system is solved, and *Monte Carlo methods*, in which the random history of a particle is simulated and the results of many random histories are averaged. Deterministic methods tend to be faster than Monte Carlo methods, but they include undesirable discretization errors in space, angle, and energy that are not present in Monte Carlo methods. On the other hand, Monte Carlo solutions include statistical errors, which are not present in deterministic solutions. In this thesis, we propose several Monte Carlo methods that use information obtained from computationally inexpensive deterministic methods to distribute Monte Carlo particles advantageously throughout shielding problems, in order to acquire the data necessary to optimize the shielding design. Techniques that couple deterministic and Monte Carlo methods in such a manner are described as *hybrid methods*.

Due to the difficulty in solving radiation shielding problems, Monte Carlo methods must employ "nonanalog" or "variance reduction" techniques to obtain useful

solutions. These techniques *bias* the physical (or analog) transport processes (e.g. scattering, distance-to-next collision, etc), resulting in Monte Carlo particle distributions that are artificial, or unphysical. Despite the biased (nonanalog) physics, nonanalog Monte Carlo methods can still acquire non-biased estimates of the solution by carefully adjusting the *statistical weight* of the particle to ensure that the resulting statistical game remains "fair". For shielding problems, the objective of these nonanalog techniques is to transport a statistically significant number of Monte Carlo particles to the regions of phase-space that are important to the calculation – usually the "deep" parts of the problems, where relatively few physical particles exist. Typical variance reduction techniques include *implicit capture*, *geometric splitting*, and *weight windows*.

For the past few decades, the most common type of shielding problem simulated using Monte Carlo methods has been the *source-detector problem*, in which a response is desired in a single location in space. In these problems, the source and detector are separated by a non-trivial distance, the geometry is often complicated, and the neutron flux experiences significant attenuation (by 10 or more orders of magnitude) from the source to the detector. Traditionally, the nonanalog Monte Carlo methods used to solve these problems have required significant user input to generate and sufficiently optimize the biasing parameters necessary to obtain a statistically reliable solution. For example, determining weight window or geometric splitting parameters required that an experienced engineer, familiar with the physics and geometry of the problem and the Monte carlo methodology, tinker with the biasing parameters until a suitable solution was obtained. To a large degree, this laborious task can now be replaced by automated processes that rely on a deterministic adjoint solution to set the biasing parameters – the so-called *hybrid methods*.

The adjoint flux, or "importance" function, has been used considerably to set the biasing parameters in nonanalog Monte Carlo simulations, since it indicates which regions of phase space are important to the detector [1–27]. Biasing parameters based on this important function allow Monte Carlo particles to be "guided" toward the important regions. Early work by Kalos [1] and Coveyou [3] demonstrated the merits of using the "importance" function to advantageously bias the Monte Carlo physics; however, these demonstrations were limited to simple problems, due to limited computational power. As computational power increased, production-level codes were developed that could solve more complicated source-detector shielding problems with multi-dimensional geometries; these include MORSE/SAS4 [17, 18], MCBEND [19, 20]. AVATAR [21], TRIPOLI [12–14], and A^{3}MCNP [25–27], each of

which utilizes the deterministic adjoint solution to set the biasing parameters.

Specifically, MORSE/SAS4 incorporates an automated procedure that utilizes a 1-D discrete ordinates adjoint solution for source energy biasing, energy biasing at collisions sites, splitting and Russian rouletting, and path length stretching. The commercial code MCBEND uses a 3-D adjoint diffusion code to generate biasing parameters for space- and energy-dependent geometric splitting and Russian roulette. AVATAR utilized a 3-D discrete ordinates adjoint solution to generate space-, angle-, and energy-dependent weight windows for MCNP. The French code TRIPOLI has several means to generate the adjoint solution, including a method based on graph theory, collision probabilities, and a 2-D discrete ordinates adjoint solver; the adjoint solution is used for exponential biasing, quota sampling, and collision biasing. Finally, A^{3}MCNP utilizes a 3D discrete ordinates adjoint solver for space- and energy-dependent source biasing and weight windows.

In addition to production-level codes, the LIFT method [22,23] was developed at the University of Michigan to approximate the zero-variance solution for the source-detector problem. It uses a deterministic estimate of the adjoint solution for source biasing, collision biasing, and path length biasing.

Recently, as computational power has become more readily available, there has been interest in obtaining the solution in a much larger region of space than just a small detector. Several methods have been developed that achieve this, including Cooper's weight window method [28] and FW-CADIS [29, 30]. Cooper's method utilizes a forward deterministic solution to set a space-, angle-, and energy-dependent weight window for obtaining a solution throughout the entire system. FW-CADIS uses both a forward and adjoint solution to set a space- and energy-dependent weight window for obtaining a solution in any selected region of space, including the entire system.

In principle, the new work contained in this thesis has many of the same biasing elements that have been implemented in the codes and methods mentioned above: source biasing, path length biasing, collision biasing, and weight windows. The fundamental difference, however, is that here these biasing techniques are not viewed as individual techniques that can produce better results if used correctly; rather, they are seen as elements of a comprehensive tool set to distribute Monte Carlo particles in a user-specified way. *Using these methods, the user can control the distribution of Monte Carlo particles throughout the system in space, angle and energy.* These techniques can be applied to every type of problem, from the classic source-detector problem, in which a single response value is desired, to a global problem, in which

the user requires accurate estimates of the angular neutron flux in all phase-space. Obviously, the distribution of Monte Carlo particles that optimally solves the classic source-detector problem is different from the particle distribution that optimally solves the global problem in phase space.

To achieve the user-specified particle distributions, we consider two techniques: weight window techniques, which impose a requirement on the Monte Carlo particle distribution without changing the underlying neutron physics, and a technique called the *Transform approach*, which comprehensively uses many of the standard biasing techniques to modify the particle physics to achieve the user-specified distribution of Monte Carlo particles. These two approaches – the weight window and Transform approach – exist at the extremities of a continuum of methods that are collectively described by the *General Transform approach*. On one end of the continuum are weight windows, which do not inherently alter the neutron physics (except through implicit capture), and on the other end is the Transform approach, which biases all the neutron physics (i.e. the emission of source particles, distance-to-next collision, and the exiting state of a collided particle). Although this thesis only considers the Transform approach and weight windows, the General Transform approach provides a means to bias the physics in a particular way and yet achieve the user-specified distribution by applying the complementary weight window.

Although the weight window approach is not new, it appears that there is little precise information in the literature about the effect of a given weight window on the Monte Carlo particle distribution, even though one of the main objectives of the weight window is to control the population of Monte Carlo particles. (The other objective of the weight window is to constrain the weight of the particle, ensuring that high-weight particles do not produce a high variance in the solution estimate and that low-weight particles are not tracked when their contribution to the solution estimate is insignificant.) The Monte Carlo particle distribution resulting from a weight window is explained in some detail in this thesis.

The Transform approach, which comprehensively changes the particle physics to achieve the user specified distribution, is also described at length, including all the various effects on the Monte Carlo simulation. As mentioned, this approach contains many of the familiar biasing techniques; however, the biasing is the result of a simple transform that is introduced into the neutron transport equation, not by specifically altering certain physics that the user decides may be beneficial to the simulation. The Transform approach does allow some flexibility in which specific physics are altered, but generally it is most beneficial to modify the physics that result from the

transform.

Implementing the weight window and Transform approach requires that the user specify the Monte Carlo particle distribution. We expect that each problem has a corresponding Monte Carlo particle distribution that optimizes the solution we seek. In this work, we choose to distribute Monte Carlo particles according to the *contributon flux* [31–37], or a modified form of the contributon flux, which identifies the regions of the problem that are important to the desired solution. Within the shielding community, the contributon concept is well-known and understood to convey theoretical information about the most likely paths that Monte Carlo particles travel to contribute to a detector response. This information can then be used to provide qualitative guidance to better optimize the shielding design. In this thesis, we make practical use of the contributon concept, by choosing to distribute Monte Carlo particles throughout phase space in ways that are consistent with the contributon flux. To our knowledge, the work presented in this thesis represents the first specific application of the contributon concept to a broad class of practical problems.

For the classic source-detector problem, the contributon flux identifies the optimal paths that source particles travel in phase space to contribute to the detector response. For global calculations, a modified form of the contributon flux is used to distribute particles in the important regions of phase space. It should be noted that the contributon flux identifies regions in phase space that are important to the *desired solution* while the adjoint flux identifies regions that are important to the *detector*, not necessarily the solution. This is most evident in the classic source-detector problem, in which the forward source region is extremely important to the solution (i.e. the detector response) yet is of relatively little importance to the detector, as determined by the adjoint flux.

Finally, it should be made clear that while the techniques developed in this thesis allow Monte Carlo practitioners to populate regions of phase space according to a specific prescription, they do not directly control the usual statistical metrics that are used to judge nonanalog Monte Carlo methods, such as the figure of merit. However, even though no theoretical basis is derived that links the particle distribution to a statistical metric such as the figure of merit, Monte Carlo particles still populate the system in a simulation, and it seems logical to try to distribute them throughout phase space in a way that would beneficially affect the statistical efficiency of the method. In our numerical simulations, we do in fact see a correlation between putting particles in a region and an increased figure of merit.

The remainder of this thesis is organized as follows:

Chapter II: Steady State-Neutral Particle Transport

In this chapter we present the steady state, continuous energy, neutral particle transport equation for general geometry. We then derive the multigroup approximation to the transport equation, the standard forward and adjoint diffusion approximations to multigroup transport, and a transport-based correction to the diffusion equations. Finally, we describe the solution of the transport equation using the Monte Carlo method with several variance reduction techniques.

Chapter III: Spatially-Discretized Multigroup Diffusion Equations

We present the derivation of a new cell-edge multigroup diffusion discretization scheme on a three-dimensional Cartesian grid. We then derive grid-based diffusion coefficients that preserve the asymptotic behavior of the transport solution. This spatial discretization and the grid-based diffusion coefficients are applicable to both forward and adjoint diffusion. The resulting discrete diffusion method is used as the deterministic "transport" solver for the numerical work presented in this thesis.

Chapter IV: Theory

In this chapter, we present a thorough discussion of the weight window and Transform approaches. This includes defining the Monte Carlo particle flux and deriving expressions that describe the means by which the weight window method and the Transform approach controls the Monte Carlo particle flux distribution. We also describe the Monte Carlo sampling techniques and solution estimators for both approaches.

Chapter V: Source-Detector Problems

Here we introduce the first class of shielding problems in which we are interested – *source-detector problems*. Two types of source-detector problems are described – the *flux* and *response problems* – and solution schemes are devised using the weight window and Transform approach to distribute particles according to the contributon flux. A basic test problem is used to validate the theory and assess the performance of each method.

Chapter VI: Source-Region Problems

The second class of shielding problems is considered here – *source-region problems*. Again, two types of source-region problems are described – the *flux* and *response problems* – and solution schemes are devised using the weight window and Transform approach to distribute particles according to the contributon flux, or a slightly modified form of the contributon flux. The same test problem is used to validate the theory and assess the performance of each method.

Chapter VII: Global Problems

The final class of shielding problems that we discuss is introduced here – *global problems*. The two types of global problems are described – the *flux* and *response problems* – and solution schemes are devised using the weight window and Transform approach to distribute particles according to the contributon flux, or a slightly modified form of the contributon flux. The same test problem is used to validate the theory and assess the performance of each method.

Chapter VIII: Challenge Problems

In this chapter, we describe a more realistic 3-D multigroup shielding problem to determine whether the weight window and Transform approaches are capable of obtaining the desired solution, and to validate the theory and assess the performance of each method. We consider the source-detector, source-region, and global response problems.

Chapter IX: Conclusions

Here we review the main ideas and sum up the results presented in the thesis. We also discuss some interesting and promising ideas for future work.

Chapter II

Steady State Neutral-Particle Transport

In this chapter we present the steady state, continuous energy, neutral particle transport equation for general geometry. We then derive the multigroup approximation to the transport equation, the standard forward and adjoint diffusion approximations to multigroup transport, and a transport-based correction to the diffusion equations. Finally, we describe the solution of the transport equation using the Monte Carlo method with several variance reduction techniques.

2.1 The Steady-State Neutral-Particle Transport Equation

The neutral particle transport equation is a linear integro-differential Boltzmann equation that quantitatively describes neutron balance throughout phase space. For radiation transport problems, phase space is the seven-dimensional space consisting of three variables to represent a particle's spatial location, two variables to represent a particle's direction of flight, one variable to represent a particle's kinetic energy, and a time variable. In general, the Boltzmann transport equation describes the distribution of particles throughout phase space or, for time-dependent problems, the evolution of the particle distribution in time. For this thesis, the only problems considered are time-independent, or steady state. For these problems, the Boltzmann equation relates the rate at which particles stream through an element of phase space, the rate at which particles collide in that element, the rate at which particles scatter into that element, and the rate at which particles are emitted within that element, whether by fission or a fixed source.

The linear integro-differential Boltzmann equation for steady-state, continuous-

energy, neutral-particle transport is given by:

$$\begin{aligned}\boldsymbol{\Omega}\cdot\nabla\psi(\mathbf{x},\boldsymbol{\Omega},E)+\Sigma_t(\mathbf{x},E)\psi(\mathbf{x},\boldsymbol{\Omega},E)&\\ =\int_0^\infty\int_{4\pi}\Sigma_s(\mathbf{x},\boldsymbol{\Omega}'\cdot\boldsymbol{\Omega},E'\to E)\psi(\mathbf{x},\boldsymbol{\Omega}',E')d\Omega'dE'+Q(\mathbf{x},\boldsymbol{\Omega},E),&\\ \mathbf{x}\in\mathcal{V},\ \ \boldsymbol{\Omega}\in 4\pi,\ \ 0<E<\infty,&\end{aligned}\tag{2.1a}$$

with boundary condition

$$\psi(\mathbf{x},\boldsymbol{\Omega},E)=\psi_b(\mathbf{x},\boldsymbol{\Omega},E),\quad \mathbf{x}\in\partial\mathcal{V},\ \ \boldsymbol{\Omega}\cdot\mathbf{n}(\mathbf{x})<0,\ \ 0<E<\infty.\tag{2.1b}$$

The variables and parameters are defined as follows:

$$\begin{aligned}\mathbf{x} &= \text{position, } (\mathbf{x}\in\mathcal{V}), && (2.2a)\\ \boldsymbol{\Omega} &= \text{direction, } (|\boldsymbol{\Omega}|=1), && (2.2b)\\ E &= \text{kinetic energy, } (0<E<\infty), && (2.2c)\\ \psi(\mathbf{x},\boldsymbol{\Omega},E) &= \text{angular flux,} && (2.2d)\\ \Sigma_t(\mathbf{x},E) &= \text{total cross section,} && (2.2e)\\ \Sigma_s(\mathbf{x},\boldsymbol{\Omega}'\cdot\boldsymbol{\Omega},E'\to E) &= \text{differential scattering cross section,} && (2.2f)\\ Q(\mathbf{x},\boldsymbol{\Omega},E) &= \text{internal source,} && (2.2g)\\ \psi_b(\mathbf{x},\boldsymbol{\Omega},E) &= \begin{cases}0 & \text{, vacuum boundary,}\\ \psi(\mathbf{x},\boldsymbol{\Omega}_r,E) & \text{, reflecting boundary,}\end{cases} && (2.2h)\\ \boldsymbol{\Omega}_r &= \text{angle of reflection,} &&\\ &= \boldsymbol{\Omega}-2\,(\boldsymbol{\Omega}\cdot\mathbf{n})\,\mathbf{n}, && (2.2i)\\ \mathbf{n}(\mathbf{x}) &= \text{unit outward normal, } (\mathbf{x}\in\partial\mathcal{V}). && (2.2j)\end{aligned}$$

For three-dimensional problems, the position $\mathbf{x}$ is a three-element vector (i.e. $\mathbf{x}=(x,y,z)$) while the direction $\boldsymbol{\Omega}$ is a three-element unit vector whose components are defined by the polar angle ϕ and the azimuthal angle γ. That is, the direction vector is given by:

$$\begin{aligned}\boldsymbol{\Omega}&=\Omega_1\,\mathbf{i}+\Omega_2\,\mathbf{j}+\Omega_3\,\mathbf{k}\\ &=\cos\phi\,\mathbf{i}+\sin\phi\,(\cos\gamma\,\mathbf{j}+\sin\gamma\,\mathbf{k})\\ &=\mu\,\mathbf{i}+\sqrt{1-\mu^2}\,(\cos\gamma\,\mathbf{j}+\sin\gamma\mathbf{k}),\end{aligned}\tag{2.3}$$

where

$$\begin{aligned}\phi &= \text{polar angle, } (0 \leq \phi \leq \pi/2),\\ \gamma &= \text{azimuthal angle, } (0 \leq \gamma < 2\pi),\\ \mu &= \cos\phi, (-1 \leq \mu \leq 1).\end{aligned} \tag{2.4}$$

Thus, the direction vector is completely determined by specifying the pair (μ, γ).

The differential scattering cross section can be expressed as a linear combination of the Legendre polynomials,

$$\Sigma_s(\mathbf{x}, \mathbf{\Omega}' \cdot \mathbf{\Omega}, E' \rightarrow E) = \sum_{n=0}^{\infty} \frac{2n+1}{4\pi} \Sigma_{sn}(\mathbf{x}, E' \rightarrow E) P_n(\mathbf{\Omega}' \cdot \mathbf{\Omega}), \tag{2.5}$$

where the expansion coefficient, $\Sigma_{sn}(\mathbf{x}, E' \rightarrow E)$, is defined as

$$\Sigma_{sn}(\mathbf{x}, E' \rightarrow E) = \int_{4\pi} \Sigma_s(\mathbf{x}, \mathbf{\Omega}' \cdot \mathbf{\Omega}, E' \rightarrow E) P_n(\mathbf{\Omega}' \cdot \mathbf{\Omega}) d\Omega'. \tag{2.6}$$

According to the *addition theorem*, a Legendre polynomial of order n can be expressed in terms of the spherical harmonic functions as

$$P_n(\mathbf{\Omega}' \cdot \mathbf{\Omega}) = \frac{4\pi}{2n+1} \sum_{m=-n}^{m=n} Y_{n,m}(\mathbf{\Omega}) Y^*_{n,m}(\mathbf{\Omega}'), \tag{2.7}$$

where the spherical harmonics function $Y_{n,m}(\mathbf{\Omega})$ is defined as

$$Y_{n,m}(\mathbf{\Omega}) = Y_{n,m}(\mu, \gamma) = \left[\frac{2n+1}{4\pi} \frac{(n-|m|)!}{(n+|m|)!}\right]^{1/2} (-1)^{\frac{m+|m|}{2}} P_n^{|m|}(\mu) e^{im\gamma} \tag{2.8}$$

and $P_n^{|m|}(\mu)$ are the associated Legendre polynomials. They are defined for $n \geq 0$ and $0 \leq m \leq n$ by:

$$P_n^m(\mu) = (1-\mu^2)^{m/2} \frac{d^m}{d\mu^m} P_n(\mu). \tag{2.9}$$

For this thesis, we will only consider isotropic scattering, in which the series expansion is truncated after the first term ($N = 0$). Thus, Eq. 2.5 reduces to

$$\Sigma_s(\mathbf{x}, \mathbf{\Omega}' \cdot \mathbf{\Omega}, E' \rightarrow E) = \frac{1}{4\pi} \Sigma_{s0}(\mathbf{x}, E' \rightarrow E). \tag{2.10}$$

2.2 The Multigroup Approximation

In order to solve the transport equation deterministically, we must transform it into a system of discrete unknowns that can be solved algebraically. To discretize in energy, we employ the ubiquitous *multigroup approximation*. Due to its widespread use, much effort has been invested in generating the multigroup constants that result from this approximation.

To derive the multigroup approximation, we operate on the continuous-energy transport equation (Eqs. 2.1) by $\int_{E_g}^{E_{g-1}}(\cdot)\,dE$, where g is the energy group corresponding to the range $(E_g, E_{g-1}]$. The energy group structure is determined by the boundaries, $\{E_g\}_{g=0}^{G}$, and the number of groups, G; these are selected based on some consideration of both the accuracy and the computational speed. In order to complete the derivation and arrive at the standard multigroup equations, we use the approximation $\psi(\mathbf{x},\mathbf{\Omega},E) = \varphi(\mathbf{x},E)\Psi(\mathbf{x},\mathbf{\Omega})$, where $\varphi(\mathbf{x},E)$ is the neutron energy spectrum. The spatial dependence of the neutron energy spectrum generally corresponds to the various material regions that exist within a given system.

The standard multigroup transport equations are:

$$\begin{aligned}\mathbf{\Omega}\cdot\nabla\psi_g(\mathbf{x},\mathbf{\Omega}) + \Sigma_{t,g}(\mathbf{x})\psi_g(\mathbf{x},\mathbf{\Omega}) \\ = \sum_{g'=1}^{G}\int_{4\pi}\Sigma_{s,g'\to g}(\mathbf{x},\mathbf{\Omega}'\cdot\mathbf{\Omega})\psi_{g'}(\mathbf{x},\mathbf{\Omega}')d\Omega' + Q_g(\mathbf{x},\mathbf{\Omega}), \\ \mathbf{x}\in\mathcal{V}, \quad \mathbf{\Omega}\in 4\pi, \quad 1\le g\le G,\end{aligned} \tag{2.11a}$$

with boundary condition

$$\psi_g(\mathbf{x},\mathbf{\Omega}) = \psi_{b,g}(\mathbf{x},\mathbf{\Omega}), \quad \mathbf{x}\in\partial\mathcal{V}, \quad \mathbf{\Omega}\cdot\mathbf{n}(\mathbf{x}) < 0, \quad 1\le g\le G. \tag{2.11b}$$

We have defined the following variables and parameters:

$$\psi_g(\mathbf{x},\mathbf{\Omega}) = \int_{E_g}^{E_{g-1}}\psi(\mathbf{x},\mathbf{\Omega},E)dE, \tag{2.12a}$$

$$\Sigma_{t,g}(\mathbf{x}) = \frac{\int_{E_g}^{E_{g-1}}\Sigma_t(\mathbf{x},E)\,\varphi(\mathbf{x},E)dE}{\int_{E_g}^{E_{g-1}}\varphi(\mathbf{x},E)dE}, \tag{2.12b}$$

$$\Sigma_{s,g'\to g}(\mathbf{x},\mathbf{\Omega}'\cdot\mathbf{\Omega}) = \frac{\int_{E_{g'}}^{E_{g'-1}}\int_{E_g}^{E_{g-1}}\Sigma_s(\mathbf{x},\mathbf{\Omega}'\cdot\mathbf{\Omega},E'\to E)dE\,\varphi(\mathbf{x},E')dE'}{\int_{E_{g'}}^{E_{g'-1}}\varphi(\mathbf{x},E')dE'}, \tag{2.12c}$$

$$Q_g(\mathbf{x}, \mathbf{\Omega}) = \int_{E_g}^{E_{g-1}} Q(\mathbf{x}, \mathbf{\Omega}, E) dE, \tag{2.12d}$$

$$\psi_{b,g}(\mathbf{x}, \mathbf{\Omega}) = \begin{cases} 0 & , \text{ vacuum boundary,} \\ \psi_g(\mathbf{x}, \mathbf{\Omega}_r) & , \text{ reflecting boundary.} \end{cases} \tag{2.12e}$$

2.3 The Forward Multigroup Diffusion Approximation

The diffusion equation is a low-order, angle-independent approximation to the transport equation. Despite its range of limited accuracy, it has become the computational workhorse of the reactor physics community. This is primarily due to the relatively low computational cost required to solve the diffusion equation compared to the full transport equation. In this section, we derive the forward multigroup diffusion equations.

To derive the diffusion equations, we operate on the multigroup transport equation (Eq. 2.11a) by $\int_{4\pi}(\cdot)d\Omega$ and $\int_{4\pi} \mathbf{\Omega}(\cdot)d\Omega$. The first operation gives the zeroth angular moment of the multigroup transport equation:

$$\nabla \cdot \mathbf{J}_g(\mathbf{x}) + \Sigma_{t,g}(\mathbf{x})\phi_g(\mathbf{x}) = \sum_{g'=1}^{G} \Sigma_{s0,g' \to g}(\mathbf{x})\phi_{g'}(\mathbf{x}) + Q_g(\mathbf{x})$$
$$\mathbf{x} \in \mathcal{V}, \quad 1 \leq g \leq G. \tag{2.13}$$

The second operation results in the first angular moment of the multigroup transport equation:

$$\nabla \cdot \int_{4\pi} \mathbf{\Omega}\mathbf{\Omega}\psi_g(\mathbf{x}, \mathbf{\Omega}) d\Omega + \Sigma_{t,g}(\mathbf{x})\mathbf{J}_g(\mathbf{x}) = \sum_{g'=1}^{G} \Sigma_{s1,g' \to g}(\mathbf{x})\, \mathbf{J}_{g'}(\mathbf{x}) + \mathbf{Q}_{1,g}$$
$$\mathbf{x} \in \mathcal{V}, \quad 1 \leq g \leq G. \tag{2.14}$$

where we define the scalar flux $\phi_g(\mathbf{x})$, the current $\mathbf{J}_g(\mathbf{x})$, and the zeroth and first moments of the source as:

$$\phi_g(\mathbf{x}) = \int_{4\pi} \psi_g(\mathbf{x}, \mathbf{\Omega}) d\Omega, \tag{2.15}$$

$$\mathbf{J}_g(\mathbf{x}) = \int_{4\pi} \mathbf{\Omega}\psi_g(\mathbf{x}, \mathbf{\Omega}) d\Omega, \tag{2.16}$$

$$Q_g(\mathbf{x}) = \int_{4\pi} Q_g(\mathbf{x}, \mathbf{\Omega}) d\Omega, \tag{2.17}$$

$$\mathbf{Q}_{1,g}(\mathbf{x}) = \int_{4\pi} \mathbf{\Omega} Q_g(\mathbf{x}, \mathbf{\Omega}) d\Omega. \tag{2.18}$$

To complete the derivation, we must introduce three approximations into Eq. 2.14.

1. The angular flux is approximated by a linear function in angle. This is called the *P1 approximation*,

$$\psi_g(\mathbf{x}, \mathbf{\Omega}) \cong \frac{1}{4\pi} \left[\phi_g(\mathbf{x}) + 3\mathbf{\Omega} \cdot \mathbf{J}_g(\mathbf{x}) \right]. \tag{2.19}$$

2. The first angular moment of the differential scattering cross-section, $\Sigma_{s1,g' \to g}(\mathbf{x})$, is approximated by

$$\Sigma_{s1,g' \to g}(\mathbf{x}) \cong \delta_{g',g} \sum_{g''=1}^{G} \Sigma_{s1,g'' \to g}(\mathbf{x}). \tag{2.20}$$

3. The source, $Q_g(\mathbf{x}, \mathbf{\Omega})$, is isotropic. Under this assumption, the first moment of the source becomes zero:

$$\mathbf{Q}_{1,g} \cong 0. \tag{2.21}$$

In general, none of these approximations may be true; nevertheless, this is what is done to arrive at the following equation, known as *Fick's Law*:

$$\mathbf{J}_g(\mathbf{x}) = -D_g(\mathbf{x}) \nabla \phi_g(\mathbf{x}). \tag{2.22}$$

The diffusion coefficient, $D_g(\mathbf{x})$, is given by

$$D_g(\mathbf{x}) = \frac{1}{3 \left(\Sigma_{t,g}(\mathbf{x}) - \sum_{g''=1}^{G} \Sigma_{s1,g'' \to g}(\mathbf{x}) \right)}. \tag{2.23}$$

Finally, substituting Eq. 2.22 into Eq. 2.14, we obtain the multigroup diffusion equations:

$$-\nabla \cdot D_g(\mathbf{x}) \nabla \phi_g(\mathbf{x}) + \Sigma_{t,g}(\mathbf{x}) \phi_g(\mathbf{x}) = \sum_{g'=1}^{G} \Sigma_{s0,g' \to g}(\mathbf{x}) \phi_{g'}(\mathbf{x}) + Q_g(\mathbf{x}),$$
$$\mathbf{x} \in \mathcal{V}, \quad 1 \leq g \leq G. \tag{2.24}$$

To obtain the multigroup diffusion boundary condition, we operate on the multigroup transport boundary condition (Eq. 2.11b) by $\int_{\mathbf{\Omega} \cdot \mathbf{n}(\mathbf{x}) \leq 0} |\mathbf{\Omega} \cdot \mathbf{n}(\mathbf{x})| (\cdot) d\Omega$, introduce

the P1 approximation (Eq. 2.19) for the case of vacuum boundary conditions, and use Fick's Law (Eq. 2.22) where necessary. We obtain:

$$0 = \begin{cases} \phi_g(\mathbf{x}) + \mathbf{n}(\mathbf{x}) \cdot 2D_g(\mathbf{x}) \nabla \phi_g(\mathbf{x}) & \text{, vacuum boundary,} \\ \mathbf{n}(\mathbf{x}) \cdot D_g(\mathbf{x}) \nabla \phi_g(\mathbf{x}) & \text{, reflecting boundary.} \end{cases} \tag{2.25}$$

2.4 Transport-Corrected Multigroup Diffusion

The transport-corrected multigroup diffusion equation has the same form as the standard multigroup diffusion equation, with the exception that the diffusion coefficient is modified to more accurately preserve the asymptotic solution of the transport equation. (This is not to be confused with asymptotic limits to the transport equation.) The asymptotic solution to the transport equation is the solution that dominates away from boundaries, sources and material interfaces. For three-dimensional multigroup transport problems, the asymptotic solution is assumed to be a planar solution, separable in angle and space:

$$\psi_g(\mathbf{x}, \mathbf{\Omega}) = f_g(\mathbf{\Omega}) \mathrm{e}^{\lambda_g^{tr} \Sigma_{t,g} (\mathbf{x} \cdot \boldsymbol{\omega})}, \tag{2.26}$$

where $f_g(\mathbf{\Omega})$ is the angular distribution of the flux, λ_g^{tr} is the exponential attenuation parameter that contains information from the transport equation, and $\boldsymbol{\omega}$ is any unit vector that is proportional to the gradient of the scalar flux and is obtained from numerically solving the standard diffusion equations.

For multigroup diffusion problems, the analogous expression is the homogeneous solution to the diffusion equation:

$$\phi_g(\mathbf{x}) = A_g \mathrm{e}^{\sqrt{\frac{\Sigma_{R,g}}{D_g}} (\mathbf{x} \cdot \boldsymbol{\omega})}, \tag{2.27}$$

where $\Sigma_{R,g} = \Sigma_{t,g} - \Sigma_{s,g \to g}$ and is known as the removal cross-section.

By equating the exponential attenuation lengths from transport and diffusion, we obtain a new expression for the diffusion coefficient in terms of the transport attenuation parameter, λ_g^{tr}:

$$D_g(\mathbf{x}) = \frac{\Sigma_{R,g}(\mathbf{x})}{\left[\lambda_g^{tr}(\mathbf{x}) \Sigma_{t,g}(\mathbf{x})\right]^2}, \tag{2.28}$$

where we have specifically designated spatial dependence due to regional differences

in material properties. This newly-defined diffusion coefficient has the property of preserving the exponential attenuation rate of the transport solution.

One way to calculate $\lambda_g^{tr}(\mathbf{x})$ is to consider the following within-group transport equation away from sources, boundaries and material interfaces:

$$\boldsymbol{\Omega} \cdot \nabla \psi_g(\mathbf{x}, \boldsymbol{\Omega}) + \Sigma_{t,g} \psi_g(\mathbf{x}, \boldsymbol{\Omega}) = \int_{4\pi} \Sigma_{s,g\to g}(\boldsymbol{\Omega}' \cdot \boldsymbol{\Omega}) \psi_g(\mathbf{x}, \boldsymbol{\Omega}') d\Omega'. \tag{2.29}$$

Upon substituting the asymptotic solution (Eq. 2.26) into the above transport equation, we get the following expression:

$$\Sigma_{t,g} \left[1 + \lambda_g^{tr} \, \boldsymbol{\Omega} \cdot \boldsymbol{\omega}\right] f_g(\boldsymbol{\Omega}) = \int_{4\pi} \Sigma_{s,g\to g}(\boldsymbol{\Omega}' \cdot \boldsymbol{\Omega}) f_g(\boldsymbol{\Omega}') d\Omega'. \tag{2.30}$$

A solution to this equation is $f_g(\boldsymbol{\Omega}) = F_g(\boldsymbol{\Omega} \cdot \boldsymbol{\omega})$. This can be seen by using the spherical harmonics to evaluate the scattering integral:

$$\begin{aligned}
&\int_{4\pi} \Sigma_{s,g\to g}(\boldsymbol{\Omega}' \cdot \boldsymbol{\Omega}) F_g(\boldsymbol{\Omega}' \cdot \boldsymbol{\omega}) d\Omega' \\
&\qquad = \sum_{n=0}^{\infty} \sum_{p=0}^{\infty} \sum_{m=-n}^{n} \sum_{q=-p}^{p} \Sigma_{sn,g\to g} F_{p,g} Y_{n,m}(\boldsymbol{\Omega}) Y_{p,q}^*(\boldsymbol{\omega}) \int_{4\pi} Y_{p,q}(\boldsymbol{\Omega}') Y_{n,m}^*(\boldsymbol{\Omega}') d\Omega' \\
&\qquad = \sum_{n=0}^{\infty} \frac{2n+1}{4\pi} \Sigma_{sn,g\to g} F_{n,g} P_n(\boldsymbol{\Omega} \cdot \boldsymbol{\omega}).
\end{aligned} \tag{2.31}$$

We have made the following definitions:

$$\Sigma_{sn,g\to g} = \int_{4\pi} \Sigma_{s,g\to g}(\boldsymbol{\Omega} \cdot \boldsymbol{\Omega}') P_n(\boldsymbol{\Omega} \cdot \boldsymbol{\Omega}') d\Omega = 2\pi \int_{-1}^{1} \Sigma_{s,g\to g}(\mu) P_n(\mu) d\mu, \tag{2.32}$$

$$F_{n,g} = \int_{4\pi} F_g(\boldsymbol{\Omega} \cdot \boldsymbol{\omega}) P_n(\boldsymbol{\Omega} \cdot \boldsymbol{\omega}) d\Omega = 2\pi \int_{-1}^{1} F_g(\mu) P_n(\mu) d\mu. \tag{2.33}$$

Inserting this result into Eq. 2.30, and only considering anisotropic scattering of order N (i.e. $\Sigma_{sn,g\to g} = 0$ for $n > N$), we obtain the expression,

$$\left[1 + \lambda_g^{tr} \, \boldsymbol{\Omega} \cdot \boldsymbol{\omega}\right] F_g(\boldsymbol{\Omega} \cdot \boldsymbol{\omega}) = \sum_{n=0}^{N} \frac{2n+1}{4\pi} \frac{\Sigma_{sn,g\to g}}{\Sigma_{t,g}} F_{n,g} P_n(\boldsymbol{\Omega} \cdot \boldsymbol{\omega}). \tag{2.34}$$

The right side of the equation is a polynomial of order N, which indicates that we

will have a solution of the form,

$$F_g(\mathbf{\Omega}\cdot\boldsymbol{\omega}) = \sum_{n=0}^{N} a_{n,g} \frac{(\mathbf{\Omega}\cdot\boldsymbol{\omega})^n}{1+\lambda_g^{tr}\,\mathbf{\Omega}\cdot\boldsymbol{\omega}}, \quad a_{0,g}=1. \tag{2.35}$$

To solve for the unknowns, λ_g^{tr} and $\{a_{n,g}\}_{n=1}^{N}$, we insert this expression for $F_g(\mathbf{\Omega}\cdot\boldsymbol{\omega})$ into the left hand side of Eq. 2.34 and equate the coefficients of the powers of $\mathbf{\Omega}\cdot\boldsymbol{\omega}$. This results in a linear system of $N+1$ equations and $N+1$ unknowns. (The zeroth coefficient, $a_{0,g}$, was chosen to be unity as a means to normalize the expression.) For isotropic scattering ($N=0$),

$$F_g(\mathbf{\Omega}\cdot\boldsymbol{\omega}) = \frac{1}{1+\lambda_g^{tr}\,\mathbf{\Omega}\cdot\boldsymbol{\omega}}, \tag{2.36}$$

$$F_{0,g} = \frac{2\pi}{\lambda_g^{tr}} \ln\left(\frac{1+\lambda_g^{tr}}{1-\lambda_g^{tr}}\right). \tag{2.37}$$

Using these results, we obtain the following transcendental equation that can be solved for λ_g^{tr}:

$$1 = \frac{\Sigma_{s,0,g\to g}}{2\lambda_g^{tr}\Sigma_{t,g}} \ln\left(\frac{1+\lambda_g^{tr}}{1-\lambda_g^{tr}}\right). \tag{2.38}$$

This transcendental expression, which is sometimes referred to as a dispersion relation, can be solved to obtain a value for λ_g^{tr}. Similarly, we can obtain dispersion relations for higher order scattering, which can be solved to obtain λ_g^{tr}.

The transport-corrected diffusion equation (with its modified diffusion coefficient given by Eq. 2.28) preserves the asymtotic solution of the analytic transport solution in each energy group. This property makes the solution of this equation useful for shielding problems by more accurately preserving the exponential attenuation rate of the solution.

The spatial discretization scheme for the multigroup diffusion equations, whether transport-corrected or standard, are described in the next chapter.

2.5 The Adjoint Multigroup Diffusion Approximation

The adjoint multigroup diffusion equation is similar in form to the forward multigroup diffusion equation. It can be derived in the same manner as was done to obtain

forward diffusion. The adjoint multigroup diffusion equation is given by:

$$-\nabla \cdot D_g(\mathbf{x})\nabla\phi_g^*(\mathbf{x}) + \Sigma_{t,g}(\mathbf{x})\phi_g^*(\mathbf{x}) = \sum_{g'=1}^{G} \Sigma_{s,g\to g'}(\mathbf{x})\phi_{g'}^*(\mathbf{x}) + Q_g(\mathbf{x})$$
$$\mathbf{x} \in \mathcal{V}, \quad 1 \leq g \leq G, \tag{2.39}$$

with the parameters defined as they were for forward diffusion. The adjoint multigroup diffusion boundary condition is given by

$$0 = \begin{cases} \phi_g^*(\mathbf{x}) + \mathbf{n}(\mathbf{x}) \cdot 2D_g(\mathbf{x})\nabla\phi_g^*(\mathbf{x}) & \text{, vacuum boundary,} \\ \mathbf{n}(\mathbf{x}) \cdot D_g(\mathbf{x})\nabla\phi_g^*(\mathbf{x}) & \text{, reflecting boundary.} \end{cases} \tag{2.40}$$

The adjoint diffusion equation is most commonly used for deterministic perturbation analysis and for generating weight windows for source-detector Monte Carlo simulations. In this thesis, we use the adjoint solution for several of the methods discussed in later chapters.

A transport-corrected adjoint solution can also be obtained by using Eq. 2.28 for the diffusion coefficient, where λ_g^{tr} is still determined using Eqs. 2.34 and Eq. 2.35, since the within-group equation is the same for the forward and adjoint problems.

2.6 Analog Monte Carlo for Radiation Transport

The Monte Carlo method can be used to solve radiation transport problems by simulating the history of individual particles and averaging the results over many histories to obtain quantities of interest, such as the scalar flux or some response. Each particle history is governed by probability distributions that determine the detailed characteristics of the history, including the particle's birth (i.e. location, direction, energy) and its interactions (i.e. capture, scatter, fission, etc.) as it streams through various media. In order to understand the method, we need to describe the probability distributions related to each aspect of the particle's history. In this section, we present the probability distributions for analog Monte Carlo and describe how to sample from them. For simplicity, we impose a Cartesian grid upon the system composed of N_{cells} cells, in which the quantities of interest will be obtained. Each cell $C_{i,j,k}$ is defined by a spatial element $\mathcal{V}_c$ where c is an integer that represents the map $c = i + jI + kIJ$ for $i \in [0, I-1]$, $j \in [0, J-1]$, and $k \in [0, K-1]$. The element $\mathcal{V}_c$ is defined for all $\mathbf{x} = (x, y, z)$ such that $x \in [x_{i-1/2}, x_{i+1/2}]$, $y \in [y_{j-1/2}, y_{j+1/2}]$,

and $z \in [z_{k-1/2}, z_{k+1/2}]$ where $\{x_{i+1/2}\}_{i=0}^{I}$, $\{y_{j+1/2}\}_{j=0}^{J}$, $\{z_{k+1/2}\}_{k=0}^{K}$ are the planes that make up the Cartesian grid. The volume of the element $\mathcal{V}_c$ is defined as $V_c = (x_{i+1/2} - x_{i-1/2})(y_{j+1/2} - y_{j-1/2})(z_{k+1/2} - z_{k-1/2})$.

2.6.1 Sampling for an Interior Source

The probability distribution that corresponds to an interior source is given by:

$$p(\mathbf{x}, \mathbf{\Omega}, E) = \frac{Q(\mathbf{x}, \mathbf{\Omega}, E)}{\int_V \int_{4\pi} \int_0^\infty Q(\mathbf{x}, \mathbf{\Omega}, E) dV d\Omega dE}. \tag{2.41}$$

For this thesis we only consider isotropic, spatially-uniform sources within each spatial element $\mathcal{V}_c$:

$$Q(\mathbf{x}, \mathbf{\Omega}, E) = \frac{Q_c(E)}{4\pi}, \quad \mathbf{x} \in \mathcal{V}_c,\ \mathbf{\Omega} \in 4\pi,\ 0 < E < \infty. \tag{2.42}$$

This source distribution allows us to rewrite the joint probability distribution as

$$\begin{aligned} p(\mathbf{x}, \mathbf{\Omega}, E) &= p(\mathbf{x}, \mathbf{\Omega}, E \,|\, \mathbf{x} \in \mathcal{V}_c) \cdot p(\mathbf{x} \in \mathcal{V}_c) \\ &= p(x \,|\, x \in [x_{i-1/2}, x_{i+1/2}]) \cdot p(y \,|\, y \in [y_{j-1/2}, y_{j+1/2}]) \\ &\quad \cdot p(z \,|\, z \in [z_{k-1/2}, z_{k+1/2}]) \cdot p(\mu) \cdot p(\gamma) \\ &\quad \cdot p(E \,|\, \mathbf{x} \in \mathcal{V}_c) \cdot p(\mathbf{x} \in \mathcal{V}_c), \end{aligned} \tag{2.43}$$

where we make the following definitions for the probability distributions:

$$p(x \,|\, x \in [x_{i-1/2}, x_{i+1/2}]) = \frac{1}{x_{i+1/2} - x_{i-1/2}}, \tag{2.44}$$

$$p(y \,|\, y \in [y_{j-1/2}, y_{j+1/2}]) = \frac{1}{y_{j+1/2} - y_{j-1/2}}, \tag{2.45}$$

$$p(z \,|\, z \in [z_{k-1/2}, z_{k+1/2}]) = \frac{1}{z_{k+1/2} - z_{k-1/2}}, \tag{2.46}$$

$$p(\mu) = \frac{1}{2}, \tag{2.47}$$

$$p(\gamma) = \frac{1}{2\pi}, \tag{2.48}$$

$$p(E \,|\, \mathbf{x} \in \mathcal{V}_c) = \frac{Q_c(E)}{\int_0^\infty Q_c(E') dE'}, \tag{2.49}$$

$$p(\mathbf{x} \in \mathcal{V}_c) = \frac{V_c \int_0^\infty Q_c(E) dE}{\sum_{c=1}^{N_{\text{cells}}} V_c \int_0^\infty Q_c(E) dE}. \tag{2.50}$$

To obtain the multigroup probability distribution, we integrate $p(\mathbf{x}, \mathbf{\Omega}, E)$ over the energy range of a group g and use the multigroup definition for the source to obtain:

$$p(g \,|\, \mathbf{x} \in \mathcal{V}_c) = \frac{Q_{c,g}}{\sum_{g'=1}^{G} Q_{c,g'}}, \tag{2.51}$$

$$p(\mathbf{x} \in \mathcal{V}_c) = \frac{\sum_{g=1}^{G} V_c Q_{c,g}}{\sum_{c=1}^{N_{\text{cells}}} \sum_{g=1}^{G} V_c Q_{c,g}}. \tag{2.52}$$

All these probability distributions except the continuous-energy distribution can be directly sampled by inverting the cumulative probability distribution. (It is possible to directly sample the continuous-energy distribution if the indefinite integral of the source $Q_c(E)$ is invertible.) Doing this, we obtain the following results that determine the initial state of the particle ($\xi \in [0, 1]$):

$$x = x_{i-1/2} + \xi \left(x_{i+1/2} - x_{i-1/2} \right), \tag{2.53}$$

$$y = y_{j-1/2} + \xi \left(y_{j+1/2} - y_{j-1/2} \right), \tag{2.54}$$

$$z = z_{k-1/2} + \xi \left(z_{k+1/2} - z_{k-1/2} \right), \tag{2.55}$$

$$\mu = -1 + 2\xi, \tag{2.56}$$

$$\gamma = 2\pi\xi, \tag{2.57}$$

$$E = E_0 \text{ if } \xi = \frac{\int_0^{E_0} Q_c(E')dE'}{\int_0^{\infty} Q_c(E')dE'}, \tag{2.58}$$

$$\mathbf{x} \in \mathcal{V}_{c_0} \text{ if } \sum_{c=1}^{c_0-1} V_c \int_0^{\infty} Q_c(E)dE \leq \xi \leq \sum_{c=1}^{c_0} V_c \int_0^{\infty} Q_c(E)dE. \tag{2.59}$$

where, for each equation above, every ξ represents a different random number. For the multigroup distribution, we use the following relations:

$$g = g_0 \text{ if } \sum_{g'=1}^{g_0-1} Q_{c,g'} < \xi \leq \sum_{g'=1}^{g_0} Q_{c,g'}, \tag{2.60}$$

$$\mathbf{x} \in \mathcal{V}_{c_0} \text{ if } \sum_{c=1}^{c_0-1} \sum_{g=1}^{G} V_c Q_{c,g} \leq \xi \leq \sum_{c=1}^{c_0} \sum_{g=1}^{G} V_c Q_{c,g}. \tag{2.61}$$

These relations determine a particle's initial state $(\mathbf{x}, \mathbf{\Omega}, E)$, or $(\mathbf{x}, \mathbf{\Omega}, g)$ for the multigroup problem. As long as the particle's energy is greater than zero, it begins to move throughout the system. The distance that it travels before colliding with an atom (or molecule) in the medium is described next.

2.6.2 Sampling the Distance-To-Next Collision

The probability distribution that determines the distance-to-next collision can be obtained from the expression

$$p(s) = \mathrm{C}\,\frac{\psi(s)}{\psi(0)}, \tag{2.62}$$

where C is the normalization constant and $\psi(s)$ is the flux determined by the equation that describes transport through a constant medium along the trajectory of a particle:

$$\begin{aligned} \frac{d\psi}{ds}(s) + \Sigma_t \psi(s) &= 0, \\ \psi(0) &= \psi_0. \end{aligned} \tag{2.63}$$

The solution to this equation is

$$\psi(s) = \psi_0 e^{-\Sigma_t s}. \tag{2.64}$$

The resulting probability distribution function, then, is given by

$$p(s) = \Sigma_t e^{-\Sigma_t s}. \tag{2.65}$$

To sample from this distribution, we simply invert the cumulative probability distribution to obtain ($\xi \in [0, 1]$):

$$s = -\frac{\log(\xi)}{\Sigma_t(E)}, \tag{2.66}$$

where we have included the energy dependence of $\Sigma_t(E)$, since the energy does not change along the trajectory. The multigroup distribution is found by simply setting $\Sigma_t(E) = \Sigma_{t,g}$ over the energy range $(E_g, E_{g-1}]$, where $\Sigma_{t,g}$ is given by Eq. 2.12b. This results in the following expression:

$$s = -\frac{\log(\xi)}{\Sigma_{t,g}}. \tag{2.67}$$

Once a distance has been sampled, the particle is moved to the new location and it is determined whether the particle has leaked out of the system or remains in the

system and collides. If the particle has exited the system, the particle history is terminated; otherwise, the particle is either captured or scattered.

2.6.3 Sampling the Collision Type: Capture or Scatter

The analog Monte Carlo method simulates the actual physical reactions that occur as particles move throughout the system. In shielding applications, when a particle collides with an atom (or molecule) of the medium, it either scatters or is captured according to some probability. The probability that a particle collision results in a scattering event is given by

$$p_{\text{scat}}(\mathbf{x}, E) = \frac{\Sigma_s(\mathbf{x}, E)}{\Sigma_t(\mathbf{x}, E)}, \tag{2.68}$$

where the spatial dependence is due to regional material differences. If $\xi \leq p_{\text{scat}}(\mathbf{x}, E)$, the collision results in a scattering event; otherwise, the particle is captured.

2.6.4 Sampling the Scattering Distribution

If a particle undergoes a scattering event, then the outgoing energy and direction must be determined. The probability that a particle scatters from energy E' to E, and from direction $\mathbf{\Omega}'$ to $\mathbf{\Omega}$ is given by the normalized scattering kernel:

$$p(\mathbf{x}, \mathbf{\Omega}' \cdot \mathbf{\Omega}, E' \to E) = \frac{\Sigma_s(\mathbf{x}, \mathbf{\Omega}' \cdot \mathbf{\Omega}, E' \to E)}{\Sigma_s(\mathbf{x}, E')}. \tag{2.69}$$

Using Eq. 2.10, this distribution can be written as

$$\begin{aligned} p(\mathbf{x}, \mathbf{\Omega}' \cdot \mathbf{\Omega}, E' \to E) &= p(\mathbf{x}, E' \to E) \cdot p(\mathbf{x}, \mathbf{\Omega}' \cdot \mathbf{\Omega} \,|\, E' \to E) \\ &= \frac{\Sigma_{s0}(\mathbf{x}, E' \to E)}{\Sigma_s(\mathbf{x}, E')} \cdot \sum_{n=0}^{N} \frac{2n+1}{4\pi} P_n(\mathbf{\Omega}' \cdot \mathbf{\Omega}) \frac{\Sigma_{sn}(\mathbf{x}, E' \to E)}{\Sigma_{s0}(\mathbf{x}, E' \to E)}, \end{aligned} \tag{2.70}$$

where $p(\mathbf{x}, \mathbf{\Omega}' \cdot \mathbf{\Omega} \,|\, E' \to E)$ is the conditional probability distribution function for the outgoing direction $\mathbf{\Omega}$, given that the outgoing energy is E. For scattering of order $N \leq 2$, the cumulative conditional probability distribution function can be inverted and directly sampled. For higher order scattering, the cumulative conditional probability distribution is a polynomial of order $n > 3$; a root solver must be used to solve this, though, typically rejection sampling is used on the conditional probability distribution function. The probability density function that describes the outgoing

energy can be solved directly by inverting the cumulative distribution function if the function is simple enough, or through rejection sampling if the function is too complicated or is more efficiently sampled through rejection. The multigroup distribution is given by simply substituting $\Sigma_{sn}(\mathbf{x}, E' \rightarrow E) = \Sigma_{sn,g' \rightarrow g}(\mathbf{x})$ and $\Sigma_s(\mathbf{x}, E) = \Sigma_{s,g}(\mathbf{x})$. We obtain:

$$\begin{aligned} p_{g' \rightarrow g}(\mathbf{x}, \boldsymbol{\Omega}' \cdot \boldsymbol{\Omega}) &= p_{g' \rightarrow g}(\mathbf{x}) \cdot p(\mathbf{x}, \boldsymbol{\Omega}' \cdot \boldsymbol{\Omega} \,|\, g' \rightarrow g) \\ &= \frac{\Sigma_{s0,g' \rightarrow g}(\mathbf{x})}{\Sigma_{s,g'}(\mathbf{x})} \cdot \sum_{n=0}^{N} \frac{2n+1}{4\pi} P_n(\boldsymbol{\Omega}' \cdot \boldsymbol{\Omega}) \frac{\Sigma_{sn,g' \rightarrow g}(\mathbf{x}, \boldsymbol{\Omega}' \cdot \boldsymbol{\Omega})}{\Sigma_{s0,g' \rightarrow g}(\mathbf{x})}, \end{aligned} \tag{2.71}$$

where $\Sigma_{sn,g' \rightarrow g}(\mathbf{x})$ is defined by Eq. 2.32 and $p(\mathbf{x}, \boldsymbol{\Omega}' \cdot \boldsymbol{\Omega} \,|\, g' \rightarrow g)$ is the conditional probability distribution for the outgoing direction $\boldsymbol{\Omega}$, given that the particle exits the scattering event in group g. This distribution is sampled in the same manner as in the continuous energy case. The discrete probability distribution that determines the group the particle is in after a scattering event is sampled in the typical way ($\xi \in [0, 1]$):

$$g = g_s \text{ if } \sum_{g''=1}^{g_s - 1} p_{g' \rightarrow g''}(\mathbf{x}) < \xi \leq \sum_{g''=1}^{g_s} p_{g' \rightarrow g''}(\mathbf{x}). \tag{2.72}$$

2.7 Particle Weight

A useful concept in Monte Carlo simulations is the statistical weight of the particle. For analog simulations, the concept of weight is less important, but variance reduction techniques require the notion of particle weight. The general idea of particle weight is to allow a particle to represent a different number of physical particles as it moves throughout phase-space. In analog simulations, a particle begins with weight $w_0 = 1$, and as the particle moves throughout the system, its weight w does not change. This means that the particle always represents the same number of physical particles no matter where it exists in phase-space. For problems where there are large variations in particle density throughout phase-space, it is not optimal to require a simulation particle to always represent the same number of physical particles as it moves through phase space. In non-analog Monte Carlo simulations, we allow the particle weight to vary. The fraction (or multiple) of a physical particle that the simulation particle represents at any point in phase-space can be determined by the simple ratio, w/w_0. In general, the particle weight shows up in every interaction and tally event during the particle history. However, for analog Monte Carlo schemes,

the weight does not change throughout the particle history, so there has been no mention of this in the previous sections on particle interactions.

2.8 Estimators

In Monte Carlo simulations, we wish to obtain estimates of some quantity of interest, such as the the scalar flux or a response. The two basic estimators that are used to obtain these estimates are the path length estimator and the collision estimator. Both of these estimators require a bin structure in which to tally. A common bin structure is an energy set defined by the boundaries $\{E_g\}_{g=0}^{G}$, and a spatial element set $\{\mathcal{V}_c\}_{c=1}^{N_{\text{cells}}}$ with each element having a volume V_c. The bin structure can also include an angular set; but, for this thesis, we do not use one.

2.8.1 Path Length Estimator

The nth simulation particle provides a path length estimate for the scalar flux given by

$$\phi_{c,g,n}^{\text{path}} = \frac{Q_T}{V_c} \sum_{i=1}^{I_{c,g,n}} l_i \, w_i, \tag{2.73}$$

where Q_T is total system source rate, $I_{c,g,n}$ is the number of track lengths generated by the nth simulation particle in volume V_c and in energy group g, l_i is an individual track length, and w_i is the weight of the particle as it generates the track length l_i. Note that since the track length and weight are independent of energy, this estimator is valid for a continuous-energy as well as multigroup simulation. If we were to use this type of estimator to obtain a response, then we would need to include the energy-dependent response in the summation of the track lengths. That is,

$$\mathcal{R}_{c,g,n}^{\text{path}} = \frac{Q_T}{V_c} \sum_{i=1}^{I_{c,g,n}} \mathcal{R}_c(E_i) \, l_i \, w_i, \tag{2.74}$$

where $\mathcal{R}_c(E_i)$ represents the response of a particle with energy E_i. For the multigroup problem, $\mathcal{R}_c(E_i) = \mathcal{R}_{c,g}$.

To obtain the mean value for the scalar flux and the variance of the mean for a simulation with N particles, we use the following equations:

$$\phi_{c,g} = \frac{1}{N}\sum_{n=1}^{N}\phi_{c,g,n}^{\text{path}} \tag{2.75}$$

$$= \frac{Q_T}{N\,V_c}\sum_{n=1}^{N}\sum_{i=1}^{I_{c,g,n}} l_i\,w_i, \tag{2.76}$$

$$\text{Var}[\phi_{c,g}] = \frac{1}{N-1}\sum_{n=1}^{N}(\phi_{c,g,n}^{\text{path}} - \phi_{c,g})^2 \tag{2.77}$$

$$= \frac{N}{N-1}\left[\frac{Q_T^2}{N\,V_c^2}\sum_{n=1}^{N}\left(\sum_{i=1}^{I_{c,g,n}} l_i\,w_i\right)^2 - \phi_{c,g}^2\right]. \tag{2.78}$$

During the simulation, the only quantities that need to be stored are the weighted total path length for the mean and the weighted total path length squared for the variance of the mean. Similar expressions can be written down to obtain a response.

2.8.2 Collision Estimator

The nth simulation particle provides a collision estimator for the scalar flux that is given by

$$\phi_{c,g,n}^{\text{coll}} = \frac{Q_T}{V_c}\sum_{i=1}^{I_{c,g,n}}\frac{w_i}{\Sigma_{t,c}(E_i)}, \tag{2.79}$$

where $I_{c,g,n}$ is the number of collisions by the nth simulation particle in volume V_c in energy group g, w_i is the weight of the particle when it collides with a nucleus, and E_i is the energy in the range $(E_g, E_{g-1}]$ at which the particle collides. The multigroup version of this estimator simply replaces $\Sigma_{t,c}(E_i)$ with $\Sigma_{t,c,g}$, which results in the following:

$$\phi_{c,g,n}^{\text{coll}} = \frac{Q_T}{V_c}\sum_{i=1}^{I_{c,g,n}}\frac{w_i}{\Sigma_{t,c,g}}. \tag{2.80}$$

Just like the path length estimator, the collision estimator can also be used to obtain a response:

$$\mathcal{R}_{c,g,n}^{\text{coll}} = \frac{Q_T}{V_c}\sum_{i=1}^{I_{c,g,n}}\frac{\mathcal{R}_c(E_i)\,w_i}{\Sigma_{t,c}(E_i)}, \tag{2.81}$$

where $\mathcal{R}_c(E_i)$ again represents the response of a particle with energy E_i. For the multigroup problem, $\mathcal{R}_c(E_i) = \mathcal{R}_{c,g}$ and $\Sigma_{t,c}(E_i) = \Sigma_{t,c,g}$.

The mean and the variance of the mean are determined in the same way as the

for the path length estimator:

$$\phi_{c,g} = \frac{1}{N}\sum_{n=1}^{N}\phi_{c,g,n}^{\text{coll}} \tag{2.82}$$

$$= \frac{Q_T}{N\,V_c}\sum_{n=1}^{N}\sum_{i=1}^{I_{c,g,n}}\frac{w_i}{\Sigma_t(E_i)}, \tag{2.83}$$

$$\text{Var}[\phi_{c,g}] = \frac{1}{N-1}\sum_{n=1}^{N}(\phi_{c,g,n}^{\text{coll}} - \phi_{c,g})^2 \tag{2.84}$$

$$= \frac{N}{N-1}\left[\frac{Q_T^2}{N\,V_c^2}\sum_{n=1}^{N}\left(\sum_{i=1}^{I_{c,g,n}}\frac{w_i}{\Sigma_t(E_i)}\right)^2 - \phi_{c,g}^2\right]. \tag{2.85}$$

We again note that during the simulation, the only quantities that need to be stored are the sums of the weighted inverse total cross-section for the mean and this quantity squared for the variance of the mean. The multigroup expression simply replaces $\Sigma_t(E_i)$ with $\Sigma_{t,g}$. Similar expressions exist for obtaining a response.

2.9 Central Limit Theorem

The Central Limit Theorem states that, if a distribution with a mean μ and a variance σ^2 is sampled from, the distribution of the mean approaches a normal distribution with mean μ and variance σ^2/N as the sample size, N, increases. Due to this theorem, some fundamental properties of the normal distribution may be used to describe the statistical characteristics of the estimators. For example, the normal distribution has the following property

$$P\left(|\bar{X}_N - \mu| < l\frac{\sigma_N}{\sqrt{N}}\right) < C_l, \tag{2.86}$$

where $\bar{X}_N$ is the sample mean with a sample size of N, σ_N is the sample standard deviation from the original distribution (meaning $\sigma_N/\sqrt{N}$ is the estimate of the standard deviation of the normal distribution), and C_l is the confidence level associated with the confidence interval, a measure of the number of standard deviations l. For l = 1, 2, and 3 standard deviations, the associated confidence level is C_l = 0.683, 0.954, and 0.997, respectively. This means that, if the sample size is large enough, the distribution of the sample mean is nearly Gaussian, implying that 68.3% of the values sampled lie within one standard deviation of the true mean, 95.4% of the

values lie within two standard deviations of the true mean, and 99.7% of the values lie within three standard deviations of the true mean. The smaller the variance, the more sharply peaked the Gaussian distribution, resulting in values of the sample mean that are much closer to the true mean. For this reason, techniques have been developed in Monte Carlo simulations to reduce the variance.

2.10 Variance Reduction

The analog Monte Carlo method was described in Section 2.6. For problems with high scattering ratios and small optical thicknesses, the analog Monte Carlo method is sufficient, but for most real world problems, variance reduction techniques must be employed. Two common techniques are *implicit capture* (sometimes called *survival biasing*) and *weight windows* [38–40].

2.10.1 Implicit Capture

A simple way to decrease the variance is to simulate capture implicitly. Instead of ending a simulation particle's history by capture, the particle's weight is reduced by the probability that the particle survives the collision event and scatters. That is, if the weight of the particle is w_i upon entering a collision event at $(\mathbf{x}, \mathbf{\Omega}, E)$, then the weight at which the particle exits the collision event w_f is given by:

$$w_f = w_i \frac{\Sigma_s(\mathbf{x}, E)}{\Sigma_t(\mathbf{x}, E)}. \tag{2.87}$$

The multigroup equivalent is given by:

$$w_f = w_i \frac{\Sigma_{s,g}(\mathbf{x})}{\Sigma_{t,g}(\mathbf{x})}. \tag{2.88}$$

This technique generally allows more Monte Carlo particles to penetrate to greater distances, which results in the accumulation of more data for each of the tallies. However, in the deeper parts of the problem, the particle weights can vary substantially, resulting in an undesirably large variance associated with high-weight particles, and undesirably long computation times for low-weight particles. To mitigate these effects, we introduce another variance reduction technique – *weight windows*.

2.10.2 Weight Windows

The basic idea of the weight window is to constrain the weight of Monte Carlo particles to lie within some specified range $[w_l, w_u]$. The upper and lower bound are chosen in reference to a central point, w_c, within the range: $w_l = w_c/m$ and $w_u = mw_c$ where m is usually chosen to be roughly 3. In general, the weight window center w_c can be a function of space, energy and angle, but this thesis restricts its use to space and energy only.

Since the weight window constrains the weight of Monte Carlo particles, we can use weight windows in conjunction with implicit capture to mitigate the effect of high-weight particles on the variance and of low-weight particles on the computation time. If a particle's weight exceeds the upper bound of the weight window, w_u, then the particle is *split* into several particles whose weights will lie within the weight window. That is, if $w > w_u$, we split the particle into n new particles each having weight w_{split}:

$$n = \text{Round}\left(\frac{w_u}{w}\right), \tag{2.89}$$

$$w_{split} = \frac{w}{n}, \tag{2.90}$$

where the function Round() represents standard rounding. We note that the total weight of the original particle is conserved in splitting (i.e. $w = nw_{split}$). Most Monte Carlo algorithms only track one particle at a time, meaning that $n-1$ particles must be "banked" until one of the split particles is terminated. Then the rest of the particles are allowed to finish, one at a time. If the weight window center is chosen poorly, much splitting can occur, resulting in a massive particle bank that quickly depletes computer memory.

To constrain the particle weight at the lower bound, *Russian roulette* is performed. When $w < w_l$, we sample a random number $\xi \in [0, 1]$ and either terminate the particle or reset its weight to w_c:

$$\begin{aligned} &\text{if } \xi < \frac{w}{w_c}, \quad \text{reset } w = w_c, \\ &\text{if } \xi > \frac{w}{w_c}, \quad \text{terminate } w = 0. \end{aligned} \tag{2.91}$$

Russian roulette does not preserve the weight for an individual history, but for a

large number of histories the weight is preserved on the average. That is,

$$\begin{aligned} w_{avg} &= w_c \cdot p_{reset} + 0 \cdot p_{terminate} \\ &= w_c \cdot \frac{w}{w_c} + 0 \cdot \left(1 - \frac{w}{w_c}\right) \\ &= w. \end{aligned} \tag{2.92}$$

It should be apparent that Russian roulette and splitting can be applied to continuous energy problems as well as multigroup problems. For continuous energy problems, $w_c = w_c(\mathbf{x}, E)$ and for multigroup problems $w_c = w_{c,g}(\mathbf{x})$. In subsequent chapters, a fuller explanation will be given of weight windows, especially related to the choice of w_c.

Chapter III

Spatially-Discretized Transport-Corrected Multigroup Diffusion Equations

The spatial discretization of the diffusion equation is derived in this chapter for standard diffusion, but with modifications for the transport-corrected diffusion equation. The spatially-discretized transport-corrected diffusion equation attempts to preserve the asymptotic transport solution on any Cartesian grid. Wherever a deterministic estimate of the forward or adjoint scalar flux is required for the work presented in this thesis, we use the solution to the spatially-discretized transport-corrected diffusion equations presented in this chapter.

3.1 The Cell-Edge Diffusion Discretization

To obtain a diffusion equation that can be solved deterministically, a spatial approximation must be introduced. The spatial approximation that we use is called the *cell-edge diffusion discretization*. To derive this approximation, we utilize the widely-used finite volume method for numerical discretization, which involves integrating the equation over a finite volume surrounding a grid point. In 3-D Cartesian geometry, this volume is a hexahedral box. The bounds of integration, which determine the box volume, are determined according to the location of the corner point within the rectilinear grid, shown in Figure 3.1. The four types of grid point locations are the following: interior, face, edge, and corner.

Using the finite volume method, we can derive a set of discretized equations that describe the scalar flux at every grid point, $\phi_{g,i+1/2,j+1/2,k+1/2}$, for $i \in [0, I]$, $j \in [0, J]$, and $k \in [0, K]$. We assume that within each cell (defined by the eight grid points that make up its corners) the material properties are uniform. However, since the finite volume is fixed about a grid point (i.e. one of the cell corners), there will be constants

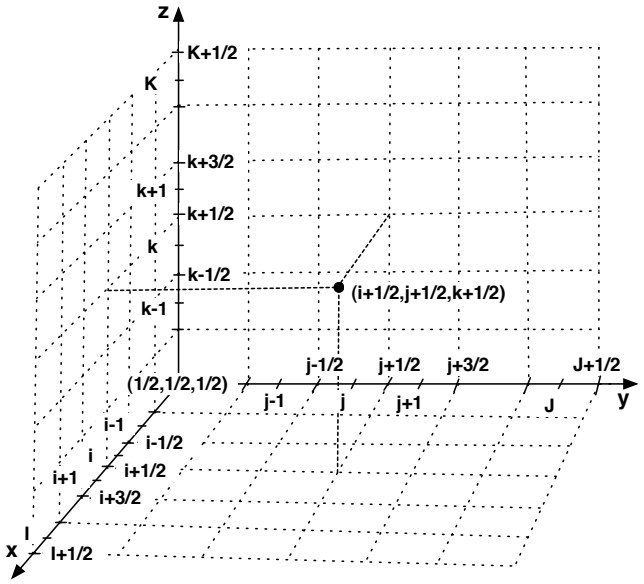

Figure 3.1: Three-dimensional grid for the cell-edge diffusion discretization.

such as cross sections that will be averages of all the cell constants that surround the grid point. To simplify the derivation, we use the following nomenclature to describe these cell-averaged constants and the basic features of the mesh:

Basic Mesh Parameters and Definitions

$$\Delta x_i = \text{length of cell (i,j,k) in the x-direction,} \tag{3.1a}$$

$$\Delta y_j = \text{length of cell (i,j,k) in the y-direction,} \tag{3.1b}$$

$$\Delta z_k = \text{length of cell (i,j,k) in the z-direction,} \tag{3.1c}$$

$$V_{i,j,k} = \Delta x_i \Delta y_j \Delta z_k, \tag{3.1d}$$

$$x_0 = x_{1/2}, \tag{3.1e}$$

$$x_{I+1} = x_{I+1/2}, \tag{3.1f}$$

$$y_0 = y_{1/2}, \tag{3.1g}$$

$$y_{J+1} = y_{J+1/2}, \tag{3.1h}$$

$$z_0 = z_{1/2}, \tag{3.1i}$$

$$z_{K+1} = z_{K+1/2}. \tag{3.1j}$$

Volume-Weighted Cross-Sections and Source

$$\bar{\Sigma}^{\text{interior}}_{g,i,j,k} = \frac{1}{8}\big[(\Sigma_g V)_{i,j,k} + (\Sigma_g V)_{i,j+1,k} + (\Sigma_g V)_{i,j,k+1} + (\Sigma_g V)_{i,j+1,k+1} + (\Sigma_g V)_{i+1,j,k} + (\Sigma_g V)_{i+1,j+1,k} + (\Sigma_g V)_{i+1,j,k+1} + (\Sigma_g V)_{i+1,j+1,k+1}\big], \quad (3.2a)$$

$$\bar{\Sigma}^{\text{x-face}}_{g,i,j,k} = \frac{1}{8}\big[(\Sigma_g V)_{i,j,k} + (\Sigma_g V)_{i,j+1,k} + (\Sigma_g V)_{i,j,k+1} + (\Sigma_g V)_{i,j+1,k+1}\big], \quad (3.2b)$$

$$\bar{\Sigma}^{\text{y-face}}_{g,i,j,k} = \frac{1}{8}\big[(\Sigma_g V)_{i,j,k} + (\Sigma_g V)_{i+1,j,k} + (\Sigma_g V)_{i,j,k+1} + (\Sigma_g V)_{i+1,j,k+1}\big], \quad (3.2c)$$

$$\bar{\Sigma}^{\text{z-face}}_{g,i,j,k} = \frac{1}{8}\big[(\Sigma_g V)_{i,j,k} + (\Sigma_g V)_{i+1,j,k} + (\Sigma_g V)_{i,j+1,k} + (\Sigma_g V)_{i+1,j+1,k}\big], \quad (3.2d)$$

$$\bar{\Sigma}^{\text{x-edge}}_{g,i,j,k} = \frac{1}{8}\big[(\Sigma_g V)_{i,j,k} + (\Sigma_g V)_{i+1,j,k}\big], \quad (3.2e)$$

$$\bar{\Sigma}^{\text{y-edge}}_{g,i,j,k} = \frac{1}{8}\big[(\Sigma_g V)_{i,j,k} + (\Sigma_g V)_{i,j+1,k}\big], \quad (3.2f)$$

$$\bar{\Sigma}^{\text{z-edge}}_{g,i,j,k} = \frac{1}{8}\big[(\Sigma_g V)_{i,j,k} + (\Sigma_g V)_{i,j,k+1}\big], \quad (3.2g)$$

$$\bar{\Sigma}^{\text{corner}}_{g,i,j,k} = \frac{1}{8}\big[(\Sigma_g V)_{i,j,k}\big]. \quad (3.2h)$$

Discretized Diffusion Operator

$$X^{\text{interior}}_{g,i,j,k} = \frac{1}{4}\left[\left(\frac{D_g V}{\Delta x^2}\right)_{i,j,k} + \left(\frac{D_g V}{\Delta x^2}\right)_{i,j+1,k} + \left(\frac{D_g V}{\Delta x^2}\right)_{i,j,k+1} + \left(\frac{D_g V}{\Delta x^2}\right)_{i,j+1,k+1}\right], \quad (3.3a)$$

$$Y^{\text{interior}}_{g,i,j,k} = \frac{1}{4}\left[\left(\frac{D_g V}{\Delta y^2}\right)_{i,j,k} + \left(\frac{D_g V}{\Delta y^2}\right)_{i+1,j,k} + \left(\frac{D_g V}{\Delta y^2}\right)_{i,j,k+1} + \left(\frac{D_g V}{\Delta y^2}\right)_{i+1,j,k+1}\right], \quad (3.3b)$$

$$Z^{\text{interior}}_{g,i,j,k} = \frac{1}{4}\left[\left(\frac{D_g V}{\Delta z^2}\right)_{i,j,k} + \left(\frac{D_g V}{\Delta z^2}\right)_{i+1,j,k} + \left(\frac{D_g V}{\Delta z^2}\right)_{i,j+1,k} + \left(\frac{D_g V}{\Delta z^2}\right)_{i+1,j+1,k}\right], \quad (3.3c)$$

$$X^{\text{y-face}}_{g,i,j,k} = \frac{1}{4}\left[\left(\frac{D_g V}{\Delta x^2}\right)_{i,j,k} + \left(\frac{D_g V}{\Delta x^2}\right)_{i,j,k+1}\right], \quad (3.3d)$$

$$X^{\text{z-face}}_{g,i,j,k} = \frac{1}{4}\left[\left(\frac{D_g V}{\Delta x^2}\right)_{i,j,k} + \left(\frac{D_g V}{\Delta x^2}\right)_{i,j+1,k}\right], \quad (3.3e)$$

$$Y^{\text{x-face}}_{g,i,j,k} = \frac{1}{4}\left[\left(\frac{D_g V}{\Delta y^2}\right)_{i,j,k} + \left(\frac{D_g V}{\Delta y^2}\right)_{i,j,k+1}\right], \quad (3.3f)$$

$$Y^{\text{z-face}}_{g,i,j,k} = \frac{1}{4}\left[\left(\frac{D_g V}{\Delta y^2}\right)_{i,j,k} + \left(\frac{D_g V}{\Delta y^2}\right)_{i+1,j,k}\right], \quad (3.3g)$$

$$Z^{\text{x-face}}_{g,i,j,k} = \frac{1}{4}\left[\left(\frac{D_g V}{\Delta z^2}\right)_{i,j,k} + \left(\frac{D_g V}{\Delta z^2}\right)_{i,j+1,k}\right], \tag{3.3h}$$

$$Z^{\text{y-face}}_{g,i,j,k} = \frac{1}{4}\left[\left(\frac{D_g V}{\Delta z^2}\right)_{i,j,k} + \left(\frac{D_g V}{\Delta z^2}\right)_{i+1,j,k}\right], \tag{3.3i}$$

$$X^{\text{edge}}_{g,i,j,k} = \frac{1}{4}\left[\left(\frac{D_g V}{\Delta x^2}\right)_{i,j,k}\right], \tag{3.3j}$$

$$Y^{\text{edge}}_{g,i,j,k} = \frac{1}{4}\left[\left(\frac{D_g V}{\Delta y^2}\right)_{i,j,k}\right], \tag{3.3k}$$

$$Z^{\text{edge}}_{g,i,j,k} = \frac{1}{4}\left[\left(\frac{D_g V}{\Delta z^2}\right)_{i,j,k}\right]. \tag{3.3l}$$

Area (on Boundary)

$$\bar{A}^{\text{x-face}}_{g,i,j,k} = \frac{1}{4}\left[(\Delta y\Delta z)_{i,j,k} + (\Delta y\Delta z)_{i,j+1,k} + (\Delta y\Delta z)_{i,j,k+1} + (\Delta y\Delta z)_{i,j+1,k+1}\right], \tag{3.4a}$$

$$\bar{A}^{\text{x-face, y-edge}}_{g,i,j,k} = \frac{1}{4}\left[(\Delta y\Delta z)_{i,j,k} + (\Delta y\Delta z)_{i,j+1,k}\right], \tag{3.4b}$$

$$\bar{A}^{\text{x-face, z-edge}}_{g,i,j,k} = \frac{1}{4}\left[(\Delta y\Delta z)_{i,j,k} + (\Delta y\Delta z)_{i,j,k+1}\right], \tag{3.4c}$$

$$\bar{A}^{\text{x-face, corner}}_{g,i,j,k} = \frac{1}{4}\left[(\Delta y\Delta z)_{i,j,k}\right], \tag{3.4d}$$

$$\bar{A}^{\text{y-face}}_{g,i,j,k} = \frac{1}{4}\left[(\Delta x\Delta z)_{i,j,k} + (\Delta x\Delta z)_{i+1,j,k} + (\Delta x\Delta z)_{i,j,k+1} + (\Delta x\Delta z)_{i+1,j,k+1}\right], \tag{3.4e}$$

$$\bar{A}^{\text{y-face, x-edge}}_{g,i,j,k} = \frac{1}{4}\left[(\Delta x\Delta z)_{i,j,k} + (\Delta x\Delta z)_{i+1,j,k}\right], \tag{3.4f}$$

$$\bar{A}^{\text{y-face, z-edge}}_{g,i,j,k} = \frac{1}{4}\left[(\Delta x\Delta z)_{i,j,k} + (\Delta x\Delta z)_{i,j,k+1}\right], \tag{3.4g}$$

$$\bar{A}^{\text{y-face, corner}}_{g,i,j,k} = \frac{1}{4}\left[(\Delta x\Delta z)_{i,j,k}\right], \tag{3.4h}$$

$$\bar{A}^{\text{z-face}}_{g,i,j,k} = \frac{1}{4}\left[(\Delta x\Delta y)_{i,j,k} + (\Delta x\Delta y)_{i+1,j,k} + (\Delta x\Delta y)_{i,j+1,k} + (\Delta x\Delta y)_{i+1,j+1,k}\right], \tag{3.4i}$$

$$\bar{A}^{\text{z-face, x-edge}}_{g,i,j,k} = \frac{1}{4}\left[(\Delta x\Delta y)_{i,j,k} + (\Delta x\Delta y)_{i+1,j,k}\right], \tag{3.4j}$$

$$\bar{A}^{\text{z-face, y-edge}}_{g,i,j,k} = \frac{1}{4}\left[(\Delta x\Delta y)_{i,j,k} + (\Delta x\Delta y)_{i,j+1,k}\right], \tag{3.4k}$$

$$\bar{A}^{\text{z-face, corner}}_{g,i,j,k} = \frac{1}{4}\left[(\Delta x\Delta y)_{i,j,k}\right]. \tag{3.4l}$$

When the multigroup diffusion equation is integrated over the finite volume, there are three types of integrals that must be evaluated in terms of the unknown flux variables in order to solve the resulting equations – reaction rate integrals, diffusion

rate integrals, and leakage rate integrals. To evaluate these, we must use the following approximations:

1. Reaction Rate Integrals

$$\int_{z_k}^{z_{k+1}} \int_{y_j}^{y_{j+1}} \int_{x_i}^{x_{i+1}} \Sigma_g(\mathbf{x})\phi_g(\mathbf{x})dxdydz \approx \phi_{g,i+1/2,j+1/2,k+1/2}\bar{\Sigma}_{g,i,j,k}. \tag{3.5}$$

2. Diffusion Rate Integrals

$$\int_{z_k}^{z_{k+1}} \int_{y_j}^{y_{j+1}} D_g(x_i, y, z)\frac{\partial \phi_g}{\partial x}(x_i, y, z)dydz \approx X_{g,i,j,k}\left(\phi_{g,i+1/2,j+1/2,k+1/2} - \phi_{g,i-1/2,j+1/2,k+1/2}\right), \tag{3.6a}$$

$$\int_{z_k}^{z_{k+1}} \int_{x_i}^{x_{i+1}} D_g(x, y_j, z)\frac{\partial \phi_g}{\partial y}(x, y_j, z)dxdz \approx Y_{g,i,j,k}\left(\phi_{g,i+1/2,j+1/2,k+1/2} - \phi_{g,i+1/2,j-1/2,k+1/2}\right), \tag{3.6b}$$

$$\int_{y_j}^{y_{j+1}} \int_{x_i}^{x_{i+1}} D_g(x, y, z_k)\frac{\partial \phi_g}{\partial z}(x, y, z_k)dxdy \approx Z_{g,i,j,k}\left(\phi_{g,i+1/2,j+1/2,k+1/2} - \phi_{g,i+1/2,j+1/2,k-1/2}\right). \tag{3.6c}$$

3. Leakage Rate Integrals

$$\int_{z_k}^{z_{k+1}} \int_{y_j}^{y_{j+1}} D_g(x_i, y, z)\frac{\partial \phi_g}{\partial x}(x_i, y, z)dydz \approx A_{g,i,j,k}\phi_{g,i+1/2,j+1/2,k+1/2}, \quad x_i = 0, X, \tag{3.7a}$$

$$\int_{z_k}^{z_{k+1}} \int_{x_i}^{x_{i+1}} D_g(x, y_j, z)\frac{\partial \phi_g}{\partial y}(x, y_j, z)dxdz \approx A_{g,i,j,k}\phi_{g,i+1/2,j+1/2,k+1/2}, \quad y_j = 0, Y, \tag{3.7b}$$

$$\int_{y_j}^{y_{j+1}} \int_{x_i}^{x_{i+1}} D_g(x, y, z_k)\frac{\partial \phi_g}{\partial z}(x, y, z_k)dxdy \approx A_{g,i,j,k}\phi_{g,i+1/2,j+1/2,k+1/2}, \quad z_k = 0, Z. \tag{3.7c}$$

where $\bar{\Sigma}_{g,i,j,k}$ is defined by Eqs. 3.2, $X_{g,i,j,k}$, $Y_{g,i,j,k}$, and $Z_{g,i,j,k}$ are defined by Eqs. 3.3, and $A_{g,i,j,k}$ is defined by Eqs. 3.4. The specific constant depends on the type of grid point (i.e. interior, face, edge, or corner).

Interior

For an interior grid point, we operate on the diffusion equation (Eq. 2.24) by $\int_{z_k}^{z_{k+1}} \int_{y_j}^{y_{j+1}} \int_{x_i}^{x_{i+1}} (\cdot) dxdydz$ to obtain the following equation:

$$\begin{aligned} &- Z^{\text{interior}}_{g,i,j,k} \phi_{g,i+1/2,j+1/2,k-1/2} - Y^{\text{interior}}_{g,i,j,k} \phi_{g,i+1/2,j-1/2,k+1/2} - X^{\text{interior}}_{g,i,j,k} \phi_{g,i-1/2,j+1/2,k+1/2} \\ &\quad + C^{\text{interior}}_{g,i,j,k} \phi_{g,i+1/2,j+1/2,k+1/2} - X^{\text{interior}}_{g,i+1,j,k} \phi_{g,i+3/2,j+1/2,k+1/2} \\ &\quad - Y^{\text{interior}}_{g,i,j+1,k} \phi_{g,i+1/2,j+3/2,k+1/2} - Z^{\text{interior}}_{g,i,j,k+1} \phi_{g,i+1/2,j+1/2,k+3/2} \\ &\quad = S^{\text{interior}}_{g,i,j,k}, \\ &\quad 1 \le g \le G,\ 1 \le i \le I-1,\ 1 \le j \le J-1,\ 1 \le k \le K-1, \end{aligned} \tag{3.8}$$

where

$$\begin{aligned} C^{\text{interior}}_{g,i,j,k} &= X^{\text{interior}}_{g,i,j,k} + X^{\text{interior}}_{g,i+1,j,k} + Y^{\text{interior}}_{g,i,j,k} + Y^{\text{interior}}_{g,i,j+1,k} + Z^{\text{interior}}_{g,i,j,k} \\ &\quad + Z^{\text{interior}}_{g,i,j,k+1} + \bar{\Sigma}^{\text{interior}}_{R,g,i,j,k}, \end{aligned} \tag{3.9a}$$

$$S^{\text{interior}}_{g,i,j,k} = \sum_{\substack{g'=1 \\ g' \neq g}}^{G} \bar{\Sigma}^{\text{interior}}_{s,g' \to g,i,j,k} \phi_{g',i+1/2,j+1/2,k+1/2} + \bar{Q}^{\text{interior}}_{g,i,j,k}. \tag{3.9b}$$

Face: x=0

For a boundary grid point on the face $x = 0$, we operate on the diffusion equation (Eq. 2.24) by $\int_{z_k}^{z_{k+1}} \int_{y_j}^{y_{j+1}} \int_{x_{1/2}}^{x_1} (\cdot) dxdydz$ and use the boundary condition (Eq. 2.25) to obtain the following equation:

$$\begin{aligned} &- Z^{\text{x-face}}_{g,1,j,k} \phi_{g,1/2,j+1/2,k-1/2} - Y^{\text{x-face}}_{g,1,j,k} \phi_{g,1/2,j-1/2,k+1/2} \\ &\quad + C^{\text{x-face}}_{g,1,j,k} \phi_{g,1/2,j+1/2,k+1/2} - X^{\text{interior}}_{g,1,j,k} \phi_{g,3/2,j+1/2,k+1/2} \\ &\quad - Y^{\text{x-face}}_{g,1,j+1,k} \phi_{g,1/2,j+3/2,k+1/2} - Z^{\text{x-face}}_{g,1,j,k+1} \phi_{g,1/2,j+1/2,k+3/2} \\ &\quad = S^{\text{x-face}}_{g,1,j,k}, \\ &\quad 1 \le g \le G,\ 1 \le j \le J-1,\ 1 \le k \le K-1, \end{aligned} \tag{3.10}$$

where

$$C^{\text{x-face}}_{g,1,j,k} = B^{\text{x-face}}_{g,1,j,k} + X^{\text{interior}}_{g,1,j,k} + Y^{\text{x-face}}_{g,1,j,k} + Y^{\text{x-face}}_{g,1,j+1,k} + Z^{\text{x-face}}_{g,1,j,k} + Z^{\text{x-face}}_{g,1,j,k+1} + \bar{\Sigma}^{\text{x-face}}_{R,g,1,j,k}, \tag{3.11a}$$

$$B^{\text{x-face}}_{g,1,j,k} = \begin{cases} \frac{A^{\text{x-face}}_{g,1,j,k}}{2} & , \text{ vacuum boundary,} \\ 0 & , \text{ reflecting boundary,} \end{cases} \tag{3.11b}$$

$$S^{\text{x-face}}_{g,1,j,k} = \sum_{\substack{g'=1 \\ g' \neq g}}^{G} \bar{\Sigma}^{\text{x-face}}_{s,g' \to g,1,j,k} \phi_{g',1/2,j+1/2,k+1/2} + \bar{Q}^{\text{x-face}}_{g,1,j,k}. \tag{3.11c}$$

Face: x=X

For a boundary grid point on the face $x = X$, we operate on the diffusion equation (Eq. 2.24) by $\int_{z_k}^{z_{k+1}} \int_{y_j}^{y_{j+1}} \int_{x_I}^{x_{I+1/2}} (\cdot) dx dy dz$ and use the boundary condition (Eq. 2.25) to obtain the following equation:

$$\begin{aligned} &- Z^{\text{x-face}}_{g,I,j,k} \phi_{g,I+1/2,j+1/2,k-1/2} - Y^{\text{x-face}}_{g,I,j,k} \phi_{g,I+1/2,j-1/2,k+1/2} \\ &\quad - X^{\text{interior}}_{g,I,j,k} \phi_{g,I-1/2,j+1/2,k+1/2} + C^{\text{x-face}}_{g,I,j,k} \phi_{g,I+1/2,j+1/2,k+1/2} \\ &\quad\quad - Y^{\text{x-face}}_{g,I,j+1,k} \phi_{g,I+1/2,j+3/2,k+1/2} - Z^{\text{x-face}}_{g,I,j,k+1} \phi_{g,I+1/2,j+1/2,k+3/2} \\ &\quad\quad\quad = S^{\text{x-face}}_{g,I,j,k}, \\ &\quad\quad 1 \leq g \leq G,\ 1 \leq j \leq J-1,\ 1 \leq k \leq K-1, \end{aligned} \tag{3.12}$$

where

$$C^{\text{x-face}}_{g,I,j,k} = X^{\text{interior}}_{g,I,j,k} + B^{\text{x-face}}_{g,I,j,k} + Y^{\text{x-face}}_{g,I,j,k} + Y^{\text{x-face}}_{g,I,j+1,k} + Z^{\text{x-face}}_{g,I,j,k} + Z^{\text{x-face}}_{g,I,j,k+1} + \bar{\Sigma}^{\text{x-face}}_{R,g,I,j,k}, \tag{3.13a}$$

$$B^{\text{x-face}}_{g,I,j,k} = \begin{cases} \frac{A^{\text{x-face}}_{g,I,j,k}}{2} & , \text{ vacuum boundary,} \\ 0 & , \text{ reflecting boundary,} \end{cases} \tag{3.13b}$$

$$S^{\text{x-face}}_{g,I,j,k} = \sum_{\substack{g'=1 \\ g' \neq g}}^{G} \bar{\Sigma}^{\text{x-face}}_{s,g' \to g,I,j,k} \phi_{g',I+1/2,j+1/2,k+1/2} + \bar{Q}^{\text{x-face}}_{g,I,j,k}. \tag{3.13c}$$

Face: y=0

For a boundary grid point on the face $y = 0$, we operate on the diffusion equation (Eq. 2.24) by $\int_{z_k}^{z_{k+1}} \int_{y_{1/2}}^{y_1} \int_{x_i}^{x_{i+1}} (\cdot) dx dy dz$ and use the boundary condition (Eq. 2.25)

to obtain the following equation:

$$
\begin{aligned}
&- Z^{\text{y-face}}_{g,i,1,k}\phi_{g,i+1/2,1/2,k-1/2} - X^{\text{y-face}}_{g,i,1,k}\phi_{g,i-1/2,1/2,k+1/2} \\
&\quad + C^{\text{y-face}}_{g,i,1,k}\phi_{g,i+1/2,1/2,k+1/2} - X^{\text{y-face}}_{g,i+1,1,k}\phi_{g,i+3/2,1/2,k+1/2} \\
&\quad - Y^{\text{interior}}_{g,i,1,k}\phi_{g,i+1/2,3/2,k+1/2} - Z^{\text{y-face}}_{g,i,1,k+1}\phi_{g,i+1/2,1/2,k+3/2} \\
&\quad = S^{\text{y-face}}_{g,i,1,k}, \\
&\quad 1 \le g \le G,\ 1 \le i \le I-1,\ 1 \le k \le K-1,
\end{aligned} \tag{3.14}
$$

where

$$
\begin{aligned}
C^{\text{y-face}}_{g,i,1,k} &= X^{\text{y-face}}_{g,i,1,k} + X^{\text{y-face}}_{g,i+1,1,k} + B^{\text{y-face}}_{g,i,1,k} + Y^{\text{interior}}_{g,i,1,k} + Z^{\text{y-face}}_{g,i,1,k} \\
&\quad + Z^{\text{y-face}}_{g,i,1,k+1} + \bar{\Sigma}^{\text{y-face}}_{R,g,i,1,k},
\end{aligned} \tag{3.15a}
$$

$$
B^{\text{y-face}}_{g,i,1,k} = \begin{cases} \frac{A^{\text{y-face}}_{g,i,1,k}}{2} & \text{, vacuum boundary,} \\ 0 & \text{, reflecting boundary,} \end{cases} \tag{3.15b}
$$

$$
S^{\text{y-face}}_{g,i,1,k} = \sum_{\substack{g'=1 \\ g' \neq g}}^{G} \bar{\Sigma}^{\text{y-face}}_{s,g' \to g,i,1,k}\phi_{g',i+1/2,1/2,k+1/2} + \bar{Q}^{\text{y-face}}_{g,i,1,k}. \tag{3.15c}
$$

Face: y=Y

For a boundary grid point on the face $y = Y$, we operate on the diffusion equation (Eq. 2.24) by $\int_{z_k}^{z_{k+1}} \int_{y_J}^{y_{J+1/2}} \int_{x_i}^{x_{i+1}} (\cdot) dx dy dz$ and use the boundary condition (Eq. 2.25) to obtain the following equation:

$$
\begin{aligned}
&- Z^{\text{y-face}}_{g,i,J,k}\phi_{g,i+1/2,J+1/2,k-1/2} - Y^{\text{interior}}_{g,i,J,k}\phi_{g,i+1/2,J-1/2,k+1/2} \\
&\quad - X^{\text{y-face}}_{g,i,J,k}\phi_{g,i-1/2,J+1/2,k+1/2} + C^{\text{y-face}}_{g,i,J,k}\phi_{g,i+1/2,J+1/2,k+1/2} \\
&\quad - X^{\text{y-face}}_{g,i+1,J,k}\phi_{g,i+3/2,J+1/2,k+1/2} - Z^{\text{y-face}}_{g,i,J,k+1}\phi_{g,i+1/2,J+1/2,k+3/2} \\
&\quad = S^{\text{y-face}}_{g,i,J,k}, \\
&\quad 1 \le g \le G,\ 1 \le i \le I-1,\ 1 \le k \le K-1,
\end{aligned} \tag{3.16}
$$

where

$$
\begin{aligned}
C^{\text{y-face}}_{g,i,J,k} &= X^{\text{y-face}}_{g,i,J,k} + X^{\text{y-face}}_{g,i+1,J,k} + Y^{\text{interior}}_{g,i,J,k} + B^{\text{y-face}}_{g,i,J,k} + Z^{\text{y-face}}_{g,i,J,k} \\
&\quad + Z^{\text{y-face}}_{g,i,J,k+1} + \bar{\Sigma}^{\text{y-face}}_{R,g,i,J,k},
\end{aligned} \tag{3.17a}
$$

$$B^{\text{y-face}}_{g,i,J,k} = \begin{cases} \frac{A^{\text{y-face}}_{g,i,J,k}}{2} & \text{, vacuum boundary,} \\ 0 & \text{, reflecting boundary,} \end{cases} \tag{3.17b}$$

$$S^{\text{y-face}}_{g,i,J,k} = \sum_{\substack{g'=1 \\ g' \neq g}}^{G} \bar{\Sigma}^{\text{y-face}}_{s,g' \to g,i,J,k} \phi_{g',i+1/2,J+1/2,k+1/2} + \bar{Q}^{\text{y-face}}_{g,i,J,k}. \tag{3.17c}$$

Face: z=0

For a boundary grid point on the face $z = 0$, we operate on the diffusion equation (Eq. 2.24) by $\int_{z_{1/2}}^{z_1} \int_{y_j}^{y_{j+1}} \int_{x_i}^{x_{i+1}} (\cdot) dx dy dz$ and use the boundary condition (Eq. 2.25) to obtain the following equation:

$$\begin{aligned} &- Y^{\text{z-face}}_{g,i,j,1} \phi_{g,i+1/2,j-1/2,1/2} - X^{\text{z-face}}_{g,i,j,1} \phi_{g,i-1/2,j+1/2,1/2} \\ &\quad + C^{\text{z-face}}_{g,i,j,1} \phi_{g,i+1/2,j+1/2,1/2} - X^{\text{z-face}}_{g,i+1,j,1} \phi_{g,i+3/2,j+1/2,1/2} \\ &\quad\quad - Y^{\text{z-face}}_{g,i,j+1,1} \phi_{g,i+1/2,j+3/2,1/2} - Z^{\text{interior}}_{g,i,j,1} \phi_{g,i+1/2,j+1/2,3/2} \\ &\quad\quad\quad = S^{\text{z-face}}_{g,i,j,1}, \\ &\quad\quad 1 \leq g \leq G,\ 1 \leq i \leq I-1,\ 1 \leq j \leq J-1, \end{aligned} \tag{3.18}$$

where

$$\begin{aligned} C^{\text{z-face}}_{g,i,j,1} &= X^{\text{z-face}}_{g,i,j,1} + X^{\text{z-face}}_{g,i+1,j,1} + Y^{\text{z-face}}_{g,i,j,1} + Y^{\text{z-face}}_{g,i,j+1,1} + B^{\text{z-face}}_{g,i,j,1} \\ &\quad + Z^{\text{interior}}_{g,i,j,1} + \bar{\Sigma}^{\text{z-face}}_{R,g,i,j,1}, \end{aligned} \tag{3.19a}$$

$$B^{\text{z-face}}_{g,i,j,1} = \begin{cases} \frac{A^{\text{z-face}}_{g,i,j,1}}{2} & \text{, vacuum boundary,} \\ 0 & \text{, reflecting boundary,} \end{cases} \tag{3.19b}$$

$$S^{\text{z-face}}_{g,i,j,1} = \sum_{\substack{g'=1 \\ g' \neq g}}^{G} \bar{\Sigma}^{\text{z-face}}_{s,g' \to g,i,j,1} \phi_{g',i+1/2,j+1/2,1/2} + \bar{Q}^{\text{z-face}}_{g,i,j,1}. \tag{3.19c}$$

Face: z=Z

For a boundary grid point on the face $z = Z$, we operate on the diffusion equation (Eq. 2.24) by $\int_{z_K}^{z_{K+1/2}} \int_{y_j}^{y_{j+1}} \int_{x_i}^{x_{i+1}} (\cdot) dx dy dz$ and use the boundary condition (Eq. 2.25) to obtain the following equation:

$$
\begin{aligned}
&- Z^{\text{interior}}_{g,i,j,K}\phi_{g,i+1/2,j+1/2,K-1/2} - Y^{\text{z-face}}_{g,i,j,K}\phi_{g,i+1/2,j-1/2,K+1/2} \\
&\quad - X^{\text{z-face}}_{g,i,j,K}\phi_{g,i-1/2,j+1/2,K+1/2} + C^{\text{z-face}}_{g,i,j,K}\phi_{g,i+1/2,j+1/2,K+1/2} \\
&\quad\quad - X^{\text{z-face}}_{g,i+1,j,K}\phi_{g,i+3/2,j+1/2,K+1/2} - Y^{\text{z-face}}_{g,i,j+1,K}\phi_{g,i+1/2,j+3/2,K+1/2} \\
&\quad\quad\quad = S^{\text{z-face}}_{g,i,j,K}, \\
&\quad 1 \le g \le G,\ 1 \le i \le I-1,\ 1 \le j \le J-1,
\end{aligned} \tag{3.20}
$$

where

$$
\begin{aligned}
C^{\text{z-face}}_{g,i,j,K} &= X^{\text{z-face}}_{g,i,j,K} + X^{\text{z-face}}_{g,i+1,j,K} + Y^{\text{z-face}}_{g,i,j,K} + Y^{\text{z-face}}_{g,i,j+1,K} + Z^{\text{interior}}_{g,i,j,K} \\
&\quad + B^{\text{z-face}}_{g,i,j,K} + \bar{\Sigma}^{\text{z-face}}_{R,g,i,j,K},
\end{aligned} \tag{3.21a}
$$

$$
B^{\text{z-face}}_{g,i,j,K} = \begin{cases} \frac{A^{\text{z-face}}_{g,i,j,K}}{2} & , \text{ vacuum boundary,} \\ 0 & , \text{ reflecting boundary,} \end{cases} \tag{3.21b}
$$

$$
S^{\text{z-face}}_{g,i,j,K} = \sum_{\substack{g'=1 \\ g' \ne g}}^{G} \bar{\Sigma}^{\text{z-face}}_{s,g' \to g,i,j,K}\phi_{g',i+1/2,j+1/2,K+1/2} + \bar{Q}^{\text{z-face}}_{g,i,j,K}. \tag{3.21c}
$$

X-Edge: y=0, z=0

For a boundary grid point on the edge $(x, 0, 0)$, we operate on the diffusion equation (Eq. 2.24) by $\int_{z_{1/2}}^{z_1}\int_{y_{1/2}}^{y_1}\int_{x_i}^{x_{i+1}}(\cdot)dxdydz$ and use the boundary condition (Eq. 2.25) to obtain the following equation:

$$
\begin{aligned}
&- X^{\text{edge}}_{g,i,1,1}\phi_{g,i-1/2,1/2,1/2} + C^{\text{x-edge}}_{g,i,1,1}\phi_{g,i+1/2,1/2,1/2} - X^{\text{edge}}_{g,i+1,1,1}\phi_{g,i+3/2,1/2,1/2} \\
&\quad - Y^{\text{z-face}}_{g,i,1,1}\phi_{g,i+1/2,3/2,1/2} - Z^{\text{y-face}}_{g,i,1,1}\phi_{g,i+1/2,1/2,3/2} \\
&\quad\quad = S^{\text{x-edge}}_{g,i,1,1}, \\
&\quad 1 \le g \le G,\ 1 \le i \le I-1,
\end{aligned} \tag{3.22}
$$

where

$$
\begin{aligned}
C^{\text{x-edge}}_{g,i,1,1} &= X^{\text{edge}}_{g,i,1,1} + X^{\text{edge}}_{g,i+1,1,1} + B^{\text{y-face, x-edge}}_{g,i,1,1} + Y^{\text{z-face}}_{g,i,1,1} + B^{\text{z-face, x-edge}}_{g,i,1,1} \\
&\quad + Z^{\text{y-face}}_{g,i,1,1} + \bar{\Sigma}^{\text{x-edge}}_{R,g,i,1,1},
\end{aligned} \tag{3.23a}
$$

$$
B^{\text{y-face,x-edge}}_{g,i,1,1} = \begin{cases} \frac{A^{\text{y-face, x-edge}}_{g,i,1,1}}{2} & , \text{ vacuum boundary,} \\ 0 & , \text{ reflecting boundary,} \end{cases} \tag{3.23b}
$$

$$B^{\text{z-face,x-edge}}_{g,i,1,1} = \begin{cases} \frac{A^{\text{z-face, x-edge}}_{g,i,1,1}}{2} & \text{, vacuum boundary,} \\ 0 & \text{, reflecting boundary,} \end{cases} \tag{3.23c}$$

$$S^{\text{x-edge}}_{g,i,1,1} = \sum_{\substack{g'=1 \\ g' \neq g}}^{G} \bar{\Sigma}^{\text{x-edge}}_{s,g' \to g,i,1,1} \phi_{g',i+1/2,1/2,1/2} + \bar{Q}^{\text{x-edge}}_{g,i,1,1}. \tag{3.23d}$$

X-Edge: y=Y, z=0

For a boundary grid point on the edge $(x, Y, 0)$, we operate on the diffusion equation (Eq. 2.24) by $\int_{z_{1/2}}^{z_1} \int_{y_J}^{y_{J+1/2}} \int_{x_i}^{x_{i+1}} (\cdot) dx dy dz$ and use the boundary condition (Eq. 2.25) to obtain the following equation:

$$\begin{aligned} &- Y^{\text{z-face}}_{g,i,J,1} \phi_{g,i+1/2,J-1/2,1/2} - X^{\text{edge}}_{g,i,J,1} \phi_{g,i-1/2,J+1/2,1/2} + C^{\text{x-edge}}_{g,i,J,1} \phi_{g,i+1/2,J+1/2,1/2} \\ &\quad - X^{\text{edge}}_{g,i+1,J,1} \phi_{g,i+3/2,J+1/2,1/2} - Z^{\text{y-face}}_{g,i,J,1} \phi_{g,i+1/2,J+1/2,3/2} \\ &\qquad = S^{\text{x-edge}}_{g,i,J,1}, \\ &\qquad 1 \leq g \leq G,\ 1 \leq i \leq I-1, \end{aligned} \tag{3.24}$$

where

$$\begin{aligned} C^{\text{x-edge}}_{g,i,J,1} &= X^{\text{edge}}_{g,i,J,1} + X^{\text{edge}}_{g,i+1,J,1} + Y^{\text{z-face}}_{g,i,J,1} + B^{\text{y-face, x-edge}}_{g,i,J,1} + B^{\text{z-face, x-edge}}_{g,i,J,1} \\ &\quad + Z^{\text{y-face}}_{g,i,J,1} + \bar{\Sigma}^{\text{x-edge}}_{R,g,i,J,1}, \end{aligned} \tag{3.25a}$$

$$B^{\text{y-face,x-edge}}_{g,i,J,1} = \begin{cases} \frac{A^{\text{y-face, x-edge}}_{g,i,J,1}}{2} & \text{, vacuum boundary,} \\ 0 & \text{, reflecting boundary,} \end{cases} \tag{3.25b}$$

$$B^{\text{z-face,x-edge}}_{g,i,J,1} = \begin{cases} \frac{A^{\text{z-face, x-edge}}_{g,i,J,1}}{2} & \text{, vacuum boundary,} \\ 0 & \text{, reflecting boundary,} \end{cases} \tag{3.25c}$$

$$S^{\text{x-edge}}_{g,i,J,1} = \sum_{\substack{g'=1 \\ g' \neq g}}^{G} \bar{\Sigma}^{\text{x-edge}}_{s,g' \to g,i,J,1} \phi_{g',i+1/2,J+1/2,1/2} + \bar{Q}^{\text{x-edge}}_{g,i,J,1}. \tag{3.25d}$$

X-Edge: y=0, z=Z

For a boundary grid point on the edge $(x, 0, Z)$, we operate on the diffusion equation (Eq. 2.24) by $\int_{z_K}^{z_{K+1/2}} \int_{y_{1/2}}^{y_1} \int_{x_i}^{x_{i+1}} (\cdot) dx dy dz$ and use the boundary condition

(Eq. 2.25) to obtain the following equation:

$$
\begin{aligned}
&- Z^{\text{y-face}}_{g,i,1,K}\phi_{g,i+1/2,1/2,K-1/2} - X^{\text{edge}}_{g,i,1,K}\phi_{g,i-1/2,1/2,K+1/2} + C^{\text{x-edge}}_{g,i,1,K}\phi_{g,i+1/2,1/2,K+1/2} \\
&\quad - X^{\text{edge}}_{g,i+1,1,K}\phi_{g,i+3/2,1/2,K+1/2} - Y^{\text{z-face}}_{g,i,1,K}\phi_{g,i+1/2,3/2,K+1/2} \\
&\qquad = S^{\text{x-edge}}_{g,i,1,K}, \\
&\qquad 1 \le g \le G,\ 1 \le i \le I-1,
\end{aligned} \tag{3.26}
$$

where

$$
\begin{aligned}
C^{\text{x-edge}}_{g,i,1,K} &= X^{\text{edge}}_{g,i,1,K} + X^{\text{edge}}_{g,i+1,1,K} + B^{\text{y-face, x-edge}}_{g,i,1,K} + Y^{\text{z-face}}_{g,i,1,K} + Z^{\text{y-face}}_{g,i,1,K} \\
&\quad + B^{\text{z-face, x-edge}}_{g,i,1,K} + \bar{\Sigma}^{\text{x-edge}}_{R,g,i,1,K},
\end{aligned} \tag{3.27a}
$$

$$
B^{\text{y-face,x-edge}}_{g,i,1,K} = \begin{cases} \frac{A^{\text{y-face, x-edge}}_{g,i,1,K}}{2} & \text{, vacuum boundary,} \\ 0 & \text{, reflecting boundary,} \end{cases} \tag{3.27b}
$$

$$
B^{\text{z-face,x-edge}}_{g,i,1,K} = \begin{cases} \frac{A^{\text{z-face, x-edge}}_{g,i,1,K}}{2} & \text{, vacuum boundary,} \\ 0 & \text{, reflecting boundary,} \end{cases} \tag{3.27c}
$$

$$
S^{\text{x-edge}}_{g,i,1,K} = \sum_{\substack{g'=1 \\ g' \neq g}}^{G} \bar{\Sigma}^{\text{x-edge}}_{s,g' \to g,i,1,K}\phi_{g',i+1/2,1/2,K+1/2} + \bar{Q}^{\text{x-edge}}_{g,i,1,K}. \tag{3.27d}
$$

X-Edge: y=Y, z=Z

For a boundary grid point on the edge (x, Y, Z), we operate on the diffusion equation (Eq. 2.24) by $\int_{z_K}^{z_{K+1/2}} \int_{y_J}^{y_{J+1/2}} \int_{x_i}^{x_{i+1}} (\cdot) dx dy dz$ and use the boundary condition (Eq. 2.25) to obtain the following equation:

$$
\begin{aligned}
&- Z^{\text{y-face}}_{g,i,J,K}\phi_{g,i+1/2,J+1/2,K-1/2} - Y^{\text{z-face}}_{g,i,J,K}\phi_{g,i+1/2,J-1/2,K+1/2} - X^{\text{edge}}_{g,i,J,K}\phi_{g,i-1/2,J+1/2,K+1/2} \\
&\quad + C^{\text{x-edge}}_{g,i,J,K}\phi_{g,i+1/2,J+1/2,K+1/2} - X^{\text{edge}}_{g,i+1,J,K}\phi_{g,i+3/2,J+1/2,K+1/2} \\
&\qquad = S^{\text{x-edge}}_{g,i,J,K}, \\
&\qquad 1 \le g \le G,\ 1 \le i \le I-1,
\end{aligned} \tag{3.28}
$$

where

$$
\begin{aligned}
C^{\text{x-edge}}_{g,i,J,K} &= X^{\text{edge}}_{g,i,J,K} + X^{\text{edge}}_{g,i+1,J,K} + Y^{\text{z-face}}_{g,i,J,K} + B^{\text{y-face, x-edge}}_{g,i,J,K} + Z^{\text{y-face}}_{g,i,J,K} \\
&\quad + B^{\text{z-face, x-edge}}_{g,i,J,K} + \bar{\Sigma}^{\text{x-edge}}_{R,g,i,J,K},
\end{aligned} \tag{3.29a}
$$

$$B^{\text{y-face,x-edge}}_{g,i,J,K} = \begin{cases} \frac{A^{\text{y-face, x-edge}}_{g,i,J,K}}{2} & \text{, vacuum boundary,} \\ 0 & \text{, reflecting boundary,} \end{cases} \tag{3.29b}$$

$$B^{\text{z-face,x-edge}}_{g,i,J,K} = \begin{cases} \frac{A^{\text{z-face, x-edge}}_{g,i,J,K}}{2} & \text{, vacuum boundary,} \\ 0 & \text{, reflecting boundary,} \end{cases} \tag{3.29c}$$

$$S^{\text{x-edge}}_{g,i,J,K} = \sum_{\substack{g'=1 \\ g' \neq g}}^{G} \bar{\Sigma}^{\text{x-edge}}_{s,g' \to g,i,J,K} \phi_{g',i+1/2,J+1/2,K+1/2} + \bar{Q}^{\text{x-edge}}_{g,i,J,K}. \tag{3.29d}$$

Y-Edge: x=0, z=0

For a boundary grid point on the edge $(0, y, 0)$, we operate on the diffusion equation (Eq. 2.24) by $\int_{z_{1/2}}^{z_1} \int_{y_j}^{y_{j+1}} \int_{x_{1/2}}^{x_1} (\cdot) dx dy dz$ and use the boundary condition (Eq. 2.25) to obtain the following equation:

$$\begin{aligned} &- Y^{\text{edge}}_{g,1,j,1} \phi_{g,1/2,j-1/2,1/2} + C^{\text{y-edge}}_{g,1,j,1} \phi_{g,1/2,j+1/2,1/2} - Y^{\text{edge}}_{g,1,j+1,1} \phi_{g,1/2,j+3/2,1/2} \\ &\quad - X^{\text{z-face}}_{g,1,j,1} \phi_{g,3/2,j+1/2,1/2} - Z^{\text{x-face}}_{g,1,j,1} \phi_{g,1/2,j+1/2,3/2} \\ &\qquad = S^{\text{y-edge}}_{g,1,j,1}, \\ &\qquad 1 \leq g \leq G,\ 1 \leq j \leq J-1, \end{aligned} \tag{3.30}$$

where

$$\begin{aligned} C^{\text{y-edge}}_{g,1,j,1} = B^{\text{x-face, y-edge}}_{g,1,j,1} + X^{\text{z-face}}_{g,1,j,1} + Y^{\text{edge}}_{g,1,j,1} + Y^{\text{edge}}_{g,1,j+1,1} + B^{\text{z-face, y-edge}}_{g,1,j,1} \\ + Z^{\text{x-face}}_{g,1,j,1} + \bar{\Sigma}^{\text{y-edge}}_{R,g,1,j,1}, \end{aligned} \tag{3.31a}$$

$$B^{\text{x-face,y-edge}}_{g,1,j,1} = \begin{cases} \frac{A^{\text{x-face, y-edge}}_{g,1,j,1}}{2} & \text{, vacuum boundary,} \\ 0 & \text{, reflecting boundary,} \end{cases} \tag{3.31b}$$

$$B^{\text{z-face,y-edge}}_{g,1,j,1} = \begin{cases} \frac{A^{\text{z-face, y-edge}}_{g,1,j,1}}{2} & \text{, vacuum boundary,} \\ 0 & \text{, reflecting boundary,} \end{cases} \tag{3.31c}$$

$$S^{\text{y-edge}}_{g,1,j,1} = \sum_{\substack{g'=1 \\ g' \neq g}}^{G} \bar{\Sigma}^{\text{y-edge}}_{s,g' \to g,1,j,1} \phi_{g',1/2,j+1/2,1/2} + \bar{Q}^{\text{y-edge}}_{g,1,j,1}. \tag{3.31d}$$

Y-Edge: x=X, z=0

For a boundary grid point on the edge $(X, y, 0)$, we operate on the diffusion equation (Eq. 2.24) by $\int_{z_{1/2}}^{z_1} \int_{y_j}^{y_{j+1}} \int_{x_I}^{x_{I+1/2}} (\cdot) dx dy dz$ and use the boundary condition

(Eq. 2.25) to obtain the following equation:

$$
\begin{aligned}
&- Y^{\text{edge}}_{g,I,j,1}\phi_{g,I+1/2,j-1/2,1/2} - X^{\text{z-face}}_{g,I,j,1}\phi_{g,I-1/2,j+1/2,1/2} + C^{\text{y-edge}}_{g,I,j,1}\phi_{g,I+1/2,j+1/2,1/2} \\
&\quad - Y^{\text{edge}}_{g,I,j+1,1}\phi_{g,I+1/2,j+3/2,1/2} - Z^{\text{x-face}}_{g,I,j,1}\phi_{g,I+1/2,j+1/2,3/2} \\
&\qquad = S^{\text{y-edge}}_{g,I,j,1}, \\
&\qquad 1 \le g \le G,\ 1 \le j \le J-1,
\end{aligned} \tag{3.32}
$$

where

$$
\begin{aligned}
C^{\text{y-edge}}_{g,I,j,1} &= X^{\text{z-face}}_{g,I,j,1} + B^{\text{x-face, y-edge}}_{g,I,j,1} + Y^{\text{edge}}_{g,I,j,1} + Y^{\text{edge}}_{g,I,j+1,1} + B^{\text{z-face, y-edge}}_{g,I,j,1} \\
&\quad + Z^{\text{x-face}}_{g,I,j,1} + \bar{\Sigma}^{\text{y-edge}}_{R,g,I,j,1},
\end{aligned} \tag{3.33a}
$$

$$
B^{\text{x-face,y-edge}}_{g,I,j,1} = \begin{cases} \frac{A^{\text{x-face, y-edge}}_{g,I,j,1}}{2} & \text{, vacuum boundary,} \\ 0 & \text{, reflecting boundary,} \end{cases} \tag{3.33b}
$$

$$
B^{\text{z-face,y-edge}}_{g,I,j,1} = \begin{cases} \frac{A^{\text{z-face, y-edge}}_{g,I,j,1}}{2} & \text{, vacuum boundary,} \\ 0 & \text{, reflecting boundary,} \end{cases} \tag{3.33c}
$$

$$
S^{\text{y-edge}}_{g,I,j,1} = \sum_{\substack{g'=1 \\ g' \neq g}}^{G} \bar{\Sigma}^{\text{y-edge}}_{s,g' \to g,I,j,1}\phi_{g',I+1/2,j+1/2,1/2} + \bar{Q}^{\text{y-edge}}_{g,I,j,1}. \tag{3.33d}
$$

Y-Edge: x=0, z=Z

For a boundary grid point on the edge $(0, y, Z)$, we operate on the diffusion equation (Eq. 2.24) by $\int_{z_K}^{z_{K+1/2}} \int_{y_j}^{y_{j+1}} \int_{x_{1/2}}^{x_1} (\cdot) dx dy dz$ and use the boundary condition (Eq. 2.25) to obtain the following equation:

$$
\begin{aligned}
&- Z^{\text{x-face}}_{g,1,j,K}\phi_{g,1/2,j+1/2,K-1/2} - Y^{\text{edge}}_{g,1,j,K}\phi_{g,1/2,j-1/2,K+1/2} + C^{\text{y-edge}}_{g,1,j,K}\phi_{g,1/2,j+1/2,K+1/2} \\
&\quad - Y^{\text{edge}}_{g,1,j+1,K}\phi_{g,1/2,j+3/2,K+1/2} - X^{\text{z-face}}_{g,1,j,K}\phi_{g,3/2,j+1/2,K+1/2} \\
&\qquad = S^{\text{y-edge}}_{g,1,j,K}, \\
&\qquad 1 \le g \le G,\ 1 \le j \le J-1,
\end{aligned} \tag{3.34}
$$

where

$$
\begin{aligned}
C^{\text{y-edge}}_{g,1,j,K} &= B^{\text{x-face, y-edge}}_{g,1,j,K} + X^{\text{z-face}}_{g,1,j,K} + Y^{\text{edge}}_{g,1,j,K} + Y^{\text{edge}}_{g,1,j+1,K} + Z^{\text{x-face}}_{g,1,j,K} \\
&\quad + B^{\text{z-face, y-edge}}_{g,1,j,K} + \bar{\Sigma}^{\text{y-edge}}_{R,g,1,j,K},
\end{aligned} \tag{3.35a}
$$

$$B^{\text{x-face,y-edge}}_{g,1,j,K} = \begin{cases} \frac{A^{\text{x-face, y-edge}}_{g,1,j,K}}{2} & \text{, vacuum boundary,} \\ 0 & \text{, reflecting boundary,} \end{cases} \tag{3.35b}$$

$$B^{\text{z-face,y-edge}}_{g,1,j,K} = \begin{cases} \frac{A^{\text{z-face, y-edge}}_{g,1,j,K}}{2} & \text{, vacuum boundary,} \\ 0 & \text{, reflecting boundary,} \end{cases} \tag{3.35c}$$

$$S^{\text{y-edge}}_{g,1,j,K} = \sum_{\substack{g'=1 \\ g' \neq g}}^{G} \bar{\Sigma}^{\text{y-edge}}_{s,g' \to g,1,j,K} \phi_{g',1/2,j+1/2,K+1/2} + \bar{Q}^{\text{y-edge}}_{g,1,j,K}. \tag{3.35d}$$

Y-Edge: x=X, z=Z

For a boundary grid point on the edge (X, y, Z), we operate on the diffusion equation (Eq. 2.24) by $\int_{z_K}^{z_{K+1/2}} \int_{y_j}^{y_{j+1}} \int_{x_I}^{x_{I+1/2}} (\cdot) dxdydz$ and use the boundary condition (Eq. 2.25) to obtain the following equation:

$$\begin{aligned} &- Z^{\text{x-face}}_{g,I,j,K} \phi_{g,I+1/2,j+1/2,K-1/2} - Y^{\text{edge}}_{g,I,j,K} \phi_{g,I+1/2,j-1/2,K+1/2} - X^{\text{z-face}}_{g,I,j,K} \phi_{g,I-1/2,j+1/2,K+1/2} \\ &\quad + C^{\text{y-edge}}_{g,I,j,K} \phi_{g,I+1/2,j+1/2,K+1/2} - Y^{\text{edge}}_{g,I,j+1,K} \phi_{g,I+1/2,j+3/2,K+1/2} \\ &\quad = S^{\text{y-edge}}_{g,I,j,K}, \\ &\quad 1 \leq g \leq G,\ 1 \leq j \leq J-1, \end{aligned} \tag{3.36}$$

where

$$\begin{aligned} C^{\text{y-edge}}_{g,I,j,K} &= X^{\text{z-face}}_{g,I,j,K} + B^{\text{x-face, y-edge}}_{g,I,j,K} + Y^{\text{edge}}_{g,I,j,K} + Y^{\text{edge}}_{g,I,j+1,K} + B^{\text{x-face, y-edge}}_{g,I,j,K} \\ &\quad + Z^{\text{x-face}}_{g,I,j,K} + \bar{\Sigma}^{\text{y-edge}}_{R,g,I,j,K}, \end{aligned} \tag{3.37a}$$

$$B^{\text{x-face,y-edge}}_{g,I,j,K} = \begin{cases} \frac{A^{\text{x-face, y-edge}}_{g,I,j,K}}{2} & \text{, vacuum boundary,} \\ 0 & \text{, reflecting boundary,} \end{cases} \tag{3.37b}$$

$$B^{\text{z-face,y-edge}}_{g,I,j,K} = \begin{cases} \frac{A^{\text{z-face, y-edge}}_{g,I,j,K}}{2} & \text{, vacuum boundary,} \\ 0 & \text{, reflecting boundary,} \end{cases} \tag{3.37c}$$

$$S^{\text{y-edge}}_{g,I,j,K} = \sum_{\substack{g'=1 \\ g' \neq g}}^{G} \bar{\Sigma}^{\text{y-edge}}_{s,g' \to g,I,j,K} \phi_{g',I+1/2,j+1/2,K+1/2} + \bar{Q}^{\text{y-edge}}_{g,I,j,K}. \tag{3.37d}$$

Z-Edge: x=0, y=0

For a boundary grid point on the edge $(0, 0, z)$, we operate on the diffusion equation (Eq. 2.24) by $\int_{z_k}^{z_{k+1}} \int_{y_{1/2}}^{y_1} \int_{x_{1/2}}^{x_1} (\cdot) dxdydz$ and use the boundary condition (Eq.

2.25) to obtain the following equation:

$$
\begin{aligned}
&- Z^{\text{edge}}_{g,1,1,k}\phi_{g,1/2,1/2,k-1/2} + C^{\text{z-edge}}_{g,1,1,k}\phi_{g,1/2,1/2,k+1/2} - X^{\text{y-face}}_{g,1,1,k}\phi_{g,3/2,1/2,k+1/2} \\
&\quad - Y^{\text{x-face}}_{g,1,1,k}\phi_{g,1/2,3/2,k+1/2} - Z^{\text{edge}}_{g,1,1,k+1}\phi_{g,1/2,1/2,k+3/2} \\
&\qquad = S^{\text{z-edge}}_{g,1,1,k}, \\
&\qquad 1 \le g \le G,\ 1 \le k \le K-1,
\end{aligned} \tag{3.38}
$$

where

$$
\begin{aligned}
C^{\text{z-edge}}_{g,1,1,k} &= B^{\text{x-face, z-edge}}_{g,1,1,k} + X^{\text{y-face}}_{g,1,1,k} + B^{\text{y-face, z-edge}}_{g,1,1,k} + Y^{\text{x-face}}_{g,1,1,k} + Z^{\text{edge}}_{g,1,1,k} \\
&\quad + Z^{\text{edge}}_{g,1,1,k+1} + \bar{\Sigma}^{\text{z-edge}}_{R,g,1,1,k},
\end{aligned} \tag{3.39a}
$$

$$
B^{\text{x-face,z-edge}}_{g,1,1,k} = \begin{cases} \frac{A^{\text{x-face, z-edge}}_{g,1,1,k}}{2} & \text{, vacuum boundary,} \\ 0 & \text{, reflecting boundary,} \end{cases} \tag{3.39b}
$$

$$
B^{\text{y-face,z-edge}}_{g,1,1,k} = \begin{cases} \frac{A^{\text{y-face, z-edge}}_{g,1,1,k}}{2} & \text{, vacuum boundary,} \\ 0 & \text{, reflecting boundary,} \end{cases} \tag{3.39c}
$$

$$
S^{\text{z-edge}}_{g,1,1,k} = \sum_{\substack{g'=1 \\ g' \ne g}}^{G} \bar{\Sigma}^{\text{z-edge}}_{s,g' \to g,1,1,k}\phi_{g',1/2,1/2,k+1/2} + \bar{Q}^{\text{z-edge}}_{g,1,1,k}. \tag{3.39d}
$$

Z-Edge: x=X, y=0

For a boundary grid point on the edge $(X, 0, z)$, we operate on the diffusion equation (Eq. 2.24) by $\int_{z_k}^{z_{k+1}} \int_{y_{1/2}}^{y_1} \int_{x_I}^{x_{I+1/2}} (\cdot) dx dy dz$ and use the boundary condition (Eq. 2.25) to obtain the following equation:

$$
\begin{aligned}
&- Z^{\text{edge}}_{g,I,1,k}\phi_{g,I+1/2,1/2,k-1/2} - X^{\text{y-face}}_{g,I,1,k}\phi_{g,I-1/2,1/2,k+1/2} + C^{\text{z-edge}}_{g,I,1,k}\phi_{g,I+1/2,1/2,k+1/2} \\
&\quad - Y^{\text{x-face}}_{g,I,1,k}\phi_{g,I+1/2,3/2,k+1/2} - Z^{\text{edge}}_{g,I,1,k+1}\phi_{g,I+1/2,1/2,k+3/2} \\
&\qquad = S^{\text{z-edge}}_{g,I,1,k}, \\
&\qquad 1 \le g \le G,\ 1 \le k \le K-1,
\end{aligned} \tag{3.40}
$$

where

$$
\begin{aligned}
C^{\text{z-edge}}_{g,I,1,k} &= X^{\text{y-face}}_{g,I,1,k} + B^{\text{x-face, z-edge}}_{g,I,1,k} + B^{\text{y-face, z-edge}}_{g,I,1,k} + Y^{\text{x-face}}_{g,I,1,k} + Z^{\text{edge}}_{g,I,1,k} \\
&\quad + Z^{\text{edge}}_{g,I,1,k+1} + \bar{\Sigma}^{\text{z-edge}}_{R,g,I,1,k},
\end{aligned} \tag{3.41a}
$$

$$B^{\text{x-face,z-edge}}_{g,I,1,k} = \begin{cases} \frac{A^{\text{x-face, z-edge}}_{g,I,1,k}}{2} & \text{, vacuum boundary,} \\ 0 & \text{, reflecting boundary,} \end{cases} \tag{3.41b}$$

$$B^{\text{y-face,z-edge}}_{g,I,1,k} = \begin{cases} \frac{A^{\text{y-face, z-edge}}_{g,I,1,k}}{2} & \text{, vacuum boundary,} \\ 0 & \text{, reflecting boundary,} \end{cases} \tag{3.41c}$$

$$S^{\text{z-edge}}_{g,I,1,k} = \sum_{\substack{g'=1 \\ g'\neq g}}^{G} \bar{\Sigma}^{\text{z-edge}}_{s,g'\to g,I,1,k} \phi_{g',I+1/2,1/2,k+1/2} + \bar{Q}^{\text{z-edge}}_{g,I,1,k}. \tag{3.41d}$$

Z-Edge: x=0, y=Y

For a boundary grid point on the edge $(0, Y, z)$, we operate on the diffusion equation (Eq. 2.24) by $\int_{z_k}^{z_{k+1}} \int_{y_J}^{y_{J+1/2}} \int_{x_{1/2}}^{x_1} (\cdot) dxdydz$ and use the boundary condition (Eq. 2.25) to obtain the following equation:

$$\begin{aligned} &- Z^{\text{edge}}_{g,1,J,k} \phi_{g,1/2,J+1/2,k-1/2} - Y^{\text{x-face}}_{g,1,J,k} \phi_{g,1/2,J-1/2,k+1/2} + C^{\text{z-edge}}_{g,1,J,k} \phi_{g,1/2,J+1/2,k+1/2} \\ &\quad - X^{\text{y-face}}_{g,1,J,k} \phi_{g,3/2,J+1/2,k+1/2} - Z^{\text{edge}}_{g,1,J,k+1} \phi_{g,1/2,J+1/2,k+3/2} \\ &\qquad = S^{\text{z-edge}}_{g,1,J,k}, \\ &\qquad 1 \le g \le G,\ 1 \le k \le K-1, \end{aligned} \tag{3.42}$$

where

$$\begin{aligned} C^{\text{z-edge}}_{g,1,J,k} = B^{\text{x-face, z-edge}}_{g,1,J,k} + X^{\text{y-face}}_{g,1,J,k} + Y^{\text{x-face}}_{g,1,J,k} + B^{\text{y-face, z-edge}}_{g,1,J,k} + Z^{\text{edge}}_{g,1,J,k} \\ + Z^{\text{edge}}_{g,1,J,k+1} + \bar{\Sigma}^{\text{z-edge}}_{R,g,1,J,k}, \end{aligned} \tag{3.43a}$$

$$B^{\text{x-face,z-edge}}_{g,1,J,k} = \begin{cases} \frac{A^{\text{x-face, z-edge}}_{g,1,J,k}}{2} & \text{, vacuum boundary,} \\ 0 & \text{, reflecting boundary,} \end{cases} \tag{3.43b}$$

$$B^{\text{y-face,z-edge}}_{g,1,J,k} = \begin{cases} \frac{A^{\text{y-face, z-edge}}_{g,1,J,k}}{2} & \text{, vacuum boundary,} \\ 0 & \text{, reflecting boundary,} \end{cases} \tag{3.43c}$$

$$S^{\text{z-edge}}_{g,1,J,k} = \sum_{\substack{g'=1 \\ g'\neq g}}^{G} \bar{\Sigma}^{\text{z-edge}}_{s,g'\to g,1,J,k} \phi_{g',1/2,J+1/2,k+1/2} + \bar{Q}^{\text{z-edge}}_{g,1,J,k}. \tag{3.43d}$$

Z-Edge: x=X, y=Y

For a boundary grid point on the edge (X, Y, z), we operate on the diffusion equation (Eq. 2.24) by $\int_{z_k}^{z_{k+1}} \int_{y_J}^{y_{J+1/2}} \int_{x_I}^{x_{I+1/2}} (\cdot) dxdydz$ and use the boundary condition

(Eq. 2.25) to obtain the following equation:

$$
\begin{aligned}
&- Z^{\text{edge}}_{g,I,J,k}\phi_{g,I+1/2,J+1/2,k-1/2} - Y^{\text{x-face}}_{g,I,J,k}\phi_{g,I+1/2,J-1/2,k+1/2} - X^{\text{y-face}}_{g,I,J,k}\phi_{g,I-1/2,J+1/2,k+1/2} \\
&\quad + C^{\text{z-edge}}_{g,I,J,k}\phi_{g,I+1/2,J+1/2,k+1/2} - Z^{\text{edge}}_{g,I,J,k+1}\phi_{g,I+1/2,J+1/2,k+3/2} \\
&\quad = S^{\text{z-edge}}_{g,I,J,k}, \\
&\quad 1 \le g \le G,\ 1 \le k \le K-1,
\end{aligned} \tag{3.44}
$$

where

$$
\begin{aligned}
C^{\text{z-edge}}_{g,I,J,k} &= X^{\text{y-face}}_{g,I,J,k} + B^{\text{x-face, z-edge}}_{g,I,J,k} + Y^{\text{x-face}}_{g,I,J,k} + B^{\text{y-face, z-edge}}_{g,I,J,k} + Z^{\text{edge}}_{g,I,J,k} \\
&\quad + Z^{\text{edge}}_{g,I,J,k+1} + \bar{\Sigma}^{\text{z-edge}}_{R,g,I,J,k},
\end{aligned} \tag{3.45a}
$$

$$
B^{\text{x-face,z-edge}}_{g,I,J,k} = \begin{cases} \frac{A^{\text{x-face, z-edge}}_{g,I,J,k}}{2} & \text{, vacuum boundary,} \\ 0 & \text{, reflecting boundary,} \end{cases} \tag{3.45b}
$$

$$
B^{\text{y-face,z-edge}}_{g,I,J,k} = \begin{cases} \frac{A^{\text{y-face, z-edge}}_{g,I,J,k}}{2} & \text{, vacuum boundary,} \\ 0 & \text{, reflecting boundary,} \end{cases} \tag{3.45c}
$$

$$
S^{\text{z-edge}}_{g,I,J,k} = \sum_{\substack{g'=1 \\ g' \neq g}}^{G} \bar{\Sigma}^{\text{z-edge}}_{s,g' \to g,I,J,k}\phi_{g',I+1/2,J+1/2,k+1/2} + \bar{Q}^{\text{z-edge}}_{g,I,J,k}. \tag{3.45d}
$$

Corner: x=0, y=0, z=0

For a boundary grid point on the corner $(0,0,0)$, we operate on the diffusion equation (Eq. 2.24) by $\int_{z_{1/2}}^{z_1}\int_{y_{1/2}}^{y_1}\int_{x_{1/2}}^{x_1}(\cdot)dxdydz$ and use the boundary condition (Eq. 2.25) to obtain the following equation:

$$
\begin{aligned}
&+ C^{\text{corner}}_{g,1,1,1}\phi_{g,1/2,1/2,1/2} - X^{\text{edge}}_{g,1,1,1}\phi_{g,3/2,1/2,1/2} - Y^{\text{edge}}_{g,1,1,1}\phi_{g,1/2,3/2,1/2} \\
&\quad - Z^{\text{edge}}_{g,1,1,1}\phi_{g,1/2,1/2,3/2} = S^{\text{corner}}_{g,1,1,1}, \qquad 1 \le g \le G,
\end{aligned} \tag{3.46}
$$

where

$$
\begin{aligned}
C^{\text{corner}}_{g,1,1,1} &= B^{\text{x-face, corner}}_{g,1,1,1} + X^{\text{edge}}_{g,1,1,1} + B^{\text{y-face, corner}}_{g,1,1,1} + Y^{\text{edge}}_{g,1,1,1} + B^{\text{z-face, corner}}_{g,1,1,1} \\
&\quad + Z^{\text{edge}}_{g,1,1,1} + \bar{\Sigma}^{\text{corner}}_{R,g,1,1,1},
\end{aligned} \tag{3.47a}
$$

$$
B^{\text{x-face, corner}}_{g,1,1,1} = \begin{cases} \frac{A^{\text{x-face, corner}}_{g,1,1,1}}{2} & \text{, vacuum boundary,} \\ 0 & \text{, reflecting boundary,} \end{cases} \tag{3.47b}
$$

$$B^{\text{y-face, corner}}_{g,1,1,1} = \begin{cases} \frac{A^{\text{y-face, corner}}_{g,1,1,1}}{2} & \text{, vacuum boundary,} \\ 0 & \text{, reflecting boundary,} \end{cases} \tag{3.47c}$$

$$B^{\text{z-face, corner}}_{g,1,1,1} = \begin{cases} \frac{A^{\text{z-face, corner}}_{g,1,1,1}}{2} & \text{, vacuum boundary,} \\ 0 & \text{, reflecting boundary,} \end{cases} \tag{3.47d}$$

$$S^{\text{corner}}_{g,1,1,1} = \sum_{\substack{g'=1 \\ g' \neq g}}^{G} \bar{\Sigma}^{\text{corner}}_{s,g' \to g,1,1,1} \phi_{g',1/2,1/2,1/2} + \bar{Q}^{\text{corner}}_{g,1,1,1}. \tag{3.47e}$$

Corner: x=0, y=Y, z=0

For a boundary grid point on the corner $(0, Y, 0)$, we operate on the diffusion equation (Eq. 2.24) by $\int_{z_{1/2}}^{z_1} \int_{y_J}^{y_{J+1/2}} \int_{x_{1/2}}^{x_1} (\cdot) dx dy dz$ and use the boundary condition (Eq. 2.25) to obtain the following equation:

$$\begin{aligned} &- Y^{\text{edge}}_{g,1,J,1} \phi_{g,1/2,J-1/2,1/2} + C^{\text{corner}}_{g,1,J,1} \phi_{g,1/2,J+1/2,1/2} - X^{\text{edge}}_{g,1,J,1} \phi_{g,3/2,J+1/2,1/2} \\ &\quad - Z^{\text{edge}}_{g,1,J,1} \phi_{g,1/2,J+1/2,3/2} = S^{\text{corner}}_{g,1,J,1}, \qquad 1 \leq g \leq G, \end{aligned} \tag{3.48}$$

where

$$\begin{aligned} C^{\text{corner}}_{g,1,J,1} = {} & B^{\text{x-face, corner}}_{g,1,J,1} + X^{\text{edge}}_{g,1,J,1} + Y^{\text{edge}}_{g,1,J,1} + B^{\text{y-face, corner}}_{g,1,J,1} + B^{\text{z-face, corner}}_{g,1,J,1} \\ & + Z^{\text{edge}}_{g,1,J,1} + \bar{\Sigma}^{\text{corner}}_{R,g,1,J,1}, \end{aligned} \tag{3.49a}$$

$$B^{\text{x-face, corner}}_{g,1,J,1} = \begin{cases} \frac{A^{\text{x-face, corner}}_{g,1,J,1}}{2} & \text{, vacuum boundary,} \\ 0 & \text{, reflecting boundary,} \end{cases} \tag{3.49b}$$

$$B^{\text{y-face, corner}}_{g,1,J,1} = \begin{cases} \frac{A^{\text{y-face, corner}}_{g,1,J,1}}{2} & \text{, vacuum boundary,} \\ 0 & \text{, reflecting boundary,} \end{cases} \tag{3.49c}$$

$$B^{\text{z-face, corner}}_{g,1,J,1} = \begin{cases} \frac{A^{\text{z-face, corner}}_{g,1,J,1}}{2} & \text{, vacuum boundary,} \\ 0 & \text{, reflecting boundary,} \end{cases} \tag{3.49d}$$

$$S^{\text{corner}}_{g,1,J,1} = \sum_{\substack{g'=1 \\ g' \neq g}}^{G} \bar{\Sigma}^{\text{corner}}_{s,g' \to g,1,J,1} \phi_{g',1/2,J+1/2,1/2} + \bar{Q}^{\text{corner}}_{g,1,J,1}. \tag{3.49e}$$

Corner: x=0, y=0, z=Z

For a boundary grid point on the corner $(0, 0, Z)$, we operate on the diffusion equation (Eq. 2.24) by $\int_{z_K}^{z_{K+1/2}} \int_{y_{1/2}}^{y_1} \int_{x_{1/2}}^{x_1} (\cdot) dx dy dz$ and use the boundary condition

(Eq. 2.25) to obtain the following equation:

$$
\begin{aligned}
&- Z^{\text{edge}}_{g,1,1,K}\phi_{g,1/2,1/2,K-1/2} + C^{\text{corner}}_{g,1,1,K}\phi_{g,1/2,1/2,K+1/2} - X^{\text{edge}}_{g,1,1,K}\phi_{g,3/2,1/2,K+1/2} \\
&\quad - Y^{\text{edge}}_{g,1,1,K}\phi_{g,1/2,3/2,K+1/2} = S^{\text{corner}}_{g,1,1,K}, \qquad 1 \le g \le G, \qquad (3.50)
\end{aligned}
$$

where

$$
\begin{aligned}
C^{\text{corner}}_{g,1,1,K} &= B^{\text{x-face, corner}}_{g,1,1,K} + X^{\text{edge}}_{g,1,1,K} + B^{\text{y-face, corner}}_{g,1,1,K} + Y^{\text{edge}}_{g,1,1,K} + B^{\text{z-face, corner}}_{g,1,1,K} \\
&\quad + Z^{\text{edge}}_{g,1,1,K} + \bar{\Sigma}^{\text{corner}}_{R,g,1,1,K}, \qquad (3.51a)
\end{aligned}
$$

$$
B^{\text{x-face, corner}}_{g,1,1,K} = \begin{cases} \frac{A^{\text{x-face, corner}}_{g,1,1,K}}{2} & \text{, vacuum boundary,} \\ 0 & \text{, reflecting boundary,} \end{cases} \qquad (3.51b)
$$

$$
B^{\text{y-face, corner}}_{g,1,1,K} = \begin{cases} \frac{A^{\text{y-face, corner}}_{g,1,1,K}}{2} & \text{, vacuum boundary,} \\ 0 & \text{, reflecting boundary,} \end{cases} \qquad (3.51c)
$$

$$
B^{\text{z-face, corner}}_{g,1,1,K} = \begin{cases} \frac{A^{\text{z-face, corner}}_{g,1,1,K}}{2} & \text{, vacuum boundary,} \\ 0 & \text{, reflecting boundary,} \end{cases} \qquad (3.51d)
$$

$$
S^{\text{corner}}_{g,1,1,K} = \sum_{\substack{g'=1 \\ g' \neq g}}^{G} \bar{\Sigma}^{\text{corner}}_{s,g' \to g,1,1,K}\phi_{g',1/2,1/2,K+1/2} + \bar{Q}^{\text{corner}}_{g,1,1,K}. \qquad (3.51e)
$$

Corner: x=0, y=Y, z=Z

For a boundary grid point on the corner $(0, Y, Z)$, we operate on the diffusion equation (Eq. 2.24) by $\int_{z_K}^{z_{K+1/2}} \int_{y_J}^{y_{J+1/2}} \int_{x_{1/2}}^{x_1} (\cdot) dx dy dz$ and use the boundary condition (Eq. 2.25) to obtain the following equation:

$$
\begin{aligned}
&- Z^{\text{edge}}_{g,1,J,K}\phi_{g,1/2,J+1/2,K-1/2} - Y^{\text{edge}}_{g,1,J,K}\phi_{g,1/2,J-1/2,K+1/2} + C^{\text{corner}}_{g,1,J,K}\phi_{g,1/2,J+1/2,K+1/2} \\
&\quad - X^{\text{edge}}_{g,1,J,K}\phi_{g,3/2,J+1/2,K+1/2} = S^{\text{corner}}_{g,1,J,K}, \qquad 1 \le g \le G, \qquad (3.52)
\end{aligned}
$$

where

$$
\begin{aligned}
C^{\text{corner}}_{g,1,J,K} &= B^{\text{x-face, corner}}_{g,1,J,K} + X^{\text{edge}}_{g,1,J,K} + Y^{\text{edge}}_{g,1,J,K} + B^{\text{y-face, corner}}_{g,1,J,K} + Z^{\text{edge}}_{g,1,J,K} \\
&\quad + B^{\text{z-face, corner}}_{g,1,J,K} + \bar{\Sigma}^{\text{corner}}_{R,g,1,J,K}, \qquad (3.53a)
\end{aligned}
$$

$$
B^{\text{x-face, corner}}_{g,1,J,K} = \begin{cases} \frac{A^{\text{x-face, corner}}_{g,1,J,K}}{2} & \text{, vacuum boundary,} \\ 0 & \text{, reflecting boundary,} \end{cases} \qquad (3.53b)
$$

$$B^{\text{y-face, corner}}_{g,1,J,K} = \begin{cases} \frac{A^{\text{y-face, corner}}_{g,1,J,K}}{2} & \text{, vacuum boundary,} \\ 0 & \text{, reflecting boundary,} \end{cases} \tag{3.53c}$$

$$B^{\text{z-face, corner}}_{g,1,J,K} = \begin{cases} \frac{A^{\text{z-face, corner}}_{g,1,J,K}}{2} & \text{, vacuum boundary,} \\ 0 & \text{, reflecting boundary,} \end{cases} \tag{3.53d}$$

$$S^{\text{corner}}_{g,1,J,K} = \sum_{\substack{g'=1 \\ g' \neq g}}^{G} \bar{\Sigma}^{\text{corner}}_{s,g' \to g,1,J,K} \phi_{g',1/2,J+1/2,K+1/2} + \bar{Q}^{\text{corner}}_{g,1,J,K}. \tag{3.53e}$$

Corner: x=X, y=0, z=0

For a boundary grid point on the corner $(X, 0, 0)$, we operate on the diffusion equation (Eq. 2.24) by $\int_{z_{1/2}}^{z_1} \int_{y_{1/2}}^{y_1} \int_{x_I}^{x_{I+1/2}} (\cdot) dx dy dz$ and use the boundary condition (Eq. 2.25) to obtain the following equation:

$$\begin{aligned} &- X^{\text{edge}}_{g,I,1,1} \phi_{g,I-1/2,1/2,1/2} + C^{\text{corner}}_{g,I,1,1} \phi_{g,I+1/2,1/2,1/2} - Y^{\text{edge}}_{g,I,1,1} \phi_{g,I+1/2,3/2,1/2} \\ &\quad - Z^{\text{edge}}_{g,I,1,1} \phi_{g,I+1/2,1/2,3/2} = S^{\text{corner}}_{g,I,1,1}, \qquad 1 \leq g \leq G, \end{aligned} \tag{3.54}$$

where

$$\begin{aligned} C^{\text{corner}}_{g,I,1,1} = X^{\text{edge}}_{g,I,1,1} + B^{\text{x-face, corner}}_{g,I,1,1} + B^{\text{y-face, corner}}_{g,I,1,1} + Y^{\text{edge}}_{g,I,1,1} + B^{\text{z-face, corner}}_{g,I,1,1} \\ + Z^{\text{edge}}_{g,I,1,1} + \bar{\Sigma}^{\text{corner}}_{R,g,I,1,1}, \end{aligned} \tag{3.55a}$$

$$B^{\text{x-face, corner}}_{g,I,1,1} = \begin{cases} \frac{A^{\text{x-face, corner}}_{g,I,1,1}}{2} & \text{, vacuum boundary,} \\ 0 & \text{, reflecting boundary,} \end{cases} \tag{3.55b}$$

$$B^{\text{y-face, corner}}_{g,I,1,1} = \begin{cases} \frac{A^{\text{y-face, corner}}_{g,I,1,1}}{2} & \text{, vacuum boundary,} \\ 0 & \text{, reflecting boundary,} \end{cases} \tag{3.55c}$$

$$B^{\text{z-face, corner}}_{g,I,1,1} = \begin{cases} \frac{A^{\text{z-face, corner}}_{g,I,1,1}}{2} & \text{, vacuum boundary,} \\ 0 & \text{, reflecting boundary,} \end{cases} \tag{3.55d}$$

$$S^{\text{corner}}_{g,I,1,1} = \sum_{\substack{g'=1 \\ g' \neq g}}^{G} \bar{\Sigma}^{\text{corner}}_{s,g' \to g,I,1,1} \phi_{g',I+1/2,1/2,1/2} + \bar{Q}^{\text{corner}}_{g,I,1,1}. \tag{3.55e}$$

Corner: x=X, y=Y, z=0

For a boundary grid point on the corner $(X, Y, 0)$, we operate on the diffusion equation (Eq. 2.24) by $\int_{z_{1/2}}^{z_1} \int_{y_J}^{y_{J+1/2}} \int_{x_I}^{x_{I+1/2}} (\cdot) dx dy dz$ and use the boundary condition

(Eq. 2.25) to obtain the following equation:

$$
\begin{aligned}
&- Y^{\text{edge}}_{g,I,J,1}\phi_{g,I+1/2,J-1/2,1/2} - X^{\text{edge}}_{g,I,J,1}\phi_{g,I-1/2,J+1/2,1/2} + C^{\text{corner}}_{g,I,J,1}\phi_{g,I+1/2,J+1/2,1/2} \\
&\quad - Z^{\text{edge}}_{g,I,J,1}\phi_{g,I+1/2,J+1/2,3/2} = S^{\text{corner}}_{g,I,J,1}, \qquad 1 \le g \le G, \qquad (3.56)
\end{aligned}
$$

where

$$
\begin{aligned}
C^{\text{corner}}_{g,I,J,1} &= X^{\text{edge}}_{g,I,J,1} + B^{\text{x-face, corner}}_{g,I,J,1} + Y^{\text{edge}}_{g,I,J,1} + B^{\text{y-face, corner}}_{g,I,J,1} + B^{\text{z-face, corner}}_{g,I,J,1} \\
&\quad + Z^{\text{edge}}_{g,I,J,1} + \bar{\Sigma}^{\text{corner}}_{R,g,I,J,1}, \qquad (3.57a)
\end{aligned}
$$

$$
B^{\text{x-face, corner}}_{g,I,J,1} = \begin{cases} \frac{A^{\text{x-face, corner}}_{g,I,J,1}}{2} & \text{, vacuum boundary,} \\ 0 & \text{, reflecting boundary,} \end{cases} \qquad (3.57b)
$$

$$
B^{\text{y-face, corner}}_{g,I,J,1} = \begin{cases} \frac{A^{\text{y-face, corner}}_{g,I,J,1}}{2} & \text{, vacuum boundary,} \\ 0 & \text{, reflecting boundary,} \end{cases} \qquad (3.57c)
$$

$$
B^{\text{z-face, corner}}_{g,I,J,1} = \begin{cases} \frac{A^{\text{z-face, corner}}_{g,I,J,1}}{2} & \text{, vacuum boundary,} \\ 0 & \text{, reflecting boundary,} \end{cases} \qquad (3.57d)
$$

$$
S^{\text{corner}}_{g,I,J,1} = \sum_{\substack{g'=1 \\ g' \neq g}}^{G} \bar{\Sigma}^{\text{corner}}_{s,g' \to g,I,J,1}\phi_{g',I+1/2,J+1/2,1/2} + \bar{Q}^{\text{corner}}_{g,I,J,1}. \qquad (3.57e)
$$

Corner: x=X, y=0, z=Z

For a boundary grid point on the corner $(X, 0, Z)$, we operate on the diffusion equation (Eq. 2.24) by $\int_{z_K}^{z_{K+1/2}} \int_{y_{1/2}}^{y_1} \int_{x_I}^{x_{I+1/2}} (\cdot) dx dy dz$ and use the boundary condition (Eq. 2.25) to obtain the following equation:

$$
\begin{aligned}
&- Z^{\text{edge}}_{g,I,1,K}\phi_{g,I+1/2,1/2,K-1/2} - X^{\text{edge}}_{g,I,1,K}\phi_{g,I-1/2,1/2,K+1/2} + C^{\text{corner}}_{g,I,1,K}\phi_{g,I+1/2,1/2,K+1/2} \\
&\quad - Y^{\text{edge}}_{g,I,1,K}\phi_{g,I+1/2,3/2,K+1/2} = S^{\text{corner}}_{g,I,1,K}, \qquad 1 \le g \le G, \qquad (3.58)
\end{aligned}
$$

where

$$
\begin{aligned}
C^{\text{corner}}_{g,I,1,K} &= X^{\text{edge}}_{g,I,1,K} + B^{\text{x-face, corner}}_{g,I,1,K} + B^{\text{y-face, corner}}_{g,I,1,K} + Y^{\text{edge}}_{g,I,1,K} + Z^{\text{edge}}_{g,I,1,K} \\
&\quad + B^{\text{z-face, corner}}_{g,I,1,K} + \bar{\Sigma}^{\text{corner}}_{R,g,I,1,K}, \qquad (3.59a)
\end{aligned}
$$

$$
B^{\text{x-face, corner}}_{g,I,1,K} = \begin{cases} \frac{A^{\text{x-face, corner}}_{g,I,1,K}}{2} & \text{, vacuum boundary,} \\ 0 & \text{, reflecting boundary,} \end{cases} \qquad (3.59b)
$$

$$B^{\text{y-face, corner}}_{g,I,1,K} = \begin{cases} \frac{A^{\text{y-face, corner}}_{g,I,1,K}}{2} & \text{, vacuum boundary,} \\ 0 & \text{, reflecting boundary,} \end{cases} \tag{3.59c}$$

$$B^{\text{z-face, corner}}_{g,I,1,K} = \begin{cases} \frac{A^{\text{z-face, corner}}_{g,I,1,K}}{2} & \text{, vacuum boundary,} \\ 0 & \text{, reflecting boundary,} \end{cases} \tag{3.59d}$$

$$S^{\text{corner}}_{g,I,1,K} = \sum_{\substack{g'=1 \\ g' \neq g}}^{G} \bar{\Sigma}^{\text{corner}}_{s,g' \to g,I,1,K} \phi_{g',I+1/2,1/2,K+1/2} + \bar{Q}^{\text{corner}}_{g,I,1,K}. \tag{3.59e}$$

Corner: x=X, y=Y, z=Z

For a boundary grid point on the corner (X, Y, Z), we operate on the diffusion equation (Eq. 2.24) by $\int_{z_K}^{z_{K+1/2}} \int_{y_J}^{y_{J+1/2}} \int_{x_I}^{x_{I+1/2}} (\cdot) dxdydz$ and use the boundary condition (Eq. 2.25) to obtain the following equation:

$$\begin{aligned} &- Z^{\text{edge}}_{g,I,J,K} \phi_{g,I+1/2,J+1/2,K-1/2} - Y^{\text{edge}}_{g,I,J,K} \phi_{g,I+1/2,J-1/2,K+1/2} - X^{\text{edge}}_{g,I,J,K} \phi_{g,I-1/2,J+1/2,K+1/2} \\ &\quad + C^{\text{corner}}_{g,I,J,K} \phi_{g,I+1/2,J+1/2,K+1/2} = S^{\text{corner}}_{g,I,J,K}, \qquad 1 \leq g \leq G, \end{aligned} \tag{3.60}$$

where

$$\begin{aligned} C^{\text{corner}}_{g,I,J,K} &= X^{\text{edge}}_{g,I,J,K} + B^{\text{x-face, corner}}_{g,I,J,K} + Y^{\text{edge}}_{g,I,J,K} + B^{\text{y-face, corner}}_{g,I,J,K} + Z^{\text{edge}}_{g,I,J,K} \\ &\quad + B^{\text{z-face, corner}}_{g,I,J,K} + \bar{\Sigma}^{\text{corner}}_{R,g,I,J,K}, \end{aligned} \tag{3.61a}$$

$$B^{\text{x-face, corner}}_{g,I,J,K} = \begin{cases} \frac{A^{\text{x-face, corner}}_{g,I,J,K}}{2} & \text{, vacuum boundary,} \\ 0 & \text{, reflecting boundary,} \end{cases} \tag{3.61b}$$

$$B^{\text{y-face, corner}}_{g,I,J,K} = \begin{cases} \frac{A^{\text{y-face, corner}}_{g,I,J,K}}{2} & \text{, vacuum boundary,} \\ 0 & \text{, reflecting boundary,} \end{cases} \tag{3.61c}$$

$$B^{\text{z-face, corner}}_{g,I,J,K} = \begin{cases} \frac{A^{\text{z-face, corner}}_{g,I,J,K}}{2} & \text{, vacuum boundary,} \\ 0 & \text{, reflecting boundary,} \end{cases} \tag{3.61d}$$

$$S^{\text{corner}}_{g,I,J,K} = \sum_{\substack{g'=1 \\ g' \neq g}}^{G} \bar{\Sigma}^{\text{corner}}_{s,g' \to g,I,J,K} \phi_{g',I+1/2,J+1/2,K+1/2} + \bar{Q}^{\text{corner}}_{g,I,J,K}. \tag{3.61e}$$

3.2 Numerical Solution Technique

Equations 3.8 - 3.61 are an algebraic system of $G(I+1)(J+1)(K+1)$ equations and unknowns. To solve this system, we cast these equations in matrix form for each

group g and use a standard algorithm for the numerical solution of linear systems (e.g. conjugate gradient, gaussian elimination, etc.). For problems with no upscattering, we can obtain the scalar flux by solving these matrix equations from the highest energy group ($g = 1$) to the lowest ($g = G$). Mathematically, we represent this as

$$\mathbf{L}_g^D \boldsymbol{\phi}_g = \mathbf{S}_g, \quad g = 1 \ldots G \tag{3.62}$$

where $\mathbf{L}_g^D$ is the "diffusion" matrix, $\mathbf{S}_g$ is the source vector, which includes both the fixed source and the downscattering source, and $\boldsymbol{\phi}_g$ is the scalar flux vector that describes the spatial solution in group g.

Most shielding problems neglect upscattering, since its contribution to the scattering source is either negligible or non-existent. However, if upscattering is included, then the above technique must be modified to obtain a converged source S_g in the groups with upscattering; this is done by iterating through the groups with upscattering until the upscattering source has converged to some specified criterion.

3.3 Grid-Adjusted Diffusion Coefficient

The discretization of the diffusion equation introduces additional error in the solution. To mitigate these effects, we derive an expression for the diffusion coefficient that more accurately preserves the attenuation rate of the continuous solution in regions with uniform material properties and a uniform grid. By uniform grid, we simply mean a grid in which the dimensions of each cell $C_{i,j,k}$ within a particular region are fixed, i.e., $(\Delta x, \Delta y, \Delta z)_{i,j,k} = (c_1, c_2, c_3)$.

To begin the derivation, we compare the within-group, discretized diffusion equation to the within-group, spatially-continuous diffusion equation for a region away from sources and boundaries with uniform material properties and a uniform grid. The within-group, spatially-continuous diffusion equation is given by Eq. 2.24 with the scattering and fixed source set to zero:

$$-D_g \frac{\partial^2 \phi_g}{\partial x^2}(x,y,z) - D_g \frac{\partial^2 \phi_g}{\partial y^2}(x,y,z) - D_g \frac{\partial^2 \phi_g}{\partial z^2}(x,y,z) + \Sigma_{R,g}\phi_g(x,y,z) = 0. \tag{3.63}$$

The discretized equation that we are interested in is the one that describes diffusion at an interior grid point (Eq. 3.8) with the scattering and fixed source set to zero:

$$
\begin{aligned}
&- D_g^x \frac{\phi_{g,i+3/2,j+1/2,k+1/2} - 2\phi_{g,i+1/2,j+1/2,k+1/2} + \phi_{g,i-1/2,j+1/2,k+1/2}}{\Delta x^2} \\
&\quad - D_g^y \frac{\phi_{g,i+1/2,j+3/2,k+1/2} - 2\phi_{g,i+1/2,j+1/2,k+1/2} + \phi_{g,i+1/2,j-1/2,k+1/2}}{\Delta y^2} \\
&\quad\quad - D_g^z \frac{\phi_{g,i+1/2,j+1/2,k+3/2} - 2\phi_{g,i+1/2,j+1/2,k+1/2} + \phi_{g,i+1/2,j+1/2,k-1/2}}{\Delta z^2} \\
&\quad\quad\quad + \Sigma_{R,g}\phi_{g,i+1/2,j+1/2,k+1/2} = 0, \qquad (3.64)
\end{aligned}
$$

where we have used the assumption of uniformity of material properties and grid and have rearranged the discretized equation to more closely resemble the continuous equation. We have also denoted the discretized diffusion coefficient by the superscripts x, y, and z, indicating that we expect the coefficient to be dependent on the grid dimensions. To determine these coefficients, we insert the continuous solution (Eq. 2.27) into both equations and equate analogous terms. The discrete form of the continuous solution, ϕ_g, is a simple evaluation at the grid point:

$$
\phi_{g,i+1/2,j+1/2,k+1/2} = A_g e^{\sqrt{\frac{\Sigma_{R,g}}{D_g}}(x_{i+1/2}\omega_{g,x} + y_{j+1/2}\omega_{g,y} + z_{k+1/2}\omega_{g,z})}. \qquad (3.65)
$$

Substituting Eq. 3.65 into the within-group, spatially-continuous diffusion equation (Eq. 3.63) results in the following expression:

$$
\left\{-\Sigma_{R,g}\omega_{g,x}^2 - \Sigma_{R,g}\omega_{g,y}^2 - \Sigma_{R,g}\omega_{g,z}^2 + \Sigma_{R,g}\right\}\phi_{g,i+1/2,j+1/2,k+1/2} = 0. \qquad (3.66)
$$

Substituting Eq. 3.65 into the within-group, discretized diffusion equation (Eq. 3.64) results in the following equation:

$$
\begin{aligned}
&\left\{ -\frac{2D_g^x}{\Delta x^2}\left[\cosh\left(\omega_{g,x}\Delta x\sqrt{\frac{\Sigma_{R,g}}{D_g}}\right) - 1\right] - \frac{2D_g^y}{\Delta y^2}\left[\cosh\left(\omega_{g,y}\Delta y\sqrt{\frac{\Sigma_{R,g}}{D_g}}\right) - 1\right]\right. \\
&\quad \left. -\frac{2D_g^z}{\Delta z^2}\left[\cosh\left(\omega_{g,z}\Delta z\sqrt{\frac{\Sigma_{R,g}}{D_g}}\right) - 1\right] + \Sigma_{R,g}\right\}\phi_{g,i+1/2,j+1/2,k+1/2} = 0. \qquad (3.67)
\end{aligned}
$$

By equating the analogous terms in Eq. 3.66 and Eq. 3.67, we obtain the necessary

requirements for more accurately preserving the continuous solution:

$$D_g^x = \frac{D_g}{2} \frac{\left(\omega_{g,x}\Delta x\sqrt{\frac{\Sigma_{R,g}}{D_g}}\right)^2}{\cosh\left(\omega_{g,x}\Delta x\sqrt{\frac{\Sigma_{R,g}}{D_g}}\right)-1}, \tag{3.68a}$$

$$D_g^y = \frac{D_g}{2} \frac{\left(\omega_{g,y}\Delta y\sqrt{\frac{\Sigma_{R,g}}{D_g}}\right)^2}{\cosh\left(\omega_{g,y}\Delta y\sqrt{\frac{\Sigma_{R,g}}{D_g}}\right)-1}, \tag{3.68b}$$

$$D_g^z = \frac{D_g}{2} \frac{\left(\omega_{g,z}\Delta z\sqrt{\frac{\Sigma_{R,g}}{D_g}}\right)^2}{\cosh\left(\omega_{g,z}\Delta z\sqrt{\frac{\Sigma_{R,g}}{D_g}}\right)-1}. \tag{3.68c}$$

We note that the discretized diffusion coefficients limit to the continuous diffusion coefficient as the grid size shrinks to zero, as it should:

$$\lim_{\Delta x\to 0} D_g^x = D_g, \tag{3.69a}$$

$$\lim_{\Delta y\to 0} D_g^y = D_g, \tag{3.69b}$$

$$\lim_{\Delta z\to 0} D_g^z = D_g. \tag{3.69c}$$

To implement these grid-adjusted diffusion coefficients, we simply modify Eqs. 3.3 by substituting D_g^x for D_g in definitions for $X_{g,i,j,k}$, D_g^y for D_g in definitions for $Y_{g,i,j,k}$, and D_g^z for D_g in definitions for $Z_{g,i,j,k}$. This adjustment is particularly useful for transport-corrected diffusion, since the objective is to preserve the asymptotic transport solution for diffusion. For transport-corrected diffusion, Eqs. 3.68 become:

$$D_g^x = \frac{\Sigma_{R,g}}{\lambda_g^2\Sigma_{t,g}^2}\frac{1}{2}\frac{\left(\omega_{g,x}\Delta x\lambda_g\Sigma_{t,g}\right)^2}{\cosh\left(\omega_{g,x}\Delta x\lambda_g\Sigma_{t,g}\right)-1}, \tag{3.70a}$$

$$D_g^y = \frac{\Sigma_{R,g}}{\lambda_g^2\Sigma_{t,g}^2}\frac{1}{2}\frac{\left(\omega_{g,y}\Delta y\lambda_g\Sigma_{t,g}\right)^2}{\cosh\left(\omega_{g,y}\Delta y\lambda_g\Sigma_{t,g}\right)-1}, \tag{3.70b}$$

$$D_g^z = \frac{\Sigma_{R,g}}{\lambda_g^2\Sigma_{t,g}^2}\frac{1}{2}\frac{\left(\omega_{g,z}\Delta z\lambda_g\Sigma_{t,g}\right)^2}{\cosh\left(\omega_{g,z}\Delta z\lambda_g\Sigma_{t,g}\right)-1}, \tag{3.70c}$$

where we recall that λ_g represents an analytic approximation to the exponential attenuation parameter for the asymptotic transport solution and that $\boldsymbol{\omega}_g$ is obtained by standard diffusion. This means that in order to use grid-adjusted asymptotic diffusion, both λ_g and $\boldsymbol{\omega}_g$ must be obtained; however, the computational time required

to obtain these quantities is small compared to the computational time expended on a Monte Carlo simulation.

The spatially-discretized, transport-corrected diffusion equation (with its grid-adjusted diffusion coefficient given by Eqs. 3.70) preserves the asymtotic solution of the analytic transport solution in each energy group, for any spatial grid. This property makes the solution of this equation useful for shielding problems, by more accurately preserving the exponential attenuation rate of the solution.

3.4 The Cell-Edge Adjoint Diffusion Discretization

By comparing the forward diffusion equation (Eqs. 2.24 and 2.25) to the adjoint diffusion equation (Eqs. 2.39 and 2.40), we see that the only difference is the scattering term: for adjoint diffusion, we sum over the outgoing energy group, while for forward diffusion, we sum over the incoming energy group. Due to this minor difference, we can use all the discretized equations for adjoint diffusion with the source term $S_{g,i,j,k}$ modified by replacing $\Sigma_{s,g'\rightarrow g,i,j,k}$ with $\Sigma_{s,g\rightarrow g',i,j,k}$ in the scattering source.

To preserve the attenuation rate of the continuous standard adjoint diffusion solution or the transport-corrected adjoint diffusion solution, we use Eqs. 3.68 with D_g defined according to standard adjoint diffusion or transport-corrected adjoint diffusion and $\boldsymbol{\omega}_g$ determined by a previous adjoint diffusion solution. The solution technique is the same as described in Section 3.2 for forward diffusion, except the solution is obtained by starting from the lowest energy group ($g = G$) and working up to the highest energy group ($g = 1$).

Chapter IV

Theoretical Issues

Many different types of problems need to be solved in applications of radiation transport. One very challenging problem is the deep-penetration (shielding) problem. Deterministic and Monte Carlo methods both have difficulties solving these problems. Some common difficulties encountered in deterministic methods are ray effects, which result from solving the transport equation along a fixed number of discrete angular ordinates rather than as a continuous angular function, and spatial oscillations, which result from low-order spatial approximations and imposed closure relations that are non-physical. Advanced deterministic methods seek to minimize these effects.

The primary challenge for the Monte Carlo method is obtaining good statistical information at various locations of interest in phase-space. This is especially problematic for shielding problems, in which the solution varies by many orders of magnitude across the physical system. If an analog Monte Carlo method were employed to solve a shielding problem, an enormous amount of computational time would be required to simulate enough particles to obtain adequate statistical information in regions far from the source. In fact, even using implicit capture requires extraordinary computational resources for difficult shielding problems. The main deficiency in both analog Monte Carlo and Monte Carlo with implicit capture is that statistically significant particles are not distributed throughout phase space in an advantageous way.

For the analog Monte Carlo method, all Monte Carlo particles have the same statistical significance, since they all maintain the same weight throughout their histories; however, most of the particle histories are spent near the source, and few particles travel to the deep regions of the problem. For Monte Carlo with implicit capture, the particles still spend most of their history near the source, although they do disperse further from the source than for the analog method; however, the particle weights can vary dramatically, leading to a very large variance. In this case,

the Monte Carlo information can have poor statistical quality and require a very long run-time, due to processing particles with very low weights.

To achieve a more efficient Monte Carlo solution, we use two techniques: *weight windows* and a new technique referred to as the *Transform approach*. *Both of these techniques achieve a more efficient solution by constraining the weights of the particles and advantageously distributing the particles throughout phase space.* This chapter describes weight windows and the Transform approach in detail, with a specific emphasis on distributing Monte Carlo particles according to a user-specified distribution.

4.1 The Monte Carlo Particle Flux

The motivation for using weight windows and the Transform approach is that they allow the user to distribute Monte Carlo particles in a particular way. For this reason, we begin by defining the *Monte Carlo particle flux*, a quantity which describes how Monte Carlo particles are distributed throughout phase space.

We first define the *Monte Carlo particle density* $N_{mc}(\mathbf{x}, \mathbf{\Omega}, E, w)$:

$$\begin{aligned} &N_{mc}(\mathbf{x}, \mathbf{\Omega}, E, w) dV\, d\Omega\, dE\, dw \\ &\quad = \text{expected number of Monte Carlo particles in } dV \text{ about } \mathbf{x}, \\ &\qquad \text{traveling in directions in } d\Omega \text{ about } \mathbf{\Omega}, \text{ with energies between} \\ &\qquad E \text{ and } E + dE, \text{ with weights between } w \text{ and } w + dw. \end{aligned} \tag{4.1}$$

We now define various Monte Carlo particle flux quantities:

$$\begin{aligned} M(\mathbf{x}, \mathbf{\Omega}, E, w) &= v N_{mc}(\mathbf{x}, \mathbf{\Omega}, E, w) \\ &= \textit{weight-dependent angular Monte Carlo particle flux,} && (4.2) \\ m(\mathbf{x}, \mathbf{\Omega}, E) &= \int_0^\infty M(\mathbf{x}, \mathbf{\Omega}, E, w) dw \\ &= \textit{angular Monte Carlo particle flux,} && (4.3) \\ \mathcal{M}(\mathbf{x}, E) &= \int_{4\pi} m(\mathbf{x}, \mathbf{\Omega}, E) d\Omega \\ &= \textit{(energy-dependent) scalar Monte Carlo particle flux,} && (4.4) \\ \mathcal{M}(\mathbf{x}) &= \int_0^\infty \mathcal{M}(\mathbf{x}, E) dE \\ &= \textit{(energy-integrated) scalar Monte Carlo particle flux.} && (4.5) \end{aligned}$$

The angular Monte Carlo particle flux $m(\mathbf{x}, \mathbf{\Omega}, E)$ is analogous to the angular neutron flux $\psi(\mathbf{x}, \mathbf{\Omega}, E)$; the (energy-dependent) scalar Monte Carlo particle flux $\mathcal{M}(\mathbf{x}, E)$ is analogous to the (energy-dependent) scalar neutron flux $\phi(\mathbf{x}, E)$; and the (energy-integrated) scalar Monte Carlo particle flux $\mathcal{M}(\mathbf{x})$ is analogous to the (energy-integrated) scalar neutron flux $\phi(\mathbf{x})$. For this thesis we are interested in "controlling" the scalar Monte Carlo particle flux; both weight windows and the Transform approach allow us to do this.

In a Monte Carlo simulation, the angular neutron flux is related to the weight-dependent Monte Carlo particle flux through the following relation:

$$\psi(\mathbf{x}, \mathbf{\Omega}, E) = \int_0^\infty wM(\mathbf{x}, \mathbf{\Omega}, E, w)dw. \tag{4.6}$$

We will use the definitions of the Monte Carlo particle flux along with Eq. 4.6 to describe the weight window approach and the Transform approach in terms of the scalar Monte Carlo particle flux, $\mathcal{M}(\mathbf{x}, E)$.

4.2 Weight Windows

The use of weight windows has primarily been limited to simulating source-detector problems, in which a solution is desired at a single location in space. In these problems the source and detector are separated by a non-trivial distance, the geometry is often complicated, and the solution experiences significant attenuation (by 10 or more orders of magnitude) from the source to the detector. The weight windows are determined either from the solution of the adjoint transport equation or by an experienced engineer who is familiar with the physics and geometry of the problem and the Monte Carlo methodology. For shielding problems, several source-detector problems are simulated with each detector (or several detectors) placed in a region of interest, perhaps in a room where instrumentation exists or a corridor through which people pass.

As computational resources have become more readily available and more efficient for computationally-costly calculations, it has become reasonable to consider using Monte Carlo methods to obtain the solution *everywhere* (or in a relatively large spatial region) rather than at *specific locations* in space. To this end, weight windows have been proposed for obtaining global solutions in space [28–30,41]. In this section, we provide a more thorough understanding of the weight window, specifically by deriving a simple expression that relates the Monte Carlo particle flux to the weight

window center.

4.2.1 The Monte Carlo Particle Flux

Weight windows have been used to improve the statistical quality of the data (i.e. reduce the variance) by mitigating the effect of high-weight particles on the variance and to improve the efficiency of the calculation by eliminating the unnecessary computational time consumed by processing low-weight particles. However, little attention has been given to understanding how the energy- and space-dependent weight window center should be chosen to obtain the best solution. As mentioned, the adjoint solution is commonly used for source-detector problems, mainly due to its intuitive appeal as an *importance function* for a given detector response; however, little is known about the effect of this choice of weight windows on the simulation.

We propose using a weight window that not only constrains the weight of the particle but also distributes particles in an optimal manner. To accomplish this goal, we derive an expression that relates the weight window center, $\mathrm{w}(\mathbf{x}, E)$, and the Monte Carlo particle flux, $\mathcal{M}(\mathbf{x}, E)$.

Since the weight window constrains the particle weight about the weight window center, we consider the Monte Carlo particle distribution that results from particles at $(\mathbf{x}, E)$ having a weight that is approximately equal to the weight window center, $\mathrm{w}(\mathbf{x}, E)$. Mathematically, we express this distribution in terms of the Monte Carlo particle flux as

$$M(\mathbf{x}, \mathbf{\Omega}, E, w) \approx m(\mathbf{x}, \mathbf{\Omega}, E)\delta[w - \mathrm{w}(\mathbf{x}, E)]. \tag{4.7}$$

Then, to relate the Monte Carlo particle flux $\mathcal{M}(\mathbf{x}, E)$ to the weight weight window center $\mathrm{w}(\mathbf{x}, E)$, we substitute this approximation into Eq. 4.6 and integrate over all angles. We obtain

$$\boxed{\phi(\mathbf{x}, E) \approx \mathrm{w}(\mathbf{x}, E)\mathcal{M}(\mathbf{x}, E).} \tag{4.8}$$

We use this simple expression in two ways. First, we use it to determine the appropriate weight windows for a problem, in which a specified $\mathcal{M}(\mathbf{x}, E)$ is desired. In this case, we are most interested in the following form of Eq. 4.8:

$$\mathrm{w}(\mathbf{x}, E) = \frac{\phi(\mathbf{x}, E)}{\mathcal{M}(\mathbf{x}, E)}. \tag{4.9}$$

This expression allow us to choose weight windows based on the desired Monte Carlo particle flux. The utility of doing this will become more apparent as we demonstrate

its use for shielding problems in which a solution is required in a detector, in a significant portion of phase-space, or everywhere.

Eq. 4.8 also determines the Monte Carlo particle flux distribution that occurs when a specified set of weight windows that is used for a specific problem. These weight windows may have been generated by an experienced user or some unknown means, and their effect on the simulation is unclear. The following form of Eq. 4.8 allows one to obtain the Monte Carlo particle flux distribution that occurs when a given set of weight windows is used:

$$\mathcal{M}(\mathbf{x}, E) = \frac{\phi(\mathbf{x}, E)}{\mathrm{w}(\mathbf{x}, E)}. \tag{4.10}$$

This expression allows one to ascertain some characteristics of the simulation, such as whether to anticipate excessive splitting or Russian roulette. If the Monte Carlo particle flux distribution seems unsatisfactory, then new weight windows can be generated using Eq. 4.9 with the desired Monte Carlo particle flux distribution. (Of course, this expression also requires some knowledge of the solution ϕ, which could be obtained after the Monte Carlo solution has been acquired, using the given set of weight windows, or from an inexpensive deterministic or diffusion solution.)

In this thesis, we use an approximate deterministic solution to approximate the weight window in Eq. 4.9. Since deterministic solutions are discrete in space and energy, our weight windows are approximated as histograms in space and energy:

$$\mathrm{w}(\mathbf{x}, E) = \mathrm{w}_{c,g}, \quad \mathbf{x} \in \mathcal{V}_c, \;\; E_g < E \leq E_{g-1}. \tag{4.11}$$

Here the spatial elements $\{\mathcal{V}_c\}_{c=1}^{N_{\text{cells}}}$ comprise the spatial domain of the problem and the energy segments $\{(E_g, E_{g-1}]\}_{g=0}^{G}$ comprise the energy domain.

4.2.2 Weight Window Physics for Monte Carlo Sampling

In Chapter 2, we described the probability distributions that are applicable to neutron transport. For the most part, these relationships are still valid, except that we must include the weight of the particle in our discussion. In addition, implicit capture is always used with weight windows; for this reason, we replace the analog collision process with implicit capture. In this section we provide a brief derivation of the probability distributions and the corresponding expressions that describe the particle weight for various processes.

Sampling an Interior Source

To describe the probability distribution for an interior source that accounts for particle weight, we begin with the term in the transport equation that corresponds to an interior source and factor it into the total problem source rate Q_T, the joint probability distribution $p(\mathbf{x}, \mathbf{\Omega}, E)$, and the initial particle weight $w_0 = w_0(\mathbf{x}, E)$:

$$Q(\mathbf{x}, \mathbf{\Omega}, E) = Q_T \cdot p(\mathbf{x}, \mathbf{\Omega}, E) \cdot w_0(\mathbf{x}, E), \tag{4.12}$$

where

$$Q_T = \int_V \int_0^\infty \int_{4\pi} \frac{Q(\mathbf{x}, \mathbf{\Omega}, E)}{\mathrm{w}(\mathbf{x}, E)} d\Omega dE dV, \tag{4.13}$$

$$p(\mathbf{x}, \mathbf{\Omega}, E) = \frac{\dfrac{Q(\mathbf{x}, \mathbf{\Omega}, E)}{\mathrm{w}(\mathbf{x}, E)}}{\displaystyle\int_V \int_0^\infty \int_{4\pi} \frac{Q(\mathbf{x}, \mathbf{\Omega}, E)}{\mathrm{w}(\mathbf{x}, E)} d\Omega dE dV}, \tag{4.14}$$

$$w_0(\mathbf{x}, E) = \mathrm{w}(\mathbf{x}, E). \tag{4.15}$$

The initial particle weight is set to the center of the weight window $\mathrm{w}(\mathbf{x}, E)$ in order that there be no splitting or Russian rouletting when a particle is initialized.

For this thesis we only consider isotropic, spatially-uniform sources within each spatial element $\mathcal{V}_c$:

$$Q(\mathbf{x}, \mathbf{\Omega}, E) = \frac{Q_c(E)}{4\pi}, \quad \mathbf{x} \in \mathcal{V}_c,\ \mathbf{\Omega} \in 4\pi,\ 0 < E < \infty, \tag{4.16}$$

and an angle-independent weight window that is uniform for $E \in (E_g, E_{g-1}]$ and for $\mathbf{x} \in \mathcal{V}_c$:

$$\mathrm{w}(\mathbf{x}, E) = \mathrm{w}_{c,g}, \quad \mathbf{x} \in \mathcal{V}_c,\ E_g < E \leq E_{g-1}. \tag{4.17}$$

This source distribution and weight window allow us to rewrite the joint probability distribution as

$$\begin{aligned} p(\mathbf{x}, \mathbf{\Omega}, E) = p(&\mathbf{x} \,|\, \mathbf{x} \in \mathcal{V}_c) \\ &\cdot p(\mathbf{\Omega}) \\ &\cdot p(E \,|\, E_g < E \leq E_{g-1}, \mathbf{x} \in \mathcal{V}_c) \\ &\cdot p(E_g < E \leq E_{g-1} \,|\, \mathbf{x} \in \mathcal{V}_c) \\ &\cdot p(\mathbf{x} \in \mathcal{V}_c), \end{aligned} \tag{4.18}$$

where we make the following definitions for the probability distributions:

$$p(\mathbf{x} \,|\, \mathbf{x} \in \mathcal{V}_c) = p(x \,|\, \mathbf{x} \in \mathcal{V}_c) \cdot p(y \,|\, \mathbf{x} \in \mathcal{V}_c) \cdot p(z \,|\, \mathbf{x} \in \mathcal{V}_c), \tag{4.19}$$

$$p(x \,|\, \mathbf{x} \in \mathcal{V}_c) = \frac{1}{x_{i+1/2} - x_{i-1/2}}, \tag{4.20}$$

$$p(y \,|\, \mathbf{x} \in \mathcal{V}_c) = \frac{1}{y_{j+1/2} - y_{j-1/2}}, \tag{4.21}$$

$$p(z \,|\, \mathbf{x} \in \mathcal{V}_c) = \frac{1}{z_{k+1/2} - z_{k-1/2}}, \tag{4.22}$$

$$p(\mathbf{\Omega}) = p(\mu) \cdot p(\gamma), \tag{4.23}$$

$$p(\mu) = \frac{1}{2}, \tag{4.24}$$

$$p(\gamma) = \frac{1}{2\pi}, \tag{4.25}$$

$$p(E \,|\, E_g < E \leq E_{g-1}, \mathbf{x} \in \mathcal{V}_c) = \frac{Q_c(E)}{\displaystyle\int_{E_g}^{E_{g-1}} Q_c(E')dE'}, \tag{4.26}$$

$$p(E_g < E \leq E_{g-1} \,|\, \mathbf{x} \in \mathcal{V}_c) = \frac{\displaystyle\int_{E_g}^{E_{g-1}} \frac{Q_c(E')}{\mathrm{w}_{c,g}} dE'}{\displaystyle\sum_{g'=1}^{G} \int_{E_{g'}}^{E_{g'-1}} \frac{Q_c(E')}{\mathrm{w}_{c,g'}} dE'}, \tag{4.27}$$

$$p(\mathbf{x} \in \mathcal{V}_c) = \frac{\displaystyle\sum_{g=1}^{G} \int_{E_g}^{E_{g-1}} \frac{Q_c(E)V_c}{\mathrm{w}_{c,g}} dE}{\displaystyle\sum_{c=1}^{N_{\text{cells}}} \sum_{g=1}^{G} \int_{E_g}^{E_{g-1}} \frac{Q_c(E)V_c}{\mathrm{w}_{c,g}} dE}. \tag{4.28}$$

The total problem source rate is given by

$$Q_T = \sum_{c=1}^{N_{\text{cells}}} \sum_{g=1}^{G} \int_{E_g}^{E_{g-1}} \frac{Q_c(E)V_c}{\mathrm{w}_{c,g}} dE, \tag{4.29}$$

and the initial weight of the particle becomes

$$w_0(\mathbf{x}, E) = \mathrm{w}_{c,g}, \quad \mathbf{x} \in \mathcal{V}_c,\ E_g < E \leq E_{g-1}. \tag{4.30}$$

To obtain the multigroup probability distribution, we integrate $p(\mathbf{x}, \mathbf{\Omega}, E)$ over the energy range of a group g and use the multigroup definition for the source to

obtain:

$$1 = \int_{E_g}^{E_{g-1}} p(E \,|\, E_g < E \leq E_{g-1}, \mathbf{x} \in \mathcal{V}_c) dE, \tag{4.31}$$

$$p(g \,|\, \mathbf{x} \in V_c) = \frac{\dfrac{Q_{c,g}}{\mathrm{w}_{c,g}}}{\displaystyle\sum_{g'=1}^{G} \frac{Q_{c,g'}}{\mathrm{w}_{c,g'}}}, \tag{4.32}$$

$$p(\mathbf{x} \in \mathcal{V}_c) = \frac{\displaystyle\sum_{g=1}^{G} \frac{Q_{c,g} V_c}{\mathrm{w}_{c,g}}}{\displaystyle\sum_{c=1}^{N_{\text{cells}}} \sum_{g=1}^{G} \frac{Q_{c,g} V_c}{\mathrm{w}_{c,g}}}. \tag{4.33}$$

All these probability distributions, except the continuous-energy distribution, can be directly sampled by inverting the cumulative probability distribution. (It is possible to directly sample the continuous-energy distribution if the indefinite integral of the source $Q_c(E)$ is invertible.) When we do this, we obtain the following results that determine the initial state of the particle ($\xi \in [0, 1]$):

$$x = x_{i-1/2} + \xi \left(x_{i+1/2} - x_{i-1/2} \right), \tag{4.34}$$

$$y = y_{j-1/2} + \xi \left(y_{j+1/2} - y_{j-1/2} \right), \tag{4.35}$$

$$z = z_{k-1/2} + \xi \left(z_{k+1/2} - z_{k-1/2} \right), \tag{4.36}$$

$$\mu = -1 + 2\xi, \tag{4.37}$$

$$\gamma = 2\pi\xi, \tag{4.38}$$

$$E = E_0 \text{ if } \xi = \frac{\int_{E_g}^{E_0} Q_c(E') dE'}{\int_{E_g}^{E_{g-1}} Q_c(E') dE'}, \tag{4.39}$$

$$g = g_0 \text{ if } \sum_{g'=1}^{g_0-1} p(E_{g'} < E \leq E_{g'-1} \,|\, \mathbf{x} \in \mathcal{V}_c) < \xi \leq \sum_{g'=1}^{g_0} p(E_{g'} < E \leq E_{g'-1} \,|\, \mathbf{x} \in \mathcal{V}_c), \tag{4.40}$$

$$\mathbf{x} \in \mathcal{V}_{c_0} \text{ if } \sum_{c=1}^{c_0-1} p(\mathbf{x} \in \mathcal{V}_c) < \xi \leq \sum_{c=1}^{c_0} p(\mathbf{x} \in \mathcal{V}_c). \tag{4.41}$$

The multigroup distributions also use the above equations to sample for g and $\mathbf{x} \in \mathcal{V}_c$,

with the multigroup definition of the source.

These relations determine a particle's initial state $(\mathbf{x}, \mathbf{\Omega}, E)$, or $(\mathbf{x}, \mathbf{\Omega}, g)$ for the multigroup problem. As long as the particle's energy is greater than zero, it begins to move throughout the system. The distance it travels before colliding with an atom (or molecule) in the medium is described next.

Sampling the Distance-To-Next Collision

The distance-to-next collision is sampled as described in Chapter 2. For continuous-energy Monte Carlo, the distribution describing the distance-to-next collision is given by

$$p(s) = \Sigma_{t,c}(E) e^{-\Sigma_{t,c}(E)s}, \tag{4.42}$$

where we have assumed homogeneous material properties while a particle moves within spatial element $\mathcal{V}_c$. To sample this distribution, we invert the cumulative probability distribution to obtain

$$s = -\frac{\ln(\xi)}{\Sigma_{t,c}(E)}. \tag{4.43}$$

For multigroup problems, we replace $\Sigma_{t,c}(E)$ with $\Sigma_{t,c,g}$.

Sampling the Scattering Distribution

To determine the distribution that describes the emission of a particle after a collision and the resulting weight change, we consider the integrand of the scattering integral in the neutron transport equation. This integrand describes the discrete physics that determine the emerging state of a neutron, $(\mathbf{x}, \mathbf{\Omega}, E)$, given that it experiences a collision in phase space at $(\mathbf{x}, \mathbf{\Omega}', E')$ with $\mathbf{x} \in \mathcal{V}_c$:

$$\begin{aligned}\Sigma_{s,c}(\mathbf{\Omega}' \cdot \mathbf{\Omega}, E' \rightarrow E)\psi(\mathbf{x}, \mathbf{\Omega}', E') \\ = p_c(\mathbf{\Omega}' \cdot \mathbf{\Omega}, E' \rightarrow E) \cdot w_{scat,c}(E') \cdot R_{\text{coll},c}(\mathbf{x}, \mathbf{\Omega}', E'),\end{aligned} \tag{4.44}$$

where $p_c(\mathbf{\Omega}' \cdot \mathbf{\Omega}, E' \rightarrow E)$ is the joint probability distribution, $w_{\text{scat},c}(E')$ is the multiplicative weight change that results from the collision, and $R_{\text{coll},c}(\mathbf{x}, \mathbf{\Omega}', E')$ is the collision rate.

The probability distribution can be defined as:

$$p_c(\mathbf{\Omega}' \cdot \mathbf{\Omega}, E' \rightarrow E) = p_c(\mathbf{\Omega}' \cdot \mathbf{\Omega} \,|\, E' \rightarrow E) \cdot p_c(E' \rightarrow E), \tag{4.45}$$

where

$$p_c(\mathbf{\Omega}' \cdot \mathbf{\Omega} \,|\, E' \to E) = \frac{\Sigma_{s,c}(\mathbf{\Omega} \cdot \mathbf{\Omega}', E' \to E)}{\Sigma_{s0,c}(E' \to E)}, \tag{4.46}$$

$$p_c(E' \to E) = \frac{\Sigma_{s0,c}(E' \to E)}{\Sigma_{s,c}(E')}. \tag{4.47}$$

The multiplicative weight change is defined as

$$w_{\text{scat},c}(E) = \frac{\Sigma_{s,c}(E)}{\Sigma_{t,c}(E)}. \tag{4.48}$$

The collision rate is defined as

$$R_{\text{coll},c}(\mathbf{x}, \mathbf{\Omega}, E) = \Sigma_{t,c}(E)\psi(\mathbf{x}, \mathbf{\Omega}, E). \tag{4.49}$$

Sampling these probability distributions can be complicated for continuous-energy Monte Carlo, and many emission laws exist. For simplicity, we only show mathematically how one could sample these distributions, since this thesis is limited to multigroup computations.

To sample the energy of the emerging particle, E, we use the following expression ($\xi \in [0, 1]$):

$$E = E_0 \text{ if } \xi = \int_0^{E_0} p_c(E' \to E'')dE''. \tag{4.50}$$

To sample the initial direction, we first represent the direction vector, $\mathbf{\Omega}$, in terms of another orthonormal basis of $\mathbb{R}^3$, $\{\mathbf{\Omega}', \mathbf{\Omega}'_{\perp_1}, \mathbf{\Omega}'_{\perp_2}\}$, then sample the direction cosines with reference to this basis, and finally rotate back to the canonical basis of $\mathbb{R}^3$, $\{\mathbf{i}, \mathbf{j}, \mathbf{k}\}$. That is, we represent the outgoing direction $\mathbf{\Omega}$ as

$$\mathbf{\Omega} = \Omega_1^r \, \mathbf{\Omega}' + \Omega_2^r \, \mathbf{\Omega}'_{\perp_1} + \Omega_3^r \, \mathbf{\Omega}'_{\perp_2}. \tag{4.51}$$

After sampling the direction cosines $(\Omega_1^r, \Omega_2^r, \Omega_3^r)$, we rotate back to the canonical basis, where $\mathbf{\Omega}$ is represented as

$$\mathbf{\Omega} = \Omega_1 \mathbf{i} + \Omega_2 \mathbf{j} + \Omega_3 \mathbf{k}. \tag{4.52}$$

The rotation is given by the following equations:

$$\Omega_1 = \Omega_1^r \, \Omega'_1 + \Omega_2^r \, \Omega'_{\perp_1,1} + \Omega_3^r \, \Omega'_{\perp_2,1}, \tag{4.53a}$$

$$\Omega_2 = \Omega_1^r\,\Omega_2' + \Omega_2^r\,\Omega'_{\perp_1,2} + \Omega_3^r\,\Omega'_{\perp_2,2}, \tag{4.53b}$$

$$\Omega_3 = \Omega_1^r\,\Omega_3' + \Omega_2^r\,\Omega'_{\perp_1,3} + \Omega_3^r\,\Omega'_{\perp_2,3}. \tag{4.53c}$$

We define the orthonormal basis, $\{\mathbf{\Omega}', \mathbf{\Omega}'_{\perp_1}, \mathbf{\Omega}'_{\perp_2}\}$, noting that $\mathbf{\Omega}'$ is the incoming particle direction that is already known. The other two vectors that form the set are simply vectors that exist in the plane perpendicular to $\mathbf{\Omega}'$ and orthogonal to each other. We have defined the basis set in two ways. The first is when $\mathbf{\Omega}' = \pm\mathbf{k}$ (i.e. $\Omega_1' = 0$ and $\Omega_2' = 0$); the second is when $\mathbf{\Omega}' \neq \pm\mathbf{k}$ (i.e. either Ω_1' or Ω_2' is non-zero, or both are non-zero).

For the first case, $\mathbf{\Omega}' = \pm\mathbf{k}$, the non-canonical basis set for $\mathbb{R}^3$ is defined as

$$\mathbf{\Omega}' \quad = \Omega_3'\,\mathbf{k}, \quad \Omega_3' = \pm 1, \tag{4.54a}$$

$$\mathbf{\Omega}'_{\perp_1} = \mathbf{i}, \tag{4.54b}$$

$$\mathbf{\Omega}'_{\perp_2} = \mathbf{j}. \tag{4.54c}$$

After sampling the direction cosines in the non-canonical basis, $(\Omega_1^r, \Omega_2^r, \Omega_3^r)$, we use Eqs. 4.53 to determine the initial direction cosines in the canonical basis set, $(\Omega_1, \Omega_2, \Omega_3)$.

For the second case, $\mathbf{\Omega}' \neq \pm\mathbf{k}$, the non-canonical basis set for $\mathbb{R}^3$ is defined as

$$\mathbf{\Omega}' = \Omega_1'\mathbf{i} + \Omega_2'\mathbf{j} + \Omega_3'\mathbf{k}, \tag{4.55a}$$

$$\mathbf{\Omega}'_{\perp_1} = \frac{\Omega_2'}{\sqrt{\Omega_1'^2 + \Omega_2'^2}}\mathbf{i} - \frac{\Omega_1'}{\sqrt{\Omega_1'^2 + \Omega_2'^2}}\mathbf{j}, \tag{4.55b}$$

$$\mathbf{\Omega}'_{\perp_2} = \frac{\Omega_1'\Omega_3'}{\sqrt{\Omega_1'^2 + \Omega_2'^2}}\mathbf{i} + \frac{\Omega_2'\Omega_3'}{\sqrt{\Omega_1'^2 + \Omega_2'^2}}\mathbf{j} - \sqrt{\Omega_1'^2 + \Omega_2'^2}\mathbf{k}, \tag{4.55c}$$

where we note that $\sqrt{\Omega_1'^2 + \Omega_2'^2} \neq 0$ since $\mathbf{\Omega}' \neq \pm\mathbf{k}$. After sampling the direction cosines in the non-canonical basis, $(\Omega_1^r, \Omega_2^r, \Omega_3^r)$, we use Eqs. 4.53 to determine the initial direction cosines in the canonical basis set, $(\Omega_1, \Omega_2, \Omega_3)$.

Finally, we specify how to sample the direction cosines in the non-canonical basis, $(\Omega_1^r, \Omega_2^r, \Omega_3^r)$. When $\mathbf{\Omega}$ is represented in terms of the non-canonical basis, $\mathbf{\Omega} = \Omega_1^r\,\mathbf{\Omega}' + \Omega_2^r\,\mathbf{\Omega}'_{\perp_1} + \Omega_3^r\,\mathbf{\Omega}'_{\perp_2}$, the probability distribution for the initial direction can be written as

$$p_c(\mathbf{\Omega}' \cdot \mathbf{\Omega} \,|\, E' \to E) = p_c(\mu \,|\, E' \to E) \cdot p(\gamma), \tag{4.56}$$

where we have defined the probability distributions for the polar angle cosine μ and

the azimuthal angle γ as follows:

$$p_c(\mu \,|\, E' \to E) = \sum_{n=0}^{N} \frac{2n+1}{2} \frac{\Sigma_{s,c,n}(E' \to E)}{\Sigma_{s,c,0}(E' \to E)} P_n(\mu), \tag{4.57a}$$

$$p(\gamma) = \frac{1}{2\pi}. \tag{4.57b}$$

We can sample the probability distribution function for the azimuthal angle γ by directly inverting the cumulative distribution function: $\gamma = 2\pi\xi$ with $\xi \in [0, 1]$. The probability distribution for the polar angle cosine μ can be sampled by directly inverting the cumulative distribution function for lower order sampling or using rejection sampling for higher order scattering.

The direction cosines for $\mathbf{\Omega}$ in the rotated orthonormal basis $\{\mathbf{\Omega}', \mathbf{\Omega}'_{\perp_1}, \mathbf{\Omega}'_{\perp_2}\}$ are given by

$$\Omega_1^r = \mu, \tag{4.58a}$$

$$\Omega_2^r = \sqrt{1-\mu^2}\cos(\gamma), \tag{4.58b}$$

$$\Omega_3^r = \sqrt{1-\mu^2}\sin(\gamma). \tag{4.58c}$$

To summarize, we sample the probability distribution in Eqs. 4.57 for the outgoing direction, we use Eqs. 4.58 to obtain the direction cosines in the non-canonical basis defined by Eqs. 4.54 and Eqs. 4.55, and finally we use Eqs. 4.53 to obtain the direction cosines for the initial direction in the standard canonical basis.

The multigroup probability distributions are found by considering the analogous multigroup scattering kernel:

$$\Sigma_{s,c,g'\to g}(\mathbf{\Omega}' \cdot \mathbf{\Omega})\psi_g(\mathbf{x}, \mathbf{\Omega}') = p_c(\mathbf{\Omega}' \cdot \mathbf{\Omega}, g' \to g) \cdot w_{\text{scat},c,g'} \cdot R_{\text{coll},c,g'}(\mathbf{x}, \mathbf{\Omega}'), \tag{4.59}$$

where $p_c(\mathbf{\Omega}' \cdot \mathbf{\Omega}, g' \to g)$ is the probability distribution for the multigroup scattering process, $w_{\text{scat},c,g'}$ is the multiplicative weight change that results from the collision, and $R_{\text{coll},c,g'}(\mathbf{x}, \mathbf{\Omega}')$ is the collision rate.

The multigroup probability distribution can be defined as

$$p_c(\mathbf{\Omega}' \cdot \mathbf{\Omega}, g' \to g) = p_c(\mathbf{\Omega}' \cdot \mathbf{\Omega} \,|\, g' \to g) \cdot p_{c,g'\to g}, \tag{4.60}$$

where

$$p_c(\mathbf{\Omega}' \cdot \mathbf{\Omega} \,|\, g' \to g) = \frac{\Sigma_{s,c,g'\to g}(\mathbf{\Omega}' \cdot \mathbf{\Omega})}{\Sigma_{s0,c,g'\to g}}, \tag{4.61}$$

$$p_{c,g'\to g} = \frac{\Sigma_{s0,c,g'\to g}}{\Sigma_{s,c,g'}}. \tag{4.62}$$

The multiplicative weight change for the multigroup problem is defined as

$$w_{\text{scat},c,g} = \frac{\Sigma_{s,c,g}}{\Sigma_{t,c,g}}. \tag{4.63}$$

The multigroup collision rate is given by

$$R_{\text{coll},c,g}(\mathbf{x}, \mathbf{\Omega}) = \Sigma_{t,c,g}\psi_g(\mathbf{x}, \mathbf{\Omega}). \tag{4.64}$$

To sample the outgoing energy group, we use the following prescription:

$$g = g_0 \text{ if } \sum_{g''=1}^{g_0-1} p_{c,g'\to g''} \;<\; \xi \;\leq\; \sum_{g''=1}^{g_0} p_{c,g'\to g''}. \tag{4.65}$$

The outgoing direction is sampled the same way for multigroup problems as for continuous energy problems. The only difference is that the probability distribution for the azimuthal angle now contains multigroup cross-sections:

$$p_c(\mathbf{\Omega}' \cdot \mathbf{\Omega} \,|\, g' \to g) = p_c(\mu \,|\, g' \to g) \cdot p(\gamma), \tag{4.66}$$

where

$$p_c(\mu \,|\, g' \to g) = \sum \frac{2n+1}{2} \frac{\Sigma_{sn,c,g'\to g}}{\Sigma_{s0,c,g'\to g}} P_n(\mu), \tag{4.67}$$

$$p(\gamma) = \frac{1}{2\pi}. \tag{4.68}$$

4.2.3 Estimators

The path length estimator and the collision estimator are exactly the same as those described in Chapter 2. The bin structure that we use to tally is defined for the energy range by the boundaries $\{E_g\}_{g=0}^{G}$ and spatially by the set $\{\mathcal{V}_c\}_{c=1}^{N_{\text{cells}}}$ with each element having a volume V_c. In general, we wish to obtain an estimate of the

scalar flux $\phi(\mathbf{x}, E)$ and/or a response $\mathcal{R}(\mathbf{x})$, defined as

$$\mathcal{R}(\mathbf{x}) = \int_0^\infty \Sigma_{\mathcal{R}}(\mathbf{x}, \mathbf{E})\phi(\mathbf{x}, E)dE, \tag{4.69}$$

where $\Sigma_{\mathcal{R}}(\mathbf{x}, E)$ is the *response function* (e.g. a reaction cross-section or dose conversion factor) used to calculate an energy-integrated response such as a reaction rate or biological dose.

Path Length Estimator

The nth simulation particle provides a path length estimate for the scalar flux $\phi(\mathbf{x}, E)$ that is given by

$$\phi_{c,g,n}^{\text{path}} = \frac{Q_T}{V_c} \sum_{i=1}^{I_{c,g,n}} l_i \, w_i, \tag{4.70}$$

where Q_T is total system source rate, $I_{c,g,n}$ is the number of track lengths generated by the nth simulation particle in volume V_c and in energy group g, l_i is an individual track length, and w_i is the weight of the particle as it generates the track length l_i. Since the track length and weight are independent of energy, this estimator is valid for a continuous-energy as well as multigroup simulation.

To obtain the mean value for the scalar flux and the variance of the mean for a simulation with N particles, we use the following equations:

$$\phi_{c,g}^{\text{path}} = \frac{1}{N} \sum_{n=1}^{N} \phi_{c,g,n}^{\text{path}} \tag{4.71}$$

$$= \frac{Q_T}{N\,V_c} \sum_{n=1}^{N} \sum_{i=1}^{I_{c,g,n}} l_i \, w_i, \tag{4.72}$$

$$\text{Var}\left[\phi_{c,g}^{\text{path}}\right] = \frac{1}{N-1} \sum_{n=1}^{N} \left(\phi_{c,g,n}^{\text{path}} - \phi_{c,g}^{\text{path}}\right)^2 \tag{4.73}$$

$$= \frac{N}{N-1} \left[\frac{Q_T^2}{N\,V_c^2} \sum_{n=1}^{N} \left(\sum_{i=1}^{I_{c,g,n}} l_i \, w_i \right)^2 - \phi_{c,g}^{\text{path}^2} \right]. \tag{4.74}$$

During the simulation, the only quantities that must be stored are the total weighted path length for the mean and the total weighted path length squared for the variance of the mean.

The nth simulation particle provides a path length estimate of the response $\mathcal{R}(\mathbf{x})$

given by

$$\mathcal{R}_{c,g,n}^{\text{path}} = \frac{Q_T}{V_c} \sum_{i=1}^{I_{c,g,n}} \Sigma_{\mathcal{R},c}(E_i) l_i \, w_i, \tag{4.75}$$

where most of the parameters have been defined for the estimate of the scalar flux: E_i is the energy of the particle in the range $(E_g, E_{g-1}]$ and $\Sigma_{\mathcal{R},c}(E)$ is the response parameter in spatial element $\mathcal{V}_c$. For the multigroup estimator, we replace the continuous-energy response parameter $\Sigma_{\mathcal{R},c}(E_i)$ with the multigroup form $\Sigma_{\mathcal{R},c,g}$.

To obtain the mean value of the response and the variance of the mean response for a simulation with N particles, the following equations are used:

$$\mathcal{R}_{c,g}^{\text{path}} = \frac{1}{N} \sum_{n=1}^{N} \mathcal{R}_{c,g,n}^{\text{path}}, \tag{4.76}$$

$$\text{Var}\left[\mathcal{R}_{c,g}^{\text{path}}\right] = \frac{1}{N-1} \sum_{n=1}^{N} \left(\mathcal{R}_{c,g,n}^{\text{path}} - \mathcal{R}_{c,g}^{\text{path}}\right)^2. \tag{4.77}$$

Just like the scalar flux estimator, the only quantities that need to be stored are the total weighted path length for the mean and the total weighted path length squared for the variance of the mean, where the total weighted path length is given by the summation in Eq. 4.75

Collision Estimator

The nth simulation particle provides a collision estimate of the scalar flux $\phi(\mathbf{x}, E)$ given by

$$\phi_{c,g,n}^{\text{coll}} = \frac{Q_T}{V_c} \sum_{i=1}^{I_{c,g,n}} \frac{w_i}{\Sigma_t(E_i)}, \tag{4.78}$$

where $I_{c,g,n}$ is the number of collisions by the nth simulation particle in volume V_c in energy group g, w_i is the weight of the particle when it collides with a nucleus, and E_i is the energy in the range $(E_g, E_{g-1}]$ at which the particle collides. The multigroup version of this estimator simply replaces $\Sigma_t(E_i)$ with $\Sigma_{t,g}$.

The mean and the variance of the mean are determined in the same way as the for the path length estimator:

$$\phi_{c,g}^{\text{coll}} = \frac{1}{N}\sum_{n=1}^{N}\phi_{c,g,n}^{\text{coll}} \tag{4.79}$$

$$= \frac{Q_T}{N\,V_c}\sum_{n=1}^{N}\sum_{i=1}^{I_{c,g,n}}\frac{w_i}{\Sigma_t(E_i)}, \tag{4.80}$$

$$\text{Var}\left[\phi_{c,g}^{\text{coll}}\right] = \frac{1}{N-1}\sum_{n=1}^{N}\left(\phi_{c,g,n}^{\text{coll}} - \phi_{c,g}^{\text{coll}}\right)^2 \tag{4.81}$$

$$= \frac{N}{N-1}\left[\frac{Q_T^2}{N\,V_c^2}\sum_{n=1}^{N}\left(\sum_{i=1}^{I_{c,g,n}}\frac{w_i}{\Sigma_t(E_i)}\right)^2 - \phi_{c,g}^{\text{coll}2}\right]. \tag{4.82}$$

During the simulation, the only quantities that need to be stored are the sums of the weighted inverse total cross-section for the mean and this quantity squared for the variance of the mean. The multigroup expression replaces $\Sigma_t(E_i)$ with $\Sigma_{t,g}$.

The nth simulation particle provides a collision estimator of the response $\mathcal{R}(\mathbf{x})$ given by

$$\mathcal{R}_{c,g,n}^{\text{coll}} = \frac{Q_T}{V_c}\sum_{i=1}^{I_{c,g,n}} w_i\frac{\Sigma_{\mathcal{R},c}(E_i)}{\Sigma_{t,c}(E_i)}, \tag{4.83}$$

where most of the parameters have been defined for the estimate of the scalar flux. $\Sigma_{\mathcal{R},c}(E)$ is the response parameter in spatial element $\mathcal{V}_c$. For the multigroup estimator, we simply replace the continuous-energy response parameter $\Sigma_{\mathcal{R},c}(E_i)$ with $\Sigma_{\mathcal{R},c,g}$ and $\Sigma_{t,c}(E_i)$ with $\Sigma_{t,c,g}$.

The mean and the variance of the mean are determined in the same way as the for the path length estimator:

$$\mathcal{R}_{c,g}^{\text{coll}} = \frac{1}{N}\sum_{n=1}^{N}\mathcal{R}_{c,g,n}^{\text{coll}}, \tag{4.84}$$

$$\text{Var}\left[\mathcal{R}_{c,g}^{\text{coll}}\right] = \frac{1}{N-1}\sum_{n=1}^{N}\left(\mathcal{R}_{c,g,n}^{\text{coll}} - \mathcal{R}_{c,g}^{\text{coll}}\right)^2. \tag{4.85}$$

Just like the scalar flux estimator, the only quantities that need to be stored are the sums of the weighted inverse total cross-section for the mean and this quantity squared for the variance of the mean, where the weighted total inverse total cross-section is given by the summation in Eq. 4.83.

4.3 The General Transform

In addition to extending and clarifying weight windows, this thesis introduces a new approach to solving deep-penetration problems. We refer to this as the *General Transform*, the objective of which is the same as that of the weight windows: to advantageously distribute Monte Carlo particles throughout phase space. The General Transform consists of a wide range of techniques to "control" the Monte Carlo particle distribution, including the standard weight window approach and a new technique referred to simply as the *Transform approach*. This section describes the General Transform and then focuses exclusively on the Transform approach, which primarily achieves the objective of advantageously distributing Monte Carlo particles by modifying the particle physics rather than through a weight window.

The basic transform to be introduced into the neutron transport equation is given by

$$\psi(\mathbf{x}, \mathbf{\Omega}, E) = \hat{\mathcal{T}}(\mathbf{x}, \mathbf{\Omega}, E) f(\mathbf{x}, \mathbf{\Omega}, E). \tag{4.86}$$

Here $\psi(\mathbf{x}, \mathbf{\Omega}, E)$ is the angular neutron flux and $\hat{\mathcal{T}}(\mathbf{x}, \mathbf{\Omega}, E)$ is the deterministically-obtained "transform" function, which ensures that $f(\mathbf{x}, \mathbf{\Omega}, E)$ is approximately proportional to the user-specified Monte Carlo particle distribution. Substituting this transform into the neutron transport equation produces a transformed transport equation for $f(\mathbf{x}, \mathbf{\Omega}, E)$ describing the particle physics that disperse particles throughout the system according to the desired distribution. When the Monte Carlo method is used to simulate this equation for f, the Monte Carlo particles distribute themselves according to the user-specified distribution. To recover the actual solution ψ, the transform (Eq. 4.86) is used.

Before introducing this transform into the neutron transport equation and using the transformed equation to describe the particle physics, we develop a simple expression that relates the angular Monte Carlo particle flux $m(\mathbf{x}, \mathbf{\Omega}, E)$, the "transform" function $\hat{\mathcal{T}}(\mathbf{x}, \mathbf{\Omega}, E)$, and a weight window center $\mathrm{w}(\mathbf{x}, E)$. This expression allows us to correctly choose the "transform" function and the weight window center to achieve the desired Monte Carlo particle distribution.

4.3.1 The Monte Carlo Particle Flux

In a Monte Carlo simulation for $f(\mathbf{x}, \mathbf{\Omega}, E)$, the function f is related to the weight-dependent Monte Carlo particle flux M through the following relation (c.f.

Eq. 4.6):

$$f(\mathbf{x}, \mathbf{\Omega}, E) = \int_0^\infty wM(\mathbf{x}, \mathbf{\Omega}, E, w)dw. \tag{4.87}$$

Since a weight window is used (regardless of whether one is needed to constrain the particle weight), the weight-dependent Monte Carlo particle flux can be approximated as in Eq. 4.7 by

$$M(\mathbf{x}, \mathbf{\Omega}, E, w) \approx m(\mathbf{x}, \mathbf{\Omega}, E)\delta[w - \mathrm{w}(\mathbf{x}, E)], \tag{4.88}$$

where $m(\mathbf{x}, \mathbf{\Omega}, E)$ is the angular Monte Carlo particle flux and $\mathrm{w}(\mathbf{x}, E)$ is the weight window center. Substituting this approximation into Eq. 4.87, we obtain:

$$f(\mathbf{x}, \mathbf{\Omega}, E) \approx \mathrm{w}(\mathbf{x}, E)m(\mathbf{x}, \mathbf{\Omega}, E). \tag{4.89}$$

If the weight window is chosen to be unity, then f is proportional to the angular Monte Carlo particle flux. The implication of this is that the particle physics of the transformed transport equation for f have been modified such that $f(\mathbf{x}, \mathbf{\Omega}, E)$ is proportional to the angular Monte Carlo particle flux $m(\mathbf{x}, \mathbf{\Omega}, E)$.

Finally, substituting Eq. 4.89 into Eq. 4.86, we obtain:

$$\boxed{\psi(\mathbf{x}, \mathbf{\Omega}, E) \approx \hat{\mathcal{T}}(\mathbf{x}, \mathbf{\Omega}, E)\mathrm{w}(\mathbf{x}, E)m(\mathbf{x}, \mathbf{\Omega}, E).} \tag{4.90}$$

This expression enables the user to choose the "transform" function $\hat{\mathcal{T}}(\mathbf{x}, \mathbf{\Omega}, E)$ and a weight window $\mathrm{w}(\mathbf{x}, E)$ to ensure that the Monte Carlo particles are distributed throughout phase-space according to the user's prescription. The ability to choose the "transform" function *and* the weight window center provides the user with the flexibility to decide whether to use a weight window to achieve the user-specified Monte Carlo particle flux, to modify the particle physics to achieve the desired distribution, or some combination of both.

For a conventional weight window, we let $\hat{\mathcal{T}}(\mathbf{x}, \mathbf{\Omega}, E) = 1$. Then, $f = \psi$, indicating that the transformed transport equation is actually the neutron transport equation, as it should be for the standard weight window approach. Integrating Eq. 4.90 over all angles, we obtain the previous expression relating the weight window center to the scalar Monte Carlo particle flux (Eq. 4.8):

$$\phi(\mathbf{x}, E) \approx \mathrm{w}(\mathbf{x}, E)\mathcal{M}(\mathbf{x}, E). \tag{4.91}$$

We recall that this expression can be used to generate weight windows that produce a specified scalar Monte Carlo particle flux. Thus, the General Transform approach encompasses a strict utilization of the weight window to achieve the desired distribution. In this thesis, we will continue to refer to this strict utilization of weight windows as the *weight window approach.*

To use an approach that strictly modifies the particle physics, we let $\mathrm{w}(\mathbf{x}, E) = 1$ and choose $\hat{\mathcal{T}}(\mathbf{x}, \mathbf{\Omega}, E)$ to achieve the desired Monte Carlo particle distribution $m(\mathbf{x}, \mathbf{\Omega}, E)$:

$$\hat{\mathcal{T}}(\mathbf{x}, \mathbf{\Omega}, E) = \frac{\psi(\mathbf{x}, \mathbf{\Omega}, E)}{m(\mathbf{x}, \mathbf{\Omega}, E)}. \tag{4.92}$$

In this case, the primary objective of the weight window is not to significantly alter the Monte Carlo particle distribution, since the modified physics accomplish this; it is to ensure that the particle weight remains constrained. Since the weight window is centered about unity throughout phase-space, the modifications should function to keep the particle weight nearly constant as it moves through phase-space. We refer to this technique, which completely modifies the particle physics, simply as the *Transform approach*, dropping the identifier "General" from the description. This thesis does not investigate those techniques that exist in the continuum between the Transform approach and the weight window approach.

Just as the problem domain was discretized in space and energy to accommodate the weight window, the Transform approach also requires the same discretization, except that the "transform" function $\hat{\mathcal{T}}(\mathbf{x}, \mathbf{\Omega}, E)$ is not necessarily a histogram; it can retain a functional form in both space and angle. That is,

$$\hat{\mathcal{T}}(\mathbf{x}, \mathbf{\Omega}, E) = \hat{\mathcal{T}}_{c,g}(\mathbf{x}, \mathbf{\Omega}), \quad \mathbf{x} \in \mathcal{V}_c,\ E_g < E \leq E_{g-1},\ \mathbf{\Omega} \in 4\pi. \tag{4.93}$$

In general, this function is discontinuous across the boundary of adjacent spatial elements. This discontinuity is important when the transform (Eq. 4.86) is introduced into the neutron transport equation, since the transport equation contains a spatial derivative in the streaming term. The specific functional form of the "transform" function will be introduced later.

Ideally, the angular Monte Carlo particle flux is chosen to optimize the problem solution, which could range from calculating a single response in a detector to obtaining the angular neutron flux everywhere in phase-space. Each of these problems requires a unique Monte Carlo particle distribution to optimize their respective solutions. Despite this, we have chosen a form that seems to have a wide range of

applicability. We define the angular Monte Carlo particle flux as

$$m(\mathbf{x}, \mathbf{\Omega}, E) = \frac{\psi^{\mathrm{c}}(\mathbf{x}, \mathbf{\Omega}, E)}{B(\mathbf{x})}, \tag{4.94}$$

where $B(\mathbf{x})$ is a space-dependent parameter that corresponds to the type of problem to be solved, whether source-detector, source-region, or global. As a function, $B(\mathbf{x})$ is a simple histogram in space. The function $\psi^{\mathrm{c}}(\mathbf{x}, \mathbf{\Omega}, E)$ is known as the *angular contributon flux* (or *angular response flux*) [33]; it is defined as the product of the forward angular neutron flux and the adjoint angular neutron flux:

$$\psi^{\mathrm{c}}(\mathbf{x}, \mathbf{\Omega}, E) = \psi(\mathbf{x}, \mathbf{\Omega}, E)\psi^{*}(\mathbf{x}, \mathbf{\Omega}, E). \tag{4.95}$$

The forward angular flux ψ basically represents the relative number of particles at a point in phase-space, while the adjoint angular flux (or "importance" function) ψ^{*} represents the relative importance of a point in phase-space to the response. The product of these two represents the relative contribution of particles at that point in phase-space to the response, based on both the relative number of particles at that point and the relative importance of that point to the response. The contributon flux has mostly been understood from the perspective of the source-detector problem. However, the benefit of having a quantity, such as the contributon flux, to determine the important regions of phase-space has led us to generalize it from the source-detector problem to global problems. This will be discussed in greater detail in the chapters pertaining to the source-detector problem, the source-region problem, and the global problem.

Integrating the angular Monte Carlo particle flux over all angles, we obtain the (energy-dependent) scalar Monte Carlo particle flux:

$$\begin{aligned} \mathcal{M}(\mathbf{x}, E) &= \int_{4\pi} m(\mathbf{x}, \mathbf{\Omega}, E) d\Omega \\ &= \int_{4\pi} \frac{\psi^{\mathrm{c}}(\mathbf{x}, \mathbf{\Omega}, E)}{B(\mathbf{x})} d\Omega \\ &= \frac{\phi^{\mathrm{c}}(\mathbf{x}, E)}{B(\mathbf{x})}, \end{aligned} \tag{4.96}$$

where $\phi^{\mathrm{c}}(\mathbf{x}, E)$ is the *(energy-dependent) scalar contributon flux*. It is defined as

$$\begin{aligned}\phi^{\mathrm{c}}(\mathbf{x}, E) &= \int_{4\pi} \psi^{\mathrm{c}}(\mathbf{x}, \mathbf{\Omega}, E) d\Omega \\ &= \int_{4\pi} \psi(\mathbf{x}, \mathbf{\Omega}, E) \psi^{*}(\mathbf{x}, \mathbf{\Omega}, E) d\Omega. \end{aligned} \tag{4.97}$$

Finally, integrating Eq. 4.96 over all energy, we obtain the (energy-integrated) scalar Monte Carlo particle flux:

$$\begin{aligned}\mathcal{M}(\mathbf{x}) &= \int_{4\pi} \mathcal{M}(\mathbf{x}, E) dE \\ &= \int_{4\pi} \frac{\phi^{\mathrm{c}}(\mathbf{x}, E)}{B(\mathbf{x})} dE \\ &= \frac{\phi^{\mathrm{c}}(\mathbf{x})}{B(\mathbf{x})}, \end{aligned} \tag{4.98}$$

where $\phi^{\mathrm{c}}(\mathbf{x})$ is the *(energy-integrated) scalar contributon flux*. It is defined as

$$\begin{aligned}\phi^{\mathrm{c}}(\mathbf{x}) &= \int_{0}^{\infty} \phi^{\mathrm{c}}(\mathbf{x}, E) dE \\ &= \int_{0}^{\infty} \int_{4\pi} \psi(\mathbf{x}, \mathbf{\Omega}, E) \psi^{*}(\mathbf{x}, \mathbf{\Omega}, E) d\Omega dE. \end{aligned} \tag{4.99}$$

4.3.2 The Transformed Transport Equation

To derive the transport equation that approximately distributes particles according to a user-specified distribution, we begin with the neutron transport equation (Eq. 2.1):

$$\begin{aligned}&\mathbf{\Omega} \cdot \nabla \psi(\mathbf{x}, \mathbf{\Omega}, E) + \Sigma_t(\mathbf{x}, E) \psi(\mathbf{x}, \mathbf{\Omega}, E) \\ &\qquad = \int_{0}^{\infty} \int_{4\pi} \Sigma_s(\mathbf{x}, \mathbf{\Omega}' \cdot \mathbf{\Omega}, E' \to E) \psi(\mathbf{x}, \mathbf{\Omega}', E') d\Omega' dE' + Q(\mathbf{x}, \mathbf{\Omega}, E), \\ &\qquad\qquad \mathbf{x} \in \mathcal{V}, \quad \mathbf{\Omega} \in 4\pi, \quad 0 < E < \infty, \end{aligned} \tag{4.100a}$$

with boundary condition

$$\psi(\mathbf{x}, \mathbf{\Omega}, E) = \psi_b(\mathbf{x}, \mathbf{\Omega}, E), \quad \mathbf{x} \in \partial\mathcal{V}, \quad \mathbf{\Omega} \cdot \mathbf{n}(\mathbf{x}) < 0, \quad 0 < E < \infty. \tag{4.100b}$$

Since the "transform" function $\hat{\mathcal{T}}(\mathbf{x}, \mathbf{\Omega}, E)$ is discontinuous across the boundary of adjacent spatial elements, the transform is applied within each spatial element

that comprises the spatial domain, and an interior continuity condition is introduced to ensure that the transform is valid across the boundaries of the spatial elements. Substituting Eq. 4.86 into Eq. 4.100 and rearranging, we obtain the following transformed transport equation for $f(\mathbf{x}, \mathbf{\Omega}, E)$:

$$\begin{aligned}\mathbf{\Omega} \cdot \nabla f(\mathbf{x}, \mathbf{\Omega}, E) + \hat{\Sigma}_t(\mathbf{x}, \mathbf{\Omega}, E) f(\mathbf{x}, \mathbf{\Omega}, E) \\ = \int_0^\infty \int_{4\pi} \hat{\Sigma}_s(\mathbf{x}, \mathbf{\Omega}' \cdot \mathbf{\Omega}, E' \to E) f(\mathbf{x}, \mathbf{\Omega}', E') d\Omega' dE' + \hat{Q}(\mathbf{x}, \mathbf{\Omega}, E), \\ \mathbf{x} \in \mathcal{V}_c, \quad \mathbf{\Omega} \in 4\pi, \quad E_g < E < E_{g-1},\end{aligned} \tag{4.101a}$$

with boundary condition

$$f(\mathbf{x}, \mathbf{\Omega}, E) = \hat{\psi}_b(\mathbf{x}, \mathbf{\Omega}, E), \quad \mathbf{x} \in \partial\mathcal{V}_c, \quad \mathbf{\Omega} \cdot \mathbf{n}(\mathbf{x}) < 0, \quad 0 < E < \infty, \tag{4.101b}$$

and continuity condition

$$\hat{\mathcal{T}}(\mathbf{x}, \mathbf{\Omega}, E) f(\mathbf{x}, \mathbf{\Omega}, E)|_{\mathbf{x} \in \mathcal{V}_{c^-}} = \hat{\mathcal{T}}(\mathbf{x}, \mathbf{\Omega}, E) f(\mathbf{x}, \mathbf{\Omega}, E)|_{\mathbf{x} \in \mathcal{V}_{c^+}}. \tag{4.101c}$$

The notation $\mathcal{V}_{c^-}$ and $\mathcal{V}_{c^+}$ denotes that these elements are adjacent to one another. We have also made the following definitions:

$$\hat{\Sigma}_t(\mathbf{x}, \mathbf{\Omega}, E) = \Sigma_t(\mathbf{x}, E) + \mathbf{\Omega} \cdot \nabla \ln[\hat{\mathcal{T}}(\mathbf{x}, \mathbf{\Omega}, E)], \tag{4.102a}$$

$$\hat{\Sigma}_s(\mathbf{x}, \mathbf{\Omega}' \cdot \mathbf{\Omega}, E' \to E) = \Sigma_s(\mathbf{x}, \mathbf{\Omega}' \cdot \mathbf{\Omega}, E' \to E) \frac{\hat{\mathcal{T}}(\mathbf{x}, \mathbf{\Omega}', E')}{\hat{\mathcal{T}}(\mathbf{x}, \mathbf{\Omega}, E)}, \tag{4.102b}$$

$$\hat{Q}(\mathbf{x}, \mathbf{\Omega}, E) = \frac{Q(\mathbf{x}, \mathbf{\Omega}, E)}{\hat{\mathcal{T}}(\mathbf{x}, \mathbf{\Omega}, E)}, \tag{4.102c}$$

$$\hat{\psi}_b(\mathbf{x}, \mathbf{\Omega}, E) = \frac{\psi_b(\mathbf{x}, \mathbf{\Omega}, E)}{\hat{\mathcal{T}}(\mathbf{x}, \mathbf{\Omega}, E)}. \tag{4.102d}$$

Just as the neutron transport equation describes the interaction of neutrons in a medium, the transformed transport equation (Eq. 4.101) describes the interaction of "f-particles" in a medium. It is apparent that the form of the transformed transport equation is identical to the neutron transport equation, except that the cross-sections have been modified. Each term in the transformed transport equation shares the same meaning as in the neutron transport equation – streaming, collision, scattering source, interior source, and boundary source. The solution to this transformed equation $f(\mathbf{x}, \mathbf{\Omega}, E)$ remains positive if the "transform" function is positive.

4.3.3 The "Transform" Function, $\hat{\mathcal{T}}(\mathbf{x}, \mathbf{\Omega}, E)$

To explicitly write the probability distributions that describe the behavior of particles subjected to the transformed transport equation, the "transform" function $\hat{\mathcal{T}}(\mathbf{x}, \mathbf{\Omega}, E)$ must be approximated by simpler functions. These functions are defined in terms of the angular Monte Carlo particle flux, defined by Eq. 4.94 as:

$$m(\mathbf{x}, \mathbf{\Omega}, E) = \frac{\psi^{\mathrm{c}}(\mathbf{x}, \mathbf{\Omega}, E)}{B(\mathbf{x})}. \tag{4.103}$$

where $B(\mathbf{x})$ is the space-dependent parameter corresponding to the type of problem to be solved, whether source-detector, source-region, or global; and $\psi^{\mathrm{c}}(\mathbf{x}, \mathbf{\Omega}, E)$ is the angular contributon flux.

Having specified the general form of the angular Monte Carlo particle flux, the "transform" function is given as

$$\hat{\mathcal{T}}(\mathbf{x}, \mathbf{\Omega}, E) = \frac{B(\mathbf{x})}{\psi^*(\mathbf{x}, \mathbf{\Omega}, E)}. \tag{4.104}$$

We can approximate the adjoint angular flux within a spatial element $\mathcal{V}_c$ as the product of the adjoint scalar flux $\phi^*(\mathbf{x}, E)$ and an angular component $h_c(\mathbf{\Omega}, E)$:

$$\psi^*(\mathbf{x}, \mathbf{\Omega}, E) \approx \phi^*(\mathbf{x}, E) h_c(\mathbf{\Omega}, E), \quad \mathbf{x} \in \mathcal{V}_c. \tag{4.105}$$

The adjoint scalar flux has the prescribed functional form

$$\begin{aligned} \phi^*(\mathbf{x}, E) &= \phi^*_{c,g}(\mathbf{x}, E), \quad \mathbf{x} \in \mathcal{V}_c, \quad E_g < E \leq E_{g-1} \\ &= A_{c,g} \mathrm{e}^{\lambda_{c,g} \Sigma_{t,c}(E)(\mathbf{x} - \mathbf{x}) \cdot \boldsymbol{\omega}_{c,g}}, \end{aligned} \tag{4.106}$$

where $\mathbf{x}_c$ is an arbitrary reference point in $\mathcal{V}_c$, and $A_{c,g}$, $\lambda_{c,g}$ and $\boldsymbol{\omega}_{c,g}$ are parameters obtained from a deterministic simulation. These are explicitly defined in terms of a discrete deterministic solution in a later section. For most problems, it is unlikely that Eq. 4.105 exactly describes the deterministically-obtained adjoint angular flux within the spatial element $\mathcal{V}_c$; therefore, discontinuities exist in this approximation across cell boundaries.

The angular component $h_c(\mathbf{\Omega}, E)$ is approximated by substituting Eq. 4.105 into the homogenous mono-energetic adjoint transport equation with $\phi^*(\mathbf{x}, E)$ defined by Eq. 4.106. This adjoint transport equation for $\mathbf{x} \in \mathcal{V}_c$ is given as

$$-\boldsymbol{\Omega}\cdot\nabla\psi^*(\mathbf{x},\boldsymbol{\Omega},E)+\Sigma_{t,c}(E)\psi^*(\mathbf{x},\boldsymbol{\Omega},E)$$
$$=\int_{4\pi}\Sigma_{s,c}(\boldsymbol{\Omega}\cdot\boldsymbol{\Omega}',E)\psi^*(\mathbf{x},\boldsymbol{\Omega}',E)d\Omega',\quad \mathbf{x}\in\mathcal{V}_c. \quad (4.107)$$

Substituting Eq. 4.105 into this transport equation with $E\in(E_g,E_{g-1}]$ yields

$$\Sigma_{t,c}(E)[1-\lambda_{c,g}\boldsymbol{\Omega}\cdot\boldsymbol{\omega}_{c,g}]h_c(\boldsymbol{\Omega},E)$$
$$=\int_{4\pi}\Sigma_{s,c}(\boldsymbol{\Omega}\cdot\boldsymbol{\Omega}',E)h_c(\boldsymbol{\Omega}',E)d\Omega',\quad E_g<E\leq E_{g-1}. \quad (4.108)$$

The form of this equation is similar to Eq. 2.30 from Chapter 2 with $f_g(\boldsymbol{\Omega})=h_c(\boldsymbol{\Omega},E)$, $\lambda_g^{tr}=-\lambda_{c,g}$, and the multigroup parameters substituted for the analogous continuous energy parameters. The particular formulation of this equation, whether multigroup or continuous energy, is irrelevant to the form of the solution. Using the solution of Eq. 2.30 given in Chapter 2, we obtain the following expression for $h_c(\boldsymbol{\Omega},E)$:

$$h_c(\boldsymbol{\Omega},E)\approx\frac{\sum_{n=0}^{N}a_{n,c,g}(E)\left[\boldsymbol{\Omega}\cdot\boldsymbol{\omega}_{c,g}\right]^n}{1-\lambda_{c,g}\boldsymbol{\Omega}\cdot\boldsymbol{\omega}_{c,g}},\quad a_{0,c,g}(E)=1. \quad (4.109)$$

For a fixed energy E, an exact eigenvalue can be determined. However, since this expression uses an approximate eigenvalue $\lambda_{c,g}$ over an entire energy range, the expression itself can only be an approximation to the solution of Eq. 4.108. In practice, we do not solve this equation to determine $\lambda_{c,g}$; we use a deterministic solution to acquire it, based on the exponential attenuation of the adjoint scalar flux. This is explained in the next section.

Since this thesis only considers isotropic scattering, we use the following simple expression for the angular component:

$$h_c(\boldsymbol{\Omega},E)=h_{c,g}(\boldsymbol{\Omega}),\quad E_g<E\leq E_{g-1}$$
$$=[1-\lambda_{c,g}\boldsymbol{\Omega}\cdot\boldsymbol{\omega}_{c,g}]^{-1}. \quad (4.110)$$

For $\lambda_{c,g}\geq 1$, $h_{c,g}(\boldsymbol{\Omega})$ can become infinite or negative; both of these conditions are unphysical and can cause difficulties during the simulation. For this reason, we introduce the following bound:

$$0\leq\lambda_{c,g}\leq|\lambda_{c,g}^{tr}|, \quad (4.111)$$

where $\lambda_{c,g}^{tr}$ is obtained from solving the multigroup equivalent of Eq. 4.108. (The solution strategy is the same as that given in Chapter 2 to solve Eq. 2.30.) This condition ensures that the angular component $h_{c,g}(\mathbf{\Omega})$ remains positive and bounded.

To summarize, we define the "transform" function as

$$\hat{\mathcal{T}}(\mathbf{x}, \mathbf{\Omega}, E) = \frac{B(\mathbf{x})}{\psi^*(\mathbf{x}, \mathbf{\Omega}, E)}, \tag{4.112}$$

where $B(\mathbf{x})$ depends on the type of problem to be solved and has the form

$$B(\mathbf{x}) = B_c, \quad \mathbf{x} \in \mathcal{V}_c. \tag{4.113a}$$

The adjoint angular flux $\psi^*(\mathbf{x}, \mathbf{\Omega}, E)$ is approximated as

$$\psi^*(\mathbf{x}, \mathbf{\Omega}, E) = \phi_{c,g}^*(\mathbf{x}, E) h_{c,g}(\mathbf{\Omega}), \quad \mathbf{x} \in \mathcal{V}_c, \;\; E_g < E \leq E_{g-1}, \tag{4.113b}$$

with

$$\phi_{c,g}^*(\mathbf{x}, E) = A_{c,g} \mathrm{e}^{\lambda_{c,g} \Sigma_{t,c}(E)(\mathbf{x} - \mathbf{x}_c) \cdot \boldsymbol{\omega}_{c,g}}, \tag{4.113c}$$

$$h_{c,g}(\mathbf{\Omega}) = [1 - \lambda_{c,g} \mathbf{\Omega} \cdot \boldsymbol{\omega}_{c,g}]^{-1}. \tag{4.113d}$$

The equivalent multigroup expressions simply replace the continuous-energy cross-section with a multigroup one, i.e. $\Sigma_{t,c}(E) = \Sigma_{t,c,g}$. In the next section, we describe how to obtain the parameters $\lambda_{c,g}$ and $\boldsymbol{\omega}_{c,g}$, as well as $A_{c,g}$ and $\mathbf{x}_c$.

4.3.4 The Transform Parameters

The adjoint angular flux estimate $\psi^*(\mathbf{x}, \mathbf{\Omega}, E)$ is given by:

$$\psi^*(\mathbf{x}, \mathbf{\Omega}, E) = \phi_{c,g}^*(\mathbf{x}, E)\, h_{c,g}(\mathbf{\Omega}), \quad E_g < E \leq E_{g-1}, \;\; \mathbf{x} \in \mathcal{V}_c, \tag{4.114}$$

where

$$\phi_{c,g}^*(\mathbf{x}, E) = A_{c,g} \mathrm{e}^{\lambda_{c,g} \Sigma_{t,c}(E)(\mathbf{x} - \mathbf{x}_c) \cdot \boldsymbol{\omega}_{c,g}}, \tag{4.115}$$

$$h_{c,g}(\mathbf{\Omega}) = [1 - \lambda_{c,g} \mathbf{\Omega} \cdot \boldsymbol{\omega}_{c,g}]^{-1}. \tag{4.116}$$

To determine the parameters $A_{c,g}$, $\lambda_{c,g}$, $\mathbf{x}_c$, and $\boldsymbol{\omega}_{c,g}$, we approximate $\phi_{c,g}^*(\mathbf{x}, E)$ as

$$\phi_{c,g}^*(\mathbf{x}, E) \approx A_{c,g} \mathrm{e}^{\boldsymbol{\beta}_{c,g} \cdot (\mathbf{x} - \mathbf{x}_c)}, \quad E_g < E \leq E_{g-1}, \;\; \mathbf{x} \in \mathcal{V}_c, \tag{4.117}$$

where $\boldsymbol{\beta}_{c,g}$ is defined as $\boldsymbol{\beta}_{c,g} = \lambda_{c,g}\Sigma_{t,c,g}\boldsymbol{\omega}_{c,g}$. The expression is approximate since the continuous-energy cross-section is approximated by the multigroup cross-section, i.e., $\Sigma_{t,c}(E) \approx \Sigma_{t,c,g}$.

To determine the transform parameters, we must approximately fit these functions to a deterministic estimate of the adjoint scalar flux $\Phi^*(\mathbf{x}, E)$. In our work we use cell-edge, transport-corrected, multigroup adjoint diffusion described in Chapter 3 to obtain this adjoint scalar flux estimate.

To proceed, we recall that the subscript c is a cell index that represents the mapping from the three-dimensional Cartesian indices (i, j, k) to the one-dimensional index c: $c = i+jI+kIJ$. Using the three-dimensional notation prescribed in Chapter 3 for the cell-edge diffusion equations, we can define the parameters $\mathbf{x}_c$, $A_{c,g}$, $\lambda_{c,g}$, and $\boldsymbol{\omega}_{c,g}$.

The parameter $\mathbf{x}_c$ is any reference point in the cell $C_{i,j,k}$. We define it to be the centroid of the cell:

$$\mathbf{x}_c = \left(\frac{x_{i-1/2} + x_{i+1/2}}{2}, \frac{y_{j-1/2} + y_{j+1/2}}{2}, \frac{z_{k-1/2} + z_{k+1/2}}{2} \right). \tag{4.118}$$

Defining $\mathbf{x}_c$ as the centroid fixes the value of $A_{c,g}$ as the scalar flux estimate at the centroid of cell $C_{i,j,k}$. Since the cell-edge discretization provides the value of the flux at the corners of each cell, we approximate the value at the centroid by a simple average of the corner values:

$$\begin{aligned} A_{c,g} &= \Phi^*_{c,g}, \\ &= \frac{1}{8}\Big(\Phi^*_{g,i-1/2,j-1/2,k-1/2} + \Phi^*_{g,i-1/2,j-1/2,k+1/2} + \Phi^*_{g,i-1/2,j+1/2,k-1/2} \\ &\quad + \Phi^*_{g,i-1/2,j+1/2,k+1/2} + \Phi^*_{g,i+1/2,j-1/2,k-1/2} + \Phi^*_{g,i+1/2,j-1/2,k+1/2} \\ &\quad + \Phi^*_{g,i+1/2,j+1/2,k-1/2} + \Phi^*_{g,i+1/2,j+1/2,k+1/2} \Big). \end{aligned} \tag{4.119}$$

To obtain the remaining parameters, we first define the average flux at the centroid of each cell face:

$$\begin{aligned} \Phi^*_{g,i\pm1/2,j,k} &= \text{average flux for a face within cell } C_{i,j,k} \text{ at } (x_{i\pm1/2}, y_j, z_k), \\ &= \frac{1}{4}\Big(\Phi^*_{g,i\pm1/2,j-1/2,k-1/2} + \Phi^*_{g,i\pm1/2,j-1/2,k+1/2} \\ &\quad + \Phi^*_{g,i\pm1/2,j+1/2,k-1/2} + \Phi^*_{g,i\pm1/2,j+1/2,k+1/2} \Big), \end{aligned} \tag{4.120}$$

$$\begin{aligned}\Phi^*_{g,i,j\pm1/2,k} &= \text{average flux for a face within cell } C_{i,j,k} \text{ at } (x_i, y_{j\pm1/2}, z_k),\\ &= \frac{1}{4}\Big(\Phi^*_{g,i-1/2,j\pm1/2,k-1/2} + \Phi^*_{g,i-1/2,j\pm1/2,k+1/2}\\ &\quad + \Phi^*_{g,i+1/2,j\pm1/2,k-1/2} + \Phi^*_{g,i+1/2,j\pm1/2,k+1/2}\Big), \qquad (4.121)\\ \Phi^*_{g,i,j,k\pm1/2} &= \text{average flux for a face within cell } C_{i,j,k} \text{ at } (x_i, y_j, z_{k\pm1/2}),\\ &= \frac{1}{4}\Big(\Phi^*_{g,i-1/2,j-1/2,k\pm1/2} + \Phi^*_{g,i-1/2,j+1/2,k\pm1/2}\\ &\quad + \Phi^*_{g,i+1/2,j-1/2,k\pm1/2} + \Phi^*_{g,i+1/2,j+1/2,k\pm1/2}\Big). \qquad (4.122)\end{aligned}$$

We can now define $\boldsymbol{\beta}_{c,g} = (\beta_{c,g,x}, \beta_{c,g,y}, \beta_{c,g,z})$ by using the ratio of the average flux at the midpoints on opposing faces:

$$\begin{aligned}\beta_{c,g,x} &= \text{x-direction exponential attenuation parameter in cell } C_{i,j,k},\\ &= \frac{1}{\Delta x_i}\ln\left(\frac{\Phi^*_{g,i+1/2,j,k}}{\Phi^*_{g,i-1/2,j,k}}\right), \qquad (4.123)\\ \beta_{c,g,y} &= \text{y-direction exponential attenuation parameter in cell } C_{i,j,k},\\ &= \frac{1}{\Delta y_j}\ln\left(\frac{\Phi^*_{g,i,j+1/2,k}}{\Phi^*_{g,i,j-1/2,k}}\right), \qquad (4.124)\\ \beta_{c,g,z} &= \text{z-direction exponential attenuation parameter in cell } C_{i,j,k},\\ &= \frac{1}{\Delta z_k}\ln\left(\frac{\Phi^*_{g,i,j,k+1/2}}{\Phi^*_{g,i,j,k-1/2}}\right). \qquad (4.125)\end{aligned}$$

Finally, we define $\lambda_{c,g}$ and $\boldsymbol{\omega}_{c,g}$ in terms of $\boldsymbol{\beta}_{c,g}$:

$$\lambda_{c,g} = \begin{cases} \dfrac{||\boldsymbol{\beta}_{c,g}||_2}{\Sigma_{t,c,g}} & , \quad \dfrac{||\boldsymbol{\beta}_{c,g}||_2}{\Sigma_{t,c,g}} \leq |\lambda^{tr}_{c,g}|, \\ |\lambda^{tr}_{c,g}| & , \quad \text{otherwise}, \end{cases} \qquad (4.126)$$

$$\boldsymbol{\omega}_{c,g} = \frac{\boldsymbol{\beta}_{c,g}}{||\boldsymbol{\beta}_{c,g}||_2}. \qquad (4.127)$$

The next section discusses the modified physics that are employed during a Monte Carlo simulation of the transformed transport equation.

4.3.5 Modified Physics for Monte Carlo Sampling

To implement the Transform approach in a Monte Carlo simulation, the probability distributions that describe the particle interactions in the medium must be

defined, as well as particle weight changes at boundaries. This includes probability distributions that describe an internal source, the distance-to-next collision, and the re-emission state upon collision; and it includes the weight change that results when a particle passes through a cell boundary and the weight change that results when a particle encounters a symmetric (reflecting) boundary.

Sampling an Interior Source

In order to describe the probability distribution for an interior source that accounts for particle weight, we begin with the term in the transformed transport equation (Eq. 4.101) that corresponds to an interior source and factor it into the total problem source rate for the modified source Q_T, the joint probability distribution for the interior modified source $p(\mathbf{x}, \mathbf{\Omega}, E)$, and the initial particle weight $w_0 = w_0(\mathbf{x}, E)$:

$$\hat{Q}(\mathbf{x}, \mathbf{\Omega}, E) = \hat{Q}_T \cdot p(\mathbf{x}, \mathbf{\Omega}, E) \cdot w_0(\mathbf{x}, E). \tag{4.128}$$

As noted in Chapter 2, we only consider isotropic, spatially-uniform sources within each spatial element $\mathcal{V}_c$:

$$Q(\mathbf{x}, \mathbf{\Omega}, E) = \frac{Q_c(E)}{4\pi}, \quad \mathbf{x} \in \mathcal{V}_c, \;\; 0 < E < \infty. \tag{4.129}$$

This source distribution allows us to rewrite the joint probability distribution in terms of the following conditional and marginal probability distributions:

$$\begin{aligned} p(\mathbf{x}, \mathbf{\Omega}, E) = p(\mathbf{x} \,|\, \mathbf{x} \in \mathcal{V}_c) \\ \cdot p(\mathbf{\Omega} \,|\, E_g < E \leq E_{g-1}, \mathbf{x} \in \mathcal{V}_c) \\ \cdot p(E \,|\, E_g < E \leq E_{g-1}, \mathbf{x} \in \mathcal{V}_c) \\ \cdot p(E_g < E \leq E_{g-1} \,|\, \mathbf{x} \in \mathcal{V}_c) \\ \cdot p(\mathbf{x} \in \mathcal{V}_c), \end{aligned} \tag{4.130}$$

where we have defined the marginal and conditional distributions as:

$$p(\mathbf{x} \,|\, \mathbf{x} \in \mathcal{V}_c) = p(x \,|\, \mathbf{x} \in \mathcal{V}_c) \cdot p(y \,|\, \mathbf{x} \in \mathcal{V}_c) \cdot p(z \,|\, \mathbf{x} \in \mathcal{V}_c), \tag{4.131}$$

$$p(x \,|\, \mathbf{x} \in \mathcal{V}_c) = \frac{1}{x_{i+1/2} - x_{i-1/2}}, \tag{4.132}$$

$$p(y \,|\, \mathbf{x} \in \mathcal{V}_c) = \frac{1}{y_{j+1/2} - y_{j-1/2}}, \tag{4.133}$$

$$p(z \,|\, \mathbf{x} \in \mathcal{V}_c) = \frac{1}{z_{k+1/2} - z_{k-1/2}}, \tag{4.134}$$

$$p(\mathbf{\Omega} \,|\, E_g < E \leq E_{g-1}, \mathbf{x} \in \mathcal{V}_c) = \frac{h_{c,g}(\mathbf{\Omega})}{\int_{4\pi} h_{c,g}(\mathbf{\Omega}')d\Omega'}, \tag{4.135}$$

$$p(E \,|\, E_g < E \leq E_{g-1}, \mathbf{x} \in \mathcal{V}_c) = \frac{Q_c(E)}{\int_{E_g}^{E_{g-1}} Q_c(E')dE'}, \tag{4.136}$$

$$p(E_g < E \leq E_{g-1} \,|\, \mathbf{x} \in \mathcal{V}_c) = \frac{A_{c,g} \int_{4\pi} h_{c,g}(\mathbf{\Omega})d\Omega \int_{E_g}^{E_{g-1}} Q_c(E')dE'}{\sum_{g'=1}^{G} A_{c,g'} \int_{4\pi} h_{c,g'}(\mathbf{\Omega})d\Omega \int_{E_{g'}}^{E_{g'-1}} Q_c(E')dE'}, \tag{4.137}$$

$$p(\mathbf{x} \in \mathcal{V}_c) = \frac{\sum_{g=1}^{G} \frac{V_c A_{c,g}}{B_c} \int_{4\pi} h_{c,g}(\mathbf{\Omega})d\Omega \int_{E_g}^{E_{g-1}} Q_c(E)dE}{\sum_{c'=1}^{N_{\text{cells}}} \sum_{g=1}^{G} \frac{V_{c'} A_{c',g}}{B_{c'}} \int_{4\pi} h_{c',g}(\mathbf{\Omega})d\Omega \int_{E_g}^{E_{g-1}} Q_{c'}(E)dE}. \tag{4.138}$$

The total modified source rate is defined as

$$\hat{Q}_T = \sum_{c=1}^{N_{\text{cells}}} \sum_{g=1}^{G} \frac{V_c A_{c,g}}{B_c} \int_{4\pi} h_{c,g}(\mathbf{\Omega})d\Omega \int_{E_g}^{E_{g-1}} Q_c(E)dE. \tag{4.139}$$

The initial particle weight has been defined, noting that the particle is born within the spatial element $\mathcal{V}_c$ and within the energy range $(E_g, E_{g-1}]$:

$$w_0(\mathbf{x}, E) = \mathrm{e}^{\lambda_{c,g}\Sigma_{t,c}(E)(\mathbf{x} - \mathbf{x}_c) \cdot \boldsymbol{\omega}_{c,g}}, \quad E_g < E \leq E_{g-1}, \;\; \mathbf{x} \in \mathcal{V}_c. \tag{4.140}$$

As can be seen, the initial weight is not exactly unity. Based on numerical simulations, it was determined that using an exponential spatial distribution within the cell provided no advantage over simply using a uniform spatial distribution with an initial weight equal to the exponential shown above. It should be noted that as the cells size approaches zero, the initial weight also approaches unity.

The multigroup form of the probability distributions is found by using the definition of the multigroup source, $Q_{c,g} = \int_{E_g}^{E_{g-1}} Q_c(E)dE$, and integrating $p(\mathbf{x}, \mathbf{\Omega}, E)$ over the energy group g defined by the range $(E_g, E_{g-1}]$:

$$1 = \int_{E_g}^{E_{g-1}} p(E \,|\, E_g < E \leq E_{g-1}, \mathbf{x} \in \mathcal{V}_c)dE, \tag{4.141}$$

$$p(g \,|\, \mathbf{x} \in \mathcal{V}_c) = p(E_g < E \leq E_{g-1} \,|\, \mathbf{x} \in \mathcal{V}_c)$$
$$= \frac{A_{c,g} Q_{c,g} \int_{4\pi} h_{c,g}(\mathbf{\Omega}) d\Omega}{\sum_{g'=1}^{G} A_{c,g'} Q_{c,g'} \int_{4\pi} h_{c,g'}(\mathbf{\Omega}) d\Omega}, \tag{4.142}$$

$$p(\mathbf{x} \in \mathcal{V}_c) = \frac{\sum_{g=1}^{G} \frac{V_c A_{c,g}}{B_c} Q_{c,g} \int_{4\pi} h_{c,g}(\mathbf{\Omega}) d\Omega}{\sum_{c'=1}^{N_{cells}} \sum_{g=1}^{G} \frac{V_{c'} A_{c',g}}{B_{c'}} Q_{c',g} \int_{4\pi} h_{c',g}(\mathbf{\Omega}) d\Omega}. \tag{4.143}$$

The multigroup form of the total modified source is given by

$$\hat{Q}_T = \sum_{c=1}^{N_{cells}} \sum_{g=1}^{G} \frac{V_c A_{c,g}}{B_c} Q_{c,g} \int_{4\pi} h_{c,g}(\mathbf{\Omega}) d\Omega, \tag{4.144}$$

and the multigroup form of the initial weight is given by using $\Sigma_{t,c}(E) = \Sigma_{t,c,g}$ when $E \in (E_g, E_{g-1}]$:

$$w_{0,g}(\mathbf{x}) = \mathrm{e}^{\lambda_{c,g} \Sigma_{t,c,g} (\mathbf{x} - \mathbf{x}_c) \cdot \boldsymbol{\omega}_{c,g}}, \quad \mathbf{x} \in \mathcal{V}_c. \tag{4.145}$$

The following equations show how to sample from the probability distributions for all the variables except the initial direction ($\xi \in [0, 1]$):

$$x = x_{i-1/2} + \xi \left(x_{i+1/2} - x_{i-1/2} \right), \tag{4.146}$$

$$y = y_{j-1/2} + \xi \left(y_{j+1/2} - y_{j-1/2} \right), \tag{4.147}$$

$$z = z_{k-1/2} + \xi \left(z_{k+1/2} - z_{k-1/2} \right), \tag{4.148}$$

$$E = E_0 \text{ if } \xi = \frac{\int_{E_g}^{E_0} Q_c(E') dE'}{\int_{E_g}^{E_{g-1}} Q_c(E') dE'}, \tag{4.149}$$

$$g = g_0 \text{ if } \sum_{g'=1}^{g_0 - 1} p(E_{g'} < E \leq E_{g'-1} \,|\, \mathbf{x} \in \mathcal{V}_c)$$
$$< \xi \leq \sum_{g'=1}^{g_0} p(E_{g'} < E \leq E_{g'-1} \,|\, \mathbf{x} \in \mathcal{V}_c), \tag{4.150}$$

$$\mathbf{x} \in \mathcal{V}_{c_0} \text{ if } \sum_{c=1}^{c_0 - 1} p(\mathbf{x} \in \mathcal{V}_c) < \xi \leq \sum_{c=1}^{c_0} p(\mathbf{x} \in \mathcal{V}_c). \tag{4.151}$$

To sample from the angularly-biased distribution for the initial direction, we

represent the direction vector, $\mathbf{\Omega}$, in terms of another orthonormal basis of $\mathbb{R}^3$, $\{\boldsymbol{\omega}_{c,g}, \boldsymbol{\nu}_{c,g}, \boldsymbol{\upsilon}_{c,g}\}$, sample the direction cosines with reference to this basis, and then rotate back to the canonical basis of $\mathbb{R}^3$, $\{\mathbf{i}, \mathbf{j}, \mathbf{k}\}$. That is, we represent the initial direction $\mathbf{\Omega}$ as

$$\mathbf{\Omega} = \Omega_1^r \boldsymbol{\omega}_{c,g} + \Omega_2^r \boldsymbol{\nu}_{c,g} + \Omega_3^r \boldsymbol{\upsilon}_{c,g}, \tag{4.152}$$

and then, after sampling the direction cosines $(\Omega_1^r, \Omega_2^r, \Omega_3^r)$, we rotate back to the canonical basis, where $\mathbf{\Omega}$ is represented as

$$\mathbf{\Omega} = \Omega_1 \mathbf{i} + \Omega_2 \mathbf{j} + \Omega_3 \mathbf{k}. \tag{4.153}$$

The rotation is given by the following equations:

$$\Omega_1 = \Omega_1^r \omega_{c,g,1} + \Omega_2^r \nu_{c,g,1} + \Omega_3^r \upsilon_{c,g,1}, \tag{4.154a}$$

$$\Omega_2 = \Omega_1^r \omega_{c,g,2} + \Omega_2^r \nu_{c,g,2} + \Omega_3^r \upsilon_{c,g,2}, \tag{4.154b}$$

$$\Omega_3 = \Omega_1^r \omega_{c,g,3} + \Omega_2^r \nu_{c,g,3} + \Omega_3^r \upsilon_{c,g,3}. \tag{4.154c}$$

We have defined the orthonormal basis, $\{\boldsymbol{\omega}_{c,g}, \boldsymbol{\nu}_{c,g}, \boldsymbol{\upsilon}_{c,g}\}$, noting that $\boldsymbol{\omega}_{c,g}$ is the transform parameter that has already been defined. The other two vectors that form the set are vectors that exist in the plane perpendicular to $\boldsymbol{\omega}_{c,g}$ and orthogonal to each other. We have defined the basis set in two ways. The first is when $\boldsymbol{\omega}_{c,g} = \pm\mathbf{k}$ (i.e. $\omega_{c,g,1} = 0$ and $\omega_{c,g,2} = 0$); the second is when $\boldsymbol{\omega}_{c,g} \neq \pm\mathbf{k}$ (i.e. either $\omega_{c,g,1}$ or $\omega_{c,g,2}$ is non-zero, or both are non-zero).

For the first case, $\boldsymbol{\omega}_{c,g} = \pm\mathbf{k}$, the non-canonical basis set for $\mathbb{R}^3$ is defined as

$$\boldsymbol{\omega}_{c,g} = \omega_{c,g,3}\mathbf{k}, \quad \omega_{c,g,3} = \pm 1, \tag{4.155a}$$

$$\boldsymbol{\nu}_{c,g} = \mathbf{i}, \tag{4.155b}$$

$$\boldsymbol{\upsilon}_{c,g} = \mathbf{j}. \tag{4.155c}$$

After sampling the directions cosines in the non-canonical basis, $(\Omega_1^r, \Omega_2^r, \Omega_3^r)$, we use Eqs. 4.154 to determine the initial direction cosines in the canonical basis set, $(\Omega_1, \Omega_2, \Omega_3)$.

For the second case, $\boldsymbol{\omega}_{c,g} \neq \pm\mathbf{k}$, the non-canonical basis set for $\mathbb{R}^3$ is defined as

$$\boldsymbol{\omega}_{c,g} = \omega_{c,g,1}\mathbf{i} + \omega_{c,g,2}\mathbf{j} + \omega_{c,g,3}\mathbf{k}, \tag{4.156a}$$

$$\boldsymbol{\nu}_{c,g} = \frac{\omega_{c,g,2}}{\sqrt{\omega_{c,g,1}^2 + \omega_{c,g,2}^2}}\mathbf{i} - \frac{\omega_{c,g,1}}{\sqrt{\omega_{c,g,1}^2 + \omega_{c,g,2}^2}}\mathbf{j}, \tag{4.156b}$$

$$\boldsymbol{\upsilon}_{c,g} = \frac{\omega_{c,g,1}\omega_{c,g,3}}{\sqrt{\omega_{c,g,1}^2 + \omega_{c,g,2}^2}}\mathbf{i} + \frac{\omega_{c,g,2}\omega_{c,g,3}}{\sqrt{\omega_{c,g,1}^2 + \omega_{c,g,2}^2}}\mathbf{j} - \sqrt{\omega_{c,g,1}^2 + \omega_{c,g,2}^2}\mathbf{k}, \tag{4.156c}$$

where we note that $\sqrt{\omega_{c,g,1}^2 + \omega_{c,g,2}^2} \neq 0$ since $\boldsymbol{\omega}_{c,g} \neq \pm\mathbf{k}$. Again, after sampling the directions cosines in the non-canonical basis, $(\Omega_1^r, \Omega_2^r, \Omega_3^r)$, we use Eqs. 4.154 to determine the initial direction cosines in the canonical basis set, $(\Omega_1, \Omega_2, \Omega_3)$.

Finally, we specify how to sample the direction cosines in the non-canonical basis, $(\Omega_1^r, \Omega_2^r, \Omega_3^r)$. When $\boldsymbol{\Omega}$ is represented in terms of the non-canonical basis, $\boldsymbol{\Omega} = \Omega_1^r\boldsymbol{\omega}_{c,g} + \Omega_2^r\boldsymbol{\nu}_{c,g} + \Omega_3^r\boldsymbol{\upsilon}_{c,g}$, the angularly-biased probability distribution for the initial direction becomes

$$\begin{aligned} p(\boldsymbol{\Omega} \,|\, E_g < E \leq E_{g-1}, \mathbf{x} \in \mathcal{V}_c) &= p(\mu \,|\, E_g < E \leq E_{g-1}, \mathbf{x} \in \mathcal{V}_c) \cdot p(\gamma) \\ &= \frac{\dfrac{1}{1-\lambda_{c,g}\mu}}{\displaystyle\int_{-1}^{1} \frac{1}{1-\lambda_{c,g}\mu'} d\mu'} \cdot \frac{1}{2\pi}. \end{aligned} \tag{4.157}$$

These distributions are sampled using the following equations ($\xi \in [0,1]$):

$$\mu = \frac{1}{\lambda_{c,g}} \left[(1+\lambda_{c,g}) \left(\frac{1-\lambda_{c,g}}{1+\lambda_{c,g}} \right)^{\xi} - 1 \right], \tag{4.158a}$$

$$\gamma = 2\pi\xi. \tag{4.158b}$$

The direction cosines are given by

$$\Omega_1^r = \mu, \tag{4.159a}$$

$$\Omega_2^r = \sqrt{1-\mu^2}\cos(\gamma), \tag{4.159b}$$

$$\Omega_3^r = \sqrt{1-\mu^2}\sin(\gamma). \tag{4.159c}$$

To summarize, we use Eqs. 4.158 to sample the probability distribution for the initial direction, we use Eqs. 4.159 to obtain the direction cosines in the non-canonical basis defined by Eqs. 4.155 and Eqs. 4.156, and finally we use Eqs. 4.154 to obtain the direction cosines for the initial direction in the standard canonical basis.

Sampling the Distance-To-Next Collision

The probability distribution that determines the distance-to-next collision is obtained from the expression

$$p(s \,|\, \mathbf{\Omega}, E) = \mathrm{C}_0 \frac{f(s, \mathbf{\Omega}, E)}{f(0, \mathbf{\Omega}, E)}, \tag{4.160}$$

where C_0 is the normalization constant and $f(s, \mathbf{\Omega}, E)$ is the flux determined by the equation that describes transport through the spatial element $\mathcal{V}_c$ and along the trajectory of a particle traveling in the direction $\mathbf{\Omega}$ and with energy E:

$$\begin{aligned} \frac{\partial f}{\partial s}(s, \mathbf{\Omega}, E) + \hat{\Sigma}_{t,c}(\mathbf{\Omega}, E) f(s, \mathbf{\Omega}, E) = 0, \\ f(0, \mathbf{\Omega}, E) = f_0(\mathbf{\Omega}, E), \end{aligned} \tag{4.161}$$

where $\hat{\Sigma}_{t,c}(\mathbf{\Omega}, E)$ is the effective total interaction cross-section in the spatial element $\mathcal{V}_c$:

$$\hat{\Sigma}_{t,c}(\mathbf{\Omega}, E) = \Sigma_{t,c}(E) \left[1 - \lambda_{c,g} \mathbf{\Omega} \cdot \boldsymbol{\omega}_{c,g}\right], \quad E_g < E \leq E_{g-1}. \tag{4.162}$$

The solution to this equation is

$$f(s, \mathbf{\Omega}, E) = f_0(\mathbf{\Omega}, E) \mathrm{e}^{-\hat{\Sigma}_{t,c}(\mathbf{\Omega}, E) s}. \tag{4.163}$$

The resulting probability distribution function, then, is given by

$$p(s \,|\, \mathbf{\Omega}, E) = \hat{\Sigma}_{t,c}(\mathbf{\Omega}, E) \mathrm{e}^{-\hat{\Sigma}_{t,c}(\mathbf{\Omega}, E) s}. \tag{4.164}$$

To sample from this distribution, we invert the cumulative probability distribution to obtain ($\xi \in [0, 1]$):

$$s = -\frac{\ln(\xi)}{\hat{\Sigma}_{t,c}(\mathbf{\Omega}, E)}. \tag{4.165}$$

The multigroup expression is found by setting $\hat{\Sigma}_{t,c}(\mathbf{\Omega}, E) = \hat{\Sigma}_{t,c,g}(\mathbf{\Omega})$, where $\hat{\Sigma}_{t,c,g}(\mathbf{\Omega})$ is defined as

$$\hat{\Sigma}_{t,c,g}(\mathbf{\Omega}) = \Sigma_{t,c,g} \left[1 - \lambda_{c,g} \mathbf{\Omega} \cdot \boldsymbol{\omega}_{c,g}\right]. \tag{4.166}$$

(Dwivedi [42] proposed an importance biasing function for solving homogenous slab shielding problems that included an effective total cross-section similar to Eq. 4.166. Depinay [24] extended this work to 3-D source-detector problems by applying a

specific importance function that resullts in a similar effective total cross-section.)

The angle-dependent cross-section causes a particle to travel farthest when its direction, $\boldsymbol{\Omega}$, is equal to $\boldsymbol{\omega}_{c,g}$; it travels the shortest distance when its direction is equal to $-\boldsymbol{\omega}_{c,g}$. For most shielding problems the vector $\boldsymbol{\omega}_{c,g}$ points toward the deep regions of the problem, and thus particles have a tendency to stream farther when traveling toward the deep regions of the problem. This attribute of the modified physics allows particles to spread out more uniformly across the system.

Sampling the Scattering Distribution

The scattering distribution is probably the most challenging aspect in implementing the Transform approach. With no biasing, the scattering distribution is already complicated, with many emission laws existing for continuous-energy Monte Carlo. The Transform approach allows for variations in how we sample, but the most effective ones also tend to be the most challenging. Here, we present the sampling technique that had the most advantageous effect on the figure of merit (based on our experiments with various techniques).

To determine the scattering distribution that describes the emission of a particle, we consider the integrand of the scattering integral in the transformed transport equation (Eq. 4.101). This integrand describes the mechanics that determine the emerging state of a particle, $(\mathbf{x}, \boldsymbol{\Omega}, E)$, given that the particle had a collision in phase space at $(\mathbf{x}, \boldsymbol{\Omega}', E')$ with $\mathbf{x} \in \mathcal{V}_c$:

$$\begin{aligned}\Sigma_{s,c}(\boldsymbol{\Omega}' \cdot \boldsymbol{\Omega}, E' \rightarrow E) \frac{\psi^*(\mathbf{x}, \boldsymbol{\Omega}, E)}{\psi^*(\mathbf{x}, \boldsymbol{\Omega}', E')} f(\mathbf{x}, \boldsymbol{\Omega}', E') \\ = p_c(\boldsymbol{\Omega}' \cdot \boldsymbol{\Omega}, E' \rightarrow E) \cdot w_{\text{scat},c}(\mathbf{x}, \boldsymbol{\Omega}', E', E) \cdot R_{\text{coll},c}(\mathbf{x}, \boldsymbol{\Omega}', E'), \quad (4.167)\end{aligned}$$

where $p_c(\boldsymbol{\Omega}' \cdot \boldsymbol{\Omega}, E' \rightarrow E)$ is the joint conditional probability distribution for the modified scattering process, $w_{\text{scat},c}(\mathbf{x}, \boldsymbol{\Omega}', E', E)$ is the multiplicative weight change that results from the collision, and $R_{\text{coll},c}(\mathbf{x}, \boldsymbol{\Omega}, E)$ is the collision rate.

For a particle that collides at $\mathbf{x} \in \mathcal{V}_c$ and emerges with an energy $E \in (E_g, E_{g-1}]$, the joint probability distribution $p_c(\boldsymbol{\Omega}' \cdot \boldsymbol{\Omega}, E' \rightarrow E)$ can be defined in terms of the following conditional and marginal probability distributions:

$$\begin{aligned}p_c(\boldsymbol{\Omega}' \cdot \boldsymbol{\Omega}, E' \rightarrow E) = p_c(\boldsymbol{\Omega}' \cdot \boldsymbol{\Omega} \,|\, E' \rightarrow E) \\ \cdot p_c(E' \rightarrow E \,|\, E_g < E \leq E_{g-1}) \\ \cdot p_c(E_g < E \leq E_{g-1}), \quad (4.168)\end{aligned}$$

where we have defined the conditional probability distributions as

$$p_c(\mathbf{\Omega}' \cdot \mathbf{\Omega} \,|\, E' \to E) = \frac{h_{c,g}(\mathbf{\Omega})\Sigma_{s,c}(\mathbf{\Omega}' \cdot \mathbf{\Omega}, E' \to E)}{\displaystyle\int_{4\pi} h_{c,g}(\mathbf{\Omega}'')\Sigma_{s,c}(\mathbf{\Omega}' \cdot \mathbf{\Omega}'', E' \to E)d\Omega''}, \tag{4.169}$$

$$p_c(E' \to E \,|\, E_g < E \leq E_{g-1}) = \frac{\displaystyle\int_{4\pi} h_{c,g}(\mathbf{\Omega}'')\Sigma_{s,c}(\mathbf{\Omega}' \cdot \mathbf{\Omega}'', E' \to E)d\Omega''}{\displaystyle\int_{E_g}^{E_{g-1}} \int_{4\pi} h_{c,g}(\mathbf{\Omega}'')\Sigma_{s,c}(\mathbf{\Omega}' \cdot \mathbf{\Omega}'', E' \to E'')d\Omega''dE''}, \tag{4.170}$$

$$p_c(E_g < E \leq E_{g-1}) = \frac{\displaystyle\int_{E_g}^{E_{g-1}} A_{c,g} \int_{4\pi} h_{c,g}(\mathbf{\Omega}'')\Sigma_{s,c}(\mathbf{\Omega}' \cdot \mathbf{\Omega}'', E' \to E'')d\Omega''dE''}{\displaystyle\sum_{g''=1}^{G} \int_{E_{g''}}^{E_{g''-1}} A_{c,g''} \int_{4\pi} h_{c,g''}(\mathbf{\Omega}'')\Sigma_{s,c}(\mathbf{\Omega}' \cdot \mathbf{\Omega}'', E' \to E'')d\Omega''dE''}. \tag{4.171}$$

The collision rate is defined as

$$R_{\text{coll},c}(\mathbf{x}, \mathbf{\Omega}', E') = \hat{\Sigma}_{t,c}(\mathbf{\Omega}', E')f(\mathbf{x}, \mathbf{\Omega}', E'). \tag{4.172}$$

The multiplicative weight change for a particle that collides in $\mathcal{V}_c$ is defined as

$$\begin{aligned} w_{\text{scat},c}(\mathbf{x}, \mathbf{\Omega}', E', E) = {} & \mathrm{e}^{[\lambda_{c,g}\Sigma_{t,c}(E)\boldsymbol{\omega}_{c,g} - \lambda_{c,g'}\Sigma_{t,c}(E')\boldsymbol{\omega}_{c,g'}] \cdot (\mathbf{x} - \mathbf{x}_c)} \\ & \cdot \sum_{g''=1}^{G} \int_{E_{g''}}^{E_{g''-1}} \int_{4\pi} \frac{A_{c,g''}}{A_{c,g'}} \Sigma_{s,c}(\mathbf{\Omega}' \cdot \mathbf{\Omega}'', E' \to E'')h_{c,g''}(\mathbf{\Omega}'')d\Omega''dE'' \\ & \cdot \frac{1}{h_{c,g'}(\mathbf{\Omega}')\hat{\Sigma}_{t,c}(\mathbf{\Omega}', E')}, \quad E_{g'} < E' \leq E_{g'-1}, \;\; E_g < E \leq E_{g-1}. \end{aligned} \tag{4.173}$$

As mentioned previously, sampling these distributions is one of the more complicated aspects of continuous-energy Monte Carlo, and many scattering and emission laws exist. For simplicity, we show mathematically how one could sample these distributions, since this thesis is limited to multigroup computations ($\xi \in [0, 1]$):

$$E = E_0 \text{ if } \xi = \int_{E_{g''}}^{E_0} p_c(E' \to E'' \,|\, E_{g''} < E'' \leq E_{g''-1})dE'', \tag{4.174}$$

$$g = g_0 \text{ if } \sum_{g=1}^{g_0-1} p(E_g < E \leq E_{g-1}) \; < \; \xi \; \leq \; \sum_{g=1}^{g_0} p(E_g < E \leq E_{g-1}). \tag{4.175}$$

To sample from the angularly-biased distribution for the outgoing direction, $\mathbf{\Omega}$, we define the probability distribution as

$$p_c(\mathbf{\Omega}' \cdot \mathbf{\Omega} \,|\, E' \to E) = p(\mu \,|\, E' \to E) \cdot p(\gamma \,|\, \mu, E' \to E), \tag{4.176}$$

where we have represented both the incoming and outgoing direction vectors in the orthonormal basis introduced in the section on sampling the interior source (i.e. $\mathbf{\Omega} = \Omega_1^r \boldsymbol{\omega}_{c,g} + \Omega_2^r \boldsymbol{\nu}_{c,g} + \Omega_3^r \boldsymbol{\upsilon}_{c,g}$), and we have used the spherical harmonic expansion for the scattering cross-section:

$$p(\mu \,|\, E' \to E) = \frac{\displaystyle\sum_{n=0}^{N} \Sigma_{sn,c}(\mathbf{x}, E' \to E) Y_{n,0}(\mathbf{\Omega}') a_{n,0} \frac{P_n(\mu)}{1 - \lambda_{c,g}\mu}}{\displaystyle\sum_{n=0}^{N} \Sigma_{sn,c}(\mathbf{x}, E' \to E) Y_{n,0}(\mathbf{\Omega}') a_{n,0} \int_{-1}^{1} \frac{P_n(\mu')}{1 - \lambda_{c,g}\mu'} d\mu'}, \tag{4.177}$$

$$p(\gamma \,|\, \mu, E' \to E) = \frac{\displaystyle\sum_{n=0}^{N} \sum_{m=-n}^{n} \Sigma_{sn}(\mathbf{x}, E' \to E) Y_{n,m}(\mathbf{\Omega}') a_{n,m} \frac{P_n^{|m|}(\mu) e^{-im\gamma}}{1 - \lambda_{c,g}\mu}}{2\pi \displaystyle\sum_{n=0}^{N} \Sigma_{sn}(\mathbf{x}, E' \to E) Y_{n,0}(\mathbf{\Omega}') a_{n,0} \frac{P_n(\mu)}{1 - \lambda_{c,g}\mu}}, \tag{4.178}$$

$$a_{n,m} = (-1)^{\frac{m+|m|}{2}} \left[\frac{2n+1}{4\pi} \frac{(n-|m|)!}{(n+|m|)!} \right]^{1/2}. \tag{4.179}$$

For isotropic or linearly anisotropic scattering, these distributions can be sampled by inverting the cumulative probability distribution. For higher order scattering, rejection sampling must be used.

The multigroup probability distributions are found by considering the analogous multigroup scattering kernel:

$$\begin{aligned} &\Sigma_{s,c,g' \to g}(\mathbf{\Omega}' \cdot \mathbf{\Omega}) \frac{\psi_g^*(\mathbf{x}, \mathbf{\Omega})}{\psi_{g'}^*(\mathbf{x}, \mathbf{\Omega}')} f_{g'}(\mathbf{x}, \mathbf{\Omega}') \\ &\qquad = p_c(\mathbf{\Omega}' \cdot \mathbf{\Omega}, g' \to g) \cdot w_{\text{scat},c,g',g}(\mathbf{x}, \mathbf{\Omega}') \cdot R_{\text{coll},c,g'}(\mathbf{x}, \mathbf{\Omega}'), \end{aligned} \tag{4.180}$$

where $p_c(\mathbf{\Omega} \cdot \mathbf{\Omega}', g' \to g)$ is the joint conditional probability distribution for the multigroup scattering process, $w_{\text{scat},c,g',g}(\mathbf{x}, \mathbf{\Omega}')$ is the multiplicative weight change

that results from the collision, and $R_{\text{coll},c,g'}(\mathbf{x}, \mathbf{\Omega}')$ is the multigroup collision rate.

For a particle that collides at $\mathbf{x} \in \mathcal{V}_c$ and emerges in energy group g, the joint conditional probability distribution $p_c(\mathbf{\Omega}' \cdot \mathbf{\Omega}, g' \to g)$ can be defined as

$$p_c(\mathbf{\Omega}' \cdot \mathbf{\Omega}, g' \to g) = p_c(\mathbf{\Omega}' \cdot \mathbf{\Omega} \,|\, g' \to g) \cdot p_{c,g' \to g}, \tag{4.181}$$

where we have defined the angularly-biased probability distributions as

$$p_c(\mathbf{\Omega}' \cdot \mathbf{\Omega} \,|\, g' \to g) = \frac{\dfrac{\Sigma_{s,c,g' \to g}(\mathbf{\Omega} \cdot \mathbf{\Omega}')}{1 - \lambda_{c,g} \mathbf{\Omega} \cdot \boldsymbol{\omega}_{c,g}}}{\displaystyle\int_{4\pi} \frac{\Sigma_{s,c,g' \to g}(\mathbf{\Omega}'' \cdot \mathbf{\Omega}')}{1 - \lambda_{c,g} \mathbf{\Omega}'' \cdot \boldsymbol{\omega}_{c,g}} d\Omega''}, \tag{4.182}$$

$$p_{c,g' \to g} = \frac{\displaystyle\int_{4\pi} \frac{\Sigma_{s,c,g' \to g}(\mathbf{\Omega}' \cdot \mathbf{\Omega}'')}{1 - \lambda_{c,g} \mathbf{\Omega}'' \cdot \boldsymbol{\omega}_{c,g}} d\Omega''}{\displaystyle\sum_{g''=1}^{G} \int_{4\pi} \frac{\Sigma_{s,c,g' \to g''}(\mathbf{\Omega}' \cdot \mathbf{\Omega}'')}{1 - \lambda_{c,g''} \mathbf{\Omega}'' \cdot \boldsymbol{\omega}_{c,g''}} d\Omega''}. \tag{4.183}$$

To sample from the distribution that selects for the exiting group, we use the following criterion ($\xi \in [0, 1]$):

$$g = g_0 \text{ if } \sum_{g''=1}^{g_0 - 1} p_{c,g' \to g''} \;<\; \xi \;\leq\; \sum_{g''=1}^{g_0} p_{c,g' \to g''}. \tag{4.184}$$

The angularly-biased multigroup probability distribution that describes the outgoing angle is treated the same way as for the continuous-energy case:

$$p_c(\mathbf{\Omega}' \cdot \mathbf{\Omega} \,|\, g' \to g) = p_c(\mu \,|\, g' \to g) \cdot p_c(\gamma \,|\, \mu, g' \to g), \tag{4.185}$$

where

$$p_c(\mu \,|\, g' \to g) = \frac{\displaystyle\sum_{n=0}^{N} \Sigma_{sn,c,g' \to g} Y_{n,0}(\mathbf{\Omega}') a_{n,0} \frac{P_n(\mu)}{1 - \lambda_{c,g} \mu}}{\displaystyle\sum_{n=0}^{N} \Sigma_{sn,c,g' \to g} Y_{n,0}(\mathbf{\Omega}') \int_{-1}^{1} a_{n,0} \frac{P_n(\mu')}{1 - \lambda_{c,g} \mu'} d\mu'}, \tag{4.186}$$

$$p(\gamma \,|\, \mu, g' \to g) = \frac{\displaystyle\sum_{n=0}^{N} \sum_{m=-n}^{n} \Sigma_{sn,c,g' \to g} Y_{n,0}(\mathbf{\Omega}') a_{n,m} \frac{P_n(\mu) e^{-im\gamma}}{1 - \lambda_{c,g} \mu}}{2\pi \displaystyle\sum_{n=0}^{N} \Sigma_{sn,c,g' \to g} Y_{n,0}(\mathbf{\Omega}') a_{n,0} \frac{P_n(\mu)}{1 - \lambda_{c,g} \mu} d\mu}, \tag{4.187}$$

$$a_{n,m} = (-1)^{\frac{m+|m|}{2}} \left[\frac{2n+1}{4\pi} \frac{(n-|m|)!}{(n+|m|)!} \right]^{1/2}. \tag{4.188}$$

These distributions are sampled in the same way as the continuous-energy distributions.

A simple example that is valid for both multigroup and continuous energy is to consider the case of isotropic scattering. The probability distribution, in this case, is the same as for the interior source:

$$p_c(\mathbf{\Omega}' \cdot \mathbf{\Omega} \,|\, E' \to E) = \frac{\dfrac{1}{1 - \lambda_{c,g} \mathbf{\Omega} \cdot \boldsymbol{\omega}_{c,g}}}{\displaystyle\int_{4\pi} \frac{1}{1 - \lambda_{c,g} \mathbf{\Omega}'' \cdot \boldsymbol{\omega}_{c,g}} d\Omega''}, \tag{4.189}$$

and it is sampled in the same way as the interior source.

The multigroup collision rate is defined as

$$R_{\text{coll},c,g'}(\mathbf{x}, \mathbf{\Omega}') = \hat{\Sigma}_{t,c,g'}(\mathbf{\Omega}') f_{g'}(\mathbf{x}, \mathbf{\Omega}'), \tag{4.190}$$

where $\Sigma_{t,c,g}(\mathbf{\Omega}) = \Sigma_{t,c,g}[1 - \lambda_{c,g} \mathbf{\Omega} \cdot \boldsymbol{\omega}_{c,g}]$.

The multigroup multiplicative weight change for a particle that collides in $\mathcal{V}_c$ is defined as

$$\begin{aligned} w_{\text{scat},c,g',g}(\mathbf{x}, \mathbf{\Omega}') = {} & \mathrm{e}^{[\lambda_{c,g} \Sigma_{t,c,g} \boldsymbol{\omega}_{c,g} - \lambda_{c,g'} \Sigma_{t,c,g'} \boldsymbol{\omega}_{c,g'}] \cdot (\mathbf{x} - \mathbf{x}_c)} \\ & \cdot \sum_{g''=1}^{G} \int_{4\pi} \frac{A_{c,g''}}{A_{c,g'}} \Sigma_{s,c,g' \to g''}(\mathbf{\Omega}' \cdot \mathbf{\Omega}'') h_{c,g''}(\mathbf{\Omega}'') d\Omega'' \\ & \cdot \frac{1}{h_{c,g'}(\mathbf{\Omega}') \hat{\Sigma}_{t,c,g'}(\mathbf{\Omega}')}. \end{aligned} \tag{4.191}$$

The probability distributions defined in this section were chosen to eliminate excessive computational time, while still preserving as many of the modified physics as possible. Specifically, the probability distribution used to sample for the outgoing energy (Eq. 4.170, 4.171, 4.183) could have been defined to include the space-dependent exponential factor contained in the estimate of ψ^*. However, this results in a probability distribution that depends on the location of the collision event; thus, the probability distribution would have to be calculated on the fly, which requires much more computational cost than a prior-to-runtime construction of the probability distribution in each spatial element $\mathcal{V}_c$. Mathematically, this produces no bias in the estimate of the solution; however, it does mean that the distributions to sample for

energy are a slight approximation to a complete modification of the particle physics.

Since the weight window is centered about unity, we expect the multiplicative weight change to be approximately equal to unity as well; then, there is little or no weight change upon collision. To show the conditions that are required to effect a negligible weight change upon collision, we again consider Eq. 4.167, which describes the discrete scattering process.

$$\Sigma_{s,c}(\mathbf{\Omega}' \cdot \mathbf{\Omega}, E' \rightarrow E) \frac{\psi^*(\mathbf{x}, \mathbf{\Omega}, E)}{\psi^*(\mathbf{x}, \mathbf{\Omega}', E')} f(\mathbf{x}, \mathbf{\Omega}', E') = p_c(\mathbf{\Omega}' \cdot \mathbf{\Omega}, E' \rightarrow E) \cdot w_{\text{scat},c}(\mathbf{x}, \mathbf{\Omega}', E', E) \cdot R_{\text{coll},c}(\mathbf{x}, \mathbf{\Omega}', E'). \quad (4.192)$$

As mentioned, we have made a slight approximation to the complete modified physics by not including the space-dependent exponential factor in the probability distributions for the outgoing energy. However, to determine the conditions that result in a negligible weight change, we neglect this approximation. In this case, we define the components of the scatter kernel as

$$p_c(\mathbf{x}, \mathbf{\Omega}' \cdot \mathbf{\Omega}, E' \rightarrow E) = \frac{\Sigma_{s,c}(\mathbf{\Omega}' \cdot \mathbf{\Omega}, E' \rightarrow E)\psi^*(\mathbf{x}, \mathbf{\Omega}, E)}{\int_0^\infty \int_{4\pi} \Sigma_{s,c}(\mathbf{\Omega}' \cdot \mathbf{\Omega}", E' \rightarrow E")\psi^*(\mathbf{x}, \mathbf{\Omega}", E")d\Omega" dE"}, \quad (4.193)$$

$$w_{\text{scat},c}(\mathbf{x}, \mathbf{\Omega}', E') = \frac{\int_0^\infty \int_{4\pi} \Sigma_{s,c}(\mathbf{\Omega}' \cdot \mathbf{\Omega}", E' \rightarrow E")\psi^*(\mathbf{x}, \mathbf{\Omega}", E")d\Omega" dE"}{\hat{\Sigma}_{t,c}(\mathbf{\Omega}', E')\psi^*(\mathbf{x}, \mathbf{\Omega}', E')}, \quad (4.194)$$

$$R_{\text{coll,c}}(\mathbf{x}, \mathbf{\Omega}', E') = \hat{\Sigma}_{t,c}(\mathbf{\Omega}', E') f(\mathbf{x}, \mathbf{\Omega}', E'). \quad (4.195)$$

Then, to determine the conditions under which the weight change is negligible, we set the multiplicative weight change (Eq. 4.194) to unity and rearrange:

$$\hat{\Sigma}_{t,c}(\mathbf{\Omega}, E)\psi^*(\mathbf{x}, \mathbf{\Omega}, E) = \int_0^\infty \int_{4\pi} \Sigma_{s,c}(\mathbf{\Omega} \cdot \mathbf{\Omega}', E \rightarrow E')\psi^*(\mathbf{x}, \mathbf{\Omega}', E')d\Omega' dE'. \quad (4.196)$$

Recall that we approximate $\psi^*(\mathbf{x}, \mathbf{\Omega}, E)$ as

$$\psi^*(\mathbf{x}, \mathbf{\Omega}, E) = A_{c,g} \mathrm{e}^{\lambda_{c,g}\Sigma_{t,c}(E)(\mathbf{x} - \mathbf{x}_c) \cdot \boldsymbol{\omega}_{c,g}} h_{c,g}(\mathbf{\Omega}), \quad \mathbf{x} \in \mathcal{V}_c, \quad E_g < E \leq E_{g-1}, \quad \mathbf{\Omega} \in 4\pi. \quad (4.197)$$

Substituting this into Eq. 4.196, we recover the adjoint transport equation with no source:

$$-\boldsymbol{\Omega}\cdot\nabla\psi^*(\mathbf{x},\boldsymbol{\Omega},E)+\Sigma_{t,c}(\boldsymbol{\Omega},E)\psi^*(\mathbf{x},\boldsymbol{\Omega},E)= \int_0^\infty\int_{4\pi}\Sigma_{s,c}(\boldsymbol{\Omega}\cdot\boldsymbol{\Omega}',E\rightarrow E')\psi^*(\mathbf{x},\boldsymbol{\Omega}',E')d\Omega'dE'. \quad (4.198)$$

Thus, the conditions required for the weight change to be small or negligible are the following:

1. $\psi^*(\mathbf{x},\boldsymbol{\Omega},E)$ is well-approximated by Eq. 4.197.

2. The adjoint interior source is small compared to the adjoint scattering source within $\mathcal{V}_c$.

The second condition is dependent on the adjoint problem, specifically, whether the adjoint scattering source or the adjoint interior source dominates locally. For problems with a localized adjoint source, such as source-detector problems and to some extent source-region problems, this condition certainly holds.

Weight Change at Boundaries

Even though we are simulating the transformed equation, the objective is still to recover the solution of the original neutron transport equation, $\psi(\mathbf{x},\boldsymbol{\Omega},E)$. For non-pathological problems, the solution ψ will be continuous throughout phase space, and we require that it remain continuous in our simulation. However, since the "transform" function $\hat{\mathcal{T}}(\mathbf{x},\boldsymbol{\Omega},E)$ is, in general, discontinuous across cell interfaces, the function f must also be discontinuous. The continuity condition (Eq. 4.101c) mathematically encapsulates this property. Thus, we account for this discontinuity in the function $f(\mathbf{x},\boldsymbol{\Omega},E)$ in our Monte Carlo simulation by discontinuously adjusting the weight of the particle as it streams across cell interfaces. That is, we preserve continuity of the angular neutron flux at an interface between two cells by adjusting the weight of the Monte Carlo particle.

In order to determine the weight change as a particle streams from spatial element $\mathcal{V}_{c^-}$ to another $\mathcal{V}_{c^+}$, we use the continuity condition (Eq. 4.101c):

$$\hat{\mathcal{T}}(\mathbf{x},\boldsymbol{\Omega},E)f(\mathbf{x},\boldsymbol{\Omega},E)|_{\mathbf{x}\in\mathcal{V}_{c^-}}=\hat{\mathcal{T}}(\mathbf{x},\boldsymbol{\Omega},E)f(\mathbf{x},\boldsymbol{\Omega},E)|_{\mathbf{x}\in\mathcal{V}_{c^+}}. \quad (4.199)$$

This equation implies that if a particle with weight w^- passes through an interface

at $\mathbf{x}$, the new weight w^+ as it leaves the interface will be given by

$$w^+ = w^- \frac{\hat{\mathcal{T}}(\mathbf{x}, \mathbf{\Omega}, E)|_{\mathbf{x}\in\mathcal{V}_{c^-}}}{\hat{\mathcal{T}}(\mathbf{x}, \mathbf{\Omega}, E)|_{\mathbf{x}\in\mathcal{V}_{c^+}}}. \tag{4.200}$$

Ideally there would be no weight change as a particle passes through an interface. However, because we do not ensure continuity of the angular adjoint flux approximation $\psi^*(\mathbf{x}, \mathbf{\Omega}, E)$ (see Eq. 4.105) across cells, in addition to the problem-dependent function $B(\mathbf{x})$ already specified to be a histogram in space, a discontinuity will exist. Eq. 4.200 describes the weight change.

In addition to requiring continuity of the angular neutron flux throughout the interior phase-space of the problem, we also require continuity of ψ at symmetric (reflecting) boundaries:

$$\psi(\mathbf{x}_b, \mathbf{\Omega}_r, E) = \psi(\mathbf{x}_b, \mathbf{\Omega}, E), \tag{4.201}$$

where $\mathbf{x}_b$ is a point on the symmetric boundary, $\mathbf{\Omega}$ is the direction in which the particle was traveling before hitting the reflecting boundary, and $\mathbf{\Omega}_r$ is the reflected direction that the particle travels in after colliding with the boundary. [In terms of the incoming angle $\mathbf{\Omega}$ and the normal to the surface $\mathbf{n} = \mathbf{n}(\mathbf{x}_b)$, we can write the reflected angle as $\mathbf{\Omega}_r = \mathbf{\Omega} - 2\,(\mathbf{\Omega}\cdot\mathbf{n})\,\mathbf{n}$.]

Using the transform (Eq. 4.86), we obtain the following relation:

$$\hat{\mathcal{T}}(\mathbf{x}_b, \mathbf{\Omega}_r, E) f(\mathbf{x}_b, \mathbf{\Omega}_r, E) = \hat{\mathcal{T}}(\mathbf{x}_b, \mathbf{\Omega}, E) f(\mathbf{x}_b, \mathbf{\Omega}, E). \tag{4.202}$$

We again interpret this equation as a description of the weight change from w to w_r due to a particle hitting a reflecting boundary:

$$w_r = w \frac{\hat{\mathcal{T}}(\mathbf{x}_b, \mathbf{\Omega}, E)}{\hat{\mathcal{T}}(\mathbf{x}_b, \mathbf{\Omega}_r, E)}. \tag{4.203}$$

4.3.6 Estimators

To obtain estimates of the quantities of interest, such as the scalar flux $\phi(\mathbf{x}, E)$ or a response $\mathcal{R}(\mathbf{x})$, we use a modified path length estimator and a modified collision estimator. The bin structure that we use to tally is defined for the energy range by the boundaries $\{E_g\}_{g=0}^{G}$ and spatially by the set $\{\mathcal{V}_c\}_{c=1}^{N_{\text{cells}}}$ with each spatial element having a volume V_c.

Path Length Estimator

The nth simulation particle provides a path length estimate for the scalar flux $\phi(\mathbf{x}, E)$ that is given as the following for $E_i \in (E_g, E_{g-1}]$ and $\mathbf{x}_i \in \mathcal{V}_c$:

$$\phi_{c,g,n}^{\text{path}} = \frac{\hat{Q}_T}{V_c} \sum_{i=1}^{I_{c,g,n}} w_i \int_0^{l_i} \hat{\mathcal{T}}(\mathbf{x}_i + s\boldsymbol{\Omega}_i, \boldsymbol{\Omega}_i, E_i) ds, \tag{4.204}$$

where $\hat{Q}_T$ is the total modified source rate, $I_{c,g,n}$ is the number of track lengths generated by the nth simulation particle in volume V_c, E_i is the particle's energy, $\boldsymbol{\Omega}_i$ is the particle's direction, w_i is the particle's weight, and $\mathbf{x}_i$ is the initial spatial location of the ith streaming path, which has length l_i. Inserting the functional form of $\hat{\mathcal{T}}(\mathbf{x}, \boldsymbol{\Omega}, E)$ into the expression, we get

$$\phi_{c,g,n}^{\text{path}} = \frac{\hat{Q}_T}{V_c} \sum_{i=1}^{I_{c,g,n}} w_i \frac{\hat{\mathcal{T}}(\mathbf{x}_i, \boldsymbol{\Omega}_i, E_i) - \hat{\mathcal{T}}(\mathbf{x}_i + l_i\boldsymbol{\Omega}_i, \boldsymbol{\Omega}_i, E_i)}{\lambda_{c,g}\Sigma_{t,c}(E_i)\boldsymbol{\Omega}_i \cdot \boldsymbol{\omega}_{c,g}}. \tag{4.205}$$

We recall

$$\hat{\mathcal{T}}(\mathbf{x}, \boldsymbol{\Omega}, E) = \frac{B(\mathbf{x})}{\psi^*(\mathbf{x}, \boldsymbol{\Omega}, E)}, \tag{4.206}$$

where

$$\psi^*(\mathbf{x}, \boldsymbol{\Omega}, E) = \phi_{c,g}^*(\mathbf{x}, E) h_{c,g}(\boldsymbol{\Omega}), \quad \mathbf{x} \in \mathcal{V}_c, \quad E_g < E \leq E_{g-1}, \tag{4.207}$$

$$B(\mathbf{x}) = B_c, \quad \mathbf{x} \in \mathcal{V}_c, \tag{4.208}$$

and

$$\phi_{c,g}^*(\mathbf{x}, E) = A_{c,g} e^{\lambda_{c,g}\Sigma_{t,c}(E)(\mathbf{x} - \mathbf{x}_c) \cdot \boldsymbol{\omega}_{c,g}}, \tag{4.209}$$

$$h_{c,g}(\boldsymbol{\Omega}) = [1 - \lambda_{c,g}\boldsymbol{\Omega} \cdot \boldsymbol{\omega}_{c,g}]^{-1}. \tag{4.210}$$

The multigroup version of the path length estimator is given by replacing the continuous-energy cross-section with the multigroup one, i.e., $\Sigma_{t,c}(E) = \Sigma_{t,c,g}$.

To obtain the mean scalar flux and the variance of the mean for a simulation with N particles, the following equations are used for both continuous-energy and multigroup Monte Carlo:

$$\phi_{c,g}^{\text{path}} = \frac{1}{N} \sum_{n=1}^{N} \phi_{c,g,n}^{\text{path}}, \tag{4.211}$$

$$\text{Var}\left[\phi_{c,g}^{\text{path}}\right] = \frac{1}{N-1}\sum_{n=1}^{N}\left(\phi_{c,g,n}^{\text{path}} - \phi_{c,g}^{\text{path}}\right)^2. \tag{4.212}$$

Just as in a standard Monte Carlo simulation, the only quantities that need to be stored are the total weighted path length for the mean and the total weighted path length squared for the variance of the mean, where the total weighted path length is given by the summation in Eq. 4.205.

The nth simulation particle provides a path length estimate for the response $\mathcal{R}(\mathbf{x})$ that is given as the following ($E_i \in (E_g, E_{g-1}]$ and $\mathbf{x}_i \in \mathcal{V}_c$):

$$\mathcal{R}_{c,g,n}^{\text{path}} = \frac{\hat{Q}_T}{V_c}\sum_{i=1}^{I_{c,g,n}} w_i \Sigma_{\mathcal{R},c}(E_i)\int_0^{l_i}\hat{\mathcal{T}}(\mathbf{x}_i + s\boldsymbol{\Omega}_i, \boldsymbol{\Omega}_i, E_i)ds, \tag{4.213}$$

where most of the parameters have been defined for the estimate of the scalar flux. $\Sigma_{\mathcal{R},c}(E)$ is the response parameter in spatial element $\mathcal{V}_c$. Inserting the functional form of $\hat{\mathcal{T}}(\mathbf{x}, \boldsymbol{\Omega}, E)$ into the expression, we get

$$\mathcal{R}_{c,g,n}^{\text{path}} = \frac{\hat{Q}_T}{V_c}\sum_{i=1}^{I_{c,g,n}} w_i \Sigma_{\mathcal{R},c}(E_i)\frac{\hat{\mathcal{T}}(\mathbf{x}_i, \boldsymbol{\Omega}_i, E_i) - \hat{\mathcal{T}}(\mathbf{x}_i + l_i\boldsymbol{\Omega}_i, \boldsymbol{\Omega}_i, E_i)}{\lambda_{c,g}\Sigma_{t,c}(E_i)\boldsymbol{\Omega}_i \cdot \boldsymbol{\omega}_{c,g}}, \tag{4.214}$$

where $\hat{\mathcal{T}}(\mathbf{x}, \boldsymbol{\Omega}, E)$ has been defined above. The multigroup version is given by replacing the continuous-energy cross-section with the multigroup one (i.e. $\Sigma_{t,c}(E) = \Sigma_{t,c,g}$ and $\Sigma_{\mathcal{R},c}(E) = \Sigma_{\mathcal{R},c,g}$).

To obtain the mean value for the scalar flux and variance of the mean for a simulation with N particles, we use the following equations for both continuous-energy and multigroup Monte Carlo:

$$\mathcal{R}_{c,g}^{\text{path}} = \frac{1}{N}\sum_{n=1}^{N}\mathcal{R}_{c,g,n}^{\text{path}}, \tag{4.215}$$

$$\text{Var}\left[\mathcal{R}_{c,g}^{\text{path}}\right] = \frac{1}{N-1}\sum_{n=1}^{N}\left(\mathcal{R}_{c,g,n}^{\text{path}} - \mathcal{R}_{c,g}^{\text{path}}\right)^2. \tag{4.216}$$

Just like the scalar flux estimator, the only quantities that need to be stored are the total weighted path length for the mean and the total weighted path length squared for the variance the mean, where the total weighted path length is given by the summation in Eq. 4.214.

Collision Estimator

The nth simulation particle provides a collision estimate for the scalar flux that is given as the following for $E_i \in (E_g, E_{g-1}]$ and $\mathbf{x}_i \in \mathcal{V}_c$:

$$\phi_{c,g,n}^{\text{coll}} = \frac{\hat{Q}_T}{V_c} \sum_{i=1}^{I_{c,g,n}} w_i \frac{\hat{\mathcal{T}}(\mathbf{x}_i, \mathbf{\Omega}_i, E_i)}{\hat{\Sigma}_{t,c}(\mathbf{\Omega}_i, E_i)}, \tag{4.217}$$

where $\hat{Q}_T$ is the total modified source rate, $I_{c,g,n}$ is the number of collisions generated by the nth simulation particle in volume V_c, E_i is the particle's energy when it collides, $\mathbf{\Omega}_i$ is the particle's direction when it collides, w_i is the particle's weight when it collides, $\mathbf{x}_i$ is the particle's spatial location when it collides, and $\hat{\Sigma}_{t,c}(\mathbf{\Omega}, E)$ is the effective total cross-section. The multigroup version of this estimator replaces the continuous-energy cross-section with the multigroup one, i.e., $\Sigma_{t,c}(E) = \Sigma_{t,c,g}$.

To obtain the mean scalar flux and variance of the mean for a simulation with N particles, the following equations are used for both continuous-energy and multigroup Monte Carlo:

$$\phi_{c,g}^{\text{coll}} = \frac{1}{N} \sum_{n=1}^{N} \phi_{c,g,n}^{\text{coll}}, \tag{4.218}$$

$$\text{Var}\left[\phi_{c,g}^{\text{coll}}\right] = \frac{1}{N-1} \sum_{n=1}^{N} \left(\phi_{c,g,n}^{\text{coll}} - \phi_{c,g}^{\text{coll}}\right)^2. \tag{4.219}$$

Just as in a standard Monte Carlo simulation, the only quantities that need to be stored are the sums of the weighted inverse total effective cross-section for the mean and this quantity squared for the variance of the mean, where the weighted total inverse total cross-section is given by the summation in Eq. 4.217.

The nth simulation particle provides a collision estimate for the response $\mathcal{R}(\mathbf{x})$ that is given as the following ($E_i \in (E_g, E_{g-1}]$ and $\mathbf{x}_i \in \mathcal{V}_c$):

$$\mathcal{R}_{c,g,n}^{\text{coll}} = \frac{\hat{Q}_T}{V_c} \sum_{i=1}^{I_{c,g,n}} w_i \Sigma_{\mathcal{R},c}(E_i) \frac{\hat{\mathcal{T}}(\mathbf{x}_i, \mathbf{\Omega}_i, E_i)}{\hat{\Sigma}_{t,c}(\mathbf{\Omega}_i, E_i)}, \tag{4.220}$$

where most of the parameters have been defined for the estimate of the scalar flux, and $\Sigma_{\mathcal{R},c}(E)$ is the response parameter in spatial element $\mathcal{V}_c$. The multigroup version of this estimator replaces the continuous-energy cross-section with the multigroup one (i.e. $\Sigma_{t,c}(E) = \Sigma_{t,c,g}$ and $\Sigma_{\mathcal{R},c}(E) = \Sigma_{\mathcal{R},c,g}$).

To obtain the mean value for the scalar flux and variance of the mean for a

simulation with N particles, we use the following equations for both continuous-energy and multigroup Monte Carlo:

$$\mathcal{R}_{c,g}^{\text{coll}} = \frac{1}{N}\sum_{n=1}^{N}\mathcal{R}_{c,g,n}^{\text{coll}}, \tag{4.221}$$

$$\text{Var}\left[\mathcal{R}_{c,g}^{\text{coll}}\right] = \frac{1}{N-1}\sum_{n=1}^{N}\left(\mathcal{R}_{c,g,n}^{\text{coll}} - \mathcal{R}_{c,g}^{\text{coll}}\right)^2. \tag{4.222}$$

Just like the scalar flux estimator, the only quantities that must be stored are the sums of the weighted inverse total effective cross-section for the mean and this quantity squared for the variance of the mean, where the sum of the weighted inverse total effective cross-section is given by the summation in Eq. 4.220.

4.4 Summary

In this chapter, we have introduced the General Transform approach, which was shown to encompasses the standard *weight window approach* and a new *Transform approach*. The General Transform is given as

$$\psi(\mathbf{x},\mathbf{\Omega},E) = \hat{\mathcal{T}}(\mathbf{x},\mathbf{\Omega},E)f(\mathbf{x},\mathbf{\Omega},E), \tag{4.223}$$

which is then substituted into the neutron transport equation to obtain the transformed transport equation for f. The expression that relates the "transform" function $\hat{\mathcal{T}}(\mathbf{x},\mathbf{\Omega},E)$, the weight window center $\text{w}(\mathbf{x},E)$ and the angular Monte Carlo particle flux $m(\mathbf{x},\mathbf{\Omega},E)$ is given by

$$\psi(\mathbf{x},\mathbf{\Omega},E) \approx \hat{\mathcal{T}}(\mathbf{x},\mathbf{\Omega},E)\text{w}(\mathbf{x},E)m(\mathbf{x},\mathbf{\Omega},E). \tag{4.224}$$

To obtain the standard *weight window approach*, we set $\hat{\mathcal{T}}(\mathbf{x},\mathbf{\Omega},E) = 1$. Then, $f = \psi$, indicating that the transformed transport equation is the neutron transport equation, as it should be for the weight window approach. Finally, the weight window center is related to the scalar Monte Carlo particle flux by the expression:

$$\phi(\mathbf{x},E) \approx \text{w}(\mathbf{x},E)\mathcal{M}(\mathbf{x},E). \tag{4.225}$$

This expression allows the user to construct a weight window to achieve a certain Monte Carlo particle distribution or to determine what Monte Carlo particle distri-

bution results from a certain weight window.

To obtain the *Transform approach*, we set $\mathrm{w}(\mathbf{x}, E) = 1$. In this case, we choose the "transform" function $\hat{\mathcal{T}}(\mathbf{x}, \mathbf{\Omega}, E)$ to achieve a user-specified angular Monte Carlo particle flux. For this thesis, we have chosen a form of the angular Monte Carlo particle flux which can be applied to a wide range of problems:

$$m(\mathbf{x}, \mathbf{\Omega}, E) = \frac{\psi(\mathbf{x}, \mathbf{\Omega}, E)\psi^*(\mathbf{x}, \mathbf{\Omega}, E)}{B(\mathbf{x})} \tag{4.226}$$

Thus, the "transform" function has the following form

$$\hat{\mathcal{T}}(\mathbf{x}, \mathbf{\Omega}, E) = \frac{B(\mathbf{x})}{\psi^*(\mathbf{x}, \mathbf{\Omega}, E)}, \tag{4.227}$$

where a simple approximation to $\psi^*(\mathbf{x}, \mathbf{\Omega}, E)$ is used and $B(\mathbf{x})$ is dependent on the type of problem, whether source-detector, source-region, or global.

Both the weight window approach and the Transform approach were discussed in detail in this chapter, including theory and practical implementation details. In the following chapters, we consider the application of weight windows and the Transform approach to source-detector problems, source-region problems, and global problems. For Monte Carlo codes that already allow weight windows, the weight window approach is very easy to implement. The Transform approach requires much more effort to implement, since the particle physics are extensively modified. We also expect the computational expense per particle to be higher for the Transform approach than for weight windows; thus, for the Transform approach to be advantageous over weight windows, it must significantly reduce the variance.

Chapter V

Source-Detector Problems

Most Monte Carlo shielding simulations have focused on *source-detector* problems, in which a single *response* is desired rather than estimates of the flux at every spatial location. That is, we wish to obtain

$$\mathcal{R}_D = \frac{1}{V_D} \int_{\mathcal{V}_D} \int_0^\infty \int_{4\pi} \Sigma_{\mathcal{R}}(\mathbf{x}, E) \psi(\mathbf{x}, \mathbf{\Omega}, E) d\Omega dE dV, \tag{5.1}$$

where $\Sigma_{\mathcal{R}}(\mathbf{x}, E)$ is the *response function* and $\mathcal{V}_D$ is the detector region. For most source-detector problems, $\mathcal{V}_D$ is less than a few mean free paths thick and is typically smaller than the source region. If $\mathcal{V}_D$ is located far from the source region, then these problems tend to be easier to solve if efficient techniques are employed to guide the Monte Carlo particles from the source to the detector. A common approach is to use a weight-window that is proportional to the inverse adjoint scalar flux.

In this chapter, we solve two source-detector problems: the *response problem*, in which a single response $\mathcal{R}_D$ is desired (e.g. Eq. 5.1), and the *flux problem*, in which the energy-dependent scalar flux $\phi(\mathbf{x}, E)$ is desired in the detector region. The scalar flux $\psi(\mathbf{x}, E)$ is defined as

$$\phi(\mathbf{x}, E) = \int_{4\pi} \psi(\mathbf{x}, \mathbf{\Omega}, E) d\Omega. \tag{5.2}$$

We discuss and evaluate three solution techniques: FW-CADIS [29, 30], a weight window technique developed at Oak Ridge National Laboratory; our weight window; and the Transform approach. For most source-detector problems our weight window and FW-CADIS are similar to the standard weight window approach, in which the weight window is inversely proportional to the adjoint scalar flux $\phi^*(\mathbf{x}, E)$. However, the definition of the adjoint source depends on the type of problem – flux or response.

5.1 The Contributon Flux

In this work, we choose to distribute Monte Carlo particles according to the *contributon flux* [31–37], or a modified form of the contributon flux, which identifies the regions of the problem that are important to the desired solution. Within the shielding community, the contributon concept is well-known and understood to convey theoretical information about the most likely paths that Monte Carlo particles travel to contribute to a detector response. This information can then be used to provide qualitative guidance to better optimize the shielding design. In this thesis, we make practical use of the contributon concept, by choosing to distribute Monte Carlo particles throughout phase space in ways that are consistent with the contributon flux. To our knowledge, the work presented in this thesis represents the first specific application of the contributon concept to a broad class of practical problems.

Monte Carlo practitioners have found that, for source-detector problems, choosing a weight window that is inversely proportional to the adjoint scalar flux works well. This weight window is given by

$$\mathrm{w}(\mathbf{x}, E) = \frac{\mathrm{C}_0^{-1}}{\phi^*(\mathbf{x}, E)}, \tag{5.3}$$

where C_0 is a suitable constant. Using Eq. 4.10 from Chapter IV, we find that this weight window yields a Monte Carlo particle flux distribution that is approximately proportional to the scalar contributon flux $\phi^{\mathrm{c}}(\mathbf{x}, E)$:

$$\begin{aligned}
\mathcal{M}(\mathbf{x}, E) &= \frac{\phi(\mathbf{x}, E)}{\mathrm{w}(\mathbf{x}, E)} \\
&= \mathrm{C}_0 \phi(\mathbf{x}, E) \phi^*(\mathbf{x}, E) \\
&\approx 4\pi \mathrm{C}_0 \int_{4\pi} \psi(\mathbf{x}, \mathbf{\Omega}, E) \psi^*(\mathbf{x}, \mathbf{\Omega}, E) d\Omega \\
&= 4\pi \mathrm{C}_0 \phi^{\mathrm{c}}(\mathbf{x}, E),
\end{aligned} \tag{5.4}$$

where $\phi^{\mathrm{c}}(\mathbf{x}, E)$ is the scalar contributon flux. *Thus, the standard weight window, which has been used for the past several decades to solve source-detector problems, roughly distributes Monte Carlo particles according to the contributon flux.* To our knowledge, this relationship between the standard weight window and a Monte Carlo particle distribution that is proportional to the contributon flux has not been described in the literature.

Due to the intuitive appeal of distributing Monte Carlo particles according to the

contributon flux $\psi^c(\mathbf{x}, \mathbf{\Omega}, E) = \psi(\mathbf{x}, \mathbf{\Omega}, E)\psi^*(\mathbf{x}, \mathbf{\Omega}, E)$, which represents the relative contribution of particles at a point in phase space to the detector response (or flux), and its successful use historically, we shall continue to rely on the contributon flux as a means to distribute Monte Carlo particles. For this reason, we shall closely examine the contributon flux, specifically, the *forward contributon transport equation* and the *adjoint contributon transport equation*.

For a given adjoint and forward problem, the forward and adjoint contributon transport equations are equivalent expressions for the angular contributon flux $\psi^c(\mathbf{x}, \mathbf{\Omega}, E)$. The difference between the two is that the forward-based contributon equation describes the transport of contributons from the forward source region to the detector, with particle physics similar to those described by the forward neutron transport equation, while the adjoint-based contributon equation describes the transport of contributons from the detector to the forward source region, with particle physics similar to those described by the adjoint neutron transport equation.

To derive the forward and adjoint contributon transport equations, we begin with the forward neutron transport equation and the adjoint transport equation. The forward transport equation is given by Eq. 2.1:

$$\begin{aligned}\mathbf{\Omega} \cdot \nabla\psi(\mathbf{x}, \mathbf{\Omega}, E) + \Sigma_t(\mathbf{x}, E)\psi(\mathbf{x}, \mathbf{\Omega}, E) \\ = \int_0^\infty \int_{4\pi} \Sigma_s(\mathbf{x}, \mathbf{\Omega}' \cdot \mathbf{\Omega}, E' \to E)\psi(\mathbf{x}, \mathbf{\Omega}', E')d\Omega' dE' + Q(\mathbf{x}, \mathbf{\Omega}, E), \\ \mathbf{x} \in \mathcal{V}, \;\; \mathbf{\Omega} \in 4\pi, \;\; 0 < E < \infty,\end{aligned} \tag{5.5a}$$

with vacuum boundary condition

$$\psi(\mathbf{x}, \mathbf{\Omega}, E) = 0, \quad \mathbf{x} \in \partial\mathcal{V}, \;\; \mathbf{\Omega} \cdot \mathbf{n}(\mathbf{x}) < 0, \;\; 0 < E < \infty. \tag{5.5b}$$

The full continuous-energy adjoint neutron transport equation is given as

$$\begin{aligned}-\mathbf{\Omega} \cdot \nabla\psi^*(\mathbf{x}, \mathbf{\Omega}, E) + \Sigma_t(\mathbf{x}, E)\psi^*(\mathbf{x}, \mathbf{\Omega}, E) \\ = \int_0^\infty \int_{4\pi} \Sigma_s(\mathbf{x}, \mathbf{\Omega} \cdot \mathbf{\Omega}', E \to E')\psi^*(\mathbf{x}, \mathbf{\Omega}', E')d\Omega' dE' + Q^*(\mathbf{x}, \mathbf{\Omega}, E), \\ \mathbf{x} \in \mathcal{V}, \;\; \mathbf{\Omega} \in 4\pi, \;\; 0 < E < \infty,\end{aligned} \tag{5.6a}$$

with vacuum boundary condition

$$\psi^*(\mathbf{x}, \mathbf{\Omega}, E) = 0, \quad \mathbf{x} \in \partial\mathcal{V}, \;\; \mathbf{\Omega} \cdot \mathbf{n}(\mathbf{x}) > 0, \;\; 0 < E < \infty. \tag{5.6b}$$

Substituting $\psi = \psi^c/\psi^*$ into Eq. 5.5 and rearranging, we obtain the forward contributon transport equation:

$$\begin{aligned}\boldsymbol{\Omega}\cdot\nabla\psi^c(\mathbf{x},\boldsymbol{\Omega},E) + \{\Sigma_t(\mathbf{x},E) - \boldsymbol{\Omega}\cdot\nabla\ln[\psi^*(\mathbf{x},\boldsymbol{\Omega},E)]\}\,\psi^c(\mathbf{x},\boldsymbol{\Omega},E)\\ = \int_0^\infty\int_{4\pi}\Sigma_s(\mathbf{x},\boldsymbol{\Omega}'\cdot\boldsymbol{\Omega},E'\to E)\frac{\psi^*(\mathbf{x},\boldsymbol{\Omega},E)}{\psi^*(\mathbf{x},\boldsymbol{\Omega}',E')}\psi^c(\mathbf{x},\boldsymbol{\Omega}',E')d\Omega'dE'\\ + Q(\mathbf{x},\boldsymbol{\Omega},E)\psi^*(\mathbf{x},\boldsymbol{\Omega},E),\quad \mathbf{x}\in\mathcal{V},\ \boldsymbol{\Omega}\in 4\pi,\ 0<E<\infty,\end{aligned}\tag{5.7a}$$

with vacuum boundary condition

$$\psi^c(\mathbf{x},\boldsymbol{\Omega},E) = 0,\quad \mathbf{x}\in\partial\mathcal{V},\ \boldsymbol{\Omega}\cdot\mathbf{n}(\mathbf{x})<0,\ 0<E<\infty.\tag{5.7b}$$

This equation has the same transport features as the forward equation, except that the material-dependent parameters have been modified by the adjoint angular flux. In a Monte Carlo simulation, this equation describes most precisely how we would like to transport particles in phase space from the source to the detector in order achieve a Monte Carlo particle distribution that is proportional to the contributon flux; the weight window approach and the Transform approach both roughly accomplish this. The weight window approach does it by applying a specific weight window, while the transform does it by modifying the particle physics through the "transform" function.

Two characteristics of the forward contributon transport equation provide insight into some of the qualitative properties of the solution:

1. Forward contributons do not leak out of the system, due to an infinite effective total cross-section for contributons located on a boundary (i.e. $\mathbf{x}\in\partial\mathcal{V}$) and exiting the system (i.e. $\boldsymbol{\Omega}\cdot\mathbf{n}(\mathbf{x})>0$). For these $\mathbf{x}$ and $\boldsymbol{\Omega}$, the effective total cross-section in Eq. 5.7 can be written as

$$\begin{aligned}\Sigma_t(\mathbf{x},E) &- \boldsymbol{\Omega}\cdot\nabla\ln[\psi^*(\mathbf{x},\boldsymbol{\Omega},E)]\\ &= \frac{-\boldsymbol{\Omega}\cdot\nabla\psi^*(\mathbf{x},\boldsymbol{\Omega},E) + \Sigma_t(\mathbf{x},E)\psi^*(\mathbf{x},\boldsymbol{\Omega},E)}{\psi^*(\mathbf{x},\boldsymbol{\Omega},E)}\\ &= \frac{\int_0^\infty\int_{4\pi}\Sigma_s(\mathbf{x},\boldsymbol{\Omega}\cdot\boldsymbol{\Omega}',E\to E')\psi^*(\mathbf{x},\boldsymbol{\Omega}',E')d\Omega'dE' + Q^*(\mathbf{x},\boldsymbol{\Omega},E)}{\psi^*(\mathbf{x},\boldsymbol{\Omega},E)}\\ &\approx\infty,\quad \mathbf{x}\in\partial\mathcal{V},\ \boldsymbol{\Omega}\cdot\mathbf{n}(\mathbf{x})>0.\end{aligned}\tag{5.8}$$

   This result follows from substituting the right side of the adjoint neutron transport equation for the left side and applying the vacuum boundary condition. [We also notice that the effective total cross-section is never negative, because

the adjoint angular flux, scattering source, and fixed source are never negative.]

2. Forward contributons are removed from the system only in the detector region. This follows by examining the contributon absorption rate in an arbitrary spatial element dV about $\mathbf{x}$. The absorption rate $\mathcal{R}_{\text{abs}}(\mathbf{x})$ in dV about $\mathbf{x}$ is defined as

$$\begin{aligned}
&\mathcal{R}_{\text{abs}}(\mathbf{x})dV = \text{collision rate in } dV \text{ about } \mathbf{x} - \text{inscattering rate in } dV \text{ about } \mathbf{x} \\
&= \int_0^\infty \int_{4\pi} \left\{\Sigma_t(\mathbf{x}, E) - \mathbf{\Omega} \cdot \nabla \ln\left[\psi^*(\mathbf{x}, \mathbf{\Omega}, E)\right]\right\} \psi^{\text{c}}(\mathbf{x}, \mathbf{\Omega}, E) d\Omega dE \\
&- \int_0^\infty \int_{4\pi} \int_0^\infty \int_{4\pi} \Sigma_s(\mathbf{x}, \mathbf{\Omega}' \cdot \mathbf{\Omega}, E' \to E) \frac{\psi^*(\mathbf{x}, \mathbf{\Omega}, E)}{\psi^*(\mathbf{x}, \mathbf{\Omega}', E')} \psi^{\text{c}}(\mathbf{x}, \mathbf{\Omega}', E') d\Omega' dE' d\Omega dE \\
&= \int_0^\infty \int_{4\pi} \left\{ \frac{\int_0^\infty \int_{4\pi} \Sigma_s(\mathbf{x}, \mathbf{\Omega} \cdot \mathbf{\Omega}', E \to E') \psi^*(\mathbf{x}, \mathbf{\Omega}', E') d\Omega' dE'}{\psi^*(\mathbf{x}, \mathbf{\Omega}, E)} \right. \\
&\qquad \left. + \frac{Q^*(\mathbf{x}, \mathbf{\Omega}, E)}{\psi^*(\mathbf{x}, \mathbf{\Omega}, E)} \right\} \psi(\mathbf{x}, \mathbf{\Omega}, E) \psi^*(\mathbf{x}, \mathbf{\Omega}, E) d\Omega dE \\
&- \int_0^\infty \int_{4\pi} \int_0^\infty \int_{4\pi} \Sigma_s(\mathbf{x}, \mathbf{\Omega} \cdot \mathbf{\Omega}', E \to E') \psi^*(\mathbf{x}, \mathbf{\Omega}', E') \psi(\mathbf{x}, \mathbf{\Omega}, E) d\Omega dE d\Omega' dE' \\
&= \int_0^\infty \int_{4\pi} Q^*(\mathbf{x}, \mathbf{\Omega}, E) \psi(\mathbf{x}, \mathbf{\Omega}, E) dE d\Omega = \begin{cases} > 0, & \mathbf{x} \in \mathcal{V}_D \\ 0, & \mathbf{x} \notin \mathcal{V}_D \end{cases} . \qquad (5.9)
\end{aligned}$$

Since the detector is the only region with a positive absorption rate, contributons can only be removed from the system in the detector. Outside the detector, contributons undergo scattering events only.

Together, these two characteristics provide some insight into the qualitative form of the forward contributon solution. For the source-detector problem, we expect forward contributons to begin in the forward source region and "rattle around" the system until they are eventually removed in the detector. This results in a contributon flux that is largest along the optimal paths from the forward source to the detector. To best resolve the detector response or flux, it is desirable to distribute Monte Carlo particles in proportion to the contributon flux.

The adjoint formulation of the contributon transport equation is obtained by

substituting $\psi^* = \psi^c/\psi$ into Eq. 5.6. We obtain

$$
\begin{aligned}
-\mathbf{\Omega}\cdot\nabla\psi^c(\mathbf{x},\mathbf{\Omega},E) &+ \{\Sigma_t(\mathbf{x},E) + \mathbf{\Omega}\cdot\nabla\ln[\psi(\mathbf{x},\mathbf{\Omega},E)]\}\,\psi^c(\mathbf{x},\mathbf{\Omega},E) \\
&= \int_0^\infty\int_{4\pi}\Sigma_s(\mathbf{x},\mathbf{\Omega}\cdot\mathbf{\Omega}',E\to E')\frac{\psi(\mathbf{x},\mathbf{\Omega},E)}{\psi(\mathbf{x},\mathbf{\Omega}',E')}\psi^c(\mathbf{x},\mathbf{\Omega}',E')d\Omega' dE' \\
&+ Q^*(\mathbf{x},\mathbf{\Omega},E)\psi(\mathbf{x},\mathbf{\Omega},E), \quad \mathbf{x}\in\mathcal{V},\ \ \mathbf{\Omega}\in 4\pi,\ \ 0<E<\infty, \qquad (5.10a)
\end{aligned}
$$

with vacuum boundary condition

$$
\psi^c(\mathbf{x},\mathbf{\Omega},E) = 0, \quad \mathbf{x}\in\partial\mathcal{V},\ \ \mathbf{\Omega}\cdot\mathbf{n}(\mathbf{x})>0,\ \ 0<E<\infty. \qquad (5.10b)
$$

This equation has the same transport features as the adjoint transport equation, except that the material-dependent parameters have been modified by the forward angular flux. This equation describes a transport process that is very different from one typically used in a Monte Carlo simulation, since it describes the transport of adjoint contributons from the detector to the forward source region.

Since the objective of the weight window techniques and Transform approach is to distribute Monte Carlo particles according to the contributon flux, so this formulation provides a direct means to define an adjoint contributon source that achieves a favorable contributon distribution for the particular problem – response or flux. Specifically, since the adjoint neutron source comprises the adjoint contributon source (see Eq. 5.10) and is not defined by the problem statement, it can be chosen by the user to produce an appropriate contributon distribution. (Recall that the problem statement only specifies the forward neutron source, not the adjoint neutron source; thus, we are free to define it as we wish.) To see how the adjoint neutron source is selected, we first identify the adjoint contributon source in Eq. 5.10. It is given by the last term in the equation:

$$
Q^c(\mathbf{x},\mathbf{\Omega},E) = Q^*(\mathbf{x},\mathbf{\Omega},E)\psi(\mathbf{x},\mathbf{\Omega},E). \qquad (5.11)
$$

Then, the adjoint neutron source is defined as

$$
Q^*(\mathbf{x},\mathbf{\Omega},E) = \frac{Q^c(\mathbf{x},\mathbf{\Omega},E)}{\psi(\mathbf{x},\mathbf{\Omega},E)}, \qquad (5.12)
$$

where $Q^c(\mathbf{x},\mathbf{\Omega},E)$ has some user-specified properties. These properties depend on the type of problem – flux or response, which are discussed in subsequent sections.

The same two characteristics of the forward contributon transport equation exist

for the adjoint contributon transport equation:

1. Adjoint contributons do not leak out of the system due to an infinite effective total cross-section for contributons located on a boundary (i.e. $\mathbf{x} \in \partial\mathcal{V}$) and exiting the system (i.e. $\mathbf{\Omega} \cdot \mathbf{n}(\mathbf{x}) < 0$). For these $\mathbf{x}$ and $\mathbf{\Omega}$, the effective total cross-section in Eq. 5.10 can be written as

$$\begin{aligned}\Sigma_t(\mathbf{x}, E) + &\mathbf{\Omega} \cdot \nabla \ln\left[\psi(\mathbf{x}, \mathbf{\Omega}, E)\right] \\ &= \frac{\mathbf{\Omega} \cdot \nabla\psi(\mathbf{x}, \mathbf{\Omega}, E) + \Sigma_t(\mathbf{x}, E)\psi(\mathbf{x}, \mathbf{\Omega}, E)}{\psi(\mathbf{x}, \mathbf{\Omega}, E)} \\ &= \frac{\int_0^\infty \int_{4\pi} \Sigma_s(\mathbf{x}, \mathbf{\Omega}' \cdot \mathbf{\Omega}, E' \to E)\psi(\mathbf{x}, \mathbf{\Omega}', E')d\Omega' dE' + Q(\mathbf{x}, \mathbf{\Omega}, E)}{\psi(\mathbf{x}, \mathbf{\Omega}, E)} \\ &\approx \infty, \quad \mathbf{x} \in \partial\mathcal{V}, \;\; \mathbf{\Omega} \cdot \mathbf{n}(\mathbf{x}) < 0. \end{aligned} \tag{5.13}$$

   This result follows from substituting the right side of the forward neutron transport equation (Eq. 5.5) for the left side and applying the vacuum boundary condition. [We again note that the effective total cross-section is never negative, since the forward angular flux, scattering source, and fixed source are never negative.]

2. Adjoint contributons are removed from the system only in the forward source region. This follows by examining the contributon absorption rate in an arbitrary spatial element dV about $\mathbf{x}$. The absorption rate $\mathcal{R}_{\text{abs}}(\mathbf{x})$ in dV about $\mathbf{x}$ is defined as

   $\mathcal{R}_{\text{abs}}(\mathbf{x})dV =$ collision rate in dV about $\mathbf{x}$ $-$ inscattering rate in dV about $\mathbf{x}$

$$\begin{aligned} &= \int_0^\infty \int_{4\pi} \left\{\Sigma_t(\mathbf{x}, E) + \mathbf{\Omega} \cdot \nabla \ln\left[\psi(\mathbf{x}, \mathbf{\Omega}, E)\right]\right\} \psi^{\text{c}}(\mathbf{x}, \mathbf{\Omega}, E)d\Omega dE \\ &- \int_0^\infty \int_{4\pi} \int_0^\infty \int_{4\pi} \Sigma_s(\mathbf{x}, \mathbf{\Omega} \cdot \mathbf{\Omega}', E \to E') \frac{\psi(\mathbf{x}, \mathbf{\Omega}, E)}{\psi(\mathbf{x}, \mathbf{\Omega}', E')} \psi^{\text{c}}(\mathbf{x}, \mathbf{\Omega}', E')d\Omega' dE' d\Omega dE \end{aligned}$$

$$\begin{aligned} = \int_0^\infty \int_{4\pi} &\left\{ \frac{\int_0^\infty \int_{4\pi} \Sigma_s(\mathbf{x}, \mathbf{\Omega}' \cdot \mathbf{\Omega}, E' \to E)\psi(\mathbf{x}, \mathbf{\Omega}', E')d\Omega' dE'}{\psi(\mathbf{x}, \mathbf{\Omega}, E)} \right. \\ &\left. + \frac{Q(\mathbf{x}, \mathbf{\Omega}, E)}{\psi(\mathbf{x}, \mathbf{\Omega}, E)} \right\} \psi(\mathbf{x}, \mathbf{\Omega}, E)\psi^*(\mathbf{x}, \mathbf{\Omega}, E)d\Omega dE \\ - \int_0^\infty \int_{4\pi} \int_0^\infty \int_{4\pi} &\Sigma_s(\mathbf{x}, \mathbf{\Omega}' \cdot \mathbf{\Omega}, E' \to E)\psi(\mathbf{x}, \mathbf{\Omega}', E')\psi^*(\mathbf{x}, \mathbf{\Omega}, E)d\Omega dE d\Omega' dE' \end{aligned}$$

$$= \int_0^\infty \int_{4\pi} Q(\mathbf{x}, \mathbf{\Omega}, E)\psi^*(\mathbf{x}, \mathbf{\Omega}, E)dEd\Omega = \begin{cases} > 0, & \mathbf{x} \in \mathcal{V}_S, \\ = 0, & \mathbf{x} \notin \mathcal{V}_S, \end{cases} \tag{5.14}$$

where $\mathcal{V}_S$ is the forward source region. Since the forward source region is the only spatial region with a positive adjoint contributon absorption rate, these adjoint contributons can only be removed from the system in this region. Outside the forward source region, adjoint contributons undergo scattering events only.

Together, these two characteristics provide some insight into the qualitative form of the adjoint contributon solution. For the source-detector problem, we expect adjoint contributons to be born in the detector and "rattle around" the system until they are removed in the forward source region. This results in a contributon flux that is largest along the optimal paths from the detector to the forward source.

Although the forward and adjoint contributon equations do not share the same transport physics, they both produce the same solution: the contributon flux. In addition, they both emit source particles at the same rate: the forward contributon source emits forward contributons in the forward source region at the same rate that the adjoint contributon source emits adjoint contributons in the detector. This can be shown by integrating either the forward (or adjoint) contributon equation over space, angle and energy and substituting the equivalent expression for the effective total cross-section into the expression (see Eqs. 5.8, 5.9, 5.13, and 5.14 for examples of this substitution). This results in the classic relation between the forward and adjoint problem:

$$\int_{\mathcal{V}_S} \int_0^\infty \int_{4\pi} Q(\mathbf{x}, \mathbf{\Omega}, E)\psi^*(\mathbf{x}, \mathbf{\Omega}, E)d\Omega dEdV = \int_{\mathcal{V}_D} \int_0^\infty \int_{4\pi} Q^*(\mathbf{x}, \mathbf{\Omega}, E)\psi(\mathbf{x}, \mathbf{\Omega}, E)d\Omega dEdV. \tag{5.15}$$

Thus, two formulations of the contributon problem exist – forward and adjoint, result in the same solution, but are very different conceptually. *In this thesis, we use the adjoint contributon equation to define the adjoint neutron source and the forward contributon equation to describe the desired particle physics for an actual Monte Carlo simulation.*

In the next two sections, we describe the adjoint contributon source that is appropriate for the response problem and flux problem, respectively, and we describe how the Transform approach, our weight window, and FW-CADIS solves each of

these problems.

5.2 The Response Problem

As previously mentioned, in source-detector response problems we wish to obtain a single number – an energy-integrated response $\mathcal{R}_D$ in the detector region $\mathcal{V}_D$:

$$\mathcal{R}_D = \int_{\mathcal{V}_D} \int_0^\infty \int_{4\pi} \Sigma_{\mathcal{R}}(\mathbf{x}, E)\psi(\mathbf{x}, \mathbf{\Omega}, E)d\Omega dE dV. \tag{5.16}$$

For all three approaches – the Transform approach, our weight window, and FW-CADIS – we define the adjoint contributon source as:

$$Q^{\mathrm{c}}(\mathbf{x}, \mathbf{\Omega}, E) = \begin{cases} \Sigma_{\mathcal{R}}(\mathbf{x}, E)\psi(\mathbf{x}, \mathbf{\Omega}, E), & \text{for } \mathbf{x} \in \mathcal{V}_D, \\ 0, & \text{otherwise.} \end{cases} \tag{5.17}$$

This adjoint contributon source emits contributons (response particles) at a rate proportional to their relative contribution to the detector response in space, energy and angle. This results in a contributon distribution throughout phase-space that corresponds to the desired response.

The adjoint neutron source is determined from Eq. 5.12:

$$\begin{aligned} Q^*(\mathbf{x}, \mathbf{\Omega}, E) &= \frac{Q^{\mathrm{c}}(\mathbf{x}, \mathbf{\Omega}, E)}{\psi(\mathbf{x}, \mathbf{\Omega}, E)} \\ &= \begin{cases} \Sigma_{\mathcal{R}}(\mathbf{x}, E), & \text{for } \mathbf{x} \in \mathcal{V}_D, \\ 0, & \text{otherwise.} \end{cases} \end{aligned} \tag{5.18}$$

Historically, this is the adjoint source that is used to generate the standard weight window for the source-detector problem.

5.3 The Flux Problem

In source-detector flux problems, we wish to obtain the energy-dependent scalar flux $\phi(\mathbf{x}, E)$ in the detector region $\mathcal{V}_D$:

$$\phi(\mathbf{x}, E) = \int_{4\pi} \psi(\mathbf{x}, \mathbf{\Omega}, E)d\Omega. \tag{5.19}$$

Traditionally, the source-detector problem has focused on obtaining one value, the response. However, the methodology presented in this chapter provides no such

limitations.

Just as in the previous section on the response problem, the adjoint contributon source must be defined. For all three approaches – FW-CADIS, our weight window, and the Transform approach – the adjoint contributon source is defined as:

$$Q^{\mathrm{c}}(\mathbf{x}, \mathbf{\Omega}, E) = \begin{cases} \dfrac{\psi(\mathbf{x}, \mathbf{\Omega}, E)}{\phi(\mathbf{x}, E)}, & \text{for } \mathbf{x} \in \mathcal{V}_D, \\ 0, & \text{otherwise.} \end{cases} \tag{5.20}$$

At every spatial location $\mathbf{x}$ in the detector and for every energy E, this source emits contributons at a uniform rate (i.e. $Q^{\mathrm{c}}(\mathbf{x}, E) = \int_{4\pi} Q^{\mathrm{c}}(\mathbf{x}, \mathbf{\Omega}, E) d\Omega = 1$) with an angular distribution proportional to their contribution to the scalar flux. This corresponds to treating every spatial location $\mathbf{x} \in \mathcal{V}_D$ and energy E as equally relevant to the solution we seek – the energy-dependent scalar flux $\phi(\mathbf{x}, E)$.

The adjoint neutron source is determined from Eq. 5.12:

$$\begin{aligned} Q^{*}(\mathbf{x}, \mathbf{\Omega}, E) &= \frac{Q^{\mathrm{c}}(\mathbf{x}, \mathbf{\Omega}, E)}{\psi(\mathbf{x}, \mathbf{\Omega}, E)} \\ &= \begin{cases} \dfrac{1}{\phi(\mathbf{x}, E)}, & \text{for } \mathbf{x} \in \mathcal{V}_D, \\ 0, & \text{otherwise.} \end{cases} \end{aligned} \tag{5.21}$$

5.4 The Transform Approach

Now that the adjoint problem has been completely defined for the source-detector problem – flux or response, the Transform approach is easily implemented. The "transform" function that we use in this thesis is given by Eq. 4.104 as

$$\hat{\mathcal{T}}(\mathbf{x}, \mathbf{\Omega}, E) = \frac{B(\mathbf{x})}{\psi^{*}(\mathbf{x}, \mathbf{\Omega}, E)}. \tag{5.22}$$

This transform function produces a distribution proportional to the angular contributon flux, modified by the spatial parameter $B(\mathbf{x})$:

$$m(\mathbf{x}, \mathbf{\Omega}, E) = \frac{\psi^{\mathrm{c}}(\mathbf{x}, \mathbf{\Omega}, E)}{B(\mathbf{x})}. \tag{5.23}$$

The spatial parameter $B(\mathbf{x})$ achieves two things:

1. It flattens out the Monte Carlo particle flux in regions that have a concentration of Monte Carlo particles that is higher than in the detector. This effectively

forces particles out of regions, such as the forward source region, that are highly resolved statistically to other spatial regions that contribute to the detector response (or flux) but are less resolved.

2. It ensures that rapid changes in the Monte Carlo particle flux do not occur near the detector. This prevents excessive splitting and rouletting near the detector.

For problems in which the detector volume is "small" (at most a few mean free paths thick), the function $B(\mathbf{x})$ is set equal to unity. For detectors with a somewhat larger volume, yet still only a few mean free paths thick, the following expression is used:

$$B(\mathbf{x}) = \alpha(\mathbf{x})\tilde{\phi}^{\mathrm{c}}(\mathbf{x}) + 1 - \alpha(\mathbf{x}), \tag{5.24}$$

where

$$\tilde{\phi}^{\mathrm{c}}(\mathbf{x}) = \int_0^\infty \phi(\mathbf{x}, E)\tilde{\phi}^*(\mathbf{x}, E)dE, \tag{5.25}$$

$$\tilde{\phi}^*(\mathbf{x}, E) = \mathrm{C}_{\mathrm{norm}}\phi^*(\mathbf{x}, E), \tag{5.26}$$

$$\mathrm{C}_{\mathrm{norm}} = \left[\frac{1}{V_D}\int_{\mathcal{V}_D}\int_0^\infty \phi(\mathbf{x}, E)\phi^*(\mathbf{x}, E)dEdV\right]^{-1}, \tag{5.27}$$

$$\alpha(\mathbf{x}) = \left[1 + \mathrm{e}^{\left(\frac{\tilde{\phi}^{\mathrm{c}}_{\mathrm{max}\in\mathcal{V}_D}}{\tilde{\phi}^{\mathrm{c}}(\mathbf{x})} - \frac{\tilde{\phi}^{\mathrm{c}}(\mathbf{x})}{\tilde{\phi}^{\mathrm{c}}_{\mathrm{max}\in\mathcal{V}_D}}\right)}\right]^{-1}. \tag{5.28}$$

The function $\tilde{\phi}^{\mathrm{c}}(\mathbf{x})$ is a normalized approximation to the energy-integrated scalar contributon flux $\phi^{\mathrm{c}}(\mathbf{x})$. That is,

$$\begin{aligned}\tilde{\phi}^{\mathrm{c}}(\mathbf{x}) &= \mathrm{C}_{\mathrm{norm}}\int_0^\infty \phi(\mathbf{x}, E)\phi^*(\mathbf{x}, E)dE \\ &\approx 4\pi\mathrm{C}_{\mathrm{norm}}\int_0^\infty\int_{4\pi} \psi(\mathbf{x}, \mathbf{\Omega}, E)\psi^*(\mathbf{x}, \mathbf{\Omega}, E)d\Omega dE \\ &= 4\pi\mathrm{C}_{\mathrm{norm}}\phi^{\mathrm{c}}(\mathbf{x}).\end{aligned} \tag{5.29}$$

The normalization constant $\mathrm{C}_{\mathrm{norm}}$ scales the adjoint scalar flux to ensure that rapid changes in the Monte Carlo particle flux, resulting from splitting or Russian roulette, do not occur near the detector due to rapid changes in the spatial parameter $\alpha(\mathbf{x})$. To demonstrate this, we begin with Eq. 4.96:

$$\begin{aligned}\mathcal{M}(\mathbf{x},E) &= \frac{\phi^{\mathrm{c}}(\mathbf{x},E)}{B(\mathbf{x})} \\ &= \frac{\phi^{\mathrm{c}}(\mathbf{x},E)}{\alpha(\mathbf{x})\tilde{\phi}^{\mathrm{c}}(\mathbf{x})+1-\alpha(\mathbf{x})} \\ &\approx \phi^{\mathrm{c}}(\mathbf{x},E), \quad \text{for } \mathbf{x} \text{ near the detector.} \end{aligned} \tag{5.30}$$

The last statement follows if the detector is still relatively small. Then,

$$\begin{aligned}\tilde{\phi}^{\mathrm{c}}(\mathbf{x}) &= \mathrm{C}_{\mathrm{norm}} \int_0^\infty \phi(\mathbf{x},E)\phi^*(\mathbf{x},E)dE \\ &= \frac{\int_0^\infty \phi(\mathbf{x},E)\phi^*(\mathbf{x},E)dE}{\frac{1}{V_D}\int_{\mathcal{V}_D}\int_0^\infty \phi(\mathbf{x},E)\phi^*(\mathbf{x},E)dEdV} \qquad (5.31) \\ &\approx 1, \quad \text{for } \mathbf{x} \text{ near the detector.} \qquad (5.32)\end{aligned}$$

Finally, the spatial parameter $\alpha(\mathbf{x})$ is used to continuously adjust the distribution of the Monte Carlo particle flux $\mathcal{M}(\mathbf{x})$ from one that is proportional to the scalar contributon flux $\phi^{\mathrm{c}}(\mathbf{x})$ to one that is constant, depending on the magnitude of $\tilde{\phi}^{\mathrm{c}}(\mathbf{x})$ relative to the maximum value in the detector, $\tilde{\phi}^{\mathrm{c}}_{\mathrm{max}\in\mathcal{V}_D}$. This flattens the distribution of particles in regions, such as the forward source region, where the concentration of Monte Carlo particles may be higher than in the detector region. Effectively, this flattening forces particles into other spatial regions of the system that are less resolved statistically, and yet remain important to the detector response. To demonstrate this more clearly, let us consider what happens if $\tilde{\phi}^{\mathrm{c}}(\mathbf{x}) \ll \tilde{\phi}^{\mathrm{c}}_{\mathrm{max}\in\mathcal{V}_D}$ or $\tilde{\phi}^{\mathrm{c}}(\mathbf{x}) \gg \tilde{\phi}^{\mathrm{c}}_{\mathrm{max}\in\mathcal{V}_D}$. For $\alpha(\mathbf{x})$, this results in

$$\alpha(\mathbf{x}) = \begin{cases} 0, & \tilde{\phi}^{\mathrm{c}}(\mathbf{x}) \ll \tilde{\phi}^{\mathrm{c}}_{\mathrm{max}\in\mathcal{V}_D}, \\ 1, & \tilde{\phi}^{\mathrm{c}}(\mathbf{x}) \gg \tilde{\phi}^{\mathrm{c}}_{\mathrm{max}\in\mathcal{V}_D}. \end{cases} \tag{5.33}$$

Thus, $\alpha(\mathbf{x})$ is an exponential within the domain $[0,1]$. Using this result in Eq. 5.24, we obtain the limits of $B(\mathbf{x})$:

$$B(\mathbf{x}) = \begin{cases} 1, & \tilde{\phi}^{\mathrm{c}}(\mathbf{x}) \ll \phi^{\mathrm{c}}_{\mathrm{max}\in\mathcal{V}_D}, \\ \tilde{\phi}^{\mathrm{c}}(\mathbf{x}), & \tilde{\phi}^{\mathrm{c}}(\mathbf{x}) \ll \tilde{\phi}^{\mathrm{c}}_{\mathrm{max}\in\mathcal{V}_D}. \end{cases} \tag{5.34}$$

Finally, the Monte Carlo particle flux at the limits is obtained using Eq. 4.96:

$$\mathcal{M}(\mathbf{x}) = \begin{cases} \phi^{\mathrm{c}}(\mathbf{x}), & \tilde{\phi}^{\mathrm{c}}(\mathbf{x}) \ll \tilde{\phi}^{\mathrm{c}}_{\max\in\mathcal{V}_D}, \\ (4\pi \mathrm{C}_{\mathrm{norm}})^{-1}, & \tilde{\phi}^{\mathrm{c}}(\mathbf{x}) \gg \tilde{\phi}^{\mathrm{c}}_{\max\in\mathcal{V}_D}. \end{cases} \tag{5.35}$$

where we have used the approximation given by Eq. 5.29 to derive the result for $\tilde{\phi}^{\mathrm{c}}(\mathbf{x}) \gg \tilde{\phi}_{\max\in\mathcal{V}_D}$. Thus, $B(\mathbf{x})$ normalizes the Monte Carlo particle flux to be flat in spatial regions that would have a higher Monte Carlo particle flux than in the detector if $B(\mathbf{x})$ were equal to unity everywhere and to be proportional to the contributon flux in areas where fewer particles exist than within the detector. Effectively, this forces Monte Carlo particles to disperse from highly concentrated (resolved) regions to those that have fewer particles but still contribute to the detector response (or flux).

As noted earlier, for detectors that are smaller than the forward source region, $B(\mathbf{x}) = 1$. Under this condition (i.e. $V_D < V_S$), we expect that the form of $B(\mathbf{x})$ given by Eq. 5.24 should limit to unity. To see this, we recall that contributons are emitted and removed from the system only in the forward source region and the detector. Thus, we expect the concentration of contributons to be largest in these regions. To get a measure of the contributon flux in the detector and forward source regions, we consider the average contributon generation rate in each. We define:

$$\begin{aligned} \bar{Q}^{\mathrm{c}}_D &= \text{average adjoint contributon source rate in the detector} \\ &= \frac{1}{V_D} \int_{\mathcal{V}_D} \int_0^\infty \int_{4\pi} Q^*(\mathbf{x}, \mathbf{\Omega}, E) \psi(\mathbf{x}, \mathbf{\Omega}, E) d\Omega dE dV, \end{aligned} \tag{5.36}$$

$$\begin{aligned} \bar{Q}^{\mathrm{c}}_S &= \text{average forward contributon source rate in the forward source region} \\ &= \frac{1}{V_S} \int_{\mathcal{V}_S} \int_0^\infty \int_{4\pi} Q(\mathbf{x}, \mathbf{\Omega}, E) \psi^*(\mathbf{x}, \mathbf{\Omega}, E) d\Omega dE dV. \end{aligned} \tag{5.37}$$

Then, using the classic relation given in Eq. 5.15, the ratio of the average generation rate of contributons in the forward source region to the average generation rate in the detector is given by:

$$\frac{\bar{Q}^{\mathrm{c}}_S}{\bar{Q}^{\mathrm{c}}_D} = \frac{V_D}{V_S}. \tag{5.38}$$

This relation indicates that if the forward source region is smaller than the detector region, there will be a higher concentration of contributons in the forward source region than in the detector region, and vice versa for a forward source region that is larger than the detector. Thus, for the case $V_D < V_S$, we expect $\tilde{\phi}^{\mathrm{c}}(\mathbf{x}) < \tilde{\phi}^{\mathrm{c}}_{\max\in\mathcal{V}_D}$ for

all $\mathbf{x} \in \mathcal{V}$, which results in $\alpha(\mathbf{x}) \rightarrow 0$, or $B(\mathbf{x}) = 1$.

Finally, since $B(\mathbf{x})$ is obtained from a deterministic calculation, we describe the discretized form of this function. Consistent with the discretization notation, we use the script subscript c to represent a cell defined by the spatial element $\mathcal{V}_c$. The superscript c continues to identify the contributon flux. Using this nomenclature, $B(\mathbf{x})$ is defined as follows:

$$\begin{aligned} B(\mathbf{x}) &= B_c, \quad \mathbf{x} \in \mathcal{V}_c \\ &= \alpha_c \tilde{\phi}_c^{\mathrm{c}} + 1 - \alpha_c, \end{aligned} \tag{5.39}$$

where

$$\phi_c^{\mathrm{c}} = \mathrm{C}_{\mathrm{norm}} \sum_{g=1}^{G} \phi_{c,g} \phi_{c,g}^*, \tag{5.40}$$

$$\mathrm{C}_{\mathrm{norm}} = \left[\frac{1}{V_D} \sum_{c:\, \mathcal{V}_c \subseteq \mathcal{V}_D} \sum_{g=1}^{G} \phi_{c,g} \phi_{c,g}^* \right]^{-1}, \tag{5.41}$$

$$\alpha_c = \left[1 + \mathrm{e}^{\left(\frac{\tilde{\phi}_{\max \in \mathcal{V}_D}^{\mathrm{c}}}{\tilde{\phi}_c^{\mathrm{c}}} - \frac{\tilde{\phi}_c^{\mathrm{c}}}{\tilde{\phi}_{\max \in \mathcal{V}_D}^{\mathrm{c}}} \right)} \right]^{-1}. \tag{5.42}$$

The "transform" function has now been completely defined for the source-detector problem and can be used as described in Section 4.3 to implement the Transform approach.

5.5 Our Weight Window

In Section 4.2.1, we found that the weight window center $\mathrm{w}(\mathbf{x}, E)$ and the scalar Monte Carlo particle flux $\mathcal{M}(\mathbf{x}, E)$ are related by Eq. 4.9:

$$\mathrm{w}(\mathbf{x}, E) = \frac{\phi(\mathbf{x}, E)}{\mathcal{M}(\mathbf{x}, E)}. \tag{5.43}$$

For the source-detector flux or response problem, our weight window is used to distribute Monte Carlo particles according to the scalar contributon flux distribution, with the same modification used for the Transform approach, i.e. $B(\mathbf{x})$. We define

the Monte Carlo particle flux as

$$\mathcal{M}(\mathbf{x}, E) = \frac{\phi^{\mathrm{c}}(\mathbf{x}, E)}{B(\mathbf{x})}, \tag{5.44}$$

where the spatial parameter $B(\mathbf{x})$ was described in detail in the previous section on the Transform approach (Eq. 5.24). Then, the weight window is approximated as

$$\begin{aligned} \mathrm{w}(\mathbf{x}, E) &= \frac{B(\mathbf{x})\phi(\mathbf{x}, E)}{\phi^{\mathrm{c}}(\mathbf{x}, E)} \\ &\approx \frac{B(\mathbf{x})}{\phi^{*}(\mathbf{x}, E)}, \end{aligned} \tag{5.45}$$

where we approximate the scalar contributon flux $\phi^{\mathrm{c}}(\mathbf{x}, E)$ as

$$\phi^{\mathrm{c}}(\mathbf{x}, E) \approx \phi(\mathbf{x}, E)\phi^{*}(\mathbf{x}, E). \tag{5.46}$$

This weight window should produce a scalar Monte Carlo particle flux similar to that of the Transform approach, but without modifying any of the particle physics. The spatial parameter $B(\mathbf{x})$ accomplishes the same objectives here as it did before:

1. It flattens out the Monte Carlo particle flux $\mathcal{M}(\mathbf{x})$ in regions that have a concentration of Monte Carlo particles that is higher than in the detector, effectively forcing particles out of regions that are highly resolved statistically to other regions that contribute to the detector response but are less resolved.

2. It again ensures that rapid changes in the Monte Carlo particle flux do not occur near the detector due to rapid changes of the spatial parameter $\alpha(\mathbf{x})$ (see Eq. 5.24). This prevents excessive splitting and rouletting near the detector.

With our weight window completely defined for the source-detector problem, it can be implemented according to the specifications given in the general section on weight windows, Section 4.2.

5.6 FW-CADIS

For the source-detector problem, FW-CADIS reduces to the classical weight window, where the weight window is inversely proportional to the adjoint scalar flux:

$$\mathrm{w}(\mathbf{x}, E) = \frac{1}{\phi^{*}(\mathbf{x}, E)}. \tag{5.47}$$

According to Eq. 4.8 given in Section 4.2.1, this weight window results in a Monte Carlo particle flux that is approximately proportional to the scalar contributon flux:

$$\begin{aligned}\mathcal{M}(\mathbf{x}, E) &= \frac{\phi(\mathbf{x}, E)}{\mathrm{w}(\mathbf{x}, E)} \\ &= \phi(\mathbf{x}, E)\phi^*(\mathbf{x}, E) \\ &\approx \phi^{\mathrm{c}}(\mathbf{x}, E). \end{aligned} \tag{5.48}$$

As mentioned in Chapter IV, it is not clear from the literature whether Monte Carlo practitioners using this weight window have been aware that it distributes Monte Carlo particles according to the scalar contributon flux.

As with our weight window, all the details necessary to implement the FW-CADIS weight window are in Section 4.2.

5.7 Numerical Test Problem

To verify that the methods perform as the theory predicts, and to compare the methods for efficiency and statistical quality, we consider a relatively simple multi-group problem that 1) assesses how well the approaches perform on a multigroup shielding problem, and 2) verifies that the methods perform as the theory predicts. Specifically, we consider a homogeneous 3-group cube with a localized source in the center that emits particles in the top energy group.

5.7.1 Problem Description

For this homogenous 3-group problem, the geometry is chosen to be a 50 cm homogeneous cube with a 2 cm cubic source at its center and vacuum boundaries. Because this problem is symmetric, we only need to obtain a solution in one octant; we do this by imposing symmetric (reflecting) boundaries that pass through the center of the source. Figure 5.1 demonstrates this geometry: a 25 cm homogeneous cube with a 1 cm cubic source in the corner, symmetric boundary conditions at the planes that cut through the source, and vacuum boundaries at the exterior planes. The source is a unit source (1 $\mathrm{cm}^{-3}\mathrm{s}^{-1}$), in the first energy group only. The total cross-section is set equal to unity throughout space and energy (i.e. $\Sigma_{t,g} = 1\ \mathrm{cm}^{-1}$). The scattering matrix is provided in the material data table of Figure 5.1.

To make this problem a true source-detector problem, we placed a 1 cm cubic detector near the furthest corner from the source, 1.5 cm from all three vacuum

boundaries. The detector was not placed directly on the boundary of the system to avoid edge effects, specifically those resulting from being incapable of completely capturing the property of contributons on the boundary – no leakage due to an infinite effective total cross-section (see Section 5.1).

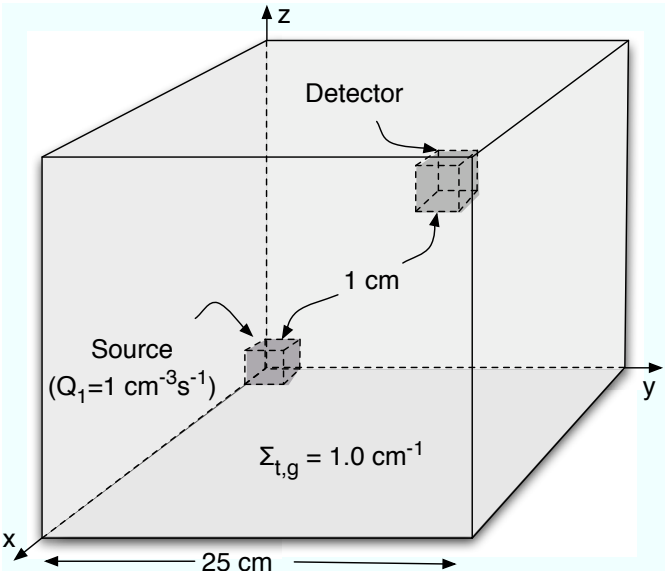

Data \ g	1	2	3
$\Sigma_{t,g}\,(cm^{-1})$	1.0	1.0	1.0
$\Sigma_{s,g\to1}\,(cm^{-1})$	0.6	0.0	0.0
$\Sigma_{s,g\to2}\,(cm^{-1})$	0.1	0.7	0.0
$\Sigma_{s,g\to3}\,(cm^{-1})$	0.05	0.1	0.8
$Q_g\,(cm^{-3}s^{-1})$	1.0	0.0	0.0

Figure 5.1: Problem Geometry and Material Properties

Figure 5.2 demonstrates that this problem is indeed a shielding problem, with the scalar flux being attenuated by 20 orders of magnitude in the first energy group, 18 orders of magnitude in the second group, nearly 16 orders of magnitude in the third group, and roughly 17 orders of magnitude in the energy-integrated (total) flux. As can be seen in Figure 5.2, the total flux is composed mostly of group-1 flux near the source and mostly of group-3 flux near the detector.

The objective of the source-detector flux problem is to obtain scalar flux $\phi_{D,g}$ for all g in the detector, where $\phi_{D,g}$ is defined as

$$\phi_{D,g} = \frac{1}{V_D}\int_{\mathcal{V}_D}\int_{E_g}^{E_{g-1}} \phi(\mathbf{x}, E)dEdV. \tag{5.49}$$

The objective of the source-detector response problem is to obtain the response $\mathcal{R}_D$ in the detector. We investigate a special response, the energy-integrated (total) flux, denoted simply as ϕ_D and defined as

$$\phi_D = \sum_{g=1}^{3} \phi_{D,g}. \tag{5.50}$$

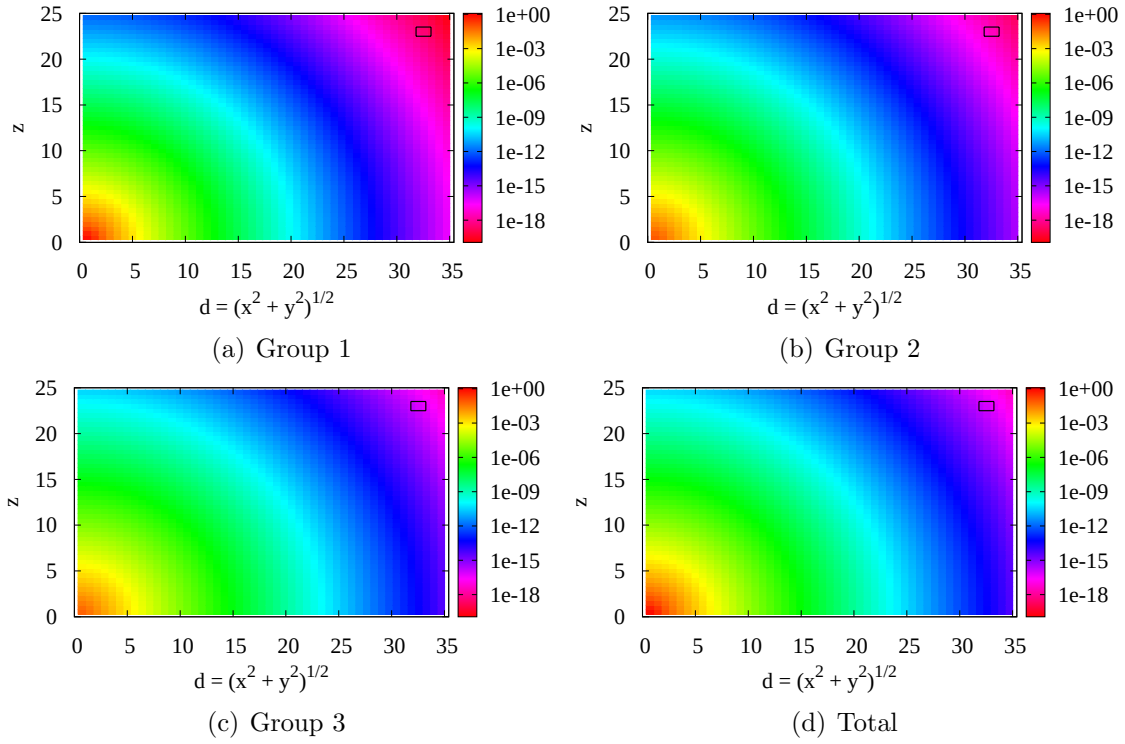

(a) Group 1 (b) Group 2

(c) Group 3 (d) Total

Figure 5.2: Scalar Flux along the plane $x = y$

(For this response, we set $\Sigma_{\mathcal{R}}(\mathbf{x}, E) = 1$.) To analyze the results, we plot the figure of merit, the simulated scalar Monte Carlo particle flux, and the theoretically predicted scalar Monte Carlo particle flux for the second energy group and the total flux. These plots appear in Figures 5.3 - 5.14 and consist of a 2D plane that stretches from the z-axis to the cube edge farthest from the source (i.e. the plane $x = y$) and the line from the source corner to the detector corner (i.e. the line $x = y = z$). These values are computed on a uniform 0.5 cm grid that is imposed on the problem geometry. Thus, the system consists of 125,000 spatial elements, each denoted by $\mathcal{V}_c$. (The source and detector each consist of eight spatial elements.)

The energy-dependent scalar Monte Carlo particle flux $\mathcal{M}_{c,g}$ and the energy-integrated scalar Monte Carlo particle flux $\mathcal{M}_c$ are volume-averaged quantities determined directly from the Monte Carlo simulation. The figures of merit (FOM) in each spatial element $\mathcal{V}_c$ are defined as

$$\mathrm{FOM}_{c,g} = \frac{1}{\dfrac{\mathrm{Var}\left[\phi_{c,g}\right]}{\phi_{c,g}^2}\mathrm{T}_{\mathrm{cpu}}},$$

$$\mathrm{FOM}_c = \frac{1}{\frac{\mathrm{Var}\left[\phi_c\right]}{\phi_c^2}\mathrm{T}_{\mathrm{cpu}}}, \tag{5.51}$$

where $\mathrm{T}_{\mathrm{cpu}}$ is the total run time, and $\phi_{c,g}$, ϕ_c, and the corresponding variances are volume-averaged quantities obtained directly from the Monte Carlo simulation.

The theoretically predicted energy-dependent scalar Monte Carlo particle flux $\tilde{M}_{c,g}$ averaged over $\mathcal{V}_c$ is given for each method as:

$$\tilde{\mathcal{M}}_{c,g}^{\mathrm{XFORM}} \approx \mathrm{C}_0 \frac{\phi_{c,g}\Phi_{c,g}^*}{B_c}, \tag{5.52}$$

$$\tilde{\mathcal{M}}_{c,g}^{\mathrm{WW}} = \mathrm{C}_0 \frac{\phi_{c,g}\Phi_{c,g}^*}{B_c}, \tag{5.53}$$

$$\tilde{\mathcal{M}}_{c,g}^{\mathrm{FWCADIS}} = \mathrm{C}_0 \phi_{c,g}\Phi_{c,g}^*, \tag{5.54}$$

where XFORM identifies the Transform approach, WW identifies our weight window, and FWCADIS identifies the FW-CADIS weight window. To remain consistent with the Monte Carlo particle flux resulting from the weight window, the Monte Carlo estimate of the forward scalar flux $\phi_{c,g}$ is treated as the "exact" forward scalar flux, and the deterministic estimate of the adjoint scalar flux $\Phi_{c,g}^*$ is used since it corresponds to the weight window. The Transform approach scalar flux estimate is an approximation of the scalar Monte Carlo flux produced by the Transform approach:

$$\begin{aligned}\mathcal{M}(\mathbf{x}, E) &= \frac{\int_{4\pi} \psi(\mathbf{x}, \mathbf{\Omega}, E)\psi^*(\mathbf{x}, \mathbf{\Omega}, E)d\Omega}{B(\mathbf{x})} \\ &\approx \mathrm{C}_0 \frac{\phi(\mathbf{x}, E)\phi^*(\mathbf{x}, E)}{B(\mathbf{x})}.\end{aligned} \tag{5.55}$$

For all three approaches, the theoretically predicted energy-integrated scalar Monte Carlo particle flux $\tilde{\mathcal{M}}_c$ is given as:

$$\tilde{\mathcal{M}}_c = \sum_{g=1}^{3} \tilde{\mathcal{M}}_{c,g}. \tag{5.56}$$

For both the response problem and flux problem, the energy-dependent scalar flux $\phi_{c,g}$ and the total scalar flux ϕ_c are tallied, even though the flux problem is tailored to obtain just $\phi_{c,g}$ and the response problem is tailored to obtain ϕ_c. To see the difference between the flux problem and the response problem, we examine the data in a representative energy group – the second group – and the data for the total

flux. We expect that the methods tailored to the flux problem will produce better statistical results for the second energy group, while those tailored to the response (total flux) problem will produce better statistical results for the total flux data.

5.7.2 Numerical Results

The group-2 data for the flux problem is presented in Figures 5.3 - 5.5, including the figure of merit, the simulated Monte Carlo particle flux, and the theoretically predicted Monte Carlo particle flux; the corresponding group-2 data for the response (total flux) problem appears in Figures 5.6 - 5.8. Likewise, the total flux data for the flux problem is presented in Figures 5.9 - 5.11 and the corresponding data for the response problem appears in Figures 5.12 - 5.14. For clarity, all the 2D figures have a black rectangle in the upper right corner to denote the detector region and a dashed line tracing out the diagonal from the source to the detector (i.e. the line $x = y = z$). The 1D figures are plots along this line with dashed vertical lines indicating the detector location. Table 5.1 and Table 5.2 provide the detector FOM and the simulated Monte Carlo particle flux, respectively, for each energy group and for all methods and problems.

Table 5.1: Detector FOM for all methods and all groups

Problem	**Method**	**FOM**			
		Group 1	**Group 2**	**Group 3**	**Total**
Flux ($\phi_{D,g}$)	**FW-CADIS**	0.502	0.949	2.043	2.204
	WW	0.496	0.989	2.125	2.308
	XFORM	6.752	6.246	7.720	8.443
Response (ϕ_D)	**FW-CADIS**	0.015	0.204	4.556	4.674
	WW	0.015	0.216	4.816	4.942
	XFORM	0.125	1.344	23.22	24.53

The data in Table 5.1 indicates that the Transform approach performs more efficiently in every energy group for both the flux problem and the response problem. For the flux problem, in which we wish to obtain statistical results in every energy group, the Transform approach FOM is 13 times greater than that of the weight window approaches in the first energy group, over 6 times greater in the second energy group, nearly 4 times greater in the third energy group, and nearly 4 times greater for the total flux. For the response problem, in which we wish to optimize the calculation to obtain the total flux, the Transform approach FOM is over 8 times greater than that of the weight window approaches in the first energy group, over 6

Table 5.2: Detector simulated MC particle flux for all methods and all groups

Problem	Method	Simulated MC Particle Flux			
		Group 1	Group 2	Group 3	Total
Flux ($\phi_{D,g}$)	FW-CADIS	0.020	0.015	0.020	0.055
	WW	0.038	0.029	0.039	0.106
	XFORM	0.111	0.081	0.100	0.293
Response (ϕ_D)	FW-CADIS	0.00016	0.0018	0.047	0.049
	WW	0.00035	0.0040	0.104	0.108
	XFORM	0.00127	0.0134	0.253	0.266

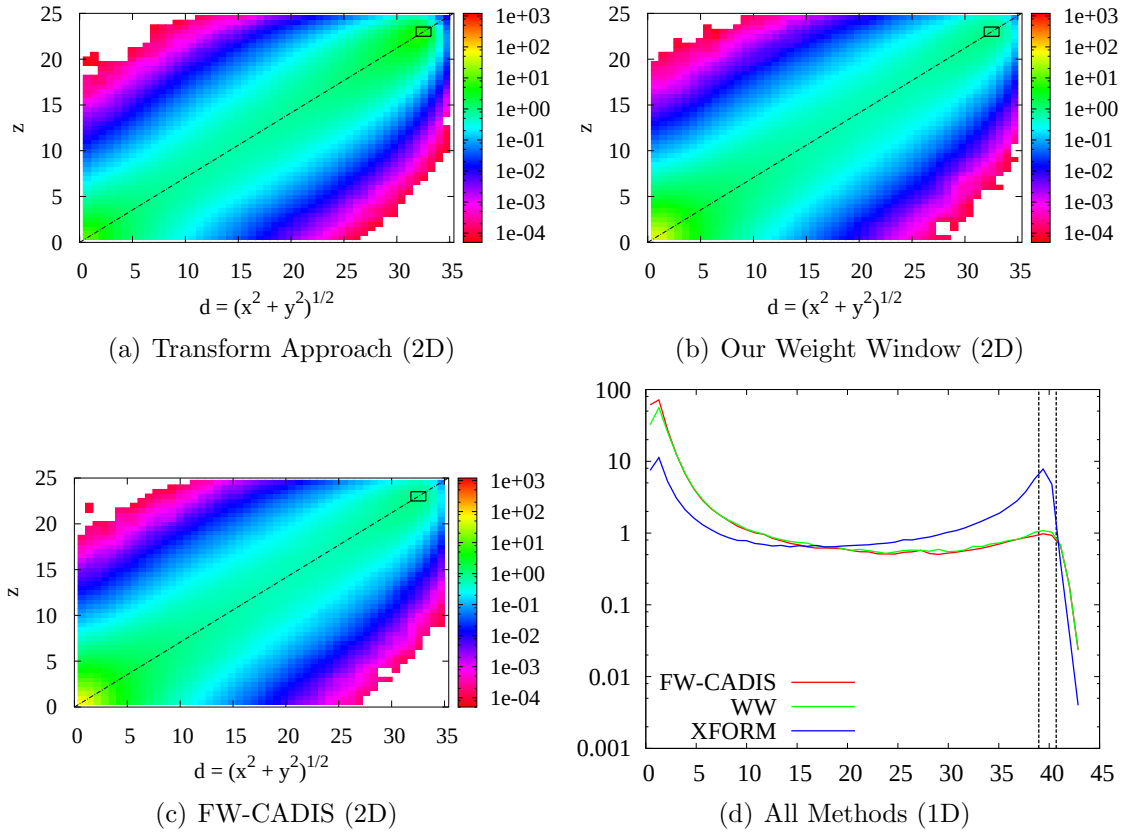

(a) Transform Approach (2D)

(b) Our Weight Window (2D)

(c) FW-CADIS (2D)

(d) All Methods (1D)

Figure 5.3: Group 2 FOM for Source-Detector (SD) Flux Problem

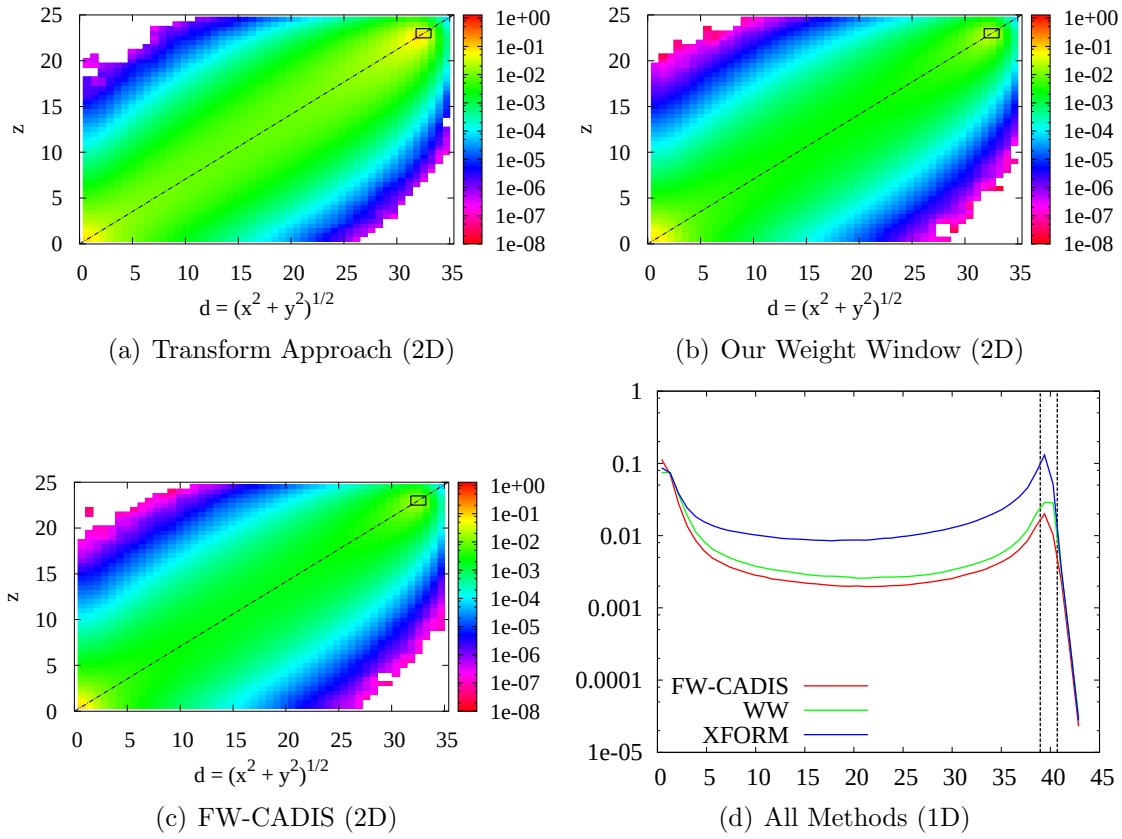

(a) Transform Approach (2D)

(b) Our Weight Window (2D)

(c) FW-CADIS (2D)

(d) All Methods (1D)

Figure 5.4: Group 2 Simulated MC Particle Flux for SD Flux Problem

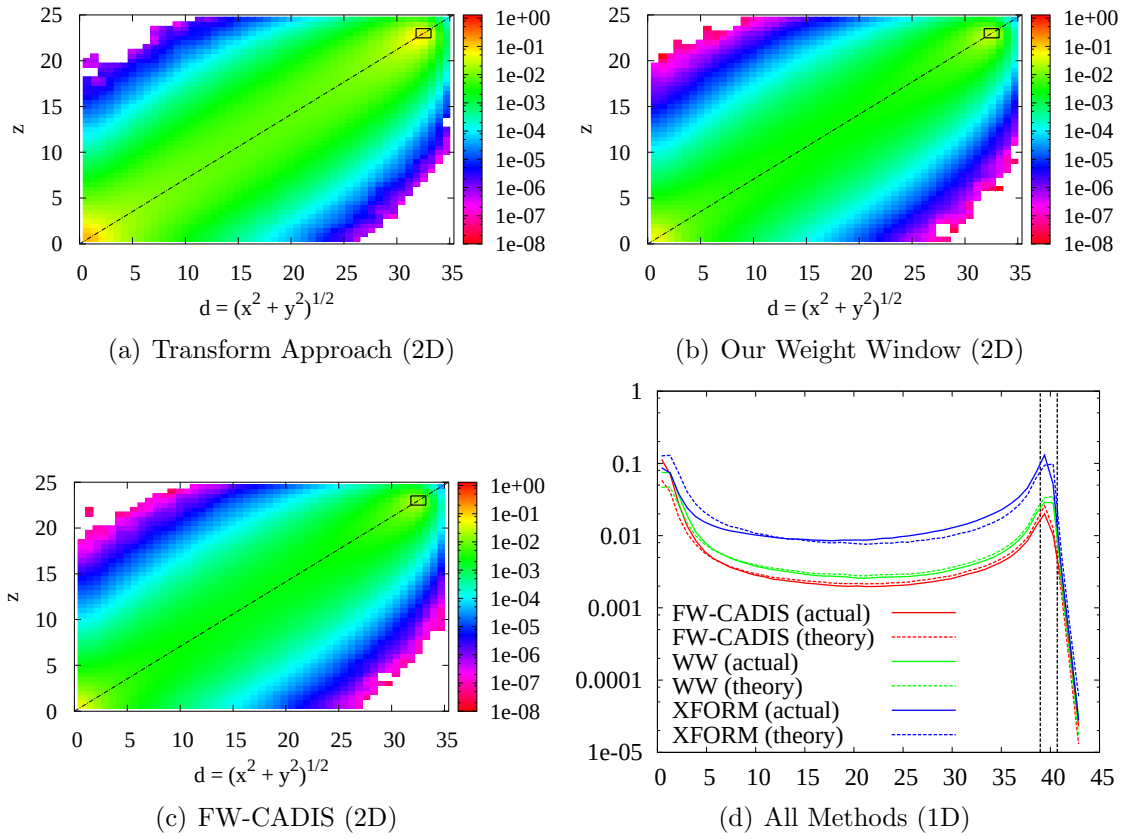

(a) Transform Approach (2D)

(b) Our Weight Window (2D)

(c) FW-CADIS (2D)

(d) All Methods (1D)

Figure 5.5: Group 2 Predicted MC Particle Flux for SD Flux Problem

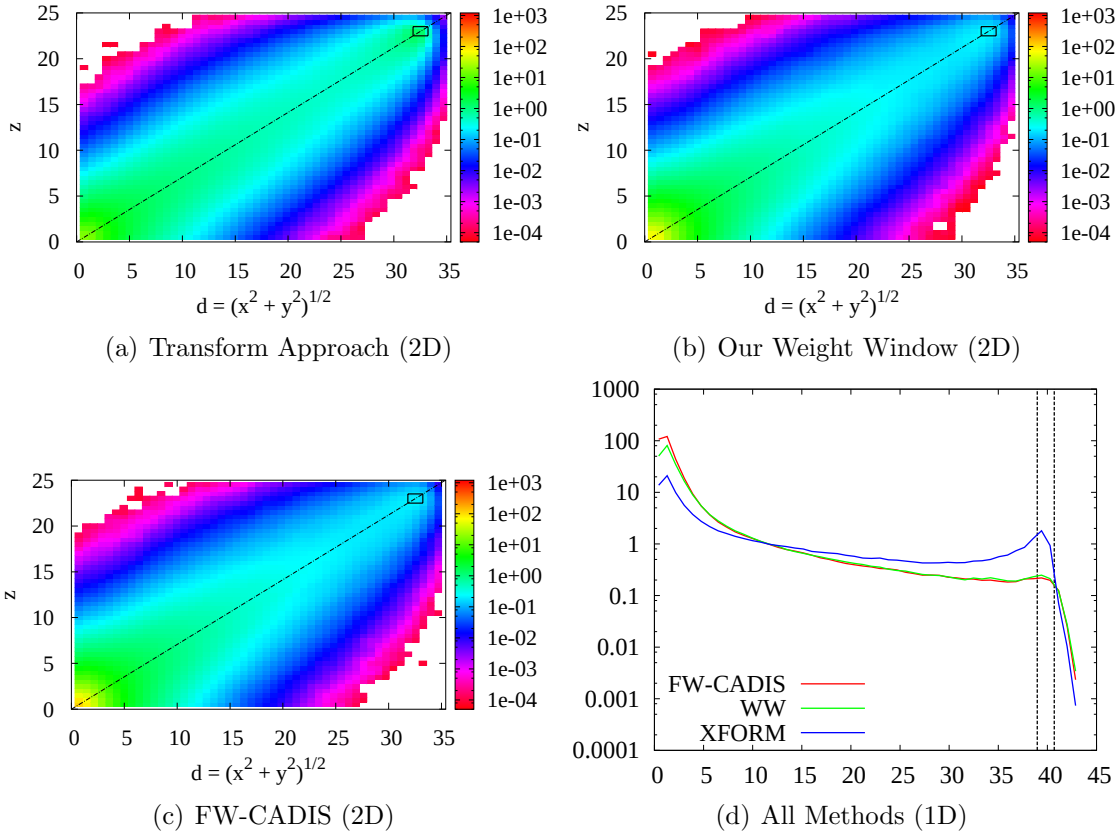

(a) Transform Approach (2D)

(b) Our Weight Window (2D)

(c) FW-CADIS (2D)

(d) All Methods (1D)

Figure 5.6: Group 2 FOM for SD Response Problem

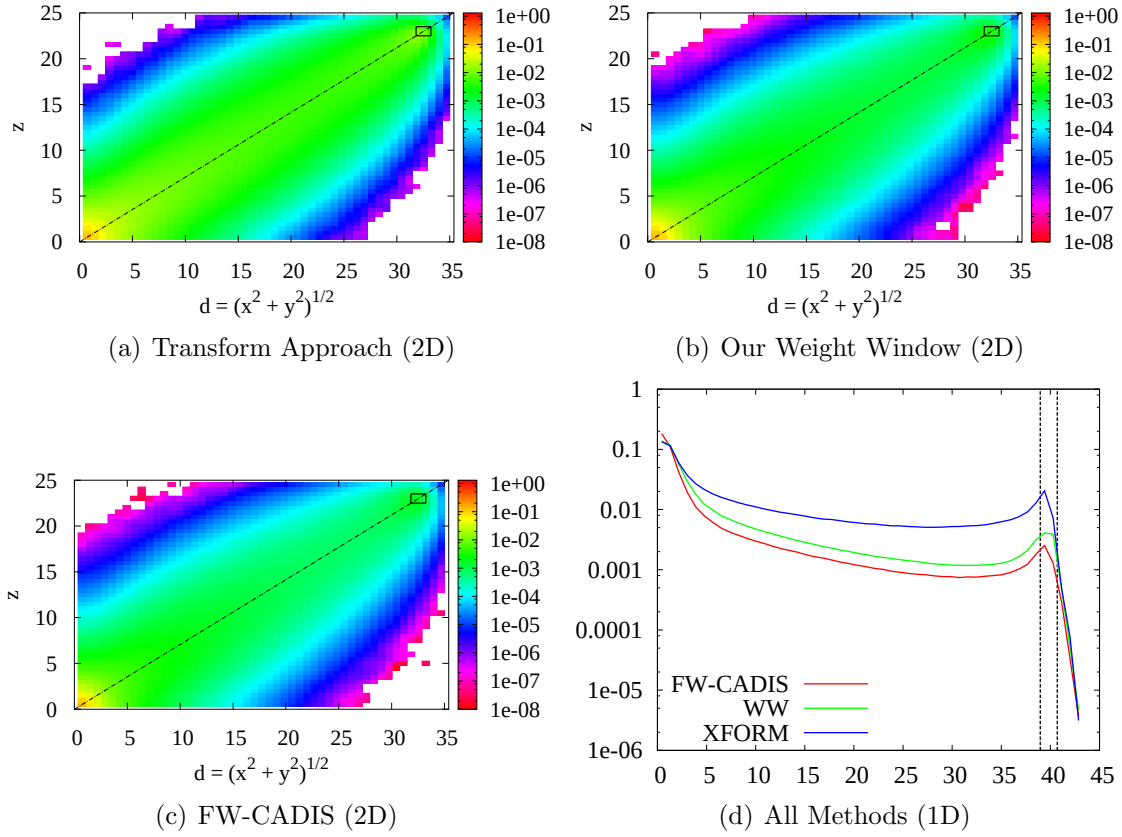

(a) Transform Approach (2D)

(b) Our Weight Window (2D)

(c) FW-CADIS (2D)

(d) All Methods (1D)

Figure 5.7: Group 2 Simulated MC Particle Flux for SD Response Problem

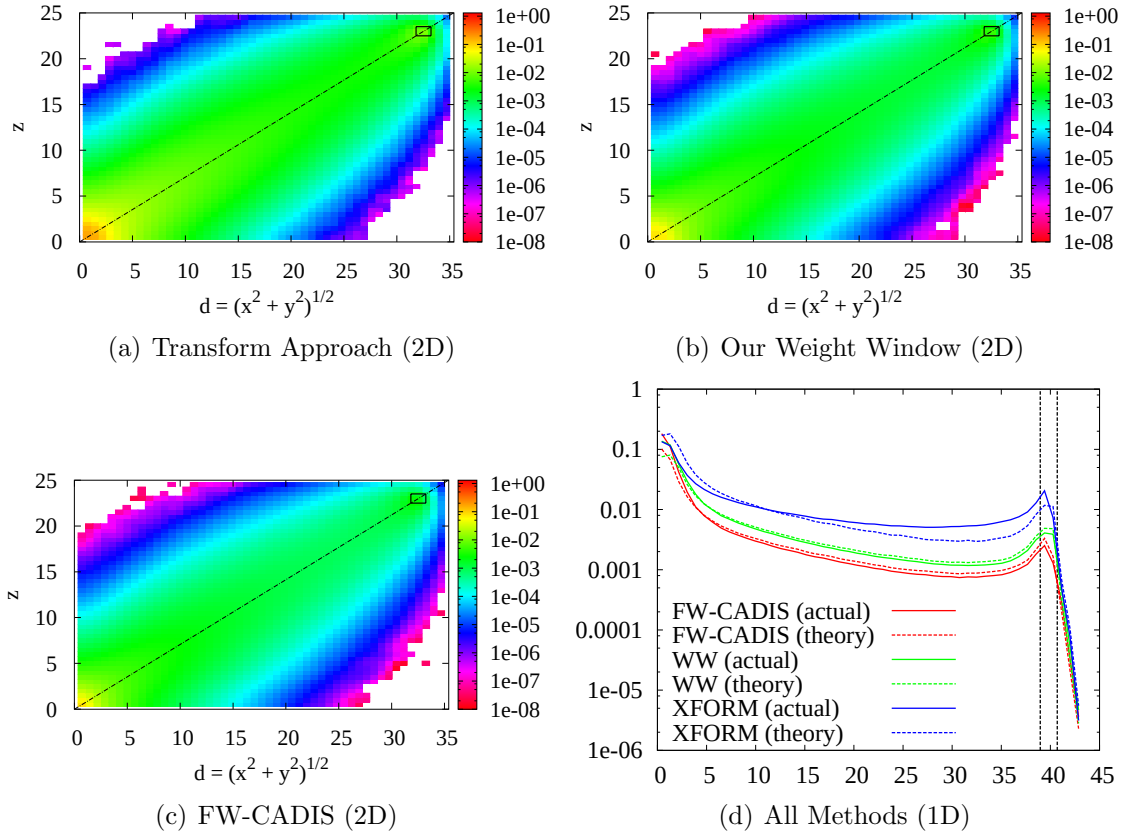

(a) Transform Approach (2D)

(b) Our Weight Window (2D)

(c) FW-CADIS (2D)

(d) All Methods (1D)

Figure 5.8: Group 2 Predicted MC Particle Flux for SD Response Problem

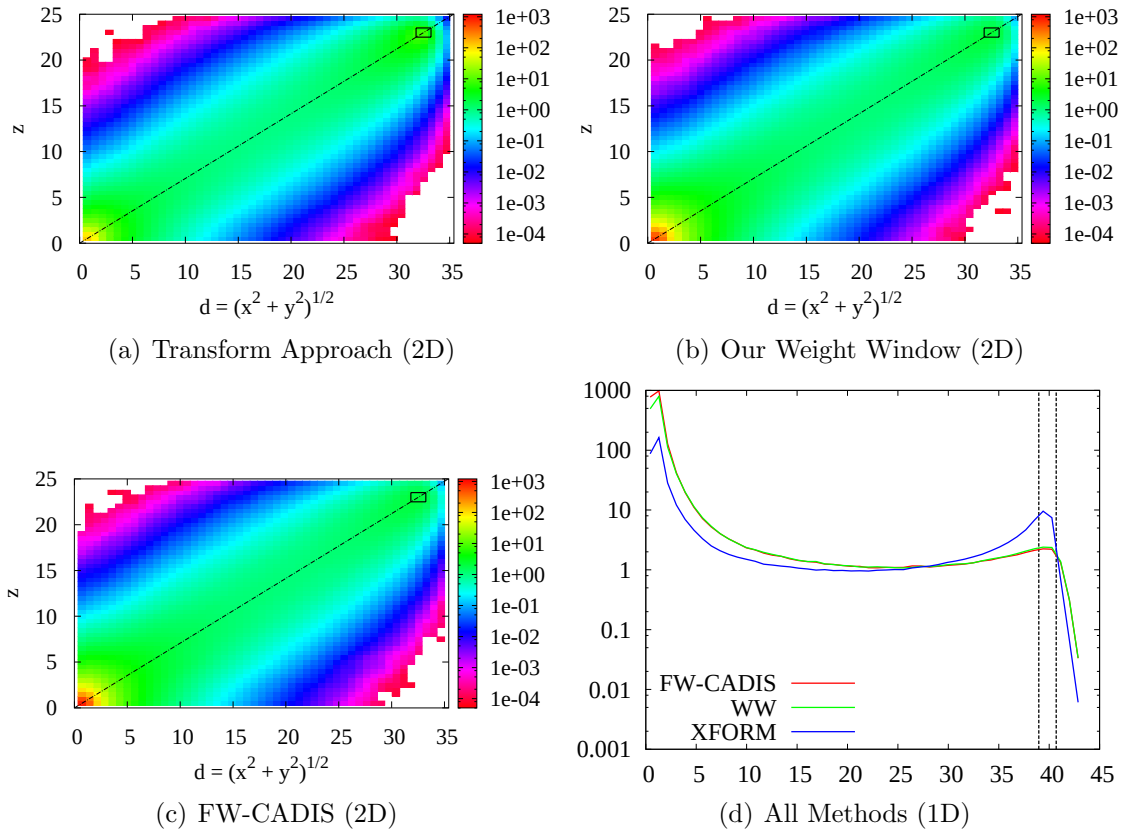

(a) Transform Approach (2D)

(b) Our Weight Window (2D)

(c) FW-CADIS (2D)

(d) All Methods (1D)

Figure 5.9: Total FOM for SD Flux Problem

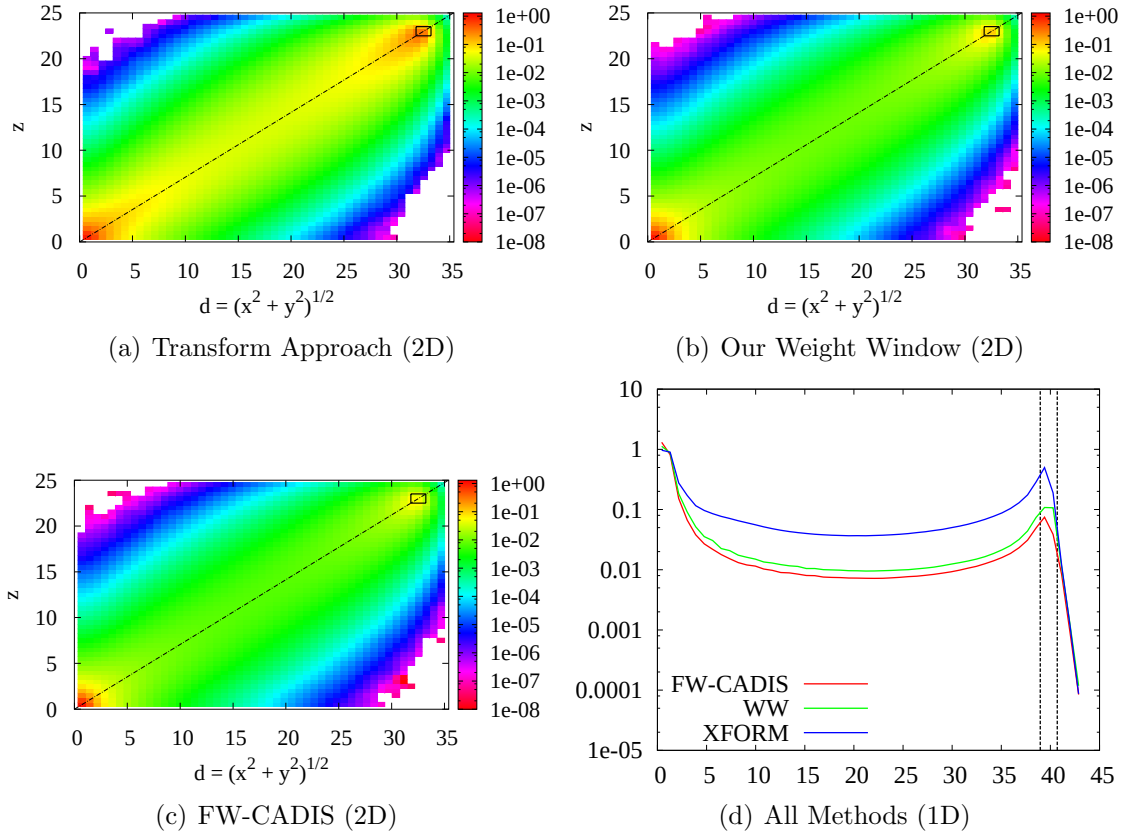

(a) Transform Approach (2D)

(b) Our Weight Window (2D)

(c) FW-CADIS (2D)

(d) All Methods (1D)

Figure 5.10: Total Simulated MC Particle Flux for SD Flux Problem

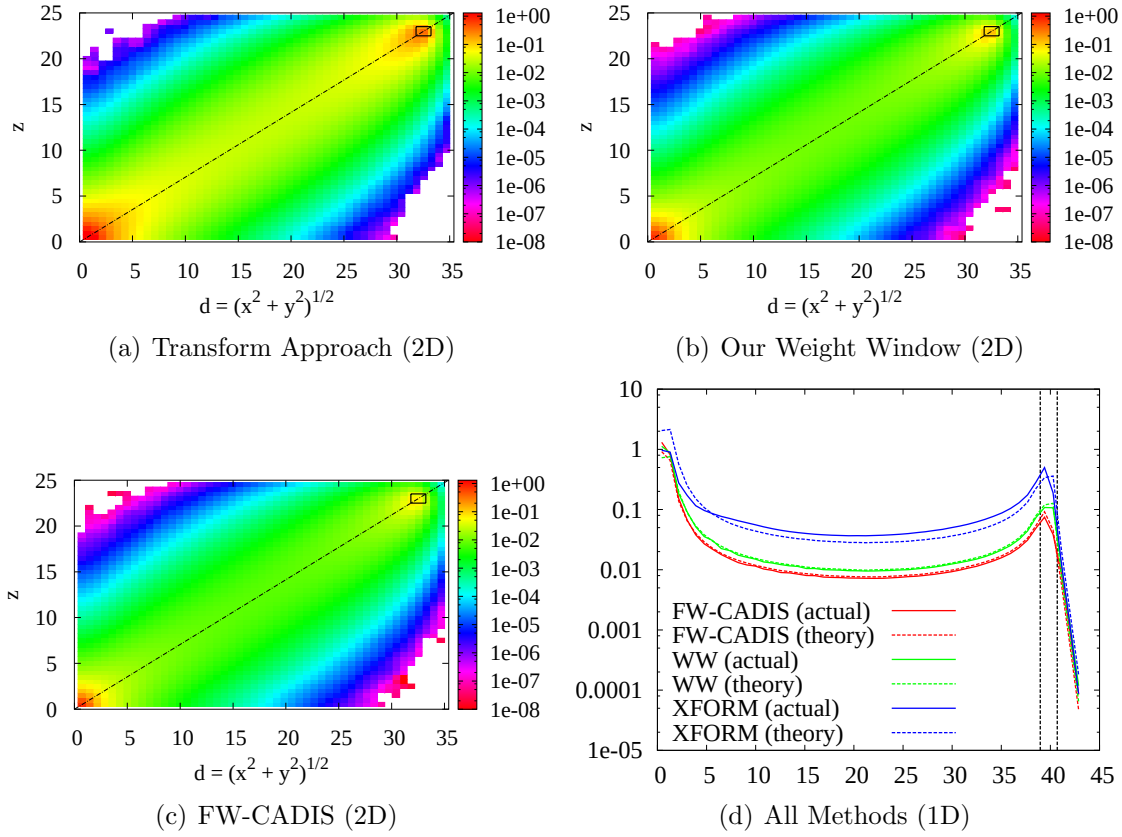

(a) Transform Approach (2D)

(b) Our Weight Window (2D)

(c) FW-CADIS (2D)

(d) All Methods (1D)

Figure 5.11: Total Predicted MC Particle Flux for SD Flux Problem

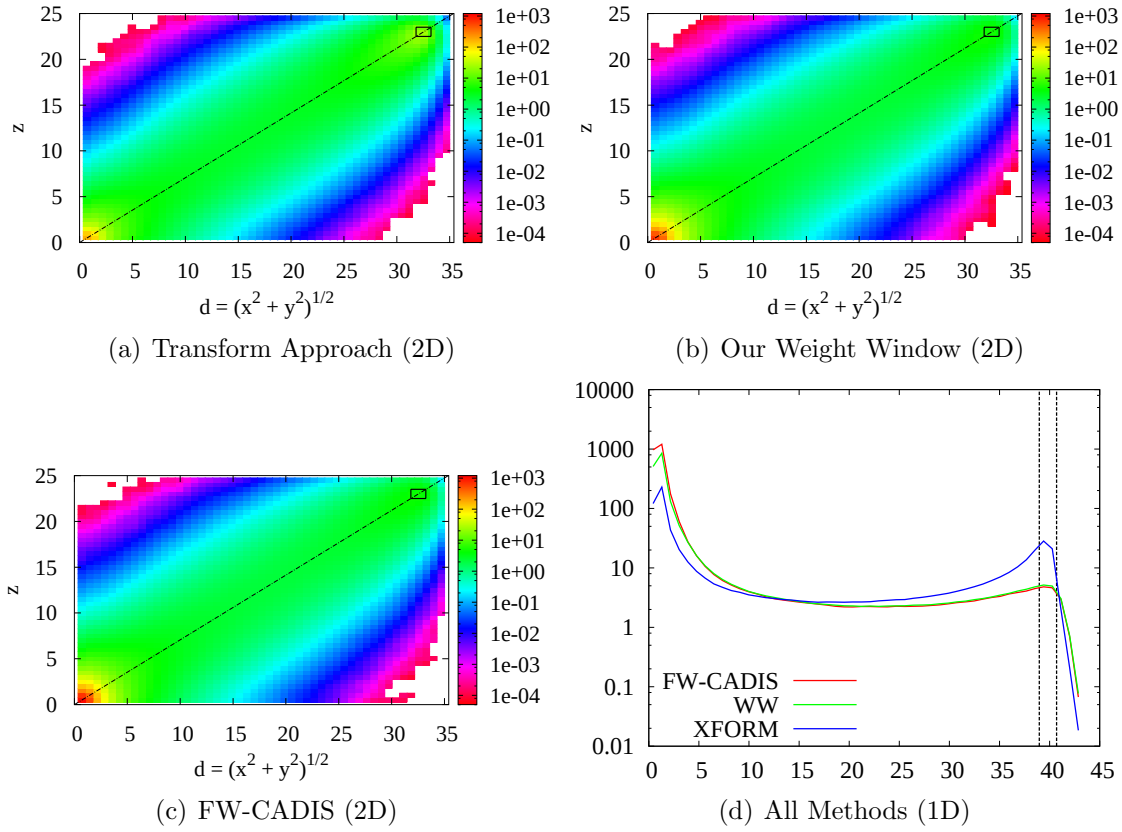

(a) Transform Approach (2D)

(b) Our Weight Window (2D)

(c) FW-CADIS (2D)

(d) All Methods (1D)

Figure 5.12: Total FOM for SD Response Problem

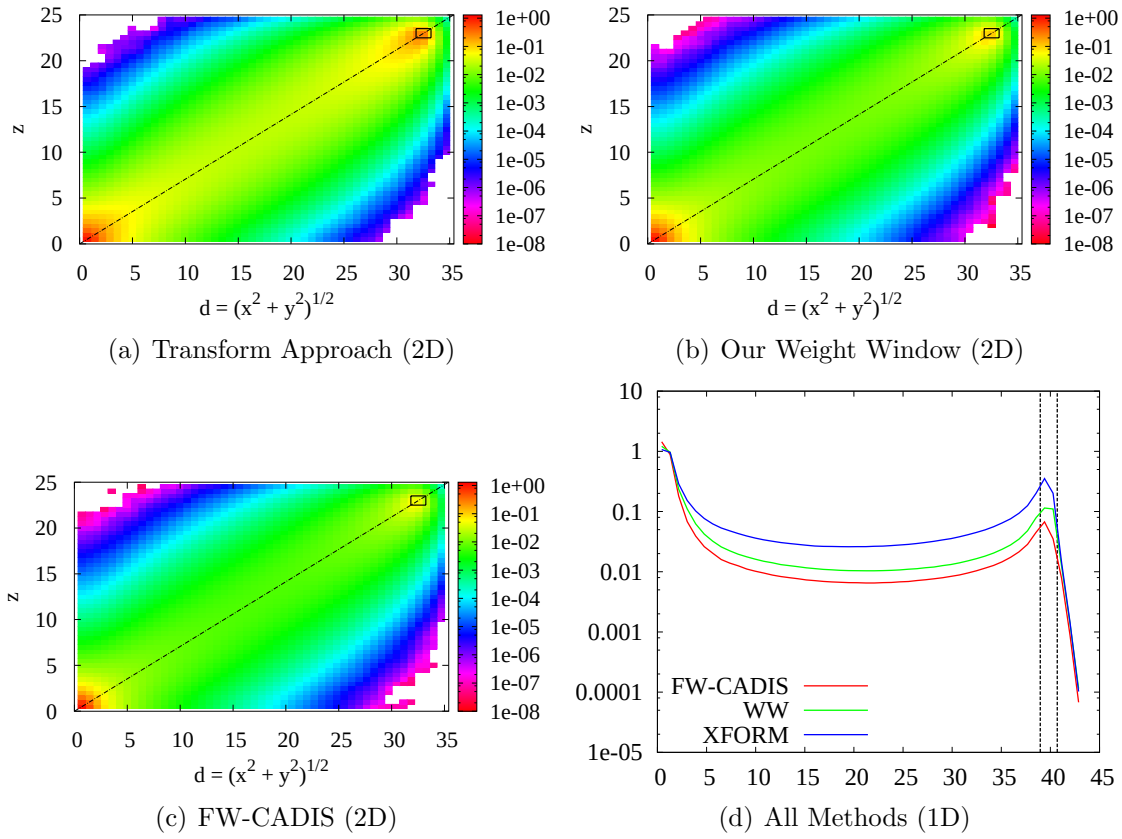

(a) Transform Approach (2D)

(b) Our Weight Window (2D)

(c) FW-CADIS (2D)

(d) All Methods (1D)

Figure 5.13: Total Simulated MC Particle Flux for SD Response Problem

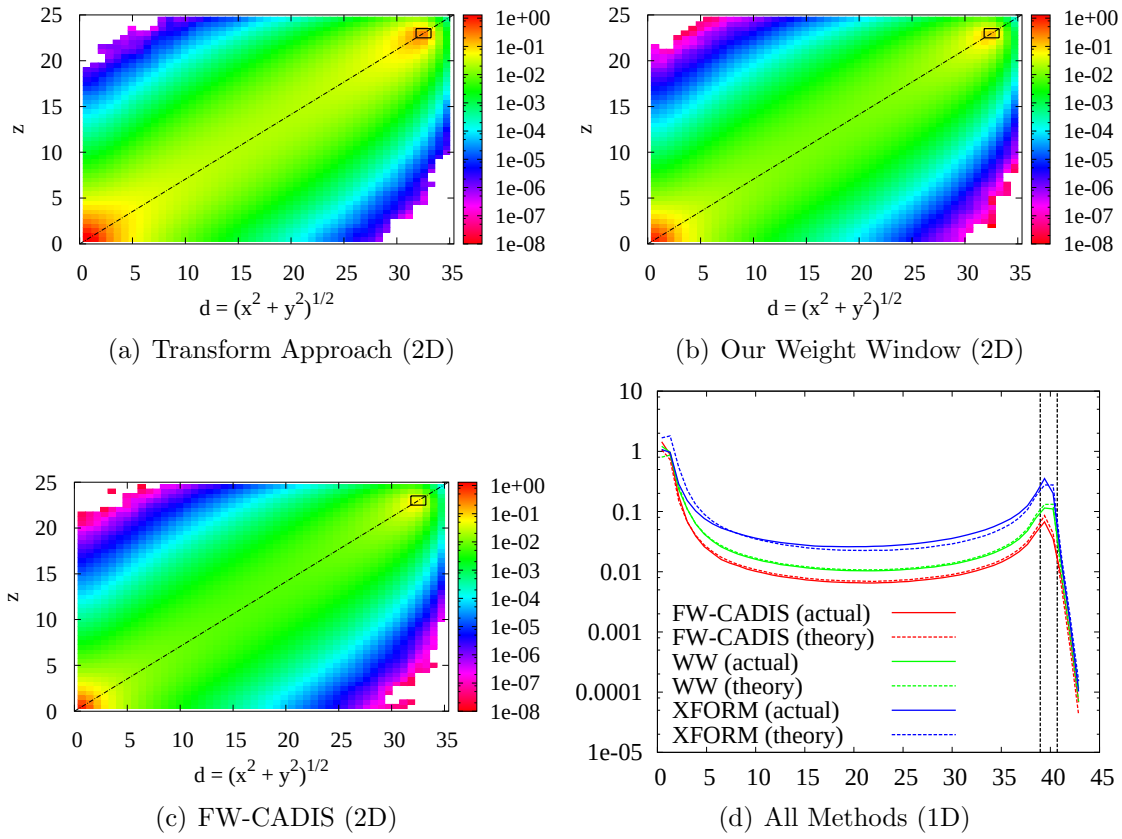

(a) Transform Approach (2D)

(b) Our Weight Window (2D)

(c) FW-CADIS (2D)

(d) All Methods (1D)

Figure 5.14: Total Predicted MC Particle Flux for SD Response Problem

time greater in the second energy group, 5 times greater in the third energy group, and nearly 5 times greater for the total flux. The weight window approaches are nearly equal since the detector is the same size as the forward source region, so that $B(\mathbf{x})$ is close to unity for our weight window.

In addition, the flux problem data in Table 5.1 demonstrate a much more uniform FOM from group to group than does the response problem data. For the flux problem data, the weight window methods both have a FOM that varies by a factor of 4 across the three energy groups, and the Transform approach has a FOM that varies by a factor of 1.3. For the response problem data, the weight window methods both have a FOM that varies by a factor of 300 across the three energy groups, and the Transform approach varies by by a factor of nearly 200. This is to be expected: the objective of the flux problem is to achieve roughly uniform results for every energy group, while the objective of the response problem is to optimize the total flux. Since most of the contribution to the total flux in the detector comes from the third energy group, the third energy group should be the most resolved statistically.

The data provided in Table 5.1 show that if the objective is to obtain good results for every energy group, the flux problem should be solved; if the objective is to obtain the total flux, the response problem should be solved. This is clearly seen by comparing the flux problem FOM to the response problem FOM for the first energy group and for the total flux. In the first energy group, the FOM values for the flux problem are 200-300 times greater than for the response problem; while for the total flux, the FOM values for the response problem are 2-3 times greater than for the flux problem. Therefore, each method has its utility.

Figures 5.3, 5.6, 5.9, and 5.12 demonstrate the distribution of the FOM in the 2D plane ($x = y$) and along the diagonal ($x = y = z$). The figures show that the FOM is greatest along the diagonal from the source to the detector. Figures 5.3 and 5.6 further clarify the difference between the flux problem and response problem, where the response problem FOM decreases much more rapidly than the flux problem FOM, due to the negligible contribution of the group-2 flux to the response (total flux). All the figures except Figure 5.6 show a saddle-like shape that peaks at the source and detector. Intuitively, this FOM distribution should resolve the detector response (flux) reasonably well, since the regions of space that have the largest contribution to the detector response (flux) are the most resolved statistically (i.e. have the largest FOM).

To explain some of the results observed in the FOM figures and table, we investigate the Monte Carlo particle flux. Specifically, we are interested in whether a

correlation exist between the FOM and the Monte Carlo particle flux, and whether the theory developed in Chapter IV accurately predicts the simulated Monte Carlo particle flux.

Table 5.2 demonstrates that, for the flux problem, all the methods approximately populate the detector with the same Monte Carlo particle flux. For all three methods, the Monte Carlo particle flux across the three energy groups varies by only a factor of roughly 1.4, a small differential compared to the physical neutron flux, which varies by nearly two orders of magnitude from the first group to the third group. For the response problem, Table 5.2 shows that the Monte Carlo particle flux varies dramatically from group 1 to group 3 – by at least two orders of magnitude. The proportion of Monte Carlo particles within each group is roughly proportional to the scalar neutron flux within each group in the detector. (The group-3 scalar neutron flux is roughly an order of magnitude larger than the group-2 scalar flux and 2 orders of magnitude larger than the group-1 scalar flux.) These results, for both the flux and response problem, are consistent with the desired objectives of each method.

To further illustrate that the simulations behave as theoretically predicted, we compare the simulated Monte Carlo particle flux to the theoretically predicted Monte Carlo particle flux. The simulated Monte Carlo particle flux is depicted in Figures 5.4, 5.7, 5.10, and 5.13 for the various problems and the corresponding predicted Monte Carlo particle flux is shown in Figures 5.5, 5.8, 5.11, and 5.14. The 1D Monte Carlo particle flux plots include both the simulated (actual) data and the predicted (theory) data to better compare the accuracy of the theory. By comparing the 1D and 2D figures, we observe that there is very good agreement between the simulated and predicted Monte Carlo particle flux. The most significant deviation exists in the Transform approach, where the predicted Monte Carlo particle flux is only an approximation. Both weight window methods, however, show nearly exact agreement between the theoretical predictions and the simulated values.

Finally, by examining the Monte Carlo particle flux figures, it is clear that a correlation exists between the Monte Carlo particle flux and the FOM, since the shape of the curves is similar. However, by comparing the FOM data in Table 5.1 with the simulated Monte Carlo particle flux data in Table 5.2, we find that they are only loosely correlated. For example, in the flux problem the weight window FOM values vary by a factor of 4 across groups while the Monte Carlo particle flux varies by only 1.4. This indicates that there are other factors besides the Monte Carlo particle flux that influence the FOM. However, it does seem that up to a point, a higher particle flux does correlate with a larger FOM. This can be observed in the response

problem data, where each group has a progressively higher FOM corresponding to a progressively higher particle flux.

5.8 Summary

In this section, we have described the source-detector problem – both the response problem and flux problem. To solve both problems, we chose to distribute the Monte Carlo particle flux according to the contributon flux (or some slightly modified form of the contributon flux) by employing an appropriate weight window or "transform" function. To implement either the weight windows or Transform approach, it was necessary to define the adjoint problem that corresponds to the intended solution – the detector flux or response. We did this by first determining an appropriate adjoint contributon source and then obtaining the corresponding adjoint neutron source. Finally, we examined a simple 3-group test problem to validate the theory and assess the performance of each method. The results indicate that the theory is correct: for a given weight window or "transform" function, the Monte Carlo particle flux is determined. The results also indicate that despite the additional computational cost per particle of the Transform approach, it produces a larger FOM than the weight window methods, since it more faithfully models the physics of the forward contributon equation. Lastly, it was determined that the FOM and the Monte Carlo particle flux are correlated, but only loosely. Thus, the theory presented here allows us to very precisely specify the Monte Carlo particle flux, but only approximately optimize the FOM.

Chapter VI

Source-Region Problems

In source-region problems, we wish to estimate a solution throughout a significant region of the system rather than just in a small detector, as in the source-detector problem. However, like the source-detector problem, there are two types of source region problems – the *flux problem* and the *response problem*. The objective of the *source-region flux problem* is to obtain the scalar neutron flux $\phi(\mathbf{x}, E)$ throughout the region of interest; the objective of the *source-region response problem* is to obtain the response

$$\mathcal{R}(\mathbf{x}) = \int_0^\infty \Sigma_{\mathcal{R}}(\mathbf{x}, E)\phi(\mathbf{x}, E)dE, \tag{6.1}$$

throughout the region of interest.

To solve these problems, we extend the concepts developed in the previous chapter for the source-detector problem. Namely, the Monte Carlo particle flux is distributed proportional to a contributon flux, since this distribution corresponds to the relative contribution of a particle at a point in phase-space to the response (or flux). As in the source-detector problem, by defining the adjoint contributon source in a specific way, a Monte Carlo particle flux distribution is achieved that corresponds to the intended solution – flux or response. From the adjoint contributon source, the adjoint neutron source is determined, and the adjoint problem can be solved and used to implement the weight window and Transform approaches.

6.1 The Response Problem

As previously mentioned, in *source-region response problems* we wish to obtain an energy-integrated response

$$\mathcal{R}(\mathbf{x}) = \int_0^\infty \int_{4\pi} \Sigma_{\mathcal{R}}(\mathbf{x}, E)\psi(\mathbf{x}, \mathbf{\Omega}, E)d\Omega dE \tag{6.2}$$

in a region $\mathcal{V}_R$ of the system $\mathcal{V}$. In all three approaches – the Transform approach, our weight window, and FW-CADIS – a suitable adjoint contributon source is defined as:

$$Q^{\mathrm{c}}(\mathbf{x}, \mathbf{\Omega}, E) = \begin{cases} \dfrac{\Sigma_{\mathcal{R}}(\mathbf{x}, E)\psi(\mathbf{x}, \mathbf{\Omega}, E)}{\int_0^\infty \int_{4\pi} \Sigma_{\mathcal{R}}(\mathbf{x}, E')\psi(\mathbf{x}, \mathbf{\Omega}', E')d\Omega' dE'}, & \text{for } \mathbf{x} \in \mathcal{V}_R, \\ 0, & \text{otherwise.} \end{cases} \tag{6.3}$$

At every point $\mathbf{x}$, this source emits contributons (response particles) at a rate proportional to their relative contribution to the spatial response $\mathcal{R}(\mathbf{x})$. Also, the total contributon emission rate is the same for every point $\mathbf{x} \in \mathcal{V}_R$, i.e.,

$$\begin{aligned} Q^{\mathrm{c}}(\mathbf{x}) &= \int_0^\infty \int_{4\pi} Q^{\mathrm{c}}(\mathbf{x}, \mathbf{\Omega}, E)d\Omega dE \\ &= 1. \end{aligned} \tag{6.4}$$

Thus, every spatial location $\mathbf{x}$ essentially functions as a point detector which emits contributons at a rate proportional to the contribution to the response $\mathcal{R}(\mathbf{x})$, and every point detector is treated with equal importance by emitting particles at the same rate. Thus, the source-region problem can be viewed as the superposition of many source-detector problems, where each detector is a point $\mathbf{x} \in \mathcal{V}_R$.

The adjoint neutron source is determined from Eq. 5.12:

$$\begin{aligned} Q^*(\mathbf{x}, \mathbf{\Omega}, E) &= \frac{Q^{\mathrm{c}}(\mathbf{x}, \mathbf{\Omega}, E)}{\psi(\mathbf{x}, \mathbf{\Omega}, E)} \\ &= \begin{cases} \dfrac{\Sigma_{\mathcal{R}}(\mathbf{x}, E)}{\int_0^\infty \int_{4\pi} \Sigma_{\mathcal{R}}(\mathbf{x}, E')\psi(\mathbf{x}, \mathbf{\Omega}', E)d\Omega' dE'}, & \text{for } \mathbf{x} \in \mathcal{V}_R, \\ 0, & \text{otherwise.} \end{cases} \end{aligned} \tag{6.5}$$

With the adjoint problem completely defined, the various methods can be implemented to solve the source-region response problem. Each method is discussed later in this chapter.

6.2 The Flux Problem

In *source-region flux problems* we wish to obtain the energy-dependent scalar flux $\phi(\mathbf{x}, E)$ in the region $\mathcal{V}_R$. Just as in the previous section on the response problem, the adjoint contributon source must be defined. For all three approaches – FW-CADIS, our weight window, and the Transform approach – a suitable adjoint contributon source is defined as:

$$Q^{\mathrm{c}}(\mathbf{x}, \mathbf{\Omega}, E) = \begin{cases} \dfrac{\psi(\mathbf{x}, \mathbf{\Omega}, E)}{\phi(\mathbf{x}, E)}, & \text{for } \mathbf{x} \in \mathcal{V}_R, \\ 0, & \text{otherwise.} \end{cases} \tag{6.6}$$

At every spatial location $\mathbf{x}$ in the region and for every energy E, this adjoint contributon source emits contributons at a uniform rate (i.e. $Q^{\mathrm{c}}(\mathbf{x}, E) = \int_{4\pi} Q^{\mathrm{c}}(\mathbf{x}, \mathbf{\Omega}, E) d\Omega = 1$) with an angular distribution proportional to their contribution to the scalar flux. Similar to the response problem, every point $\mathbf{x}$ essentially functions as a point detector that uniformly emits contributons in energy. This results in a contributon flux that corresponds most closely to obtaining a statistically resolved estimate of the scalar flux for every energy.

The adjoint neutron source is determined from Eq. 5.12:

$$\begin{aligned} Q^{*}(\mathbf{x}, \mathbf{\Omega}, E) &= \frac{Q^{\mathrm{c}}(\mathbf{x}, \mathbf{\Omega}, E)}{\psi(\mathbf{x}, \mathbf{\Omega}, E)} \\ &= \begin{cases} \dfrac{1}{\phi(\mathbf{x}, E)}, & \text{for } \mathbf{x} \in \mathcal{V}_R, \\ 0, & \text{otherwise.} \end{cases} \end{aligned} \tag{6.7}$$

6.3 The Transform Approach

Now that the adjoint problem has been completely defined for the source-region problems – flux and response – the transform approach is easily implemented. The "transform" function that we use in this thesis is given by Eq. 4.104 as

$$\hat{\mathcal{T}}(\mathbf{x}, \mathbf{\Omega}, E) = \frac{B(\mathbf{x})}{\psi^{*}(\mathbf{x}, \mathbf{\Omega}, E)}. \tag{6.8}$$

This transform function produces a angular Monte Carlo particle flux distribution proportional to the angular contributon flux, modified by the spatial parameter $B(\mathbf{x})$:

$$m(\mathbf{x}, \mathbf{\Omega}, E) = \frac{\psi^{\mathrm{c}}(\mathbf{x}, \mathbf{\Omega}, E)}{B(\mathbf{x})}. \tag{6.9}$$

For source-region problems, $B(\mathbf{x})$ [defined below in Eq. 6.10] achieves three things:

1. Within the region of interest, it results in an energy-dependent Monte Carlo particle flux $\mathcal{M}(\mathbf{x}, E)$ that is proportional to the relative contribution of the Monte Carlo particles to the response (flux) at $\mathbf{x}$ and produces an energy-integrated Monte Carlo flux $\mathcal{M}(\mathbf{x})$ that is approximately uniform across the region. Thus Monte Carlo particles are roughly distributed uniformly in space within the region and in energy according to their relative contribution to the space-dependent response or flux.

2. Outside the "detector" region, it distributes Monte Carlo particles in proportion to the contributon flux, but it flattens out the Monte Carlo particle flux in regions with a concentration of Monte Carlo particles that is higher than in the "detector" region. Effectively, this forces particles out of regions that are highly resolved statistically, such as the forward source region, into other spatial regions that contribute to the region response or flux but are less resolved.

3. It ensures that rapid changes in the Monte Carlo particle flux do not occur near the boundary of the region. This prevents excessive splitting and rouletting near the region.

The form of $B(\mathbf{x})$ for source-region problems is given as

$$B(\mathbf{x}) = \begin{cases} \tilde{\phi}^{\mathrm{c}}(\mathbf{x}), & \text{for } \mathbf{x} \in \mathcal{V}_R, \\ \alpha(\mathbf{x})\tilde{\phi}^{\mathrm{c}}(\mathbf{x}) + 1 - \alpha(\mathbf{x}), & \text{otherwise}, \end{cases} \tag{6.10}$$

where all the parameters except the normalization constant are defined exactly as they were for source-detector problems:

$$\tilde{\phi}^{\mathrm{c}}(\mathbf{x}) = \int_0^\infty \phi(\mathbf{x}, E)\tilde{\phi}^{*}(\mathbf{x}, E)dE, \tag{6.11}$$

$$\tilde{\phi}^{*}(\mathbf{x}, E) = \mathrm{C}_{\mathrm{norm}}\phi^{*}(\mathbf{x}, E), \tag{6.12}$$

$$\mathrm{C}_{\mathrm{norm}} = \left[\mathrm{A}^{-1}_{\partial\mathcal{V}_R\setminus\partial\mathcal{V}} \int_{\partial\mathcal{V}_R\setminus\partial\mathcal{V}} \int_0^\infty \phi(\mathbf{x}, E)\phi^{*}(\mathbf{x}, E)dEdA\right]^{-1}, \tag{6.13}$$

$$\alpha(\mathbf{x}) = \left[1 + \mathrm{e}^{\left(\frac{\tilde{\phi}^{\mathrm{c}}_{\max\in\mathcal{V}_R}}{\tilde{\phi}^{\mathrm{c}}(\mathbf{x})} - \frac{\tilde{\phi}^{\mathrm{c}}(\mathbf{x})}{\tilde{\phi}^{\mathrm{c}}_{\max\in\mathcal{V}_R}}\right)}\right]^{-1}. \tag{6.14}$$

Here $\tilde{\phi}^{\mathrm{c}}(\mathbf{x})$ is a normalized approximation to the energy-integrated scalar contributon flux $\phi^{\mathrm{c}}(\mathbf{x})$, $\alpha(\mathbf{x})$ is used outside the region of interest to continuously adjust the

distribution of the Monte Carlo particle flux $\mathcal{M}(\mathbf{x})$ from one that is proportional to the scalar contributon flux $\phi^{c}(\mathbf{x})$ to one that is constant (depending on the magnitude of $\tilde{\phi}^{c}(\mathbf{x})$ relative to the maximum value in the region $\tilde{\phi}^{c}_{\max\in\mathcal{V}_R}$), and $\mathrm{C}_{\mathrm{norm}}$ is a normalization constant that scales the adjoint scalar flux to ensure that rapid changes in the Monte Carlo particle flux (resulting from splitting or Russian roulette) do not occur at the boundary of the region of interest due to rapid changes in the spatial parameter $\alpha(\mathbf{x})$. The set-theory notation $\partial\mathcal{V}_R \setminus \partial\mathcal{V}$ denotes all points $\mathbf{x}$ on the boundary of the region of interest but not on the boundary of the system. This set of points constitutes a portion of the surface of the region; it has a surface area denoted by $\mathrm{A}_{\partial\mathcal{V}_R\setminus\partial\mathcal{V}}$.

To see how $B(\mathbf{x})$ accomplishes the first objective – that Monte Carlo particles are roughly distributed uniformly in space within the region and according to their relative contribution to the space dependent response or flux – we begin with Eq. 4.96:

$$\begin{aligned}\mathcal{M}(\mathbf{x},E) &= \frac{\phi^{c}(\mathbf{x},E)}{B(\mathbf{x})} \\ &= \frac{\phi^{c}(\mathbf{x},E)}{\tilde{\phi}^{c}(\mathbf{x})}, \quad \mathbf{x}\in\mathcal{V}_R \\ &\approx (4\pi C_{\mathrm{norm}})^{-1}\frac{\phi^{c}(\mathbf{x},E)}{\phi^{c}(\mathbf{x})}, \quad \mathbf{x}\in\mathcal{V}_R. \end{aligned} \tag{6.15}$$

The last statement follows from Eq. 5.29. Finally, integrating Eq. 6.15 over energy, we obtain the energy-integrated (total) Monte carlo particle flux at $\mathbf{x}\in\mathcal{V}_R$:

$$\mathcal{M}(\mathbf{x}) \approx (4\pi C_{\mathrm{norm}})^{-1}, \quad \mathbf{x}\in\mathcal{V}_R. \tag{6.16}$$

Together, Eq. 6.15 and 6.16 affirm the first objective – that the Monte Carlo particle flux is uniformly distributed in $\mathcal{V}_R$ and according to the relative contribution to the response (or flux) in energy.

The rationale for the second objective – to flatten a high concentration of Monte Carlo particles outside the region – follows from the analysis provided in Chapter V, since the form of $B(\mathbf{x})$ outside the region is the same for the source-detector problem (see Eq. 5.35). To understand how the constant $\mathrm{C}_{\mathrm{norm}}$ approximately normalizes the adjoint flux to prevent major fluctuations in the Monte Carlo particle flux near the

transition area at the region boundary, we begin with Eq. 4.96:

$$\begin{aligned}\mathcal{M}(\mathbf{x},E) &= \frac{\phi^{c}(\mathbf{x},E)}{B(\mathbf{x})} \\ &= \frac{\phi^{c}(\mathbf{x},E)}{\alpha(\mathbf{x})\tilde{\phi}^{c}(\mathbf{x})+1-\alpha(\mathbf{x})} \\ &\approx \phi^{c}(\mathbf{x},E), \quad \text{for } \mathbf{x} \text{ near the region boundary.}\end{aligned} \tag{6.17}$$

The last statement follows if the contributon flux does not vary dramatically along the boundary of the region. Then,

$$\begin{aligned}\tilde{\phi}^{c}(\mathbf{x}) &= \mathrm{C}_{\mathrm{norm}} \int_{0}^{\infty} \phi(\mathbf{x},E)\phi^{*}(\mathbf{x},E)dE \\ &= \frac{\int_{0}^{\infty} \phi(\mathbf{x},E)\phi^{*}(\mathbf{x},E)dE}{\mathrm{A}^{-1}_{\partial\mathcal{V}_R\setminus\partial\mathcal{V}} \int_{\partial\mathcal{V}_R\setminus\partial\mathcal{V}} \int_{0}^{\infty} \phi(\mathbf{x},E)\phi^{*}(\mathbf{x},E)dEdA} \\ &\approx 1, \quad \text{for } \mathbf{x} \text{ near the region boundary.}\end{aligned} \tag{6.18}$$

Thus, inside the region of interest, the source-region form of $B(\mathbf{x})$ achieves a roughly uniform Monte Carlo particle flux with an energy distribution that is proportional to the relative contribution to the spatially-dependent response or flux. Outside the region, $B(\mathbf{x})$ distributes particles according to the contributon flux except in regions with relatively high concentrations of Monte Carlo particles; in these regions, the Monte Carlo particle flux is flattened by forcing Monte Carlo particles to disperse to other statistically important regions with a lower concentrations of Monte Carlo particles.

The "transform" function has now been completely defined for the source-region problem and can be used as described in Section 4.3 to implement the Transform approach.

6.4 Our Weight Window

In Section 4.2.1, we found that the weight window center $\mathrm{w}(\mathbf{x},E)$ and the scalar Monte Carlo particle flux $\mathcal{M}(\mathbf{x},E)$ are related by Eq. 4.9:

$$\mathrm{w}(\mathbf{x},E) = \frac{\phi(\mathbf{x},E)}{\mathcal{M}(\mathbf{x},E)}. \tag{6.19}$$

For the source-region flux or response problem, our weight window is used to distribute Monte Carlo particles according to the scalar contributon flux distribution, with the same modification used for the Transform approach, i.e. $B(\mathbf{x})$. We define the Monte Carlo particle flux as

$$\mathcal{M}(\mathbf{x}, E) = \frac{\phi^{\mathrm{c}}(\mathbf{x}, E)}{B(\mathbf{x})}, \tag{6.20}$$

where the spatial parameter $B(\mathbf{x})$ was described in detail in the previous section on the Transform approach (see Eq. 6.10). Then, the weight window is approximated as

$$\begin{aligned} \mathrm{w}(\mathbf{x}, E) &= \frac{B(\mathbf{x})\phi(\mathbf{x}, E)}{\phi^{\mathrm{c}}(\mathbf{x}, E)} \\ &\approx \frac{B(\mathbf{x})}{\phi^{*}(\mathbf{x}, E)}, \end{aligned} \tag{6.21}$$

where we have approximated the scalar contributon flux $\phi^{\mathrm{c}}(\mathbf{x}, E)$ as

$$\phi^{\mathrm{c}}(\mathbf{x}, E) \approx \phi(\mathbf{x}, E)\phi^{*}(\mathbf{x}, E). \tag{6.22}$$

This weight window produces a scalar Monte Carlo particle flux similar to that of the Transform approach, but without modifying any of the particle physics. The spatial parameter $B(\mathbf{x})$ accomplishes the same objectives here:

1. Within the region of interest, it results in an energy-dependent Monte Carlo particle flux $\mathcal{M}(\mathbf{x}, E)$ that is proportional to the relative contribution of the Monte Carlo particles to the response (flux) at $\mathbf{x}$ and produces an energy-integrated Monte Carlo flux $\mathcal{M}(\mathbf{x})$ that is approximately uniform across the region. Thus, Monte Carlo particles are roughly distributed uniformly in space within the region and according to their relative contribution to the space-dependent response or flux.

2. Outside the "detector" region, it flattens out the Monte Carlo particle flux $\mathcal{M}(\mathbf{x})$ in regions with a higher concentration of Monte Carlo particles than in the "detector" region, effectively forcing particles out of those regions that are highly resolved statistically to other regions that contribute to the "detector" region response but are less resolved.

3. It ensures that rapid changes in the Monte Carlo particle flux do not occur

near the region due to rapid changes of the spatial parameter $\alpha(\mathbf{x})$ (see Eq. 6.10). This prevents excessive splitting and rouletting near the boundary of the region.

With our weight window completely defined for the source-region problem, it can be implemented according to the specifications given in the general section on weight windows, Section 4.2.

6.5 FW-CADIS

For the source-region problem, the FW-CADIS weight window maintains the form of the classical weight window, which is inversely proportional to the adjoint scalar flux:

$$\mathrm{w}(\mathbf{x}, E) = \frac{1}{\phi^*(\mathbf{x}, E)}. \tag{6.23}$$

Again, according to Eq. 4.8 given in Section 4.2.1, this weight window results in a Monte Carlo particle flux that is approximately proportional to the scalar contributon flux:

$$\begin{aligned} \mathcal{M}(\mathbf{x}, E) &= \frac{\phi(\mathbf{x}, E)}{\mathrm{w}(\mathbf{x}, E)} \\ &= \phi(\mathbf{x}, E)\phi^*(\mathbf{x}, E) \\ &\approx \phi^{\mathrm{c}}(\mathbf{x}, E). \end{aligned} \tag{6.24}$$

As with our weight window, all the details necessary to implement the FW-CADIS weight window are in Section 4.2.

6.6 Numerical Test Problem

To verify that the methods perform as the theory predicts, and to compare the methods for efficiency and statistical quality, we consider the simple 3-group problem introduced in the previous chapter with an enlarged "detector" region $\mathcal{V}_R$. Our objectives remain the same: 1) to assess how well the approaches perform on a multigroup shielding problem, and 2) to verify that the methods perform as the theory predicts.

6.6.1 Problem Description

Figure 6.1 demonstrates the geometry: a 25 cm homogeneous cube with a 1 cm cubic source in the corner, symmetric boundary conditions at the planes that cut

through the source, and vacuum boundaries at the exterior planes. The source is a unit source (1 $\text{cm}^{-3}\text{s}^{-1}$), in the first energy group only. The total cross-section is set equal to unity throughout space and energy (i.e. $\Sigma_{t,g} = 1\ \text{cm}^{-1}$). The scattering matrix is provided in the material data section of the Figure 6.1.

To make this problem a source-region problem, we select an 8 cm cubic region in the furthest corner from the source, 1.5 cm from all three vacuum boundaries. Just as in the source-detector problem, the region was selected to be away from the boundary of the system to avoid edge effects, specifically those resulting from being incapable of completely capturing the property of contributons on the boundary–no leakage due to an infinite effective total cross-section (see Section 5.1).

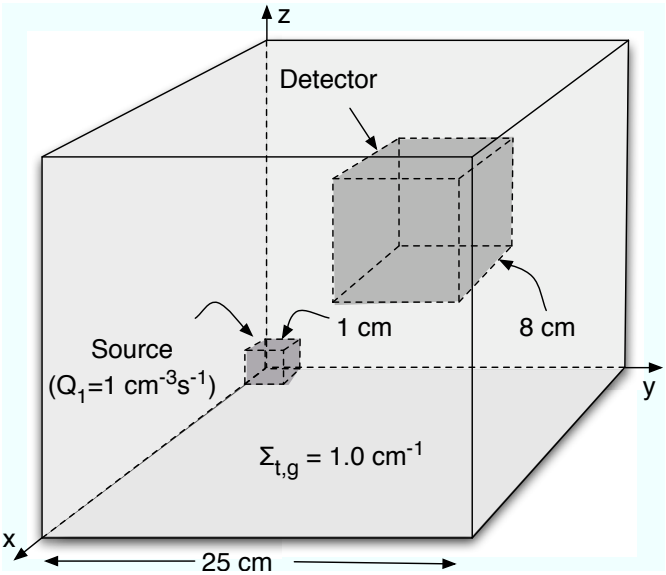

Data \ g	1	2	3
$\Sigma_{t,g}\,(cm^{-1})$	1.0	1.0	1.0
$\Sigma_{s,g\to1}\,(cm^{-1})$	0.6	0.0	0.0
$\Sigma_{s,g\to2}\,(cm^{-1})$	0.1	0.7	0.0
$\Sigma_{s,g\to3}\,(cm^{-1})$	0.05	0.1	0.8
$Q_g\,(cm^{-3}s^{-1})$	1.0	0.0	0.0

Figure 6.1: Problem Geometry and Material Properties

Figure 6.2 again demonstrates that this problem is indeed a shielding problem, with the scalar flux being attenuated by 20 orders of magnitude in the first energy group, 18 orders of magnitude in the second group, nearly 16 orders of magnitude in the third group, and roughly 17 orders of magnitude in the energy-integrated (total) flux. Within the region of interest, the scalar flux is attenuated by over 5 orders of magnitude in the first and second energy group, and nearly 5 orders of magnitude in the third energy group and for the total flux. As can be seen from the figures, the total flux is composed mostly of group-1 flux near the source and mostly of group-3 flux near the "detector" region.

The objective of the source-region flux problem is to obtain the scalar flux $\phi_{c,g}$ for every energy group g and in every spatial element $\mathcal{V}_c$ within the region $\mathcal{V}_R$, where

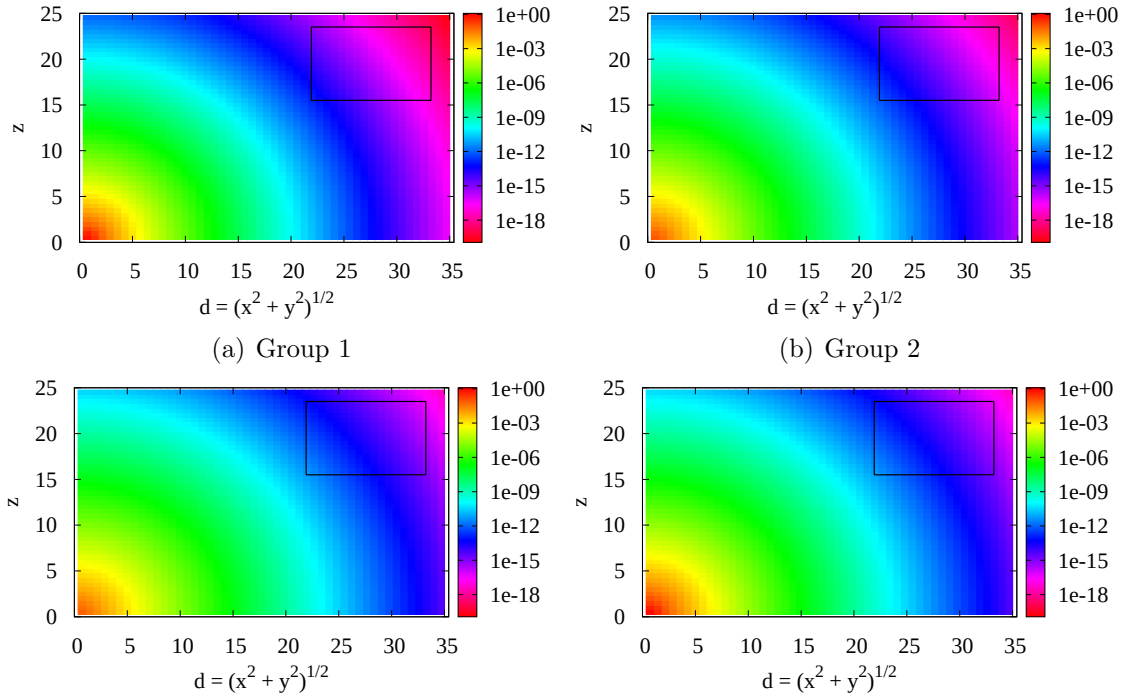

(a) Group 1 (b) Group 2

(c) Group 3 (d) Total

Figure 6.2: Scalar Flux along the plane $x = y$

the scalar flux $\phi_{c,g}$ is defined as

$$\phi_{c,g} = \frac{1}{V_c} \int_{\mathcal{V}_c} \int_{E_g}^{E_{g-1}} \phi(\mathbf{x}, E) dE dV. \tag{6.25}$$

The objective of the source-region response problem is to obtain the response $\mathcal{R}_c$ in each spatial element $\mathcal{V}_c$ within the region $\mathcal{V}_R$. We again investigate a special response, the energy-integrated (total) flux, denoted simply as ϕ_c and defined as

$$\phi_c = \sum_{g=1}^{3} \phi_{c,g}. \tag{6.26}$$

(For this response, we set $\Sigma_{\mathcal{R}}(\mathbf{x}, E) = 1$.) To analyze the results, we plot the figure of merit, the simulated scalar Monte Carlo particle flux, the theoretically predicted scalar Monte Carlo particle flux, and the region statistics for the second energy group and the total flux. These plots appear in Figures 6.3 - 6.18 and consist of a 2D plane that stretches from the z-axis to the cube edge farthest from the source (i.e. the plane $x = y$), the line from the source corner to the far corner (i.e. the line $x = y = z$), and the FOM and Monte Carlo particle flux statistics throughout the entire region

of interest. These values are computed on a uniform 0.5 cm grid that is imposed on the problem geometry. Thus, the system consists of 125,000 spatial elements, each denoted by $\mathcal{V}_c$. (The source contains 8 spatial elements and the "detector" region contains 4,096.)

The energy-dependent scalar Monte Carlo particle flux $\mathcal{M}_{c,g}$ and the energy-integrated scalar Monte Carlo particle flux $\mathcal{M}_c$ are volume-averaged quantities determined directly from the Monte Carlo simulation. The figures of merit (FOM) in each spatial element $\mathcal{V}_c$ are defined as

$$\begin{aligned} \mathrm{FOM}_{c,g} &= \frac{1}{\frac{\mathrm{Var}\left[\phi_{c,g}\right]}{\phi_{c,g}^2}\mathrm{T}_{\mathrm{cpu}}}, \\ \mathrm{FOM}_{c} &= \frac{1}{\frac{\mathrm{Var}\left[\phi_{c}\right]}{\phi_{c}^2}\mathrm{T}_{\mathrm{cpu}}}, \end{aligned} \tag{6.27}$$

where $\mathrm{T}_{\mathrm{cpu}}$ is the total run time, and $\phi_{c,g}$, ϕ_c, and the corresponding variances are volume-averaged quantities obtained directly from the Monte Carlo simulation.

The theoretically predicted energy-dependent scalar Monte Carlo particle flux $\tilde{M}_{c,g}$ averaged over $\mathcal{V}_c$ is given for each method as:

$$\tilde{\mathcal{M}}_{c,g}^{\mathrm{XFORM}} \approx \mathrm{C}_0 \frac{\phi_{c,g}\Phi_{c,g}^*}{B_c}, \tag{6.28}$$

$$\tilde{\mathcal{M}}_{c,g}^{\mathrm{WW}} = \mathrm{C}_0 \frac{\phi_{c,g}\Phi_{c,g}^*}{B_c}, \tag{6.29}$$

$$\tilde{\mathcal{M}}_{c,g}^{\mathrm{FWCADIS}} = \mathrm{C}_0 \phi_{c,g}\Phi_{c,g}^*, \tag{6.30}$$

where XFORM identifies the Transform approach, WW identifies our weight window, and FWCADIS identifies the FW-CADIS weight window. To remain consistent with the Monte Carlo particle flux resulting from the weight window, the Monte Carlo estimate of the forward scalar flux $\phi_{c,g}$ is treated as the "exact" forward scalar flux and the deterministic estimate of the adjoint scalar flux $\Phi_{c,g}^*$ is used since it corresponds to the weight window. The transform approach scalar flux estimate is an approximation of the scalar Monte Carlo flux produced by the Transform approach:

$$\begin{aligned} \mathcal{M}(\mathbf{x}, E) &= \frac{\int_{4\pi} \psi(\mathbf{x}, \mathbf{\Omega}, E)\psi^*(\mathbf{x}, \mathbf{\Omega}, E)d\Omega}{B(\mathbf{x})} \\ &\approx \mathrm{C}_0 \frac{\phi(\mathbf{x}, E)\phi^*(\mathbf{x}, E)}{B(\mathbf{x})}. \end{aligned} \tag{6.31}$$

For all three approaches, the theoretically predicted energy-integrated scalar Monte Carlo particle flux $\tilde{\mathcal{M}}_c$ is given as:

$$\tilde{\mathcal{M}}_c = \sum_{g=1}^{3} \tilde{\mathcal{M}}_{c,g}. \tag{6.32}$$

For both the response problem and flux problem, the energy-dependent scalar flux $\phi_{c,g}$ and the total scalar flux ϕ_c are tallied, even though the flux problem is tailored to obtain just $\phi_{c,g}$ and the response problem is tailored to obtain ϕ_c. To see the difference between the flux problem and the response problem, we examine the data in a representative energy group – the second group – and the data for the total flux. We expect that the methods tailored to the flux problem will produce better statistical results for the second energy group, while those tailored to the response (total flux) problem will produce better statistical results for the total flux data.

6.6.2 Numerical Results

The group-2 data for the flux problem is presented in Figures 6.3 - 6.6, including the figure of merit, the simulated Monte Carlo particle flux, the theoretically predicted Monte Carlo particle flux, and the region statistics; the corresponding group-2 data for the response (total flux) problem appears in Figures 6.7 - 6.10. Likewise, the total flux data for the flux problem is presented in Figures 6.11 - 6.14 and the corresponding data for the response problem appears in Figures 6.15 - 6.18. For clarity, all the 2D figures contain a black rectangle to denote the region and a dashed line to trace out the diagonal from the source to the far corner (i.e. the line $x = y = z$). The 1D figures are plots along this line with dashed vertical lines indicating the region location. In addition, Tables 6.1 - 6.4 and Tables 6.5 - 6.8 provide the region FOM and the simulated Monte Carlo particle flux statistics, respectively, for each energy group and for all methods and problems.

For source-region problems, in which a solution is obtained in every spatial element in the region, a single metric for assessing and comparing methods does not exist. However, one measure that conveys some information about the efficiency and accuracy of the solution in the entire region is the median FOM, since it relays that half the spatial elements in the region have an FOM below this value and half have an FOM that is greater than this value. (In addition, the maximum and minimum values of the FOM could be used to bound the FOM in the lower and upper half.) In this thesis, we use the median value as well as figures to assess and compare the

Table 6.1: Region FOM statistics for group-1 flux

Problem	Method	Group-1 FOM			
		Min	Max	Median	Mean
Flux ($\phi_{c,g}$)	FW-CADIS	0.027	0.428	0.193	0.204
	WW	0.045	0.486	0.313	0.300
	XFORM	0.081	1.675	1.073	1.024
Response (ϕ_c)	FW-CADIS	0.00041	0.040	0.0069	0.0090
	WW	0.0011	0.046	0.013	0.014
	XFORM	0.0011	1.127	0.035	0.040

Table 6.2: Region FOM statistics for group-2 flux

Problem	Method	Group-2 FOM			
		Min	Max	Median	Mean
Flux ($\phi_{c,g}$)	FW-CADIS	0.040	0.647	0.279	0.298
	WW	0.058	0.769	0.526	0.495
	XFORM	0.086	1.636	1.055	1.008
Response (ϕ_c)	FW-CADIS	0.0066	0.254	0.065	0.078
	WW	0.011	0.297	0.129	0.128
	XFORM	0.016	1.641	0.281	0.288

Table 6.3: Region FOM statistics for the group-3 flux

Problem	Method	Group-3 FOM			
		Min	Max	Median	Mean
Flux ($\phi_{c,g}$)	FW-CADIS	0.066	1.138	0.498	0.535
	WW	0.092	1.370	1.008	0.937
	XFORM	0.115	1.821	1.259	1.189
Response (ϕ_c)	FW-CADIS	0.143	2.478	1.106	1.179
	WW	0.212	2.888	2.165	2.004
	XFORM	0.322	4.875	3.376	3.185

Table 6.4: Region FOM statistics for the total flux

Problem	Method	Total Flux FOM			
		Min	Max	Median	Mean
Flux ($\phi_{c,g}$)	FW-CADIS	0.072	1.138	0.567	0.616
	WW	0.103	1.556	1.161	1.071
	XFORM	0.129	2.118	1.456	1.367
Response (ϕ_c)	FW-CADIS	0.149	2.685	1.163	1.246
	WW	0.225	2.991	2.276	2.104
	XFORM	0.339	5.324	3.702	3.469

Table 6.5: Region simulated MC particle flux for the group-1 flux

Problem	Method	Group-1 Simulated MC Particle Flux			
		Min	Max	Median	Mean
Flux ($\phi_{c,g}$)	**FW-CADIS**	4.4E-05	0.0022	0.00060	0.00072
	WW	0.032	0.050	0.040	0.040
	XFORM	0.042	0.264	0.121	0.130
Response (ϕ_c)	**FW-CADIS**	3.1E-07	0.00014	1.6E-05	2.4E-05
	WW	0.00032	0.0030	0.0010	0.0010
	XFORM	0.00042	0.013	0.0025	0.0031

Table 6.6: Region simulated MC particle flux for the group-2 flux

Problem	Method	Group-2 Simulated MC Particle Flux			
		Min	Max	Median	Mean
Flux ($\phi_{c,g}$)	**FW-CADIS**	3.8E-05	0.0019	0.00056	0.00066
	WW	0.031	0.046	0.037	0.037
	XFORM	0.041	0.162	0.103	0.103
Response (ϕ_c)	**FW-CADIS**	7.2E-06	0.00074	0.00013	0.00018
	WW	0.0044	0.015	0.0082	0.0084
	XFORM	0.0059	0.060	0.020	0.023

Table 6.7: Region simulated MC particle flux for the group-3 flux

Problem	Method	Group-3 Simulated MC Particle Flux			
		Min	Max	Median	Mean
Flux ($\phi_{c,g}$)	**FW-CADIS**	6.1E-05	0.0025	0.00082	0.00094
	WW	0.046	0.062	0.052	0.052
	XFORM	0.064	0.157	0.126	0.124
Response (ϕ_c)	**FW-CADIS**	0.00018	0.0068	0.0023	0.0026
	WW	0.117	0.156	0.135	0.135
	XFORM	0.141	0.376	0.295	0.291

Table 6.8: Region simulated MC particle flux for the total flux

Problem	Method	Total Simulated MC Particle Flux			
		Min	Max	Median	Mean
Flux ($\phi_{c,g}$)	**FW-CADIS**	0.00014	0.0065	0.0020	0.0023
	WW	0.112	0.158	0.129	0.129
	XFORM	0.146	0.569	0.351	0.357
Response (ϕ_c)	**FW-CADIS**	0.00018	0.0076	0.0024	0.0028
	WW	0.123	0.170	0.145	0.144
	XFORM	0.148	0.429	0.320	0.317

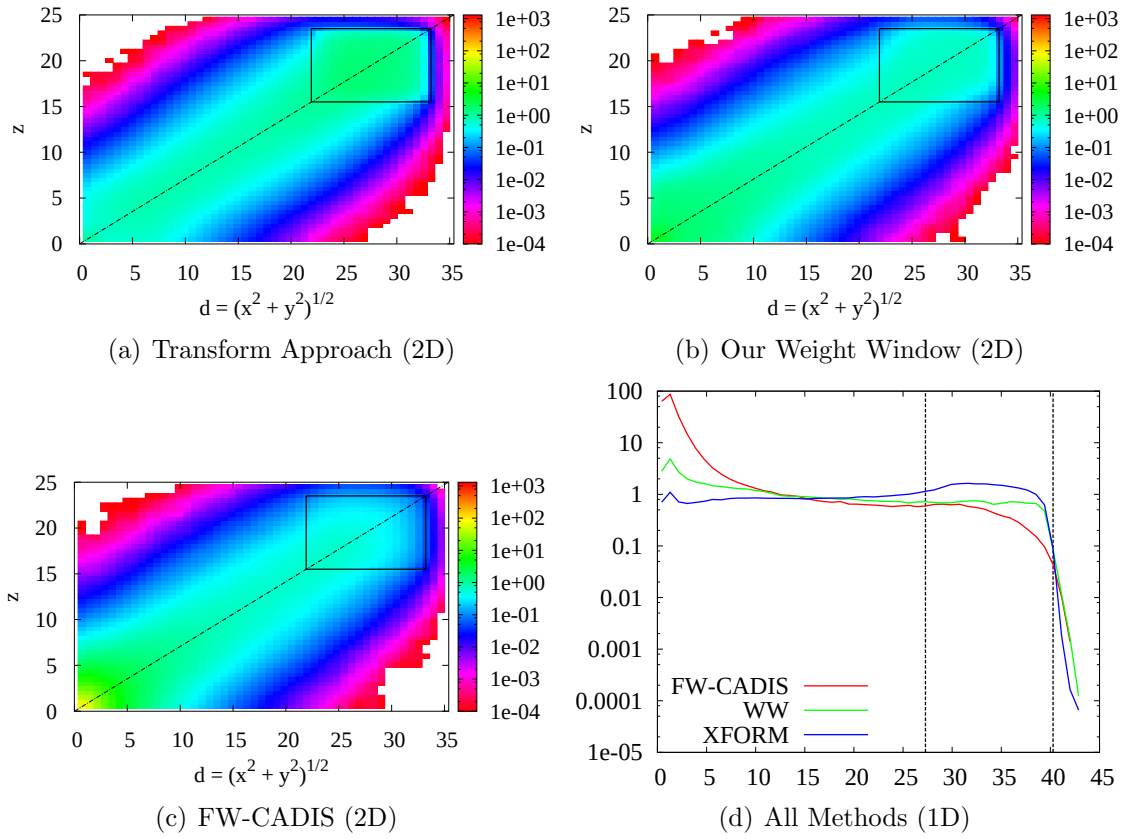

(a) Transform Approach (2D)

(b) Our Weight Window (2D)

(c) FW-CADIS (2D)

(d) All Methods (1D)

Figure 6.3: Group-2 FOM for SR Flux Problem

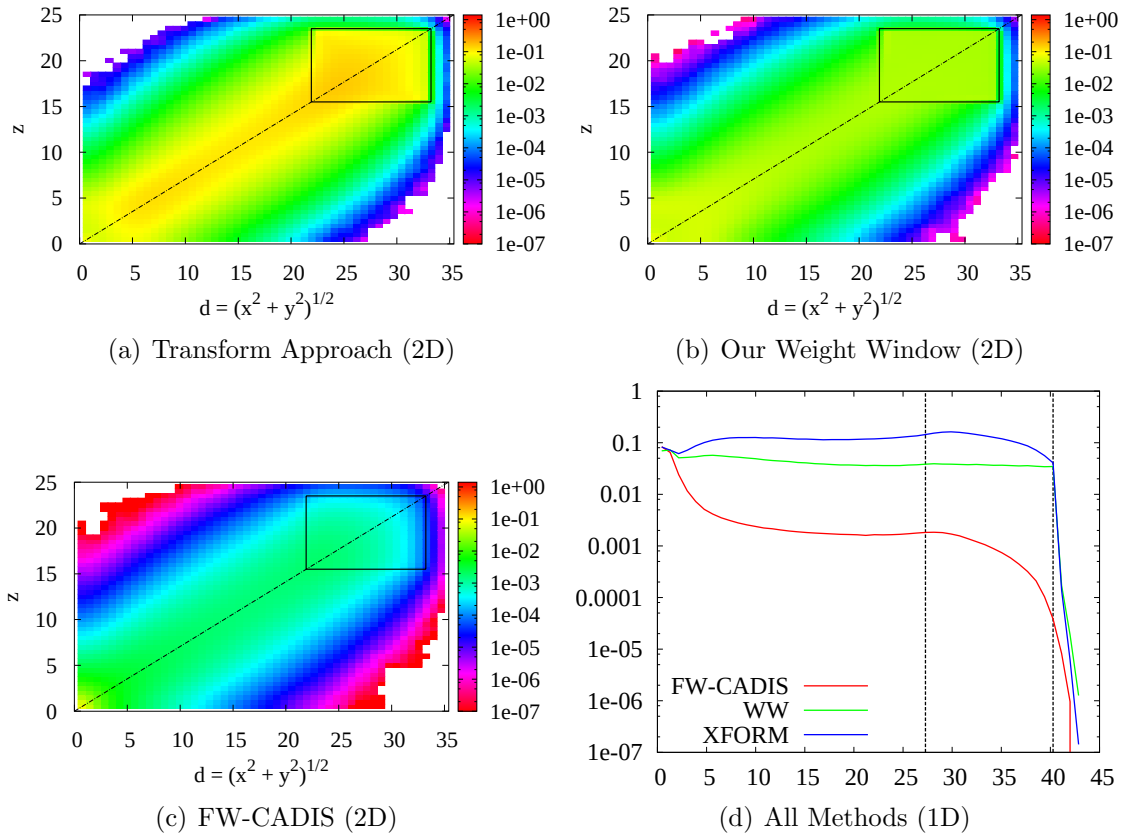

(a) Transform Approach (2D)

(b) Our Weight Window (2D)

(c) FW-CADIS (2D)

(d) All Methods (1D)

Figure 6.4: Group-2 Simulated MC Particle Flux for SR Flux Problem

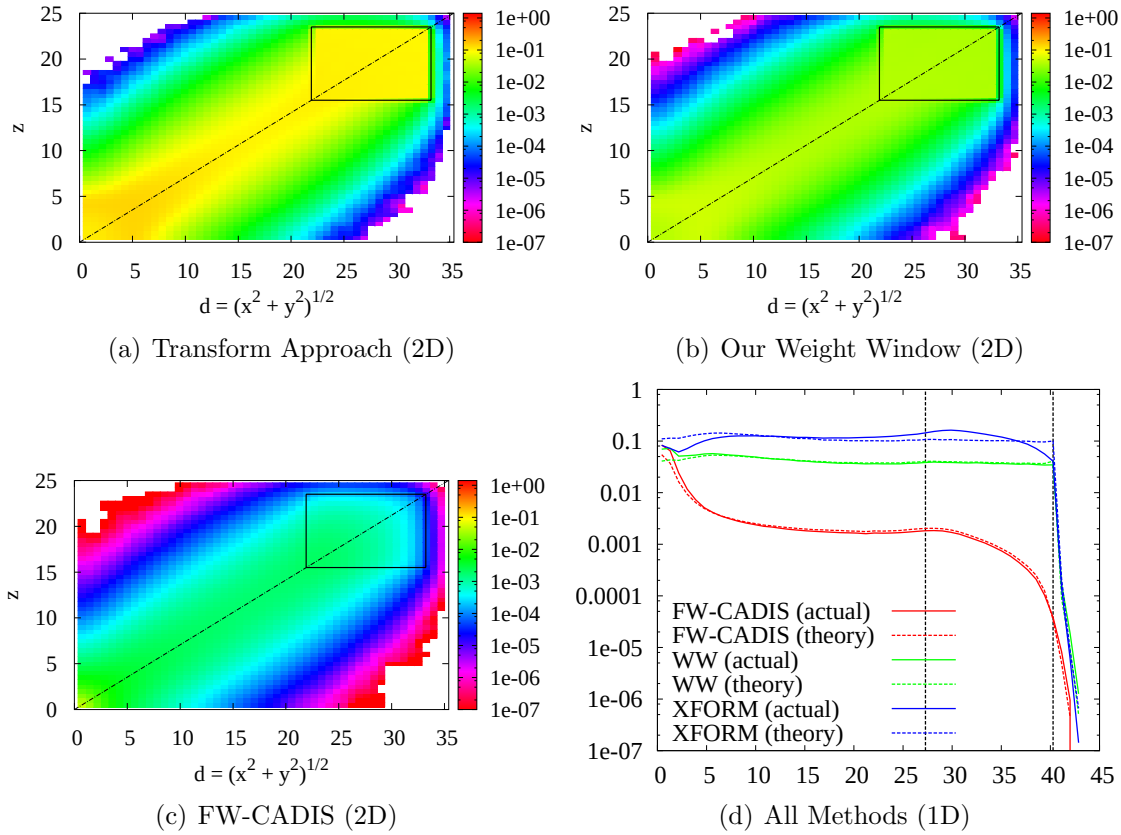

(a) Transform Approach (2D)

(b) Our Weight Window (2D)

(c) FW-CADIS (2D)

(d) All Methods (1D)

Figure 6.5: Group 2 Predicted MC Particle Flux for SR Flux Problem

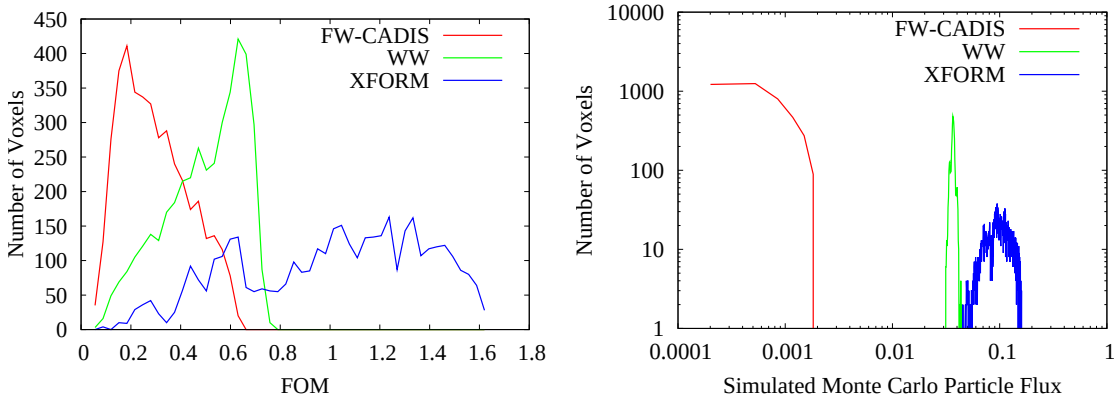

(a) Number of Voxels vs FOM

(b) Number of Voxels vs Simulated MC Flux

Figure 6.6: Group-2 Region Statistics by Number of Voxels for SR Flux Problem

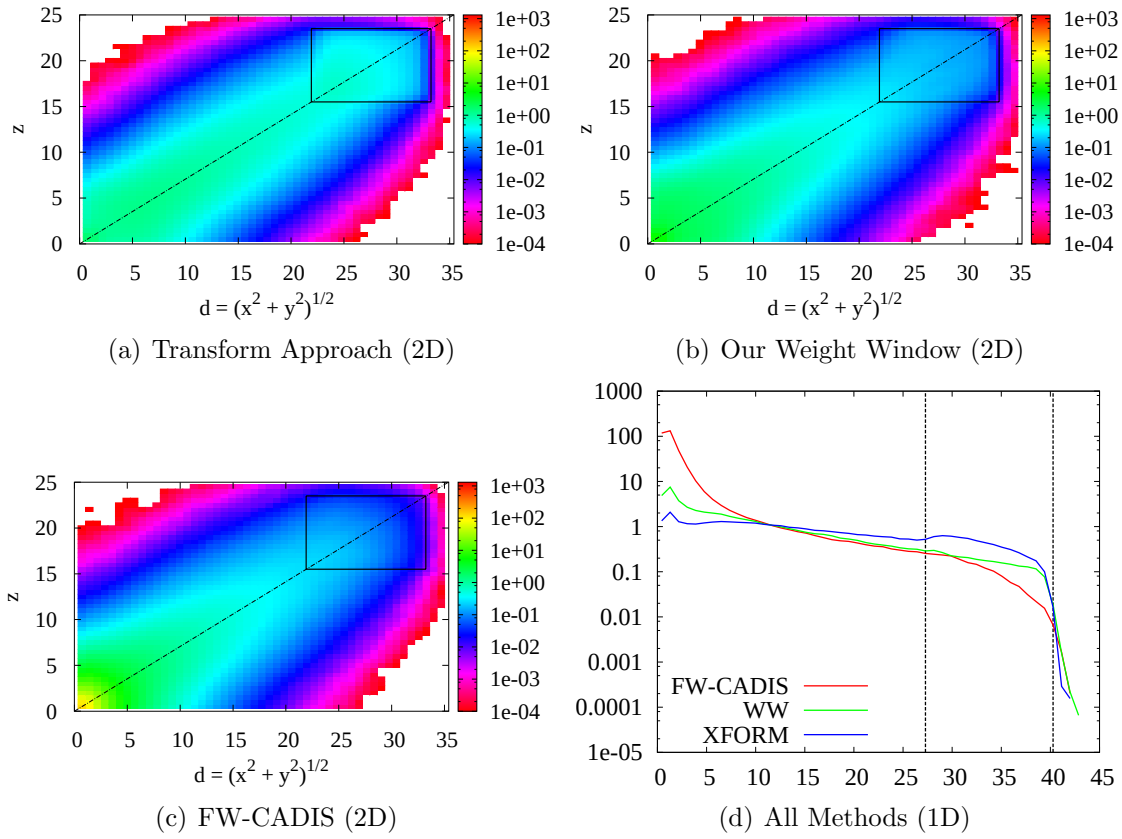

(a) Transform Approach (2D)

(b) Our Weight Window (2D)

(c) FW-CADIS (2D)

(d) All Methods (1D)

Figure 6.7: Group-2 FOM for SR Response Problem

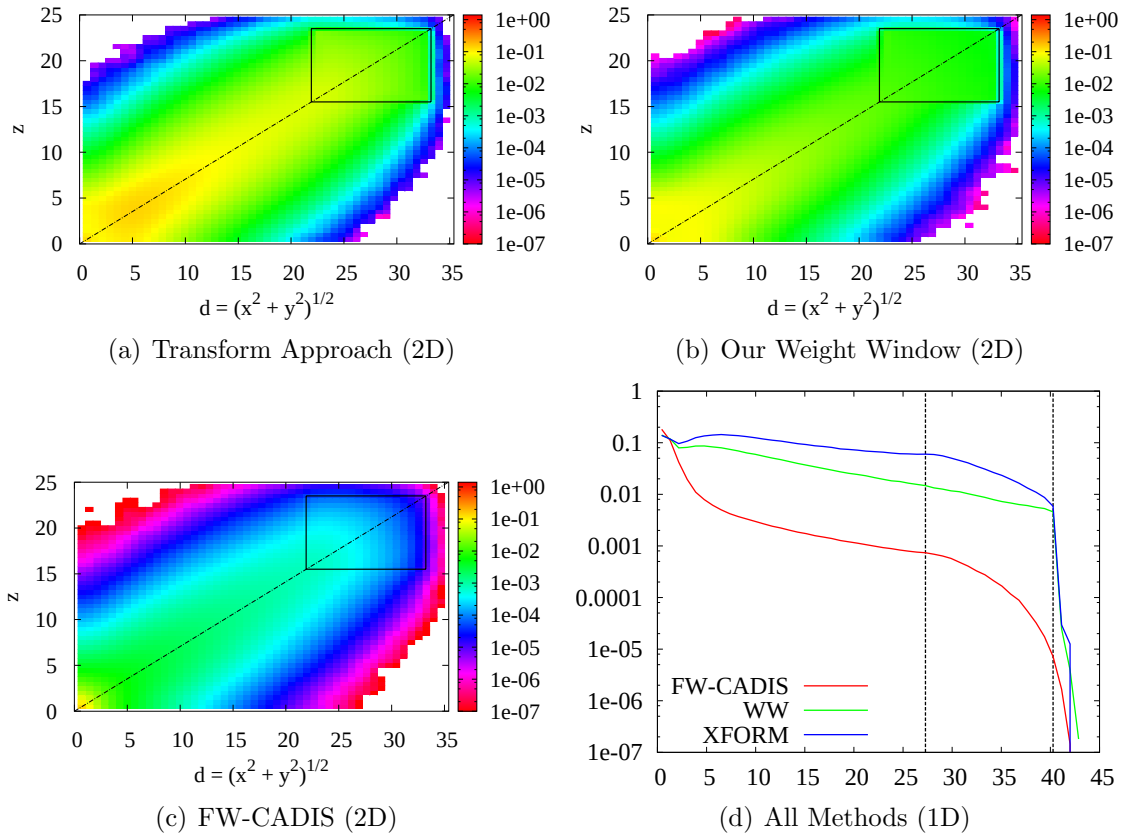

(a) Transform Approach (2D)

(b) Our Weight Window (2D)

(c) FW-CADIS (2D)

(d) All Methods (1D)

Figure 6.8: Group-2 Simulated MC Particle Flux for SR Response Problem

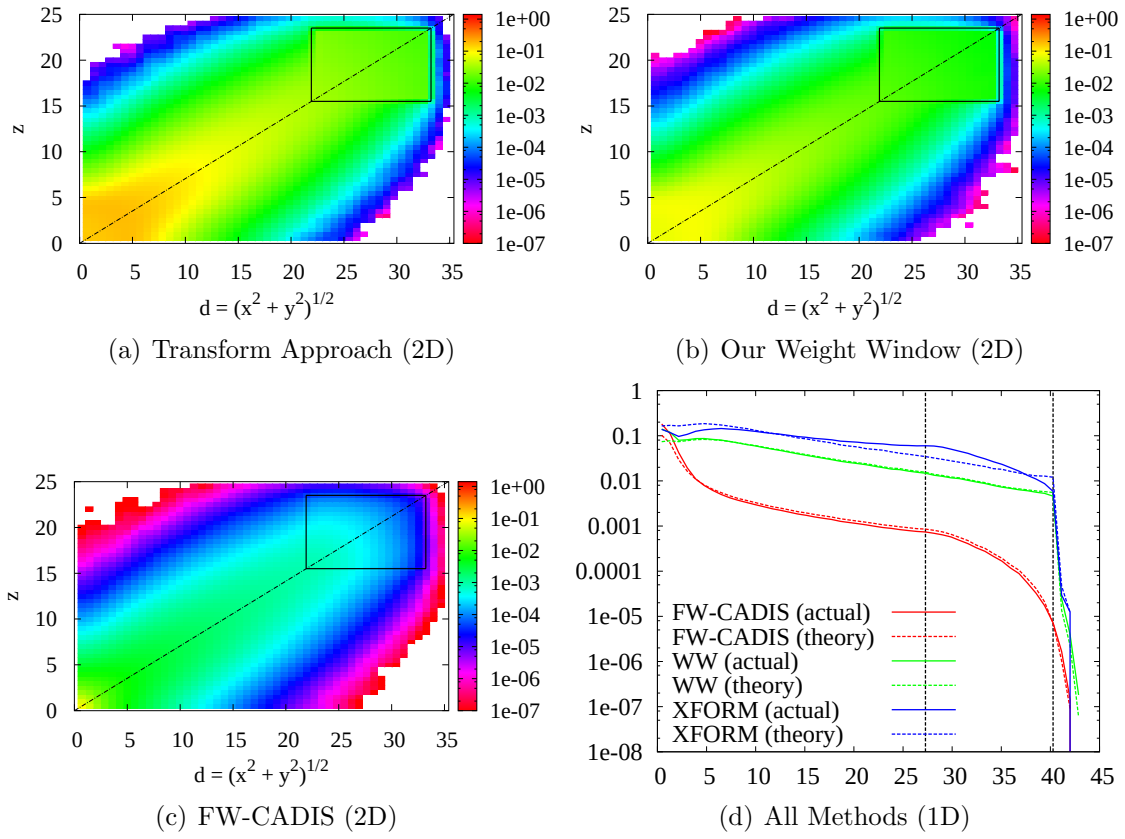

(a) Transform Approach (2D)

(b) Our Weight Window (2D)

(c) FW-CADIS (2D)

(d) All Methods (1D)

Figure 6.9: Group-2 Predicted MC Particle Flux for SR Response Problem

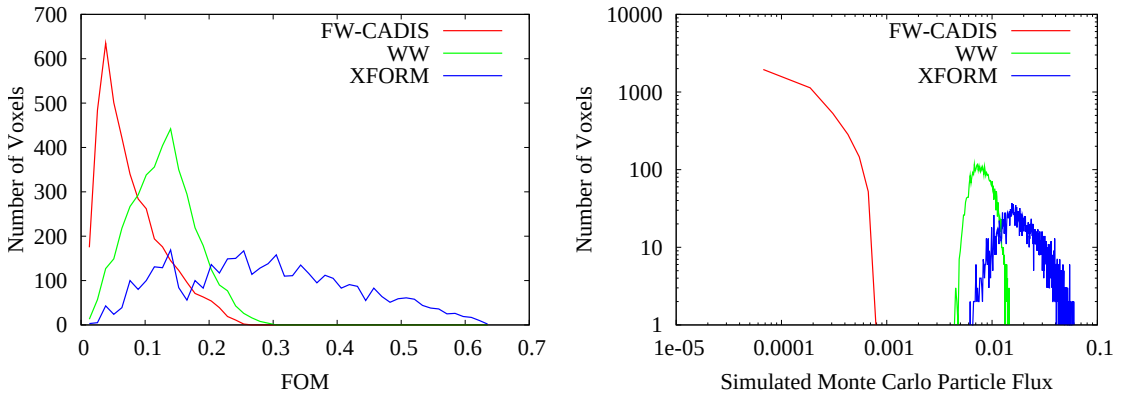

(a) Number of Voxels vs FOM

(b) Number of Voxels vs Simulated MC Flux

Figure 6.10: Group-2 Region Statistics by Number of Voxels for SR Response Problem

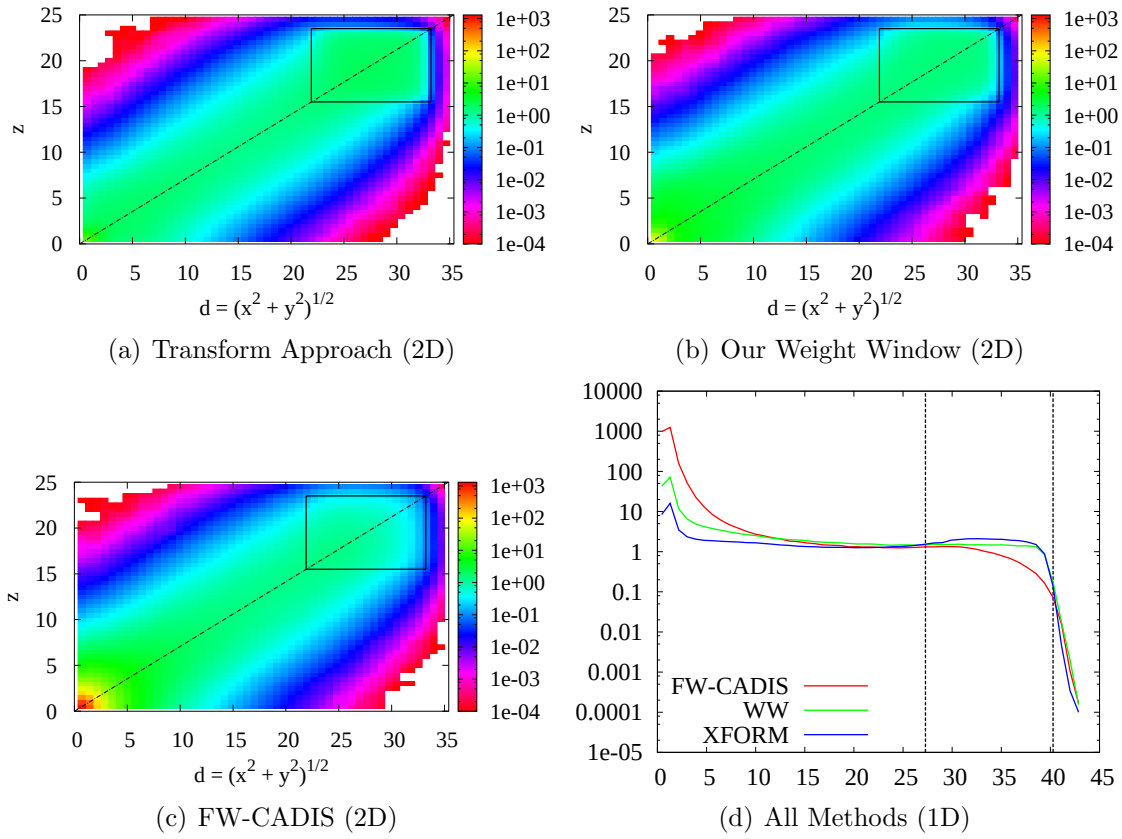

(a) Transform Approach (2D)

(b) Our Weight Window (2D)

(c) FW-CADIS (2D)

(d) All Methods (1D)

Figure 6.11: Total FOM for SR Flux Problem

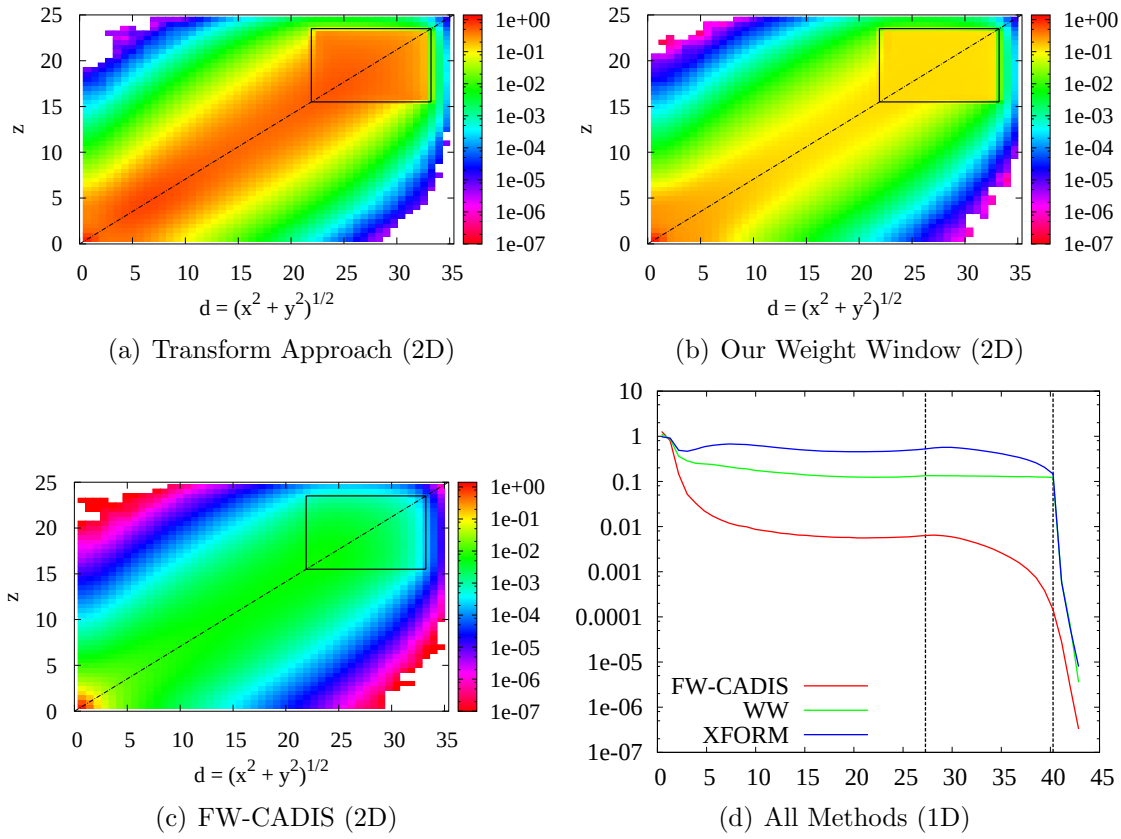

(a) Transform Approach (2D)

(b) Our Weight Window (2D)

(c) FW-CADIS (2D)

(d) All Methods (1D)

Figure 6.12: Total Simulated MC Particle Flux for SR Flux Problem

performance of the various methods.

The FOM data in Tables 6.1 - 6.4 indicate that the Transform approach performs most efficiently in every energy group for both the flux problem and the response problem, as determined by the median FOM. These tables also indicate that our weight window performs better than the FW-CADIS weight window. For the flux problem, in which we wish to obtain statistical results in every energy group, the Transform approach has a median FOM that is 3-6 times greater than that of the weight window approaches in the first energy group, 2-4 times greater in the second energy group, 1-3 times greater in the third energy group, and 1-3 times greater for the total flux. For the response problem, in which we wish to optimize the calculation to obtain the total flux, the Transform approach median FOM is 3-5 times greater than that of the weight window approaches in the first energy group, 2-4 time greater in the second energy group, 2-3 times greater in the third energy group, and 2-3 times greater for the total flux. Figures 6.6 and 6.10 present the group-2 FOM statistics for the entire region, specifically, the number of spatial elements that correspond to a particular FOM for the flux problem and response problem, respectively; Figures 6.14 and 6.18 are the corresponding FOM data for the total flux. In each figure, it is clear that the Transform approach has more spatial elements at a higher FOM than the weight window methods. Between the weight window methods, our weight window has a larger number of spatial elements at a higher FOM. Thus the figures are consistent with the analysis using the median FOM as a metric.

Just as in the source-detector flux problem, the source-region flux problem data in Tables 6.1 - 6.4 demonstrate a much more uniform median FOM from group to group than does the response problem data. For the flux problem data, the weight window methods both have a median FOM that varies by a factor of roughly 3 across the three energy groups, and the Transform approach has a median FOM that varies by a factor of 1.2. For the response problem data, the weight window methods both have a FOM that varies by a factor of 150 across the three energy groups, and the Transform approach varies by by a factor of nearly 100. This is to be expected, since the objective of the flux problem is to achieve roughly uniform results for every energy group, while the objective of the response problem is to optimize the total flux. Since most of the contribution to the total flux in the region comes from the third energy group, we expect the third energy group to be the most resolved statistically.

The data provided in Tables 6.1 - 6.4 show that if the objective is to obtain good results for every energy group, the flux problem should be solved; if the objective is to obtain the total flux, the response problem should be solved. This is clearly

seen by comparing the flux problem FOM to the response problem FOM for the first energy group and for the total flux. In the first energy group, the median FOM values for the flux problem are 25-30 times greater than for the response problem; while for the total flux, the median FOM values for the response problem are 2-3 times greater than for the flux problem. Therefore, each method has its utility.

Figures 6.3, 6.7, 6.11, and 6.15 demonstrate the distribution of the FOM in the 2D plane ($x = y$) and along the diagonal ($x = y = z$). The figures show that the FOM is greatest along the diagonal from the source to the region. Figures 6.3 and 6.7 further clarify the difference between the flux problem and response problem, where the response problem FOM decreases much more rapidly than the flux problem FOM, again due to the negligible contribution of the group-2 flux to the response (total flux). All the figures except Figure 6.7 show a saddle-like shape that peaks at the source. Intuitively, this FOM distribution should resolve the region response (flux) reasonably well, since the regions of space that have the largest contribution to the region response (flux) are the most resolved statistically.

Tables 6.5 - 6.8 demonstrate that for the flux problem, all the methods approximately populate the region with the same median Monte Carlo particle flux. For all three methods, the Monte Carlo particle flux across the three energy groups varies by only a factor of roughly 1.4, a small differential compared to the actual neutron flux which varies by nearly two orders of magnitude from the first group to the third group in the region of interest. For the response problem, Tables 6.5 - 6.8 show that the Monte Carlo particle flux varies dramatically from group 1 to group 3 – by at least two orders of magnitude. The proportion of Monte Carlo particles within each group is roughly proportional to the scalar neutron flux within each group in the region. (The group-3 scalar neutron flux is roughly an order of magnitude larger than the group-2 scalar flux and 2 orders of magnitude larger than the group-1 scalar flux.) These results, for both the flux and response problem, are consistent with the desired objectives of each method.

To further illustrate that the simulations behave as expected, the simulated Monte Carlo particle flux is compared to the theoretically predicted Monte Carlo particle flux. The simulated Monte Carlo particle flux is depicted in Figures 6.4, 6.8, 6.12, and 6.16 for the various problems and the corresponding predicted Monte Carlo particle flux is shown in Figures 6.5, 6.9, 6.13, and 6.17. The 1D Monte Carlo particle flux plots include both the simulated (actual) data and the predicted (theory) data to better compare the accuracy of the theory. By comparing the 1D and 2D figures, we observe that there is very good agreement between the simulated and predicted

Monte Carlo particle flux. The most significant deviation exists in the Transform approach, where the predicted Monte Carlo particle flux is only an approximation. Both weight window methods, however, show nearly exact agreement between the theoretical predictions and the simulated values.

Just as in the source-detector analysis, it is clear from the Monte Carlo particle flux figures that a positive correlation exists between the Monte Carlo particle flux and the FOM, since the shape of the curves is similar.

6.7 Summary

In this section, we have described source-region problems – both the response problem and flux problem. To solve these problems, we chose to distribute the Monte Carlo particle flux according to the contributon flux (or some slightly modified form of the contributon flux) by employing an appropriate weight window or "transform" function. To implement the weight windows or Transform approach, it was necessary to define the adjoint problem that corresponds to the intended solution – the region flux or response. We did this by first defining the appropriate adjoint contributon source and then deriving the corresponding adjoint neutron source. Finally, we examined a 3-group test problem to validate the theory and assess the performance of each method. The results indicate that the theory is correct: for a given weight window or "transform" function, the Monte Carlo particle flux is correctly predicted by the theory. The results also indicate that despite the additional computational cost per particle of the Transform approach, it produces a larger FOM than the weight window methods, since it more faithfully models the physics of the forward contributon equation. Also, our weight window outperforms the FW-CADIS weight window by modifying the contributon distribution with the spatial parameter $B(\mathbf{x})$. In fact, the FOM for the FW-CADIS weight window falls off by an order of magnitude inside the region of interest. Lastly, the results indicate that there is a positive correlation between the FOM and the Monte Carlo particle flux, but no exact theoretical model has been identified to predict the correlation.

Since source-region problems are really just a superposition of many source-detector problems, the prescriptions (and results) given here reduce to those in the previous chapter when the region $\mathcal{V}_R$ shrinks down to a few spatial elements. As the region expands to fill the entire space, we expect the methods to continue to perform similar to the 3-group problem tested here, except with more variation within the region $\mathcal{V}_R$. The next chapter discusses problems in which the region $\mathcal{V}_R$ expands to

fill the entire space.

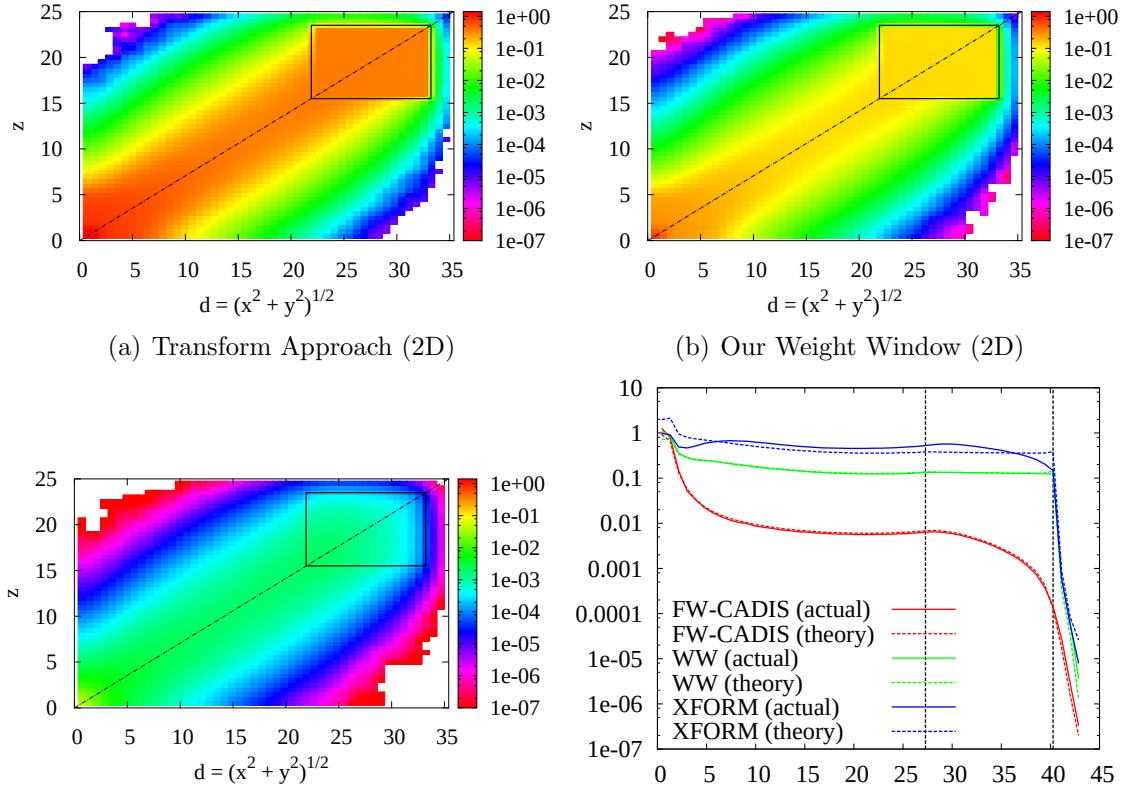

(a) Transform Approach (2D)

(b) Our Weight Window (2D)

(c) FW-CADIS (2D)

(d) All Methods (1D)

Figure 6.13: Total Predicted MC Particle Flux for the Source-Region (SR) Flux Problem

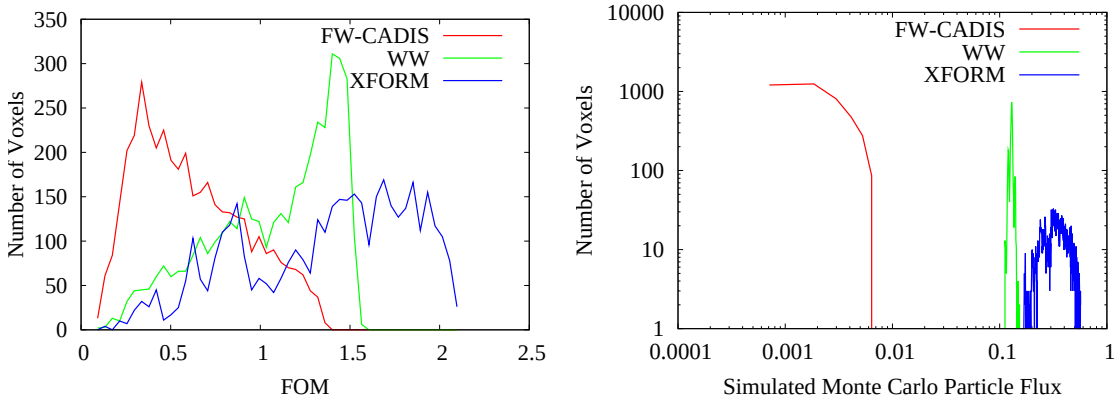

(a) Number of Voxels vs FOM (b) Number of Voxels vs Simulated MC Flux

Figure 6.14: Total Region Statistics by Number of Voxels for SR Flux Problem

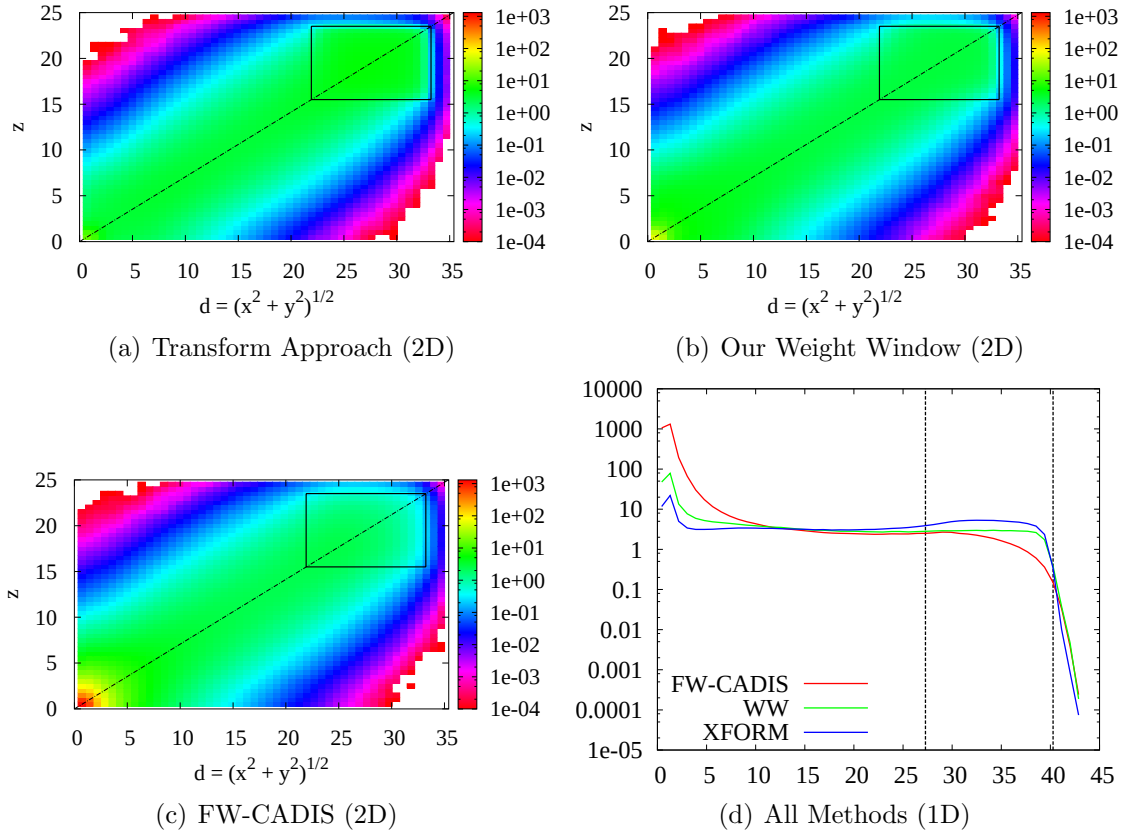

(a) Transform Approach (2D) (b) Our Weight Window (2D)

(c) FW-CADIS (2D) (d) All Methods (1D)

Figure 6.15: Total FOM for SR Response Problem

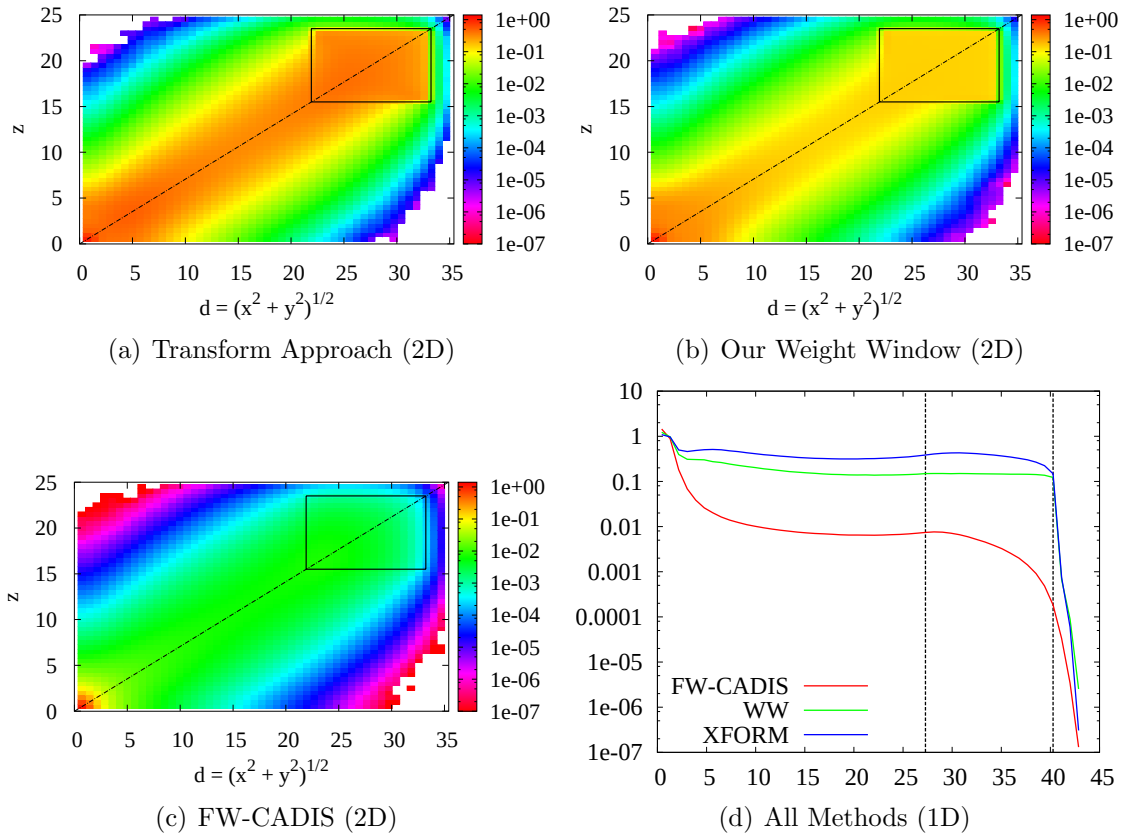

(a) Transform Approach (2D)

(b) Our Weight Window (2D)

(c) FW-CADIS (2D)

(d) All Methods (1D)

Figure 6.16: Total Simulated MC Particle Flux for SR Response Problem

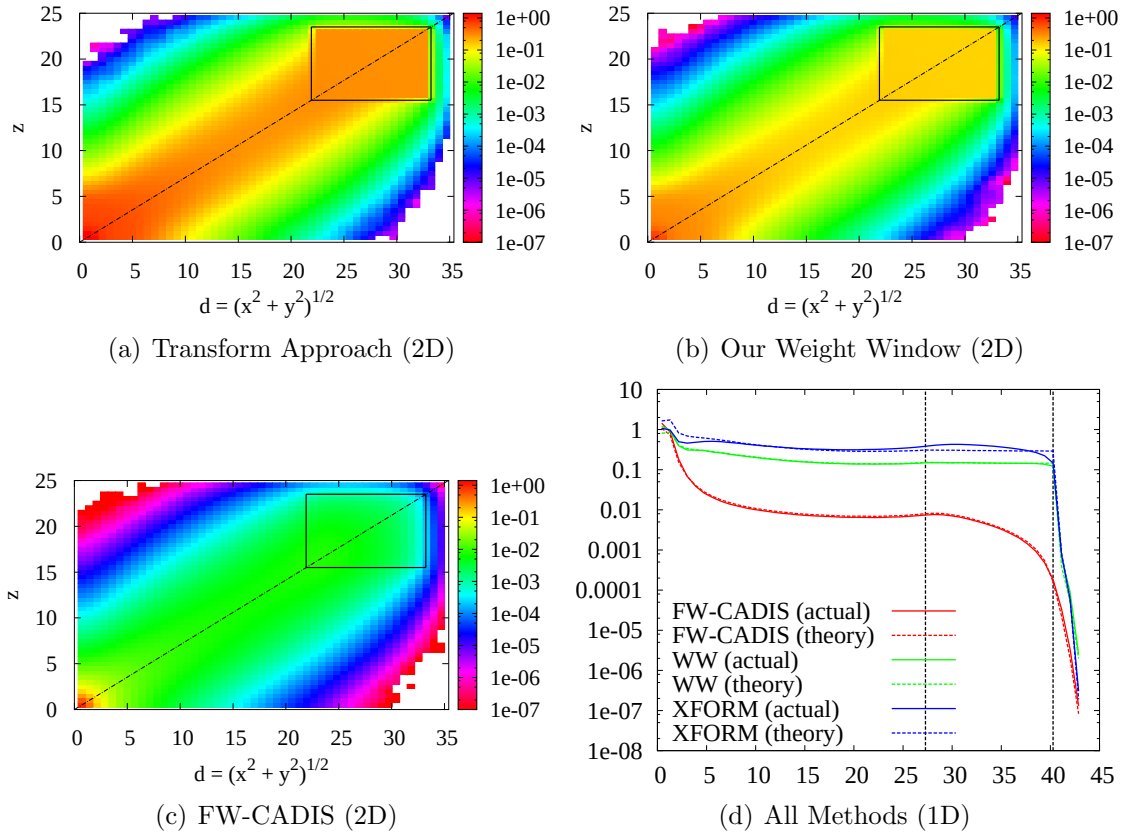

(a) Transform Approach (2D)

(b) Our Weight Window (2D)

(c) FW-CADIS (2D)

(d) All Methods (1D)

Figure 6.17: Total Predicted MC Particle Flux for SR Response Problem

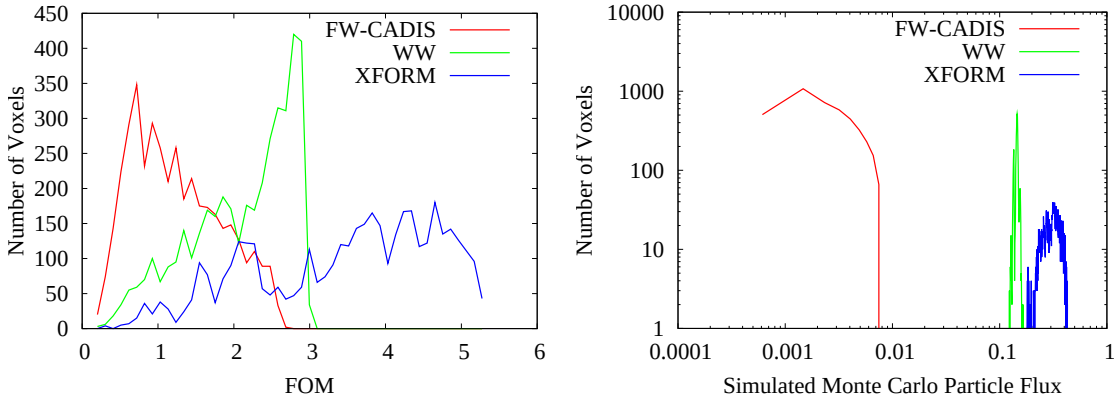

(a) Number of Voxels vs FOM

(b) Number of Voxels vs Simulated MC Flux

Figure 6.18: Total Region Statistics by Number of Voxels for SR Response Problem

Chapter VII

Global Problems

In global problems, we wish to estimate a solution throughout the entire system, rather than just in a portion of space, as in source-detector and source-region problems. However, like the source-detector and source region problems, there are two types of global problems – the *flux problem* and the *response problem*. The objective of the *global flux problem* is to obtain the scalar neutron flux $\phi(\mathbf{x}, E)$ throughout the entire system and for all energies; the objective of the *global response problem* is to estimate the response

$$\mathcal{R}(\mathbf{x}) = \int_0^\infty \Sigma_{\mathcal{R}}(\mathbf{x}, E)\phi(\mathbf{x}, E)dE, \tag{7.1}$$

throughout the system.

To solve these problems, we extend the concepts developed in the previous two chapters for the source-detector and source-region problem. Namely, the Monte Carlo particle flux is distributed proportional to a contributon flux, since this distribution corresponds to the relative contribution of a particle at a point in phase-space to the response (or flux). As in both the source-detector and source-region problems, by defining the adjoint contributon source in a specific way, a Monte Carlo particle flux distribution is achieved that corresponds to the intended solution – flux or response. From the adjoint contributon source, the adjoint neutron source is determined and the adjoint problem can be solved and used to implement the weight window and Transform approaches.

Although we choose to solve global problems by distributing Monte Carlo particles according to the contributon flux, there are other logical options that follow from the work done by Cooper [28] in developing a global weight window for monoenergetic problems. The first option – a uniform Monte Carlo particle flux distribution in

space and energy – solves the flux problem, in which an accurate estimate of the scalar flux is desired at all spatial locations and for all energy. That is, the desired Monte Carlo particle flux is given by

$$\mathcal{M}(\mathbf{x}, E) = \mathrm{C}_0^{-1}, \tag{7.2}$$

where C_0 is an arbitrary constant. According to Eq. 4.8, the weight window that accomplishes this distribution is the following:

$$\mathrm{w}(\mathbf{x}, E) = \mathrm{C}_0 \phi(\mathbf{x}, E). \tag{7.3}$$

This weight window only requires the forward solution.

Another logical Monte Carlo particle distribution that follows from Cooper's work is to disperse particles in energy according to the energy spectrum of the physical particles, but uniformly in space. That is, the desired Monte Carlo particle flux is given by

$$\mathcal{M}(\mathbf{x}, E) = \mathrm{C}_0^{-1} \frac{\phi(\mathbf{x}, E)}{\int_0^\infty \phi(\mathbf{x}, E')dE'}, \tag{7.4}$$

where C_0 is an arbitrary constant. Integrating this distribution over energy demonstrates that the energy-integrated (total) Monte Carlo particle flux is uniform in space (i.e. $\mathcal{M}(\mathbf{x}) = \mathrm{C}_0^{-1}$). Using Eq. 4.8, we obtain the weight window that accomplishes this distribution:

$$\mathrm{w}(\mathbf{x}, E) = \mathrm{C}_0 \int_0^\infty \phi(\mathbf{x}, E')dE'. \tag{7.5}$$

This weight window is energy-independent and also only requires the forward solution. Since those energies which are more populated with physical particles often tend to have a greater contribution to quantities of interest, this Monte Carlo particle distribution is perhaps more useful and practical than one that populates all space and energy equally with Monte Carlo particles.

Although these two particle distributions are specific to obtaining certain solutions, they demonstrate that other options exist to distribute Monte Carlo particles, in addition to distributing particles according to the contributon flux. Specifically, these do not require information from an adjoint calculation.

7.1 The Response Problem

As previously mentioned, in *global response problems* we wish to obtain an energy-integrated response

$$\mathcal{R}(\mathbf{x}) = \int_0^\infty \int_{4\pi} \Sigma_{\mathcal{R}}(\mathbf{x}, E)\psi(\mathbf{x}, \mathbf{\Omega}, E)d\Omega dE, \tag{7.6}$$

at all points $\mathbf{x}$ in the entire system $\mathcal{V}$.

For all three approaches – Transform approach, our weight window, and FW-CADIS, a suitable adjoint contributon source is defined as:

$$Q^{\mathrm{c}}(\mathbf{x}, \mathbf{\Omega}, E) = \frac{\Sigma_{\mathcal{R}}(\mathbf{x}, E)\psi(\mathbf{x}, \mathbf{\Omega}, E)}{\int_0^\infty \int_{4\pi} \Sigma_{\mathcal{R}}(\mathbf{x}, E')\psi(\mathbf{x}, \mathbf{\Omega}', E')d\Omega' dE'}. \tag{7.7}$$

At every point $\mathbf{x}$, this source emits contributons (response particles) at a rate proportional to their relative contribution to the spatial response $\mathcal{R}(\mathbf{x})$. Also, the total contributon emission rate is the same for every point $\mathbf{x} \in \mathcal{V}$, i.e.,

$$\begin{aligned} Q^{\mathrm{c}}(\mathbf{x}) &= \int_0^\infty \int_{4\pi} Q^{\mathrm{c}}(\mathbf{x}, \mathbf{\Omega}, E)d\Omega dE \\ &= 1. \end{aligned} \tag{7.8}$$

Thus, every spatial location $\mathbf{x}$ essentially functions as a point detector which emits contributons at a rate proportional to the contribution to the response $\mathcal{R}(\mathbf{x})$, and every point detector is treated with equal importance by emitting particles at the same rate. Thus, the global problem can also be viewed as the superposition of many source-detector problems, where each detector is a point $\mathbf{x} \in \mathcal{V}$.

The adjoint neutron source is determined from Eq. 5.12:

$$\begin{aligned} Q^*(\mathbf{x}, \mathbf{\Omega}, E) &= \frac{Q^{\mathrm{c}}(\mathbf{x}, \mathbf{\Omega}, E)}{\psi(\mathbf{x}, \mathbf{\Omega}, E)} \\ &= \frac{\Sigma_{\mathcal{R}}(\mathbf{x}, E)}{\int_0^\infty \int_{4\pi} \Sigma_{\mathcal{R}}(\mathbf{x}, E')\psi(\mathbf{x}, \mathbf{\Omega}', E)d\Omega' dE'}. \end{aligned} \tag{7.9}$$

With the adjoint problem completely defined, the various methods can be implemented to solve the global response problem. Each method is discussed later in this chapter.

7.2 The Flux Problem

In *global flux problems*, we wish to estimate the energy-dependent scalar flux $\phi(\mathbf{x}, E)$ for all energies E and for all $\mathbf{x}$ in the entire system $\mathcal{V}$. Just as in the previous section on the response problem, the adjoint contributon source must be defined. For all three approaches – Transform approach, our weight window, and FW-CADIS, a suitable contributon source is defined as:

$$Q^{\mathrm{c}}(\mathbf{x}, \mathbf{\Omega}, E) = \begin{cases} \dfrac{\psi(\mathbf{x}, \mathbf{\Omega}, E)}{\phi(\mathbf{x}, E)}, & \text{for } \mathbf{x} \in \mathcal{V}, \\ 0, & \text{otherwise.} \end{cases} \tag{7.10}$$

At every spatial location $\mathbf{x}$ and for every energy E, this adjoint contributon source emits contributons at a uniform rate (i.e. $Q^{\mathrm{c}}(\mathbf{x}, E) = \int_{4\pi} Q^{\mathrm{c}}(\mathbf{x}, \mathbf{\Omega}, E) d\Omega = 1$) with an angular distribution proportional to their contribution to the scalar flux. Similar to the response problem, every point $\mathbf{x}$ essentially functions as a point detector that uniformly emits contributons in energy. This results in a contributon flux that corresponds most closely to obtaining a statistically resolved estimate of the scalar flux for every energy.

The adjoint neutron source is determined from Eq. 5.12:

$$\begin{aligned} Q^{*}(\mathbf{x}, \mathbf{\Omega}, E) &= \frac{Q^{\mathrm{c}}(\mathbf{x}, \mathbf{\Omega}, E)}{\psi(\mathbf{x}, \mathbf{\Omega}, E)} \\ &= \begin{cases} \dfrac{1}{\phi(\mathbf{x}, E)}, & \text{for } \mathbf{x} \in \mathcal{V}, \\ 0, & \text{otherwise.} \end{cases} \end{aligned} \tag{7.11}$$

7.3 The Transform Approach

Now that the adjoint problem has been completely defined for global problems – flux and response – the transform approach is easily implemented. The "transform" function that we use in this thesis is given by Eq. 4.104 as

$$\hat{\mathcal{T}}(\mathbf{x}, \mathbf{\Omega}, E) = \frac{B(\mathbf{x})}{\psi^{*}(\mathbf{x}, \mathbf{\Omega}, E)}. \tag{7.12}$$

This produces an angular Monte Carlo particle flux distribution proportional to the angular contributon flux, modified by a spatial parameter $B(\mathbf{x})$ defined below:

$$m(\mathbf{x}, \mathbf{\Omega}, E) = \frac{\psi^{\mathrm{c}}(\mathbf{x}, \mathbf{\Omega}, E)}{B(\mathbf{x})}. \tag{7.13}$$

For global problems, $B(\mathbf{x})$ achieves one thing: it results in an energy-dependent Monte Carlo particle flux $\mathcal{M}(\mathbf{x}, E)$ that is proportional to the relative contribution of the Monte Carlo particles to the response (flux) at $\mathbf{x}$ and produces an energy-integrated Monte Carlo flux $\mathcal{M}(\mathbf{x})$ that is approximately uniform across the system. Thus, Monte Carlo particles are roughly distributed uniformly in space and in energy according to their relative contribution to the space-dependent response or flux.

The form of $B(\mathbf{x})$ for global problems is given as

$$B(\mathbf{x}) = \phi^{\mathrm{c}}(\mathbf{x}), \tag{7.14}$$

where we approximate the scalar contributon flux $\phi^{\mathrm{c}}(\mathbf{x})$ as

$$\phi^{\mathrm{c}}(\mathbf{x}) \approx \int_0^\infty \phi(\mathbf{x}, E)\phi^*(\mathbf{x}, E)dE. \tag{7.15}$$

To see how how $B(\mathbf{x})$ distributes Monte Carlo particles uniformly in space and according to their relative contribution to the space dependent response or flux, we begin with the Eq. 4.96:

$$\begin{aligned} \mathcal{M}(\mathbf{x}, E) &= \frac{\phi^{\mathrm{c}}(\mathbf{x}, E)}{B(\mathbf{x})} \\ &= \frac{\phi^{\mathrm{c}}(\mathbf{x}, E)}{\phi^{\mathrm{c}}(\mathbf{x})}. \end{aligned} \tag{7.16}$$

Integrating Eq. 7.16 over energy, we obtain the energy-integrated (total) Monte Carlo particle flux at $\mathbf{x} \in \mathcal{V}$:

$$\mathcal{M}(\mathbf{x}) \approx (4\pi C_{\mathrm{norm}})^{-1}, \quad \mathbf{x} \in \mathcal{V}. \tag{7.17}$$

Together, Eqs. 7.16 and 7.17 affirm that the distribution of the Monte Carlo particles flux is uniform in space and proportional to the relative contribution to the response (or flux) in energy, as determined by the contributon flux.

The "transform" function has now been completely defined for the global problem and can be used as described in Section 4.3 to implement the Transform approach.

7.4 Our Weight Window

In Section 4.2.1, we showed that the weight window center $\mathrm{w}(\mathbf{x}, E)$ and the scalar Monte Carlo particle flux $\mathcal{M}(\mathbf{x}, E)$ are related by Eq. 4.9:

$$\mathrm{w}(\mathbf{x}, E) = \frac{\phi(\mathbf{x}, E)}{\mathcal{M}(\mathbf{x}, E)}. \tag{7.18}$$

For the global flux or response problem, our weight window distributes Monte Carlo particles according to the scalar contributon flux distribution, with the same modification used for the Transform approach, i.e. $B(\mathbf{x})$. We define the Monte Carlo particle flux as

$$\mathcal{M}(\mathbf{x}, E) = \frac{\phi^{\mathrm{c}}(\mathbf{x}, E)}{B(\mathbf{x})}, \tag{7.19}$$

where the spatial parameter $B(\mathbf{x})$ was defined in the previous section on the Transform approach (see Eq. 7.14). Then, the weight window is approximated as

$$\begin{aligned} \mathrm{w}(\mathbf{x}, E) &= \frac{B(\mathbf{x})\phi(\mathbf{x}, E)}{\phi^{\mathrm{c}}(\mathbf{x}, E)} \\ &\approx \frac{B(\mathbf{x})}{\phi^{*}(\mathbf{x}, E)}, \end{aligned} \tag{7.20}$$

where we have approximated the scalar contributon flux $\phi^{\mathrm{c}}(\mathbf{x}, E)$ as

$$\phi^{\mathrm{c}}(\mathbf{x}, E) \approx \phi(\mathbf{x}, E)\phi^{*}(\mathbf{x}, E). \tag{7.21}$$

This weight window produces a scalar Monte Carlo particle flux similar to that of the Transform approach, but without modifying any of the particle physics. The spatial function $B(\mathbf{x})$ accomplishes the same objective here: it results in an energy-dependent Monte Carlo particle flux $\mathcal{M}(\mathbf{x}, E)$ that is proportional to the relative contribution of the Monte Carlo particles to the response (flux) at $\mathbf{x}$ and produces an energy-integrated Monte Carlo flux $\mathcal{M}(\mathbf{x})$ that is approximately uniform across the system. Thus, Monte Carlo particles are roughly distributed uniformly in space and according to their relative contribution to the space-dependent response or flux.

With our weight window completely defined for the global problem, it can be implemented according to the specifications given in the general section on weight windows, Section 4.2.

7.5 FW-CADIS

For the global problem, the FW-CADIS weight window maintains the form of the classical weight window, where the weight window is inversely proportional to the adjoint scalar flux:

$$\mathrm{w}(\mathbf{x}, E) = \frac{1}{\phi^*(\mathbf{x}, E)}. \tag{7.22}$$

Again, according to Eq. 4.8 given in Section 4.2.1, this weight window results in a Monte Carlo particle flux that is approximately proportional to the scalar contributon flux:

$$\begin{aligned} \mathcal{M}(\mathbf{x}, E) &= \frac{\phi(\mathbf{x}, E)}{\mathrm{w}(\mathbf{x}, E)} \\ &= \phi(\mathbf{x}, E)\phi^*(\mathbf{x}, E) \\ &\approx \phi^{\mathrm{c}}(\mathbf{x}, E). \end{aligned} \tag{7.23}$$

As with our weight window, all the details necessary to implement the FW-CADIS weight window are in Section 4.2.

7.6 Numerical Test Problem

To verify that the methods perform as the theory predicts, and to compare the methods for efficiency and statistical quality, we consider the 3-group problem introduced in the previous two chapters with the entire system as the solution space. Our objectives remain the same: 1) to assess how well the approaches perform on a multigroup shielding problem, and 2) to verify that the methods perform as the theory predicts.

7.6.1 Problem Description

Figure 7.1 demonstrates the geometry as before: a 25 cm homogeneous cube with a 1 cm cubic source in the corner, symmetric boundary conditions at the planes that cut through the source, and vacuum boundaries at the exterior planes. The source is a unit source (1 $\mathrm{cm}^{-3}\mathrm{s}^{-1}$), in the first energy group only. The total cross-section is set equal to unity throughout space and energy (i.e. $\Sigma_{t,g} = 1\ \mathrm{cm}^{-1}$). The scattering matrix is provided in the material data section of the Figure 7.1. For global problems, the entire system is the solution space.

Figure 7.2 demonstrates that this problem is indeed a shielding problem, with the

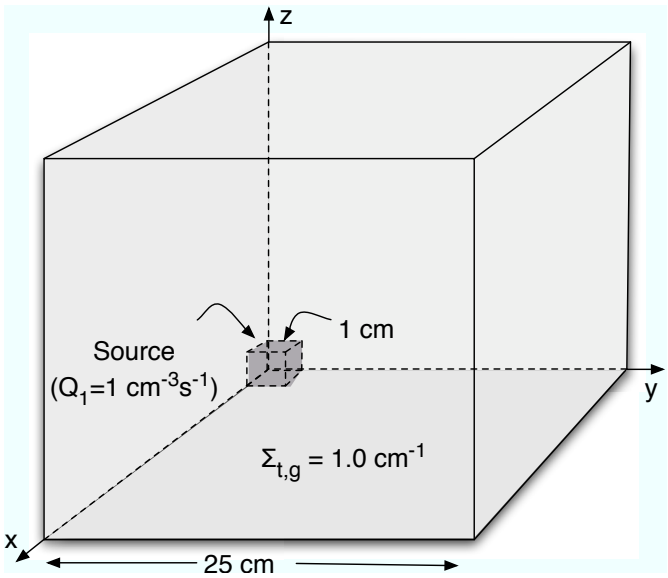

Data \ g	1	2	3
$\Sigma_{t,g}\,(cm^{-1})$	1.0	1.0	1.0
$\Sigma_{s,g\rightarrow 1}\,(cm^{-1})$	0.6	0.0	0.0
$\Sigma_{s,g\rightarrow 2}\,(cm^{-1})$	0.1	0.7	0.0
$\Sigma_{s,g\rightarrow 3}\,(cm^{-1})$	0.05	0.1	0.8
$Q_g\,(cm^{-3}s^{-1})$	1.0	0.0	0.0

Figure 7.1: Problem Geometry and Material Properties

scalar flux being attenuated by 20 orders of magnitude in the first energy group, 18 orders of magnitude in the second group, nearly 16 orders of magnitude in the third group, and roughly 17 orders of magnitude in the energy-integrated (total) flux.

The objective of the global flux problem is to obtain the scalar flux $\phi_{c,g}$ for every energy group g and in every spatial element $\mathcal{V}_c$ within the system, where the scalar flux $\phi_{c,g}$ is defined as

$$\phi_{c,g} = \frac{1}{V_c}\int_{\mathcal{V}_c}\int_{E_g}^{E_{g-1}} \phi(\mathbf{x}, E)dEdV. \tag{7.24}$$

The objective of the global response problem is to obtain the response $\mathcal{R}_c$ in each spatial element $\mathcal{V}_c$ within the system. We again investigate a special response, the energy-integrated (total) flux, denoted simply as ϕ_c and defined as

$$\phi_c = \sum_{g=1}^{3} \phi_{c,g}. \tag{7.25}$$

(For this response, we set $\Sigma_{\mathcal{R}}(\mathbf{x}, E) = 1$.) To analyze the results, we plot the figure of merit, the simulated scalar Monte Carlo particle flux, the theoretically predicted scalar Monte Carlo particle flux, and the global statistics for the second energy group and the total flux. These plots appear in Figures 7.3 - 7.18 and correspond to a 2D plane that stretches from the z-axis to the cube edge farthest from the source (i.e. the plane $x = y$), the line from the source corner to the far corner (i.e. the line

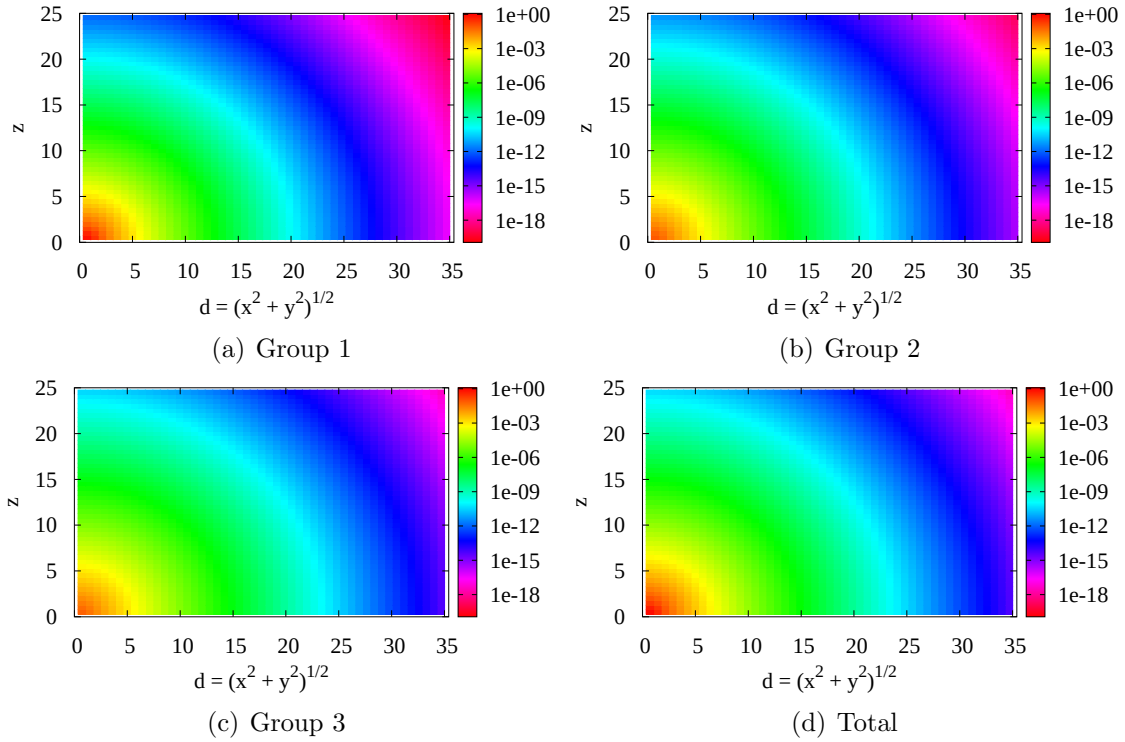

(a) Group 1 (b) Group 2

(c) Group 3 (d) Total

Figure 7.2: Scalar Flux along the plane $x = y$

$x = y = z$), and the FOM and Monte Carlo particle flux statistics throughout the entire system. These values are computed on a uniform 0.5 cm grid that is imposed on the problem geometry. Thus, the system consists of 125,000 spatial elements, each denoted by $\mathcal{V}_c$. (The source contains 8 spatial elements.)

The energy-dependent scalar Monte Carlo particle flux $\mathcal{M}_{c,g}$ and the energy-integrated scalar Monte Carlo particle flux $\mathcal{M}_c$ are volume-averaged quantities determined directly from the Monte Carlo simulation. The figures of merit (FOM) in each spatial element $\mathcal{V}_c$ are defined as

$$\begin{aligned} \mathrm{FOM}_{c,g} &= \frac{1}{\dfrac{\mathrm{Var}\left[\phi_{c,g}\right]}{\phi_{c,g}^2}\mathrm{T}_{\mathrm{cpu}}}, \\ \mathrm{FOM}_{c} &= \frac{1}{\dfrac{\mathrm{Var}\left[\phi_{c}\right]}{\phi_{c}^2}\mathrm{T}_{\mathrm{cpu}}}, \end{aligned} \tag{7.26}$$

where $\mathrm{T}_{\mathrm{cpu}}$ is the total run time, and $\phi_{c,g}$, ϕ_c, and the corresponding variances are volume-averaged quantities obtained directly from the Monte Carlo simulation.

The theoretically predicted energy-dependent scalar Monte Carlo particle flux

$\tilde{M}_{c,g}$ averaged over $\mathcal{V}_c$ is given for each method as:

$$\tilde{\mathcal{M}}_{c,g}^{\text{XFORM}} \approx \text{C}_0 \frac{\phi_{c,g}\Phi_{c,g}^*}{B_c}, \tag{7.27}$$

$$\tilde{\mathcal{M}}_{c,g}^{\text{WW}} = \text{C}_0 \frac{\phi_{c,g}\Phi_{c,g}^*}{B_c}, \tag{7.28}$$

$$\tilde{\mathcal{M}}_{c,g}^{\text{FWCADIS}} = \text{C}_0 \phi_{c,g}\Phi_{c,g}^*, \tag{7.29}$$

where XFORM identifies the Transform approach, WW identifies our weight window, and FWCADIS identifies the FW-CADIS weight window. To remain consistent with the Monte Carlo particle flux resulting from the weight window, the Monte Carlo estimate of the forward scalar flux $\phi_{c,g}$ is treated as the "exact" forward scalar flux and the deterministic estimate of the adjoint scalar flux $\Phi_{c,g}^*$ is used since it corresponds to the weight window. The transform approach scalar flux estimate is an approximation of the scalar Monte Carlo flux produced by the Transform approach:

$$\begin{aligned}\mathcal{M}(\mathbf{x}, E) &= \frac{\int_{4\pi} \psi(\mathbf{x}, \mathbf{\Omega}, E)\psi^*(\mathbf{x}, \mathbf{\Omega}, E)d\Omega}{B(\mathbf{x})} \\ &\approx \text{C}_0 \frac{\phi(\mathbf{x}, E)\phi^*(\mathbf{x}, E)}{B(\mathbf{x})}.\end{aligned} \tag{7.30}$$

For all three approaches, the theoretically predicted energy-integrated scalar Monte Carlo particle flux $\tilde{\mathcal{M}}_c$ is given as:

$$\tilde{\mathcal{M}}_c = \sum_{g=1}^{3} \tilde{\mathcal{M}}_{c,g}. \tag{7.31}$$

For both the response problem and flux problem, the energy-dependent scalar flux $\phi_{c,g}$ and the total scalar flux ϕ_c are tallied, even though the flux problem is tailored to obtain just $\phi_{c,g}$ and the response problem is tailored to obtain ϕ_c. To see the difference between the flux problem and the response problem, we examine the data in a representative energy group – the second group – and the data for the total flux. We expect that the methods tailored to the flux problem will produce better statistical results for the second energy group, while those tailored to the response (total flux) problem will produce better statistical results for the total flux data.

Even though global problems provide the solution everywhere, they require greater computational time than source-detector or even source-region problems. For this reason, it is desirable to have some measure that describes how many source-detector

calculations can be performed at the same computational cost as a single global problem. Then, if the solution is not required everywhere in the system, the user can decide whether to solve several source-detector problems or a single global problem.

To derive an expression for the number of source-detector problems that could be solved before the computational expense becomes greater than solving a single global problem, we evaluate the run time required to achieve a variance of less than some criterion ϵ in a characteristic detector volume for both the source-detector and global problems. That is, the number of source-detector problems $\mathrm{N_{SD:G}}$ that can be run in the same time as a single global problem is given by the ratio

$$\mathrm{N_{SD:G}} = \frac{\mathrm{T_{global}}}{\mathrm{T_{sd}}}, \tag{7.32}$$

where $\mathrm{T_{sd}}$ and $\mathrm{T_{global}}$ are the run times required to achieve a variance less than ϵ for the source-detector and global problems, respectively. Mathematically, we represent this condition as

$$\mathrm{Var}\left[\phi_D\right] < \epsilon, \tag{7.33}$$

where ϕ_D represents the mean Monte Carlo estimate of the the group-dependent flux or the total flux in the detector region. (For simplicity, the subscript g is not included for the group-dependent flux.) To calculate this variance in a simulation, we use the approximation

$$\mathrm{Var}\left[\phi_D\right] \approx \frac{\mathrm{Var}\left[\phi_{D,n}\right]}{N}, \tag{7.34}$$

where $\mathrm{Var}\left[\phi_{D,n}\right]$ is the sample variance, which converges to an estimate of the true variance – a constant – as the number of particles N gets large. The number of particles is related to the run time $\mathrm{T_{cpu}}$ through the approximation

$$N = \mathrm{T_{cpu}} * \mathrm{TPP}, \tag{7.35}$$

where TPP is the average time per particle for a given Monte Carlo simulation. TPP converges to a constant as N becomes large for a specific method and problem. Introducing Eqs. 7.34 and 7.35 into Eq. 7.33 results in the following run time criteria to achieve a variance of the estimated mean flux that is less than ϵ:

$$\mathrm{T_{cpu}} > \frac{\mathrm{Var}\left[\phi_{D,n}\right] * \mathrm{TPP}}{\epsilon}. \tag{7.36}$$

For a given simulation in which the sample variance and average time per particle

has converged, the numerator can be written as

$$\begin{aligned}\mathrm{Var}\left[\phi_{D,n}\right] * \mathrm{TPP} &= \mathrm{T}_0 \frac{\mathrm{Var}\left[\phi_{D,n}\right]_0}{N_0} \frac{\phi_D^2}{\phi_D^2} \\ &= \phi_D^2 \frac{\mathrm{Var}\left[\phi_D\right]_0 T_0}{\phi_D^2} \\ &= \frac{\phi_D^2}{\mathrm{FOM}_{D,0}},\end{aligned} \tag{7.37}$$

where the subscript 0 represents the fixed values obtained in a simulation: the number of particles run N_0, the actual simulation run time T_0, the calculated variance of the mean $\mathrm{Var}\left[\phi_D\right]_0$, and the corresponding $\mathrm{FOM}_{D,0}$ given by Eq. 7.26. Thus, the run time criteria to achieve a variance less than ϵ is given by

$$\mathrm{T}_{\mathrm{cpu}} > \frac{\phi_D^2}{\epsilon\, \mathrm{FOM}_{D,0}}. \tag{7.38}$$

Finally, the number of source-detector problems that can be run in the same time as one global problem to achieve a variance of exactly ϵ is given by substituting the run times given by Eq. 7.38 into Eq. 7.32 for the source-detector and global problem. The result is the following equation:

$$\mathrm{N}_{\mathrm{SD:G}} = \frac{\mathrm{FOM}_{D,\mathrm{sd}}}{\mathrm{FOM}_{D,\mathrm{global}}}, \tag{7.39}$$

where the FOMs for the source-detector and global problems are calculated in the detector region. This equation neglects the user time required to set up every source-detector problem.

7.6.2 Numerical Results

The group-2 data for the flux problem is presented in Figures 7.3 - 7.6, including the figure of merit, the simulated Monte Carlo particle flux, the theoretically predicted Monte Carlo particle flux, and the global statistics; the corresponding group-2 data for the response (total flux) problem appears in Figures 7.7 - 7.10. Likewise, the total flux data for the flux problem is presented in Figures 7.11 - 7.14 and the corresponding data for the response problem appears in Figures 7.15 - 7.18. In the 2D figures, the entire plots are relevant to the solution since global problems require the solution everywhere. The 1D figures are plots along the line where the most attenuation occurs from the source to the far corner. In addition, Tables 7.1 - 7.4

and Tables 7.5 - 7.8 provide the global FOM and the simulated Monte Carlo particle flux statistics, respectively, for each energy group and for all methods and problems.

Table 7.1: Global FOM statistics for group-1 flux

Problem	**Method**	**Group-1 FOM**			
		Min	**Max**	**Median**	**Mean**
Flux ($\phi_{c,g}$)	**FW-CADIS**	0.0021	1787	0.037	0.453
	WW	0.022	12.57	0.073	0.081
	XFORM	0.041	4.052	0.158	0.154
Response (ϕ_c)	**FW-CADIS**	1.5E-05	1491	0.0039	0.321
	WW	0.00041	11.01	0.010	0.021
	XFORM	0.00074	4.240	0.017	0.028

Table 7.2: Global FOM statistics for group-2 flux

Problem	**Method**	**Group-2 FOM**			
		Min	**Max**	**Median**	**Mean**
Flux ($\phi_{c,g}$)	**FW-CADIS**	0.0016	124.6	0.048	0.201
	WW	0.040	0.848	0.126	0.129
	XFORM	0.0532	0.294	0.183	0.175
Response (ϕ_c)	**FW-CADIS**	0.00021	175.7	0.021	0.201
	WW	0.0051	1.243	0.060	0.074
	XFORM	0.0089	0.476	0.079	0.090

Table 7.3: Global FOM statistics for the group-3 flux

Problem	Method	Group-3 FOM			
		Min	Max	Median	Mean
Flux ($\phi_{c,g}$)	**FW-CADIS**	0.0023	36.87	0.078	0.184
	WW	0.063	0.267	0.217	0.211
	XFORM	0.055	0.343	0.222	0.216
Response (ϕ_c)	**FW-CADIS**	0.0052	85.76	0.173	0.391
	WW	0.166	0.617	0.447	0.435
	XFORM	0.122	0.886	0.506	0.500

Table 7.4: Global FOM statistics for the total flux

Problem	Method	Total Flux FOM			
		Min	Max	Median	Mean
Flux ($\phi_{c,g}$)	**FW-CADIS**	0.0030	1664	0.102	0.651
	WW	0.069	11.73	0.285	0.295
	XFORM	0.0970	4.006	0.316	0.302
Response (ϕ_c)	**FW-CADIS**	0.0053	1722.685	0.195	0.872
	WW	0.170	12.72	0.507	0.502
	XFORM	0.200	4.892	0.623	0.601

Table 7.5: Global simulated MC particle flux for the group-1 flux

Problem	Method	Group-1 Simulated MC Particle Flux			
		Min	Max	Median	Mean
Flux ($\phi_{c,g}$)	**FW-CADIS**	1.9E-06	1.172	7.1E-05	0.00043
	WW	0.029	1.016	0.043	0.047
	XFORM	0.025	0.871	0.095	0.097
Response (ϕ_c)	**FW-CADIS**	3.0E-09	1.179	6.3E-06	0.00029
	WW	0.00024	1.021	0.0037	0.0084
	XFORM	0.00031	0.886	0.0061	0.014

Table 7.6: Global simulated MC particle flux for the group-2 flux

Problem	Method	Group-2 Simulated MC Particle Flux			
		Min	Max	Median	Mean
Flux ($\phi_{c,g}$)	**FW-CADIS**	1.3E-06	0.119	6.6E-05	0.00021
	WW	0.026	0.081	0.040	0.041
	XFORM	0.027	0.097	0.079	0.075
Response (ϕ_c)	**FW-CADIS**	2.0E-07	0.184	3.1E-05	0.00022
	WW	0.0037	0.151	0.018	0.022
	XFORM	0.0040	0.144	0.028	0.034

Table 7.7: Global simulated MC particle flux for the group-3 flux

Problem	**Method**	**Group-3 Simulated MC Particle Flux**			
		Min	**Max**	**Median**	**Mean**
Flux ($\phi_{c,g}$)	**FW-CADIS**	1.6E-06	0.032	9.3E-05	0.00020
	WW	0.023	0.061	0.054	0.053
	XFORM	0.028	0.127	0.090	0.088
Response (ϕ_c)	**FW-CADIS**	4.9E-05	0.088	0.00025	0.00050
	WW	0.058	0.141	0.131	0.128
	XFORM	0.059	0.302	0.196	0.194

Table 7.8: Global simulated MC particle flux for the total flux

Problem	**Method**	**Total Simulated MC Particle Flux**			
		Min	**Max**	**Median**	**Mean**
Flux ($\phi_{c,g}$)	**FW-CADIS**	5.7E-06	1.323	0.00023	0.00084
	WW	0.093	1.123	0.138	0.141
	XFORM	0.093	1.002	0.271	0.261
Response (ϕ_c)	**FW-CADIS**	5.1E-06	1.451	0.00029	0.0010
	WW	0.102	1.243	0.155	0.158
	XFORM	0.100	1.106	0.250	0.242

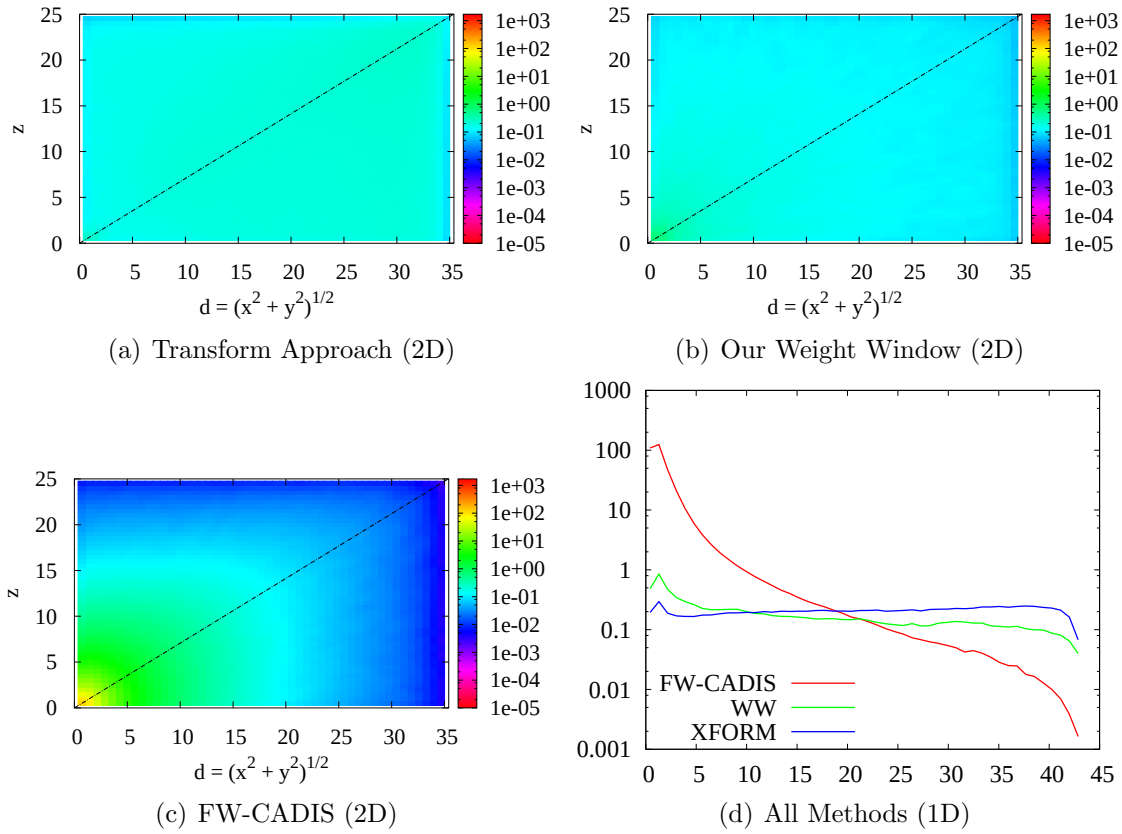

(a) Transform Approach (2D)

(b) Our Weight Window (2D)

(c) FW-CADIS (2D)

(d) All Methods (1D)

Figure 7.3: Group-2 FOM for Global Flux Problem

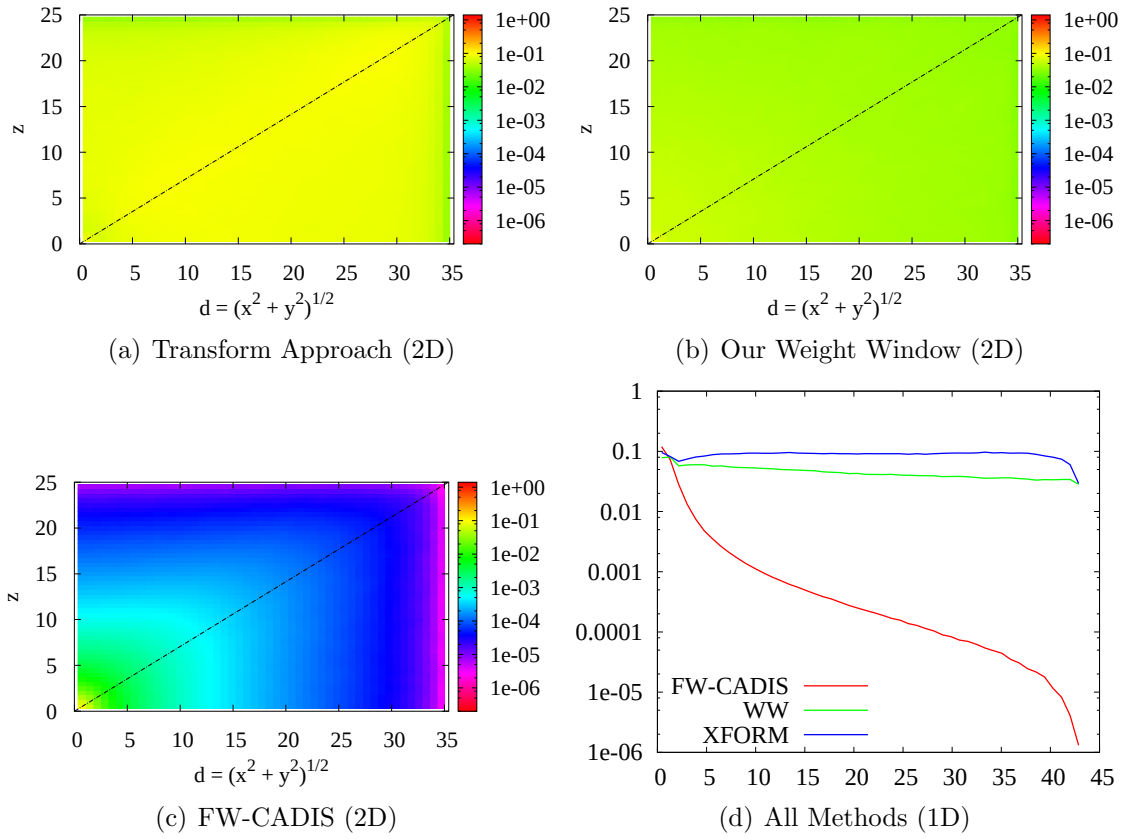

(a) Transform Approach (2D)

(b) Our Weight Window (2D)

(c) FW-CADIS (2D)

(d) All Methods (1D)

Figure 7.4: Group-2 Simulated MC Particle Flux for Global Flux Problem

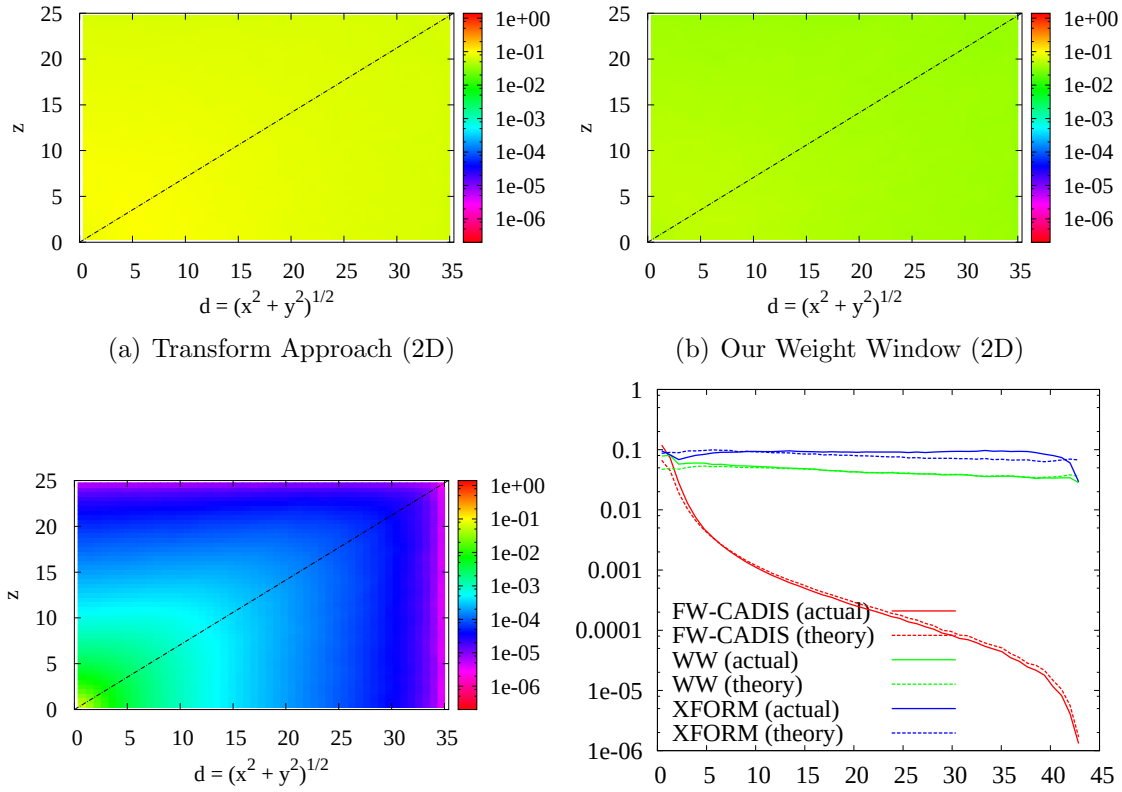

(a) Transform Approach (2D)

(b) Our Weight Window (2D)

(c) FW-CADIS (2D)

(d) All Methods (1D)

Figure 7.5: Group 2 Predicted MC Particle Flux for Global Flux Problem

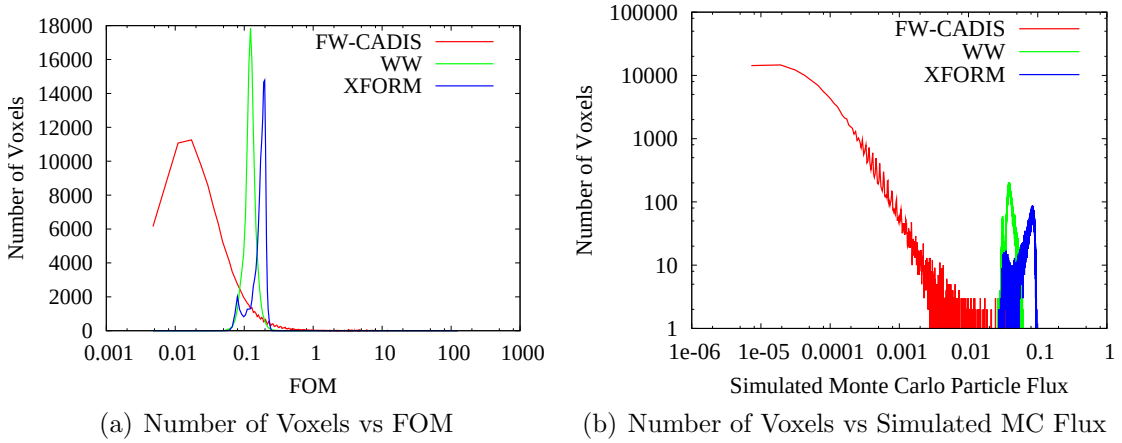

(a) Number of Voxels vs FOM

(b) Number of Voxels vs Simulated MC Flux

Figure 7.6: Group-2 Global Statistics by Number of Voxels for Global Flux Problem

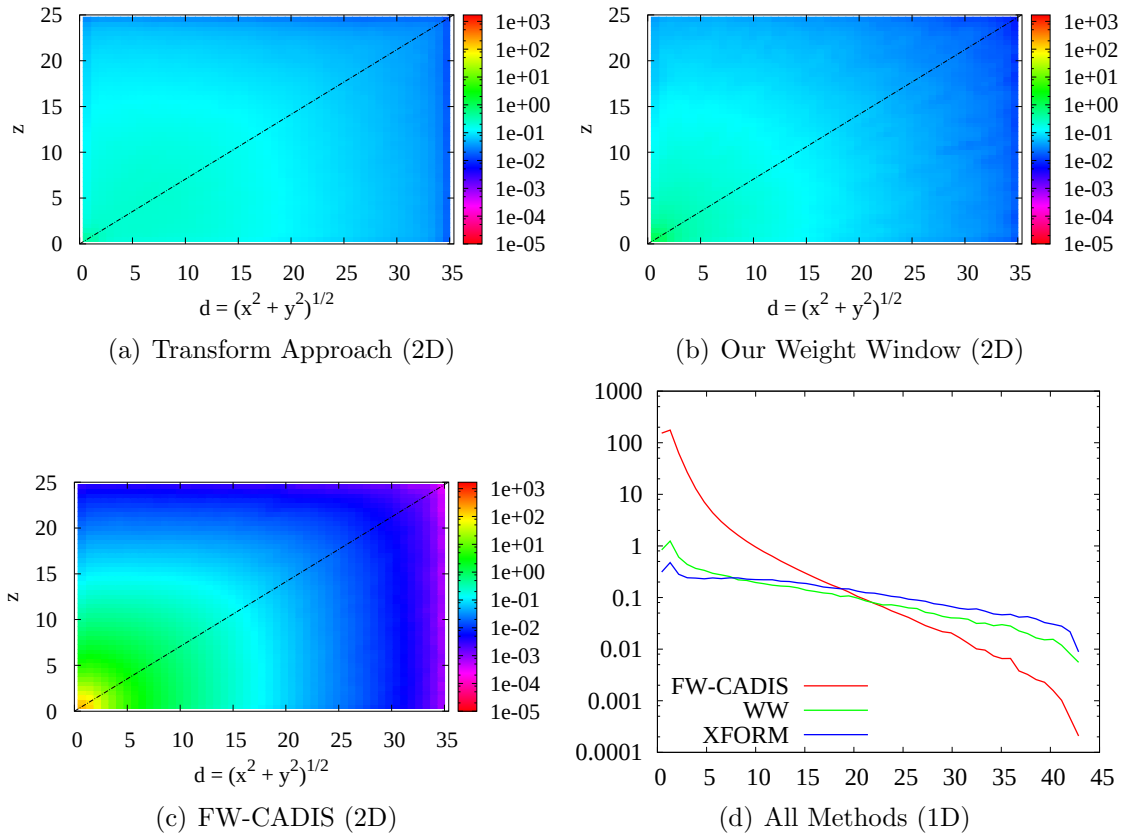

(a) Transform Approach (2D)

(b) Our Weight Window (2D)

(c) FW-CADIS (2D)

(d) All Methods (1D)

Figure 7.7: Group-2 FOM for Global Response Problem

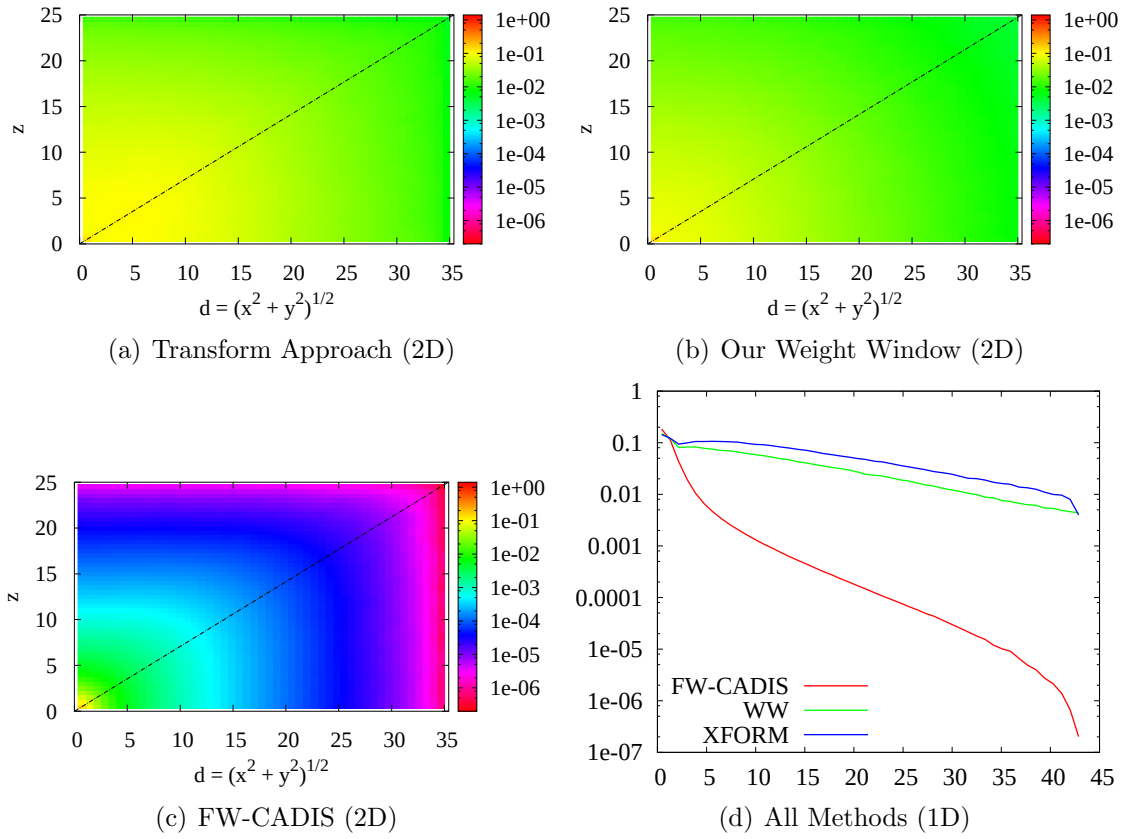

(a) Transform Approach (2D)

(b) Our Weight Window (2D)

(c) FW-CADIS (2D)

(d) All Methods (1D)

Figure 7.8: Group-2 Simulated MC Particle Flux for Global Response Problem

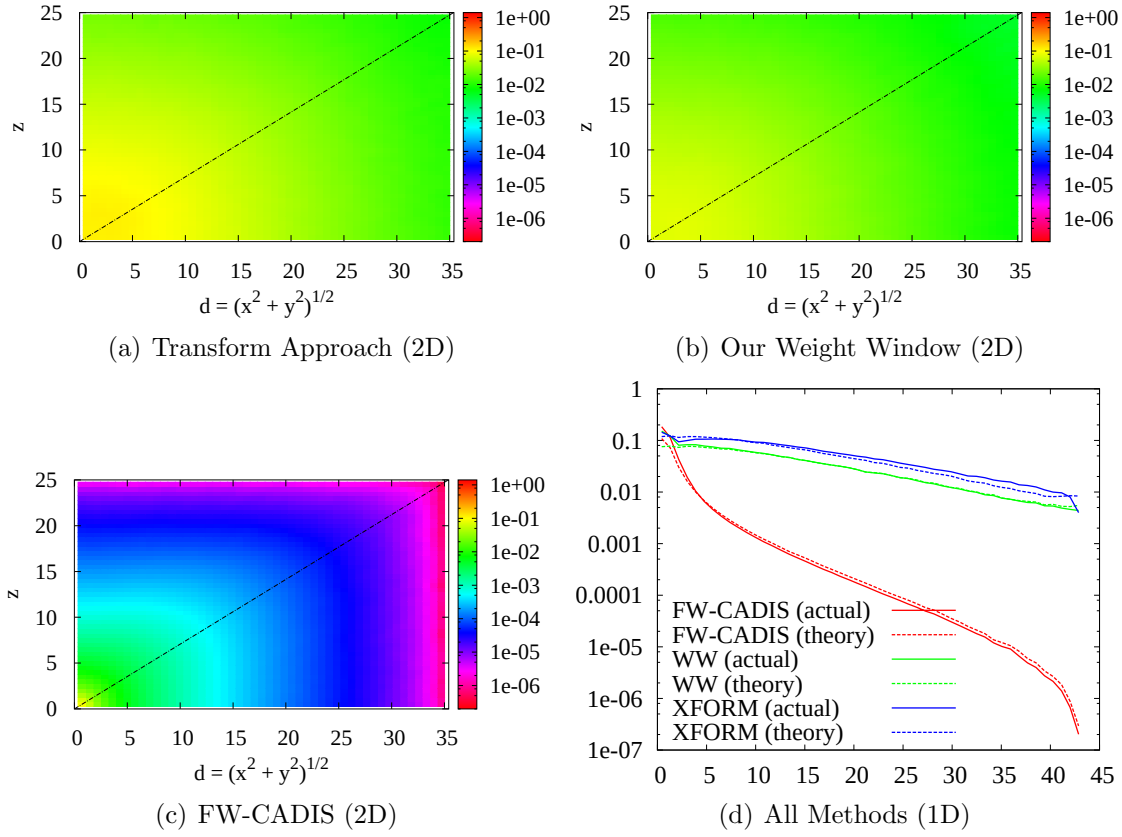

(a) Transform Approach (2D)

(b) Our Weight Window (2D)

(c) FW-CADIS (2D)

(d) All Methods (1D)

Figure 7.9: Group-2 Predicted MC Particle Flux for Global Response Problem

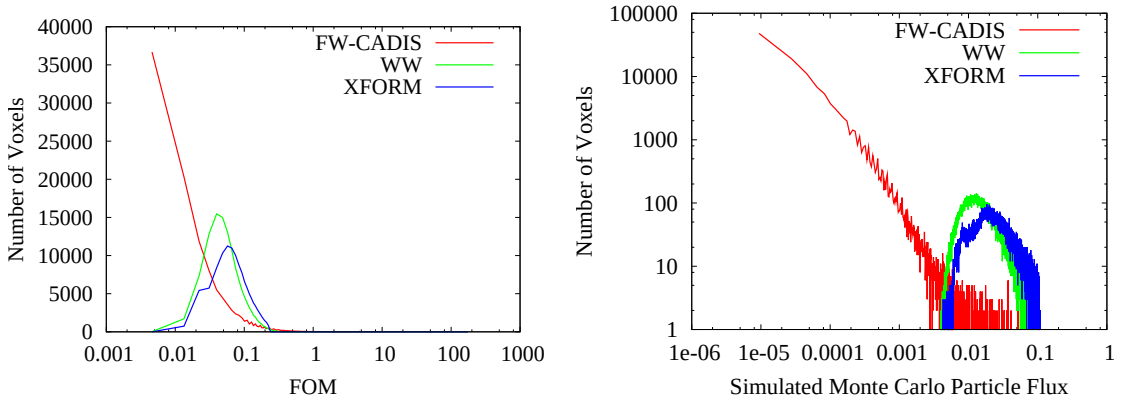

(a) Number of Voxels vs FOM

(b) Number of Voxels vs Simulated MC Flux

Figure 7.10: Group-2 Global Statistics by Number of Voxels for Global Response Problem

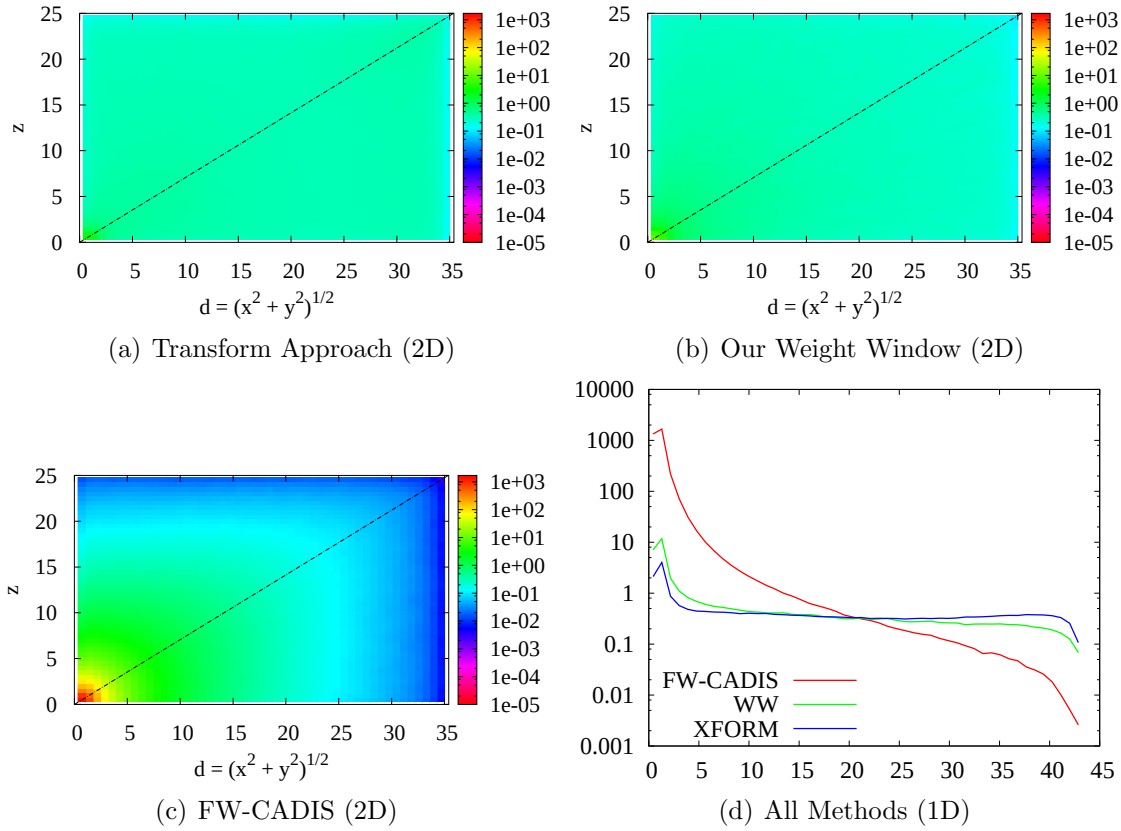

(a) Transform Approach (2D)

(b) Our Weight Window (2D)

(c) FW-CADIS (2D)

(d) All Methods (1D)

Figure 7.11: Total FOM for Global Flux Problem

Just as for source-region problems, no single metric exists for assessing and comparing methods for global problems, in which the whole system is the solution space. For this reason, we again consider the median FOM as a metric that conveys information about the efficiency and accuracy of the solution, since it relays that half the spatial elements in the region have an FOM below this value and half have an FOM that is greater than this value. (The maximum and minimum values of the FOM could be used to bound the FOM in the lower and upper half.) Therefore, we again use the median value as well as figures to assess and compare the performance of the various methods.

The FOM data in Tables 7.1 - 7.4 indicate that the Transform approach performs most efficiently in every energy group for both the flux problem and the response problem, as determined by the median FOM. The data also indicates that our weight window performs at a comparable level to the Transform approach for the second and third energy group as well as for the total flux. From this, we can infer that the additional benefit from simulating the forward contributon physics is somewhat undermined by the additional computational cost required to simulate this physics.

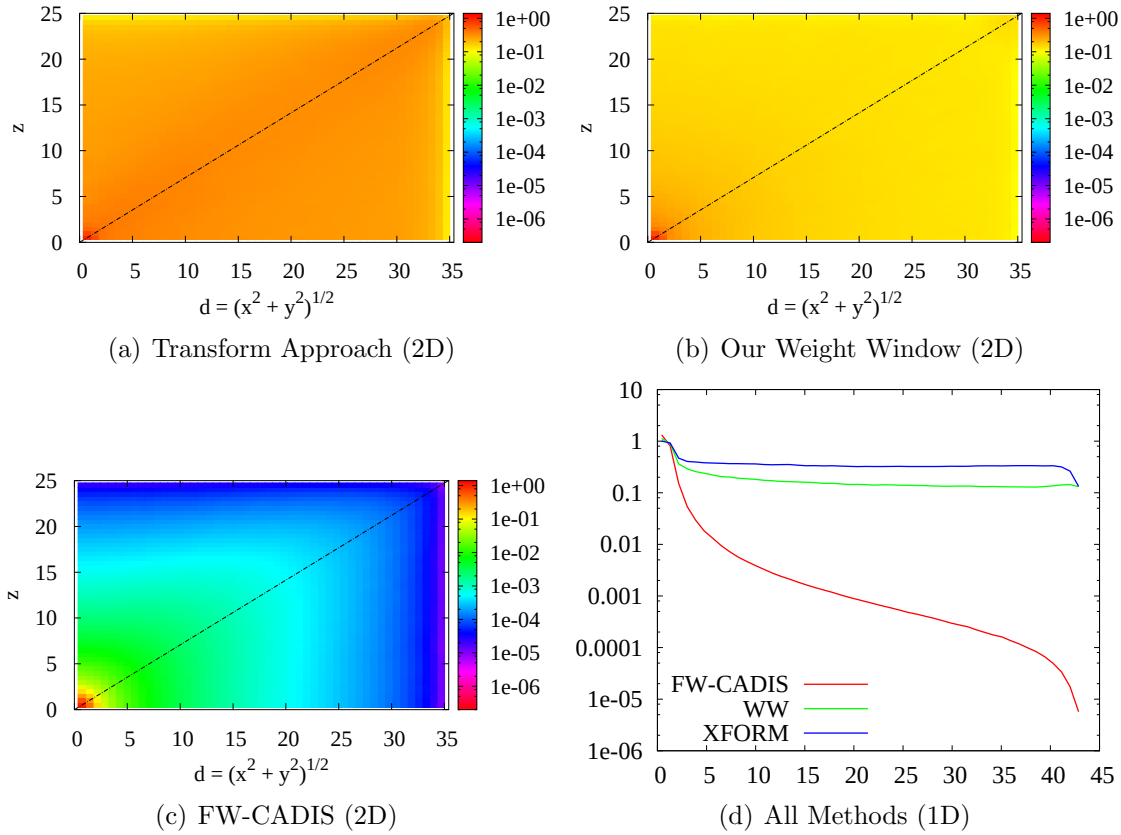

(a) Transform Approach (2D)

(b) Our Weight Window (2D)

(c) FW-CADIS (2D)

(d) All Methods (1D)

Figure 7.12: Total Simulated MC Particle Flux for Global Flux Problem

For the flux problem, in which we wish to obtain statistical results in every energy group, the Transform approach has a median FOM that is 2-4 times greater than that of the weight window approaches in the first energy group. In the second and third energy group as well as for the total flux, the median FOM for the transform approach and our weight window is roughly 3 times greater than for the FW-CADIS weight window. For the response problem, in which we wish to optimize the calculation to obtain the total flux, the Transform approach median FOM is 2-4 times greater than that of the weight window approaches in the first energy group. In the second and third energy group as well as for the total flux, the median FOM for the Transform approach and our weight window are 2.5-4 time greater than for the FW-CADIS weight window. Figures 7.6 and 7.10 present the group-2 FOM statistics for the entire region, specifically, the number of spatial elements that correspond to a particular FOM for the flux problem and response problem, respectively; Figures 7.14 and 7.18 are the corresponding FOM data for the total flux. In each figure, the Transform approach clearly has more spatial elements at a higher FOM than the FW-CADIS weight window and slightly more than our weight window. Thus the figures are

Table 7.9: Detector vs global group-1 data

Problem	Method	Detector $\mathbf{FOM_D}$	Global $\mathbf{FOM_D}$	$\mathbf{N_{D:G}}$
Flux ($\phi_{c,g}$)	**FW-CADIS**	0.502	0.0091	55
	WW	0.496	0.069	7
	XFORM	6.752	0.271	25
Response (ϕ_c)	**FW-CADIS**	0.015	0.00017	88
	WW	0.015	0.0013	12
	XFORM	0.125	0.0027	46

Table 7.10: Detector vs global group-2 data

Problem	Method	Detector $\mathbf{FOM_D}$	Global $\mathbf{FOM_D}$	$\mathbf{N_{D:G}}$
Flux ($\phi_{c,g}$)	**FW-CADIS**	0.949	0.012	79
	WW	0.989	0.098	10
	XFORM	6.246	0.230	27
Response (ϕ_c)	**FW-CADIS**	0.205	0.0019	107
	WW	0.216	0.016	14
	XFORM	1.344	0.034	40

consistent with the analysis using the median FOM as a metric.

The global flux problem data in Tables 7.1 - 7.4 demonstrate a much more uniform median FOM from group to group than does the response problem data. For the flux problem data, the weight window methods both have a median FOM that varies by a factor of nearly 3 across the three energy groups, and the Transform approach has a median FOM that varies by a factor of 1.4. For the response problem data, the weight window methods both have a FOM that varies by a factor of 45 across the three energy groups, and the Transform approach varies by a factor of nearly 30.

Table 7.11: Detector vs global group-3 data

Problem	Method	Detector $\mathbf{FOM_D}$	Global $\mathbf{FOM_D}$	$\mathbf{N_{D:G}}$
Flux ($\phi_{c,g}$)	**FW-CADIS**	2.043	0.019	108
	WW	2.125	0.187	11
	XFORM	7.720	0.335	23
Response (ϕ_c)	**FW-CADIS**	4.556	0.046	99
	WW	4.816	0.432	11
	XFORM	23.22	0.861	27

Table 7.12: Detector vs global total flux data

Problem	Method	Detector $\mathbf{FOM_D}$	Global $\mathbf{FOM_D}$	$\mathbf{N_{D:G}}$
Flux ($\phi_{c,g}$)	**FW-CADIS**	2.204	0.021	105
	WW	2.308	0.204	11
	XFORM	8.443	0.366	23
Response (ϕ_c)	**FW-CADIS**	4.674	0.048	97
	WW	4.942	0.443	11
	XFORM	24.53	0.891	28

This is to be expected, since the objective of the flux problem is to achieve roughly uniform results for every energy group, while the objective of the response problem is to optimize the total flux.

The data provided in Tables 7.1 - 7.4 show that if the objective is to obtain good results for every energy group, the flux problem should be solved; if the objective is to obtain the total flux, the response problem should be solved. This is clearly seen by comparing the flux problem FOM to the response problem FOM for the first energy group and for the total flux. In the first energy group, the median FOM values for the flux problem are 7-10 times greater than for the response problem; while for the total flux, the median FOM values for the response problem are roughly 2 times greater than for the flux problem. Therefore, each method has its utility.

Figures 7.3, 7.7, 7.11, and 7.15 demonstrate the distribution of the FOM in the 2D plane ($x = y$) and along the diagonal ($x = y = z$). Figures 7.3 and 7.7 further clarify the difference between the flux problem and response problem, where the response problem FOM decreases much more rapidly than the flux problem FOM in the second energy group away from the source, again due to the limited contribution of the group-2 flux to the response (total flux) away from the source.

Tables 7.5 - 7.8 demonstrate that for the flux problem, all the methods approximately populate the system with the same median Monte Carlo particle flux. For all three methods, the Monte Carlo particle flux across the three energy groups varies by only a factor of 1.5-3. This is a small differential compared to the actual neutron flux, which varies substantially by group across the system, especially in the deep parts of the problem where it varies by at least two orders of magnitude from the first group to the third group. For the response problem, Tables 7.5 - 7.8 shows that the Monte Carlo particle flux varies from group 1 to group 3 by a factor of 30-45. These results, for both the flux and response problem, are consistent with the desired

objectives of each method.

To further illustrate that the simulations behave as expected, the simulated Monte Carlo particle flux is compared to the theoretically predicted Monte Carlo particle flux. The simulated Monte Carlo particle flux is depicted in Figures 7.4, 7.8, 7.12, and 7.16 for the various problems and the corresponding predicted Monte Carlo particle flux is shown in Figures 7.5, 7.9, 7.13, and 7.17. The 1D Monte Carlo particle flux plots include both the simulated (actual) data and the predicted (theory) data to better compare the accuracy of the theory. By comparing the 1D and 2D figures, we observe that there is very good agreement between the simulated and predicted Monte Carlo particle flux. The most significant deviation exists in the Transform approach, where the predicted Monte Carlo particle flux is only an approximation. Both weight window methods, however, show nearly exact agreement between the theoretical predictions and the simulated values.

Just as in the source-detector and source-region analysis, it is clear from the Monte Carlo particle flux figures that a positive correlation exists between the Monte Carlo particle flux and the FOM, since the shape of the curves is similar.

Finally, Tables 7.9 – 7.12 provide data on the number of source-detector problems that could be run in the same time as one single global problem. This data is useful if the user does not need the solution everywhere, but still in a large number of locations, perhaps along the boundary of the system. The data from the FW-CADIS method demonstrates that 55 to 108 source detector problems could be run before the a global problem makes sense. This shows very clearly that, while FW-CADIS is well-suited for source-detector problems, it is less well-suited for global calculations. Our weight window demonstrates that 11 to 14 source-detector problems could be run before a global calculation would make more sense. This demonstrates how much more efficient our weight window is than the FW-CADIS for obtaining good statistical results in the deep parts of the problem for global calculations. Finally, the data for the Transform approach shows that roughly 30 source-detector problems could be solved for the cost of one global calculation. This data indicates that, although the Transform approach performs better than the weight window methods for all problems, it functions much better for source-detector problems than for global problems.

7.7 Summary

In this section, we have described global problems – both the response problem and flux problem. To solve these problems, we chose to distribute the Monte Carlo particle flux according to the contributon flux (or some slightly modified form of the contributon flux) by employing an appropriate weight window or "transform" function. To implement either the weight windows or Transform approach, it was necessary to define the adjoint problem that corresponds to the intended solution – the global flux or response. We did this by first defining an appropriate adjoint contributon source and then deriving the corresponding adjoint neutron source. Finally, we examined a 3-group test problem to validate the theory and assess the performance of each method. The results indicate that the theory is correct: for a given weight window or "transform" function, the Monte Carlo particle flux is correctly predicted by the theory. The results also indicate that the Transform approach and our weight window produce a larger FOM than the FW-CADIS weight window method; our weight window and the Transform approach have comparable FOMs. Thus for global problems, the extra computational cost per particle necessary for the Transform approach begins to undermine the benefits of more accurately simulating the forward contributon physics. Finally, the results again indicate that there is a positive correlation between the FOM and the Monte Carlo particle flux, but no exact theoretical model has been identified to predict the correlation.

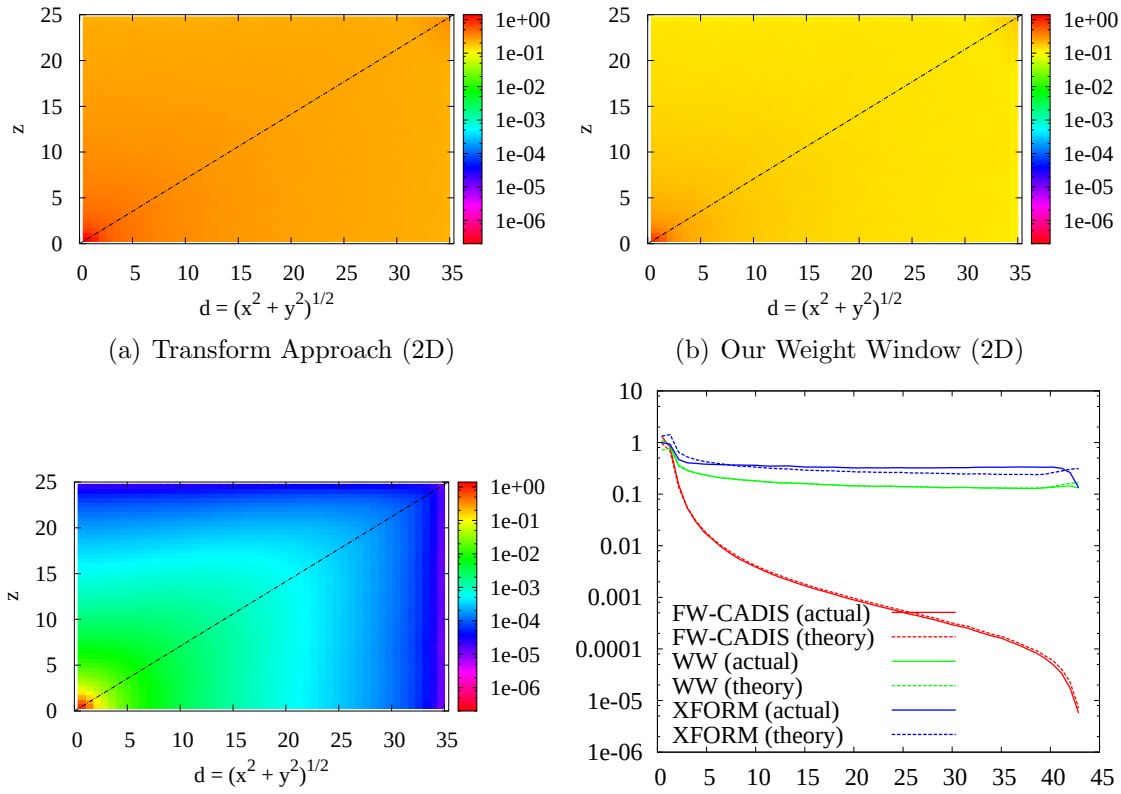

(a) Transform Approach (2D)

(b) Our Weight Window (2D)

(c) FW-CADIS (2D)

(d) All Methods (1D)

Figure 7.13: Total Predicted MC Particle Flux for Global Flux Problem

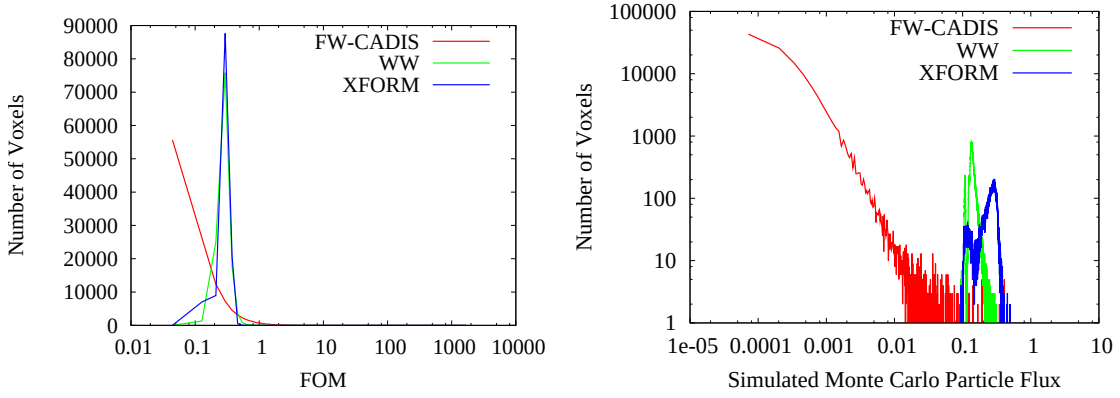

(a) Number of Voxels vs FOM

(b) Number of Voxels vs Simulated MC Flux

Figure 7.14: Total Global Statistics by Number of Voxels for Global Flux Problem

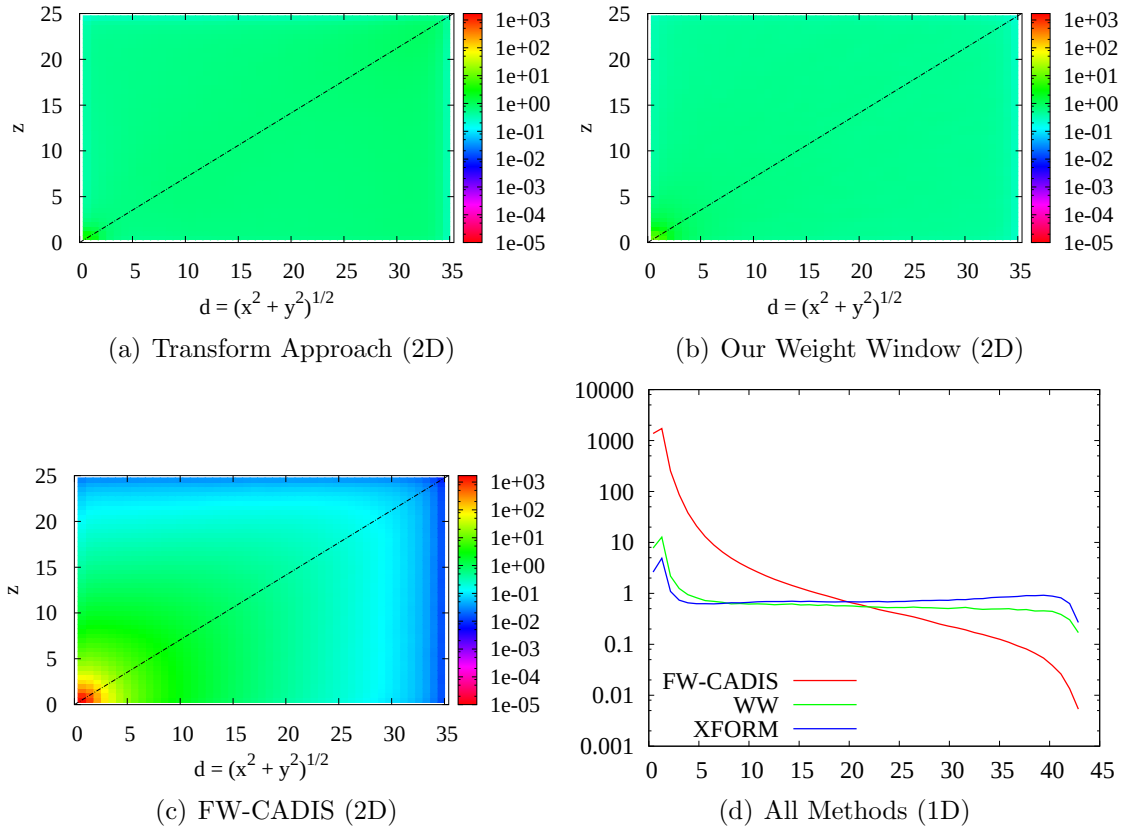

(a) Transform Approach (2D)

(b) Our Weight Window (2D)

(c) FW-CADIS (2D)

(d) All Methods (1D)

Figure 7.15: Total FOM for Global Response Problem

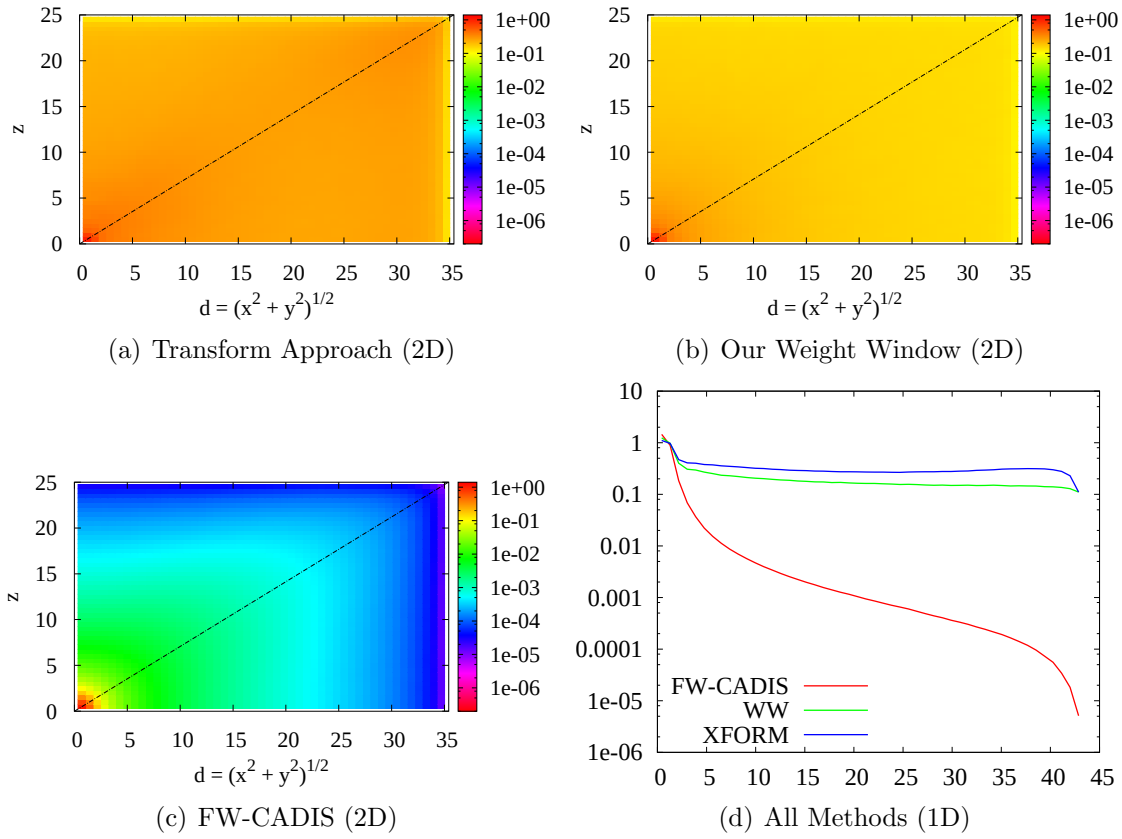

(a) Transform Approach (2D)

(b) Our Weight Window (2D)

(c) FW-CADIS (2D)

(d) All Methods (1D)

Figure 7.16: Total Simulated MC Particle Flux for Global Response Problem

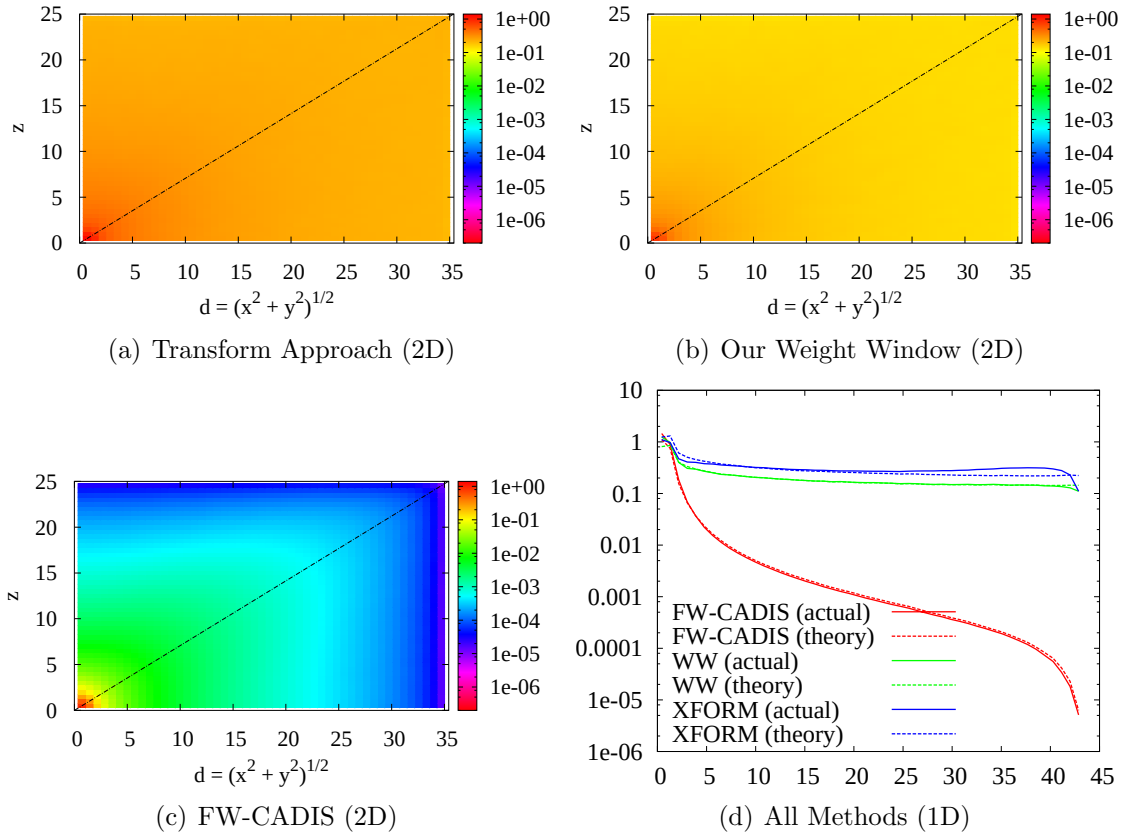

(a) Transform Approach (2D)

(b) Our Weight Window (2D)

(c) FW-CADIS (2D)

(d) All Methods (1D)

Figure 7.17: Total Predicted MC Particle Flux for Global Response Problem

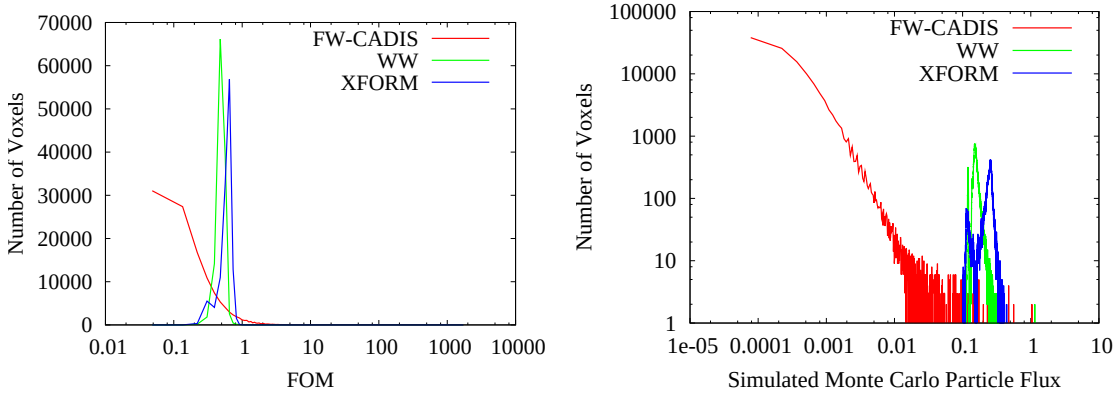

(a) Number of Voxels vs FOM

(b) Number of Voxels vs Simulated MC Flux

Figure 7.18: Total Global Statistics by Number of Voxels for Global Response Problem

Chapter VIII

Challenge Problems

In this chapter, we consider a much more challenging shielding problem than the one considered in the previous three chapters (i.e., the 3-group homogeneous cube). This problem more closely resembles a typical shielding problem with heterogenous geometry, a larger number of energy groups (ten), and coupled neutron-photon physics. For this problem, we forego attempting to acquire statistically resolved estimates of the scalar flux in every energy group – the *flux problem* – and focus on the *response problem*, in which we wish to obtain the energy-integrated response

$$\mathcal{R}(\mathbf{x}) = \int_0^\infty \Sigma_{\mathcal{R}}(\mathbf{x}, E)\phi(\mathbf{x}, E)dE, \tag{8.1}$$

in (i) a small detector, (ii) a significant region of the system, or (iii) throughout the entire system. These problems, of course, correspond to the source-detector, source-region and global response problems, respectively. (For the source-detector problem, the detector response was defined to be the volume-averaged response $\mathcal{R}_D$; however, for small detectors $\mathcal{R}(\mathbf{x}) \approx \mathcal{R}_D$.) The problem contains coupled neutron-photon physics, so we investigate both the neutron response and the photon response. As in previous chapters, we again consider the energy-integrated (total) flux for neutrons and photons, in which $\Sigma_{\mathcal{R}}(\mathbf{x}, E) = 1$.

To solve these problems, we utilize the concepts developed in the previous three chapters for the source-detector, source-region and global problems. Thus, the Monte Carlo particle flux is distributed proportional to a contributon flux, since this distribution corresponds to the relative contribution of a particle at a point in phase-space to the response (or flux). By defining the adjoint contributon source in a specific way, a Monte Carlo particle flux distribution is achieved that corresponds to the intended response – neutron or photon. From the adjoint contributon source, the adjoint neutron (or photon) source is determined, and the adjoint problem can be

solved and used to implement the weight window and Transform approaches. In this chapter, we do not repeat the implementation details for the weight window and transform approaches, since those were thoroughly discussed in previous chapters and their application here is a straighforward extension. When modifications are made to the previously developed theory, they will be highlighted and explained, if necessary.

8.1 The Neutron Response Problem

In *neutron response problems*, we wish to obtain the energy-integrated neutron response

$$\mathcal{R}_{\mathcal{N}}(\mathbf{x}) = \int_0^\infty \int_{4\pi} \Sigma_{\mathcal{R},\mathcal{N}}(\mathbf{x}, E)\psi_{\mathcal{N}}(\mathbf{x}, \mathbf{\Omega}, E)d\Omega dE, \tag{8.2}$$

for all points $\mathbf{x}$ in the space $\mathcal{V}_P$. Here, the subscript $\mathcal{N}$ identifies each parameter or function as corresponding to neutrons (i.e., neutron response, neutron response parameter, and angular neutron flux); the space $\mathcal{V}_P$ corresponds to the specific type of problem:

$$\mathcal{V}_P = \begin{cases} \mathcal{V}_D, & \text{source-detector problem,} \\ \mathcal{V}_R, & \text{source-region problem,} \\ \mathcal{V}, & \text{global problem.} \end{cases} \tag{8.3}$$

In this chapter, the detector response has a slightly different definition from its classic definition as a volume-averaged quantity $\mathcal{R}_D$. However for small detectors, $\mathcal{R}(x) \approx \mathcal{R}_D$. Therefore, for source-detector problems, we can use the methodology developed for source-region problems and expect a negligible effect on the solution as long as the detector is small.

For all three approaches (Transform approach, our weight window, and FW-CADIS) and for all three problems (source-detector, source-region, and global), a suitable adjoint contributon source is defined as:

$$Q^{\mathrm{c}}(\mathbf{x}, \mathbf{\Omega}, E) = \begin{cases} \dfrac{\Sigma_{\mathcal{R},\mathcal{N}}(\mathbf{x}, E)\psi_{\mathcal{N}}(\mathbf{x}, \mathbf{\Omega}, E)}{\int_0^\infty \int_{4\pi} \Sigma_{\mathcal{R},\mathcal{N}}(\mathbf{x}, E')\psi_{\mathcal{N}}(\mathbf{x}, \mathbf{\Omega}', E')d\Omega' dE'}, & \text{for } \mathbf{x} \in \mathcal{V}_P, \\ 0, & \text{otherwise.} \end{cases} \tag{8.4}$$

At every point $\mathbf{x} \in \mathcal{V}_P$, this source emits contributons (response particles) at a rate proportional to their relative contribution to the spatial neutron response $\mathcal{R}_{\mathcal{N}}(\mathbf{x})$.

Also, the total contributon emission rate is the same for every point $\mathbf{x} \in \mathcal{V}_P$, i.e.,

$$\begin{aligned} Q^{\mathrm{c}}(\mathbf{x}) &= \int_0^\infty \int_{4\pi} Q^{\mathrm{c}}(\mathbf{x}, \mathbf{\Omega}, E) d\Omega dE \\ &= 1. \end{aligned} \tag{8.5}$$

Thus, every spatial location $\mathbf{x}$ essentially functions as a point detector which emits contributons at a rate proportional to the contribution to the neutron response $\mathcal{R}_{\mathcal{N}}(\mathbf{x})$, and every point detector is treated with equal importance by emitting particles at the same rate.

The adjoint neutron source is determined from Eq. 5.12:

$$\begin{aligned} Q^*(\mathbf{x}, \mathbf{\Omega}, E) &= \frac{Q^{\mathrm{c}}(\mathbf{x}, \mathbf{\Omega}, E)}{\psi(\mathbf{x}, \mathbf{\Omega}, E)} \\ &= \begin{cases} \dfrac{\Sigma_{\mathcal{R}}(\mathbf{x}, E)}{\int_0^\infty \int_{4\pi} \Sigma_{\mathcal{R}}(\mathbf{x}, E') \psi(\mathbf{x}, \mathbf{\Omega}', E) d\Omega' dE'}, & \text{for } \mathbf{x} \in \mathcal{V}_P, \\ 0, & \text{otherwise.} \end{cases} \end{aligned} \tag{8.6}$$

Since the adjoint source emits only neutrons and the scattering matrix used in this problem only allows neutron-to-photon scattering, photons do not appear in the adjoint problem. Thus, it is also unnecessary to consider them in the forward problem. This results in a decoupled system in which only the neutrons must be simulated. For deterministic methods, this implies that only the energy groups corresponding to the neutrons must be considered, and for Monte Carlo methods it implies that only the neutrons must be simulated.

8.2 The Photon Response Problem

In *photon response problems*, we wish to obtain the energy-integrated photon response

$$\mathcal{R}_\gamma(\mathbf{x}) = \int_0^\infty \int_{4\pi} \Sigma_{\mathcal{R},\gamma}(\mathbf{x}, E) \psi_\gamma(\mathbf{x}, \mathbf{\Omega}, E) d\Omega dE, \tag{8.7}$$

in the space $\mathcal{V}_P$. Here, the subscript γ identifies each parameter or function as corresponding to photons (i.e., photon response, photon response parameter, and angular photon flux); the space $\mathcal{V}_P$ is again defined as

$$\mathcal{V}_P = \begin{cases} \mathcal{V}_D, & \text{source-detector problem,} \\ \mathcal{V}_R, & \text{source-region problem,} \\ \mathcal{V}, & \text{global problem.} \end{cases} \tag{8.8}$$

For all three approaches (Transform approach, our weight window, and FW-CADIS) and for all three problems (source-detector, source-region, and global), a suitable adjoint contributon source is defined as:

$$Q^{\mathrm{c}}(\mathbf{x},\mathbf{\Omega},E)=\begin{cases}\dfrac{\Sigma_{\mathcal{R},\gamma}(\mathbf{x},E)\psi_{\gamma}(\mathbf{x},\mathbf{\Omega},E)}{\int_0^{\infty}\int_{4\pi}\Sigma_{\mathcal{R},\gamma}(\mathbf{x},E')\psi_{\gamma}(\mathbf{x},\mathbf{\Omega}',E')d\Omega' dE'}, & \text{for } \mathbf{x}\in\mathcal{V}_P,\\ 0, & \text{otherwise.}\end{cases} \tag{8.9}$$

At every point $\mathbf{x}\in\mathcal{V}_P$, this source emits contributons (response particles) at a rate proportional to their relative contribution to the spatial photon response $\mathcal{R}_{\gamma}(\mathbf{x})$. Also, the total contributon emission rate is the same for every point $\mathbf{x}\in\mathcal{V}_P$, i.e.,

$$\begin{aligned}Q^{\mathrm{c}}(\mathbf{x}) &= \int_0^{\infty}\int_{4\pi} Q^{\mathrm{c}}(\mathbf{x},\mathbf{\Omega},E)d\Omega dE\\ &= 1.\end{aligned} \tag{8.10}$$

Again, this indicates that every spatial location $\mathbf{x}$ essentially functions as a point detector which emits contributons at a rate proportional to the contribution to the photon response $\mathcal{R}_{\gamma}(\mathbf{x})$, and every point detector is treated with equal importance by emitting particles at the same rate.

The adjoint photon source is determined from Eq. 5.12:

$$\begin{aligned}Q^{*}(\mathbf{x},\mathbf{\Omega},E) &= \frac{Q^{\mathrm{c}}(\mathbf{x},\mathbf{\Omega},E)}{\psi(\mathbf{x},\mathbf{\Omega},E)}\\ &= \begin{cases}\dfrac{\Sigma_{\mathcal{R}}(\mathbf{x},E)}{\int_0^{\infty}\int_{4\pi}\Sigma_{\mathcal{R}}(\mathbf{x},E')\psi(\mathbf{x},\mathbf{\Omega}',E)d\Omega' dE'}, & \text{for } \mathbf{x}\in\mathcal{V}_P\\ 0, & \text{otherwise.}\end{cases}\end{aligned} \tag{8.11}$$

Although the adjoint source only emits photons, neutrons can be produced in scattering events, since the scattering matrix used in this problem allows for neutron-to-photon scattering. Thus, neutrons appear in the adjoint problem, and for the same reason are also necessary in the forward problem. This results in a coupled system in which both neutrons and photons must be simulated. For deterministic methods, this implies that the energy groups corresponding to both the photons and neutrons must be considered, and for Monte Carlo methods it implies that photons and neutrons must be simulated.

8.3 Numerical Test Problem

For the challenge problems, our objectives are the following: 1) to test whether the methods developed in this thesis are capable of obtaining a solution in a challenging shielding problem, 2) to verify that the methods perform as the theory predicts, and 3) to compare the methods for efficiency and statistical quality. Unlike the 3-group problem in the previous three chapters, this problem was simulated on a supercomputer, for which consistent run times were difficult to obtain. For this reason, the figure of merit is less reliable as an indicator of the efficiency and statistical quality of the solution. Despite this, we still use the figure of merit to assess performance, but we use it in a more qualitative than quantitative way.

8.3.1 Problem Description

The problem consists of a shielded box of uranium oxide fuel suspended in a pool of water, with several layers of concrete and lead surrounding the pool. Specifically, the structure is a 300 cm heterogeneous cube with a 20 cm cubic source of uranium dioxide at its center, surrounded by multiple layers of concrete, steel, water, and lead for shielding. At the edges are vacuum boundaries, and running parallel to the z-axis are twelve concrete columns to support the "roof" of the structure. Because this problem is symmetric along the planes cutting through the source (i.e., the planes $x = 0$, $y = 0$ and $z = 0$ for a source centered at $(0, 0, 0)$), we only need to obtain a solution in one octant; we do this by imposing symmetric (reflecting) boundaries that pass through the center of the source along the planes mentioned. Figure 8.1 demonstrates this geometry: a 150 cm heterogeneous cube with a 10 cm cubic source of uranium oxide in the corner, surrounded by multiple layers of shielding material, with symmetric boundary conditions at the planes that cut through the source and vacuum boundaries at the exterior planes. The dimensions of each layer of shielding material are given in Figure 8.1.

Since the focus of this work is shielding problems, we imposed a fixed source on the uranium oxide cube, consisting of prompt fission neutrons and prompt fission photons, each described by an analytic expression. The prompt fission neutron source is given as

$$\chi(E) = a\mathrm{e}^{-E/b} \sinh \sqrt{cE}, \tag{8.12}$$

where $\chi(E)$ has units of neutrons MeV^{-1} $\mathrm{fission}^{-1}$ [43]. For thermal fission of U-235, $a = 0.5535$ MeV^{-1} $\mathrm{fission}^{-1}$, $b = 1.0347$ MeV, and $c = 1.6214$ MeV^{-1} [43]. The

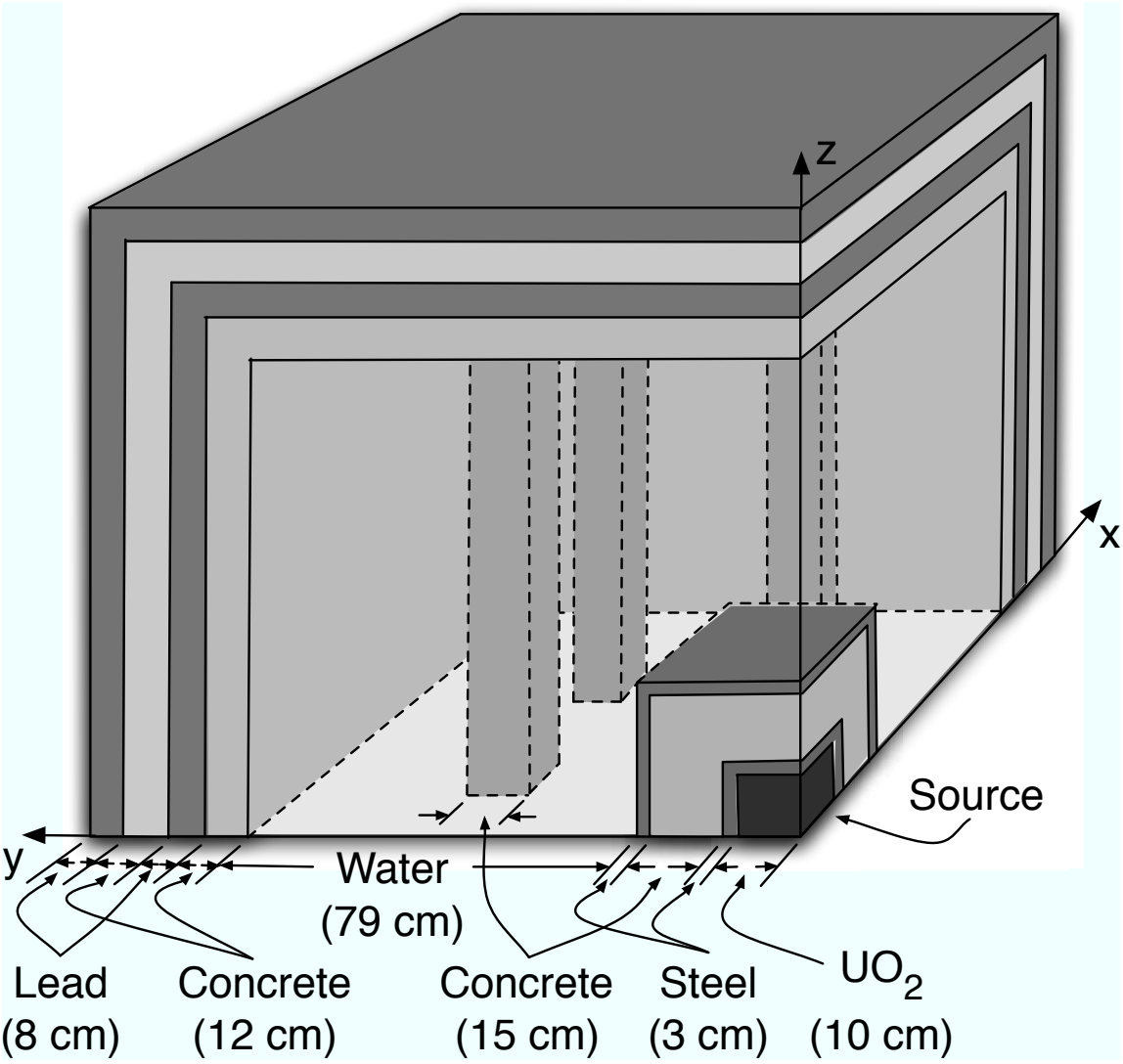

Figure 8.1: Problem Geometry

prompt fission photon source is given as

$$\mathrm{N}_\gamma(E) = \begin{cases} 6.6, & 0.1 < E < 0.6 \text{ MeV}, \\ 20.2\mathrm{e}^{-1.78E}, & 0.6 < E < 1.5 \text{ MeV}, \\ 7.2\mathrm{e}^{-1.09E}, & 1.5 < E < 10.5 \text{ MeV}, \end{cases} \tag{8.13}$$

where $\mathrm{N}_\gamma(E)$ has units of photons MeV^{-1} $\mathrm{fission}^{-1}$ [43].

These expressions are used to define the forward neutron source $Q_{\mathcal{N}}(\mathbf{x}, \mathbf{\Omega}, E)$ and

the forward photon source $Q_\gamma(\mathbf{x}, \mathbf{\Omega}, E)$:

$$Q_{\mathcal{N}}(\mathbf{x}, \mathbf{\Omega}, E) = \frac{\mathrm{C}_0}{4\pi} \frac{\chi(E)}{V_S}, \quad \mathbf{x} \in \mathcal{V}_S, \;\; \mathbf{\Omega} \in 4\pi, \;\; 0 < E < E_{\max}, \tag{8.14}$$

$$Q_{\gamma}(\mathbf{x}, \mathbf{\Omega}, E) = \frac{\mathrm{C}_0}{4\pi} \frac{\mathrm{N}_\gamma(E)}{V_S}, \quad \mathbf{x} \in \mathcal{V}_S, \;\; \mathbf{\Omega} \in 4\pi, \;\; 0 < E < E_{\max}, \tag{8.15}$$

where V_S is the volume of the source and C_0 is an arbitrary scaling factor with units of MeV^{-1} fission^{-1}. Since we are only considering multigroup problems in this thesis, we define the multigroup neutron and photon source within each spatial element $\mathcal{V}_c$ as

$$\begin{aligned} Q_{\mathcal{N},c,g} &= \int_{\mathcal{V}_c} \int_{E_g}^{E_{g-1}} Q_{\mathcal{N}}(\mathbf{x}, \mathbf{\Omega}, E) dE dV \\ &= \frac{\mathrm{C}_0}{4\pi} \frac{V_c}{V_S} \int_{E_g}^{E_{g-1}} \chi(E) dE, \end{aligned} \tag{8.16}$$

$$\begin{aligned} Q_{\gamma,c,g} &= \int_{\mathcal{V}_c} \int_{E_g}^{E_{g-1}} Q_{\gamma}(\mathbf{x}, \mathbf{\Omega}, E) dE dV \\ &= \frac{\mathrm{C}_0}{4\pi} \frac{V_c}{V_S} \int_{E_g}^{E_{g-1}} \mathrm{N}_\gamma(E) dE. \end{aligned} \tag{8.17}$$

Table 8.1 describes the energy group boundaries $\{E_g\}_{g=1}^{G}$ for the challenge problem, in which seven neutron groups and three photon groups are used. The 10-group source used for this problem appears in the Appendix within Tables B.9 and B.10, which also specify the uranium dioxide cross-sections, in addition to the fixed source.

We obtained the 10-group cross sections for the materials – concrete, water, lead, steel and uranium dioxide – by collapsing the 67-group BUGLE-96 cross-section library [44] using a simple arithmetic average over the groups within the range $[E_g, E_{g-1}]$. The cross-sections, along with the isotopic/elemental composition of the materials, appear in the Appendix.

Figure 8.2 demonstrates that this problem is indeed a shielding problem, with the total neutron scalar flux being attenuated by nearly 18 orders of magnitude, and the total photon scalar flux by roughly 15 orders of magnitude.

The objective of the response problem is to obtain the response $\mathcal{R}_c$ in each spatial element $\mathcal{V}_c$ within the space $\mathcal{V}_P$. The response that we investigate is the energy-integrated (total) flux, denoted simply as $\phi_{\mathcal{N},c}$ for neutrons and $\phi_{\gamma,c}$ for photons.

Table 8.1: Energy bounds for 10-group problem

Particle	**g**	**Energy Bound E_g (MeV)**
Neutron	0	1.7332E+01
	1	4.9659E+00
	2	2.2313E+00
	3	6.0810E-01
	4	4.0868E-02
	5	3.3546E-03
	6	1.0677E-05
	7	1.0000E-11
Photon	8	1.4000E+01
	9	5.0000E+00
	10	1.0000E+00
	11	2.0000E-01

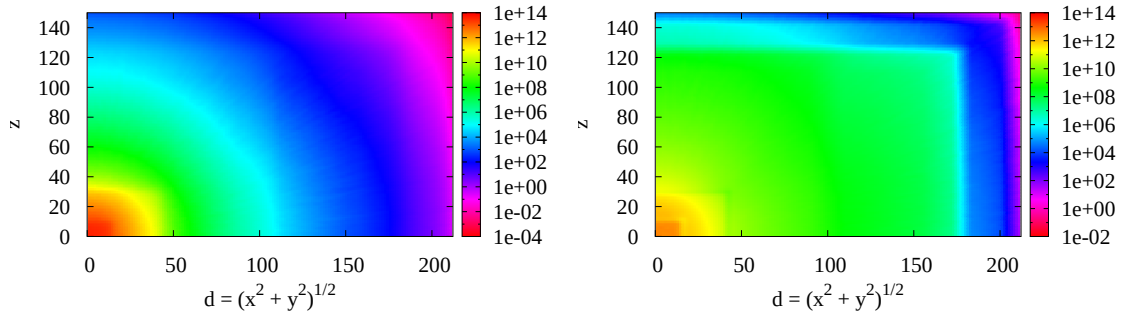

(a) Total Neutron Flux

(b) Total Photon Flux

Figure 8.2: Scalar Flux along the plane $x = y$

Mathematically, they are defined as

$$\phi_{\mathcal{N},c} = \frac{1}{V_c} \int_{\mathcal{V}_c} \int_{E_7}^{E_0} \phi(\mathbf{x}, E) dE dV, \tag{8.18}$$

$$\phi_{\gamma,c} = \frac{1}{V_c} \int_{\mathcal{V}_c} \int_{E_{11}}^{E_8} \phi(\mathbf{x}, E) dE dV, \tag{8.19}$$

where the energy bounds E_g are defined in Table 8.1.

To analyze the results, we plot the figure of merit, the simulated scalar Monte Carlo particle flux, and the theoretically predicted scalar Monte Carlo particle flux for the total neutron flux and the total photon flux. These plots appear in Figures 8.3 - 8.24 and describe a 2D plane that stretches from the z-axis to the cube edge farthest from the source (i.e. the plane $x = y$), the line from the source corner to

the far corner (i.e. the line $x = y = z$), and the FOM and Monte Carlo particle flux statistics throughout $\mathcal{V}_P$ for the source-region and global problems. (Since the detector region $\mathcal{V}_D$ is small, there is not enough data to construct a meaningful figure from the FOM and Monte Carlo particle flux data.) These values are computed on a uniform 1.0 cm grid that is imposed on the problem geometry. Thus, the system consists of 3,375,000 spatial elements, each denoted by $\mathcal{V}_c$. (The source region $\mathcal{V}_S$ contains 1000 spatial elements.)

The source-detector solution space $\mathcal{V}_D$ is a 4 cm cube located in the corner farthest from the source, 4 cm from each vacuum boundary, and contains 64 spatial elements. The space $\mathcal{V}_R$ is the 40 cm cubic region in the corner farthest from the source and contains 64,000 spatial elements. The global solution space includes all 3,375,000 spatial elements in the system $\mathcal{V}$.

The total neutron and photon scalar Monte Carlo particle fluxes are volume-averaged quantities determined directly from the Monte Carlo simulation. The figure of merit (FOM) in each spatial element $\mathcal{V}_c$ is defined as

$$\mathrm{FOM}_c = \frac{1}{\dfrac{\mathrm{Var}\left[\phi_c\right]}{\phi_c^2}\mathrm{T}_{\mathrm{cpu}}}, \tag{8.20}$$

where $\mathrm{T}_{\mathrm{cpu}}$ is the total run time, and ϕ_c and the corresponding variance are volume-averaged quantities obtained directly from the Monte Carlo simulation. In this case, ϕ_c represents either the neutron or photon scalar flux.

For each energy group, the theoretically predicted scalar Monte Carlo particle flux $\tilde{M}_{c,g}$ averaged over $\mathcal{V}_c$ is given for each method as:

$$\tilde{\mathcal{M}}_{c,g}^{\mathrm{XFORM}} \approx \mathrm{C}_1 \frac{\phi_{c,g}\Phi_{c,g}^*}{B_c}, \tag{8.21}$$

$$\tilde{\mathcal{M}}_{c,g}^{\mathrm{WW}} = \mathrm{C}_1 \frac{\phi_{c,g}\Phi_{c,g}^*}{B_c}, \tag{8.22}$$

$$\tilde{\mathcal{M}}_{c,g}^{\mathrm{FWCADIS}} = \mathrm{C}_1 \phi_{c,g}\Phi_{c,g}^*, \tag{8.23}$$

where XFORM identifies the Transform approach, WW identifies our weight window, and FWCADIS identifies the FW-CADIS weight window. To remain consistent with the Monte Carlo particle flux resulting from the weight window, the Monte Carlo estimate of the forward scalar flux $\phi_{c,g}$ is treated as the "exact" forward scalar flux, and the deterministic estimate of the adjoint scalar flux $\Phi_{c,g}^*$ is used since it corresponds to the weight window. The transform approach scalar flux estimate is an

approximation of the scalar Monte Carlo flux produced by the Transform approach:

$$\mathcal{M}(\mathbf{x}, E) = \frac{\int_{4\pi} \psi(\mathbf{x}, \mathbf{\Omega}, E)\psi^*(\mathbf{x}, \mathbf{\Omega}, E)d\Omega}{B(\mathbf{x})}$$
$$\approx \mathrm{C}_0 \frac{\phi(\mathbf{x}, E)\phi^*(\mathbf{x}, E)}{B(\mathbf{x})}. \tag{8.24}$$

For all three approaches, the theoretically predicted total Monte Carlo particle fluxes for neutrons and photons are given as:

$$\tilde{\mathcal{M}}_{\mathcal{N},c} = \sum_{g=1}^{7} \tilde{\mathcal{M}}_{c,g}, \tag{8.25}$$

$$\tilde{\mathcal{M}}_{\gamma,c} = \sum_{g=8}^{10} \tilde{\mathcal{M}}_{c,g}. \tag{8.26}$$

We recall that in the neutron response problem, photons are not simulated since they do not contribute to the neutron response; however, in the photon response problem, neutrons are simulated since they are important to the photon response, even though they are not directly included in any estimator tallies.

Just as in Chapter VII on global problems, we would like to have an expression that allows us to decide whether to run several source-detector problems or a single global problem if we really do not need the solution everywhere. The expression that was derived in Chapter VII to determine the number of source-detector problems that could be run in the same time as a single global problem to meet a variance criterion in a characteristic detector region is given by Eq. 7.39:

$$\mathrm{N_{SD:G}} = \frac{\mathrm{FOM}_{D,\mathrm{sd}}}{\mathrm{FOM}_{D,\mathrm{global}}}, \tag{8.27}$$

where the FOMs for the source-detector and global problems are calculated in the detector region. Again, this equation does not include the user time required to set up each source-detector problem.

8.3.2 Numerical Results

The data for the neutron response (total flux) problems is presented in Figures 8.3 - 8.13, including the figure of merit, the simulated Monte Carlo particle flux, and the theoretically predicted Monte Carlo particle flux; the corresponding data for the photon response (total flux) problems appears in Figures 8.14 - 8.24. For

clarity, the 2D figures associated with the source-detector and source region problems contain a black rectangle to denote the "detector" region; the 1D figures include dashed vertical lines indicating the "detector" region location. All the 2D figures also contain a dashed line to trace out the diagonal from the source to the far corner (i.e. the line $x = y = z$); the 1D figures are plots along this line. In addition, Tables 8.2 and 8.3 provide the global FOM and the simulated Monte Carlo particle flux statistics, respectively, for the source-detector, source region and global neutron response problems. Tables 8.4 and 8.5 provide the corresponding data for the source-detector, source-region and global photon response problems.

Table 8.2: FOM statistics for the total neutron flux

Response Problem	**Method**	**Total Flux FOM**			
		Min	**Max**	**Median**	**Mean**
Source-Detector	**FW-CADIS**	0.028	0.062	0.040	0.041
	WW	0.018	0.104	0.038	0.043
	XFORM	0.162	0.348	0.261	0.256
Source-Region	**FW-CADIS**	0.0022	0.105	0.034	0.035
	WW	0.0021	0.144	0.045	0.047
	XFORM	0.0045	0.182	0.119	0.112
Global	**FW-CADIS**	6.9E-05	0.785	0.0034	0.0043
	WW	0.00028	0.024	0.0045	0.0058
	XFORM	0.00074	0.021	0.0052	0.0059

Table 8.3: Monte Carlo particle flux statistics for the total neutron flux

Response Problem	**Method**	**Total Simulated MC Particle Flux**			
		Min	**Max**	**Median**	**Mean**
Source-Detector	**FW-CADIS**	0.00087	0.0019	0.0014	0.0014
	WW	0.0019	0.0021	0.0020	0.0020
	XFORM	0.0035	0.0072	0.0046	0.0050
Source-Region	**FW-CADIS**	1.6E-06	0.00014	4.1E-05	4.4E-05
	WW	0.00023	0.00042	0.00033	0.00033
	XFORM	0.00031	0.0027	0.00093	0.00091
Global	**FW-CADIS**	2.6E-08	0.0078	2.4E-06	9.1E-06
	WW	0.00016	0.0074	0.00048	0.00052
	XFORM	0.00030	0.0094	0.0011	0.0012

Table 8.4: FOM statistics for the total photon flux

Response Problem	Method	Total Flux FOM			
		Min	Max	Median	Mean
Source-Detector	FW-CADIS	0.00020	0.0035	0.0011	0.0012
	WW	0.00026	0.0032	0.0012	0.0012
	XFORM	0.00062	0.0046	0.0015	0.0016
Source-Region	FW-CADIS	3.7E-05	0.0076	0.0014	0.0016
	WW	3.9E-05	0.018	0.0042	0.0046
	XFORM	0.00011	0.024	0.0048	0.0058
Global	FW-CADIS	1.4E-05	0.592	0.0019	0.0070
	WW	4.4E-05	0.041	0.0030	0.0039
	XFORM	1.4E-05	0.028	0.0031	0.0035

Table 8.5: Monte Carlo particle flux statistics for the total photon flux

Response Problem	Method	Total Simulated MC Particle Flux			
		Min	Max	Median	Mean
Source-Detector	FW-CADIS	6.6E-05	0.00049	0.00013	0.00017
	WW	0.00020	0.00044	0.00029	0.00029
	XFORM	0.00015	0.0024	0.00027	0.00052
Source-Region	FW-CADIS	2.6E-08	0.00013	3.8E-06	6.5E-05
	WW	3.3E-05	0.0023	0.00020	0.00025
	XFORM	1.5E-05	0.014	0.00031	0.00058
Global	FW-CADIS	7.9E-14	0.00092	1.8E-05	8.1E-06
	WW	3.0E-05	0.0054	0.0011	0.0011
	XFORM	6.0E-07	0.021	0.0012	0.0015

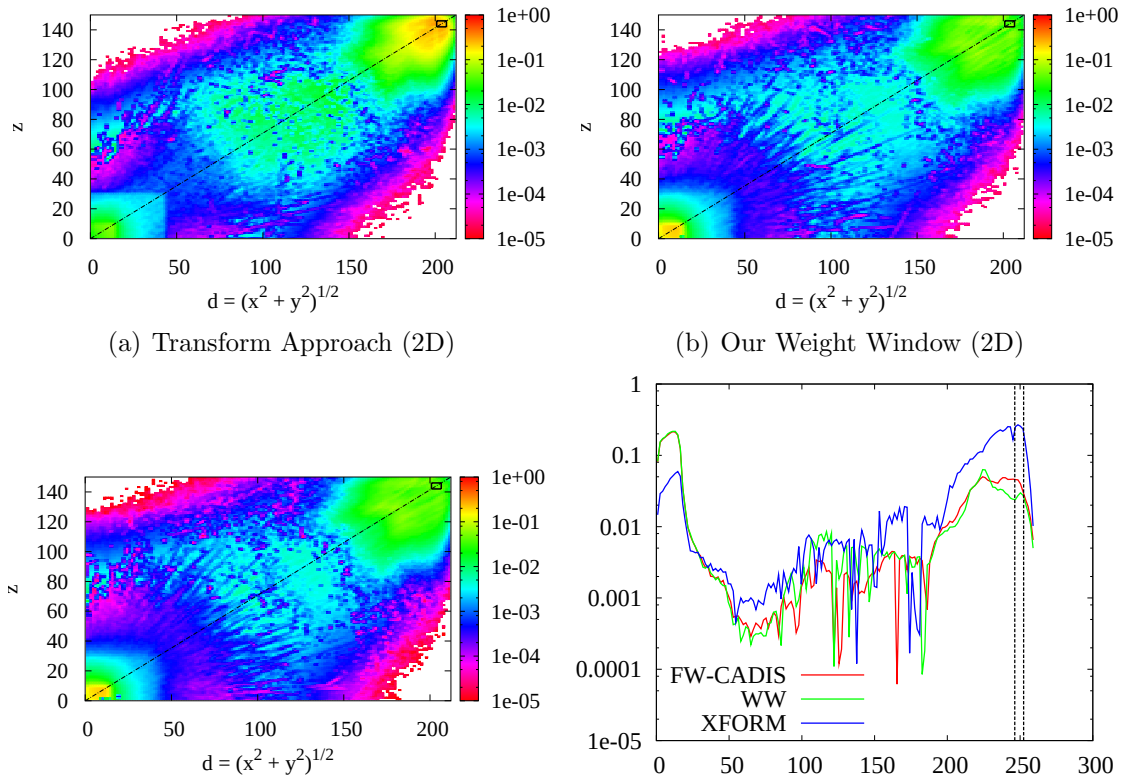

(a) Transform Approach (2D)

(b) Our Weight Window (2D)

(c) FW-CADIS (2D)

(d) All Methods (1D)

Figure 8.3: Total Flux FOM for Source-Detector (SD) Neutron Problem

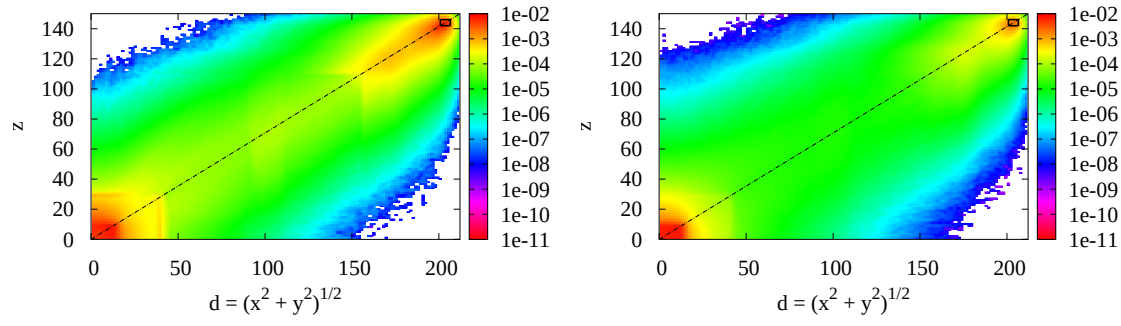

(a) Transform Approach (2D)

(b) Our Weight Window (2D)

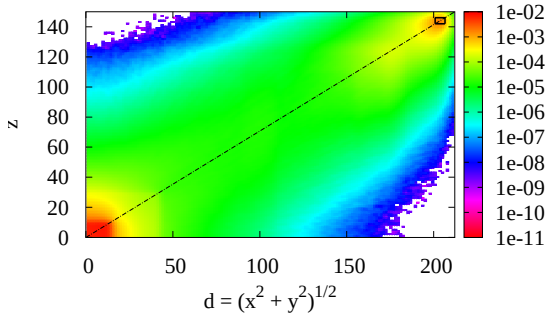

(c) FW-CADIS (2D)

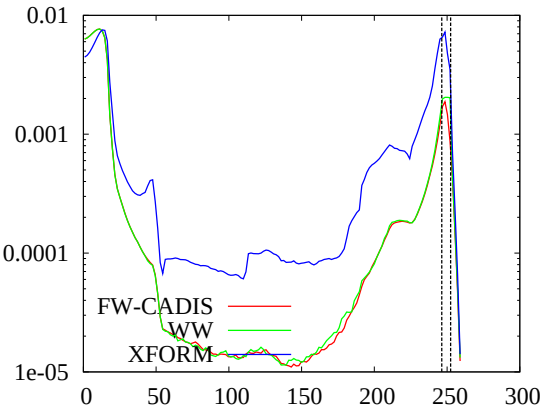

(d) All Methods (1D)

Figure 8.4: Total Simulated MC Particle Flux for SD Neutron Problem

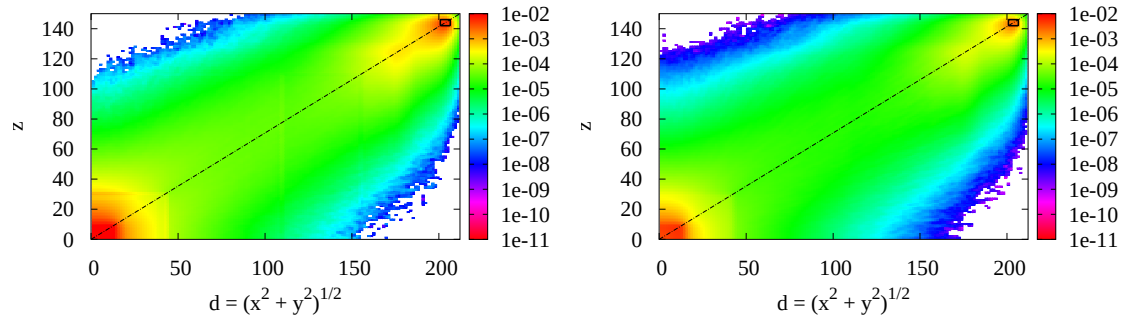

(a) Transform Approach (2D)

(b) Our Weight Window (2D)

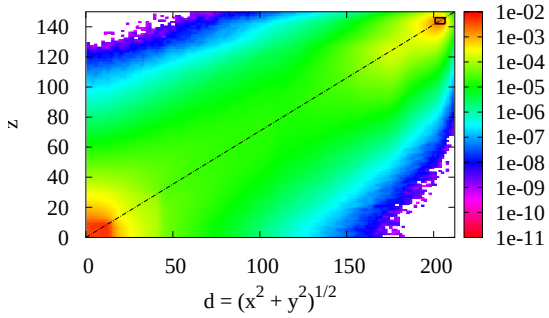

(c) FW-CADIS (2D)

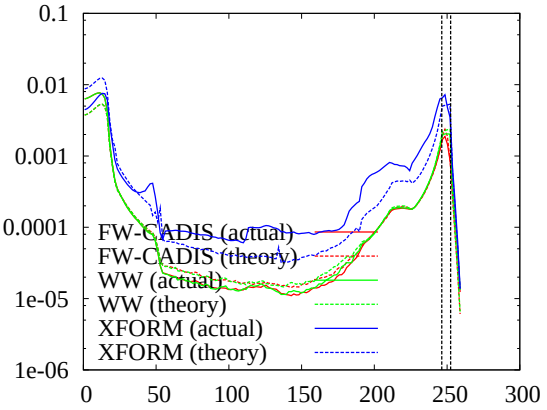

(d) All Methods (1D)

Figure 8.5: Total Predicted MC Particle Flux for SD Neutron Problem

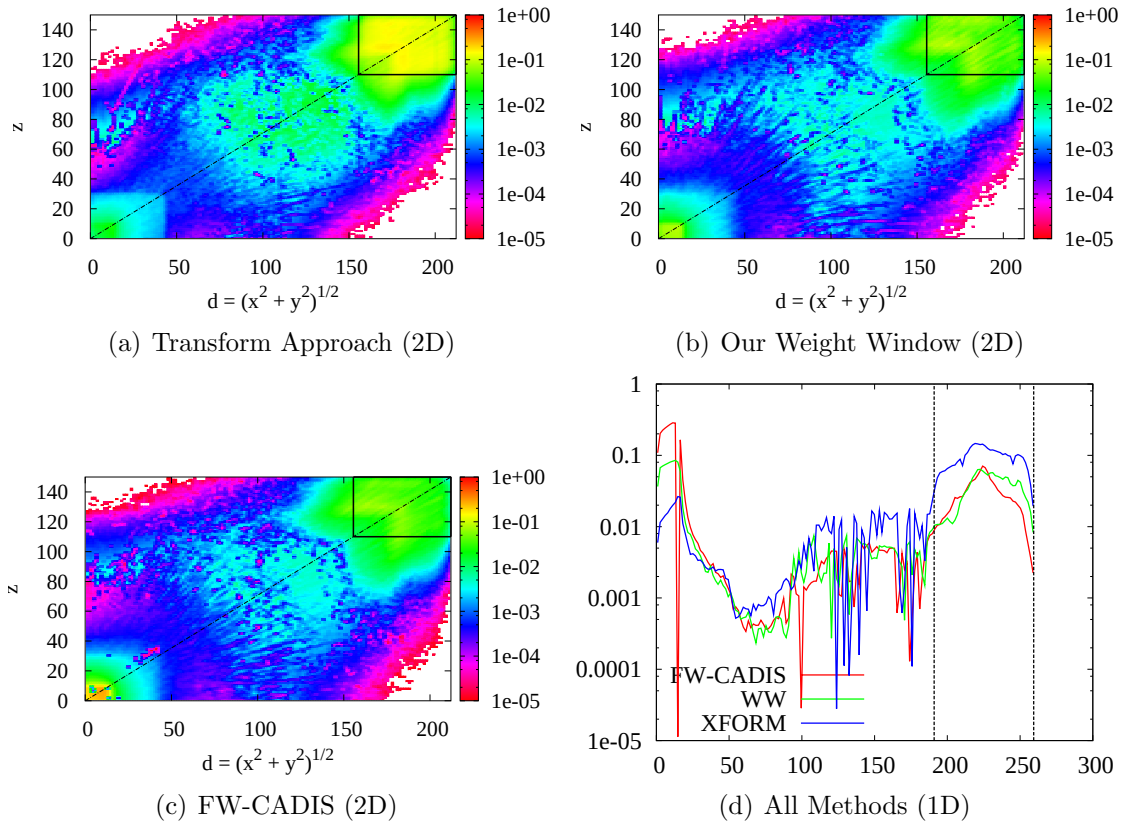

(a) Transform Approach (2D)

(b) Our Weight Window (2D)

(c) FW-CADIS (2D)

(d) All Methods (1D)

Figure 8.6: Total Flux FOM for Source-Region (SR) Neutron Problem

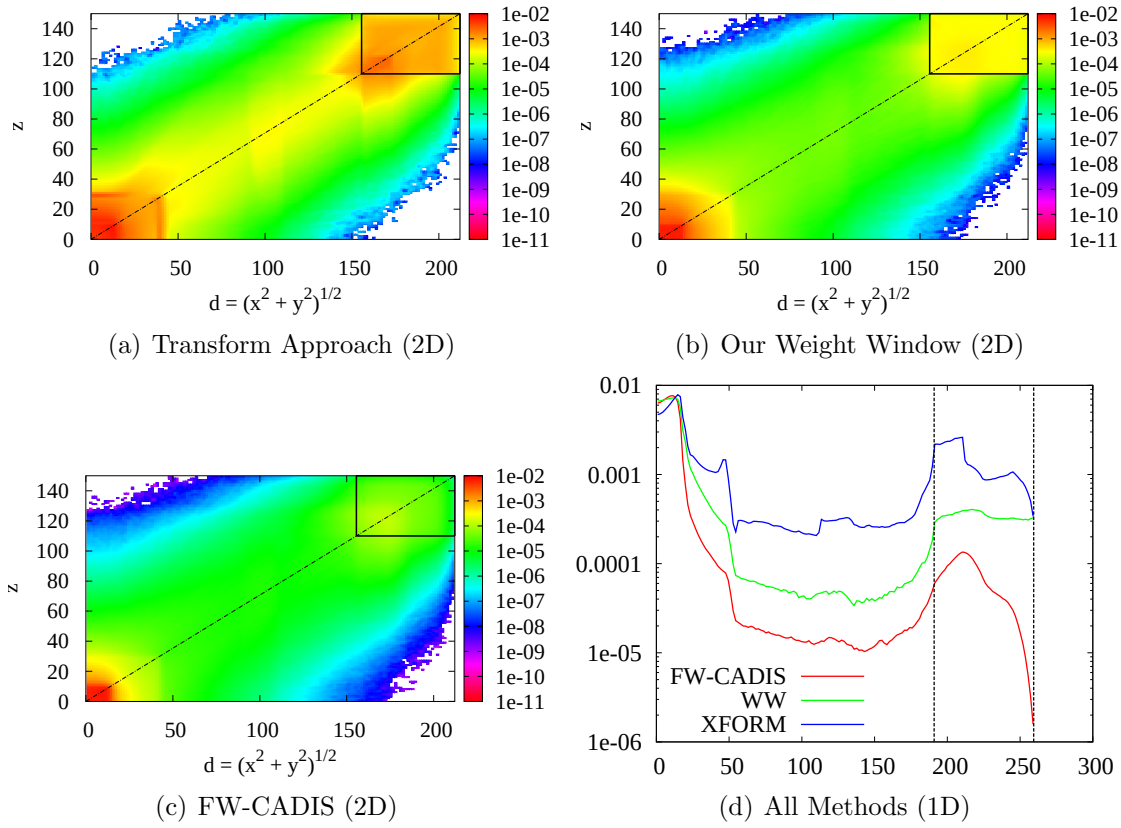

(a) Transform Approach (2D)

(b) Our Weight Window (2D)

(c) FW-CADIS (2D)

(d) All Methods (1D)

Figure 8.7: Total Simulated MC Particle Flux for SR Neutron Problem

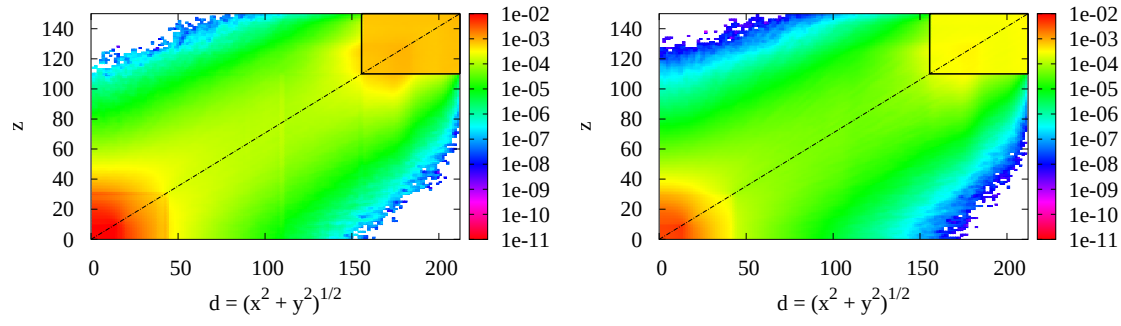

(a) Transform Approach (2D)

(b) Our Weight Window (2D)

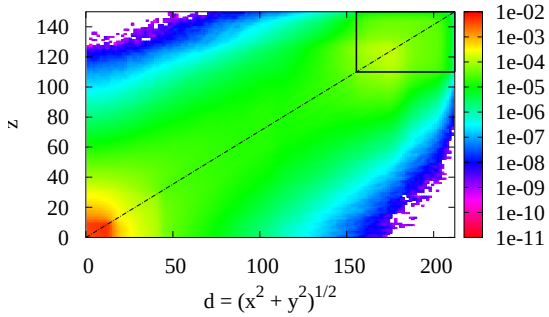

(c) FW-CADIS (2D)

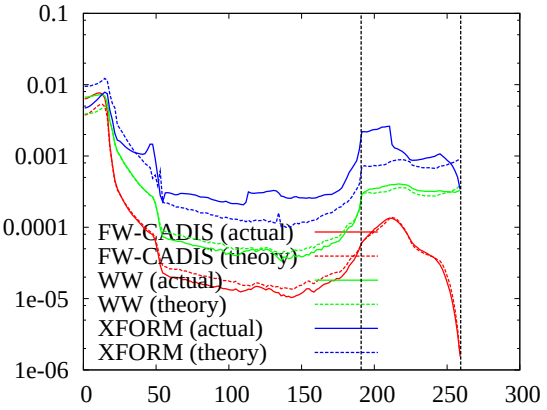

(d) All Methods (1D)

Figure 8.8: Total Predicted MC Particle Flux for SR Neutron Problem

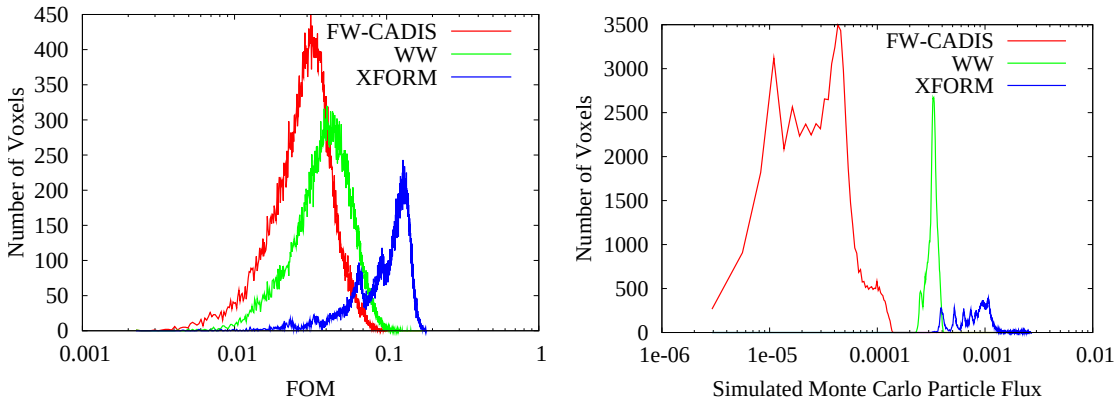

(a) Number of Voxels vs FOM (b) Number of Voxels vs Simulated MC Flux

Figure 8.9: Statistics by Number of Voxels for SR Neutron Problem

Table 8.6: Detector vs global total neutron and photon flux data

Response Problem	**Method**	**Detector $\mathbf{FOM_D}$**	**Global $\mathbf{FOM_D}$**	$\mathbf{N_{D:G}}$
Neutron ($\phi_{c,g}$)	**FW-CADIS**	0.040	0.0011	105
	WW	0.038	0.0055	11
	XFORM	0.261	0.0086	23
Photon (ϕ_c)	**FW-CADIS**	0.0011	2.45E-05	45
	WW	0.0012	0.00038	3
	XFORM	0.0015	0.00043	3

No single metric exists for assessing and comparing methods for the various problems; thus, we again consider the median FOM as a metric that conveys information about the efficiency and accuracy of the solution, since it relays that half the spatial elements in the region have an FOM below this value and half have an FOM that is greater than this value. (The maximum and minimum values of the FOM can also be used to bound the FOM in the lower and upper half.) Therefore, we again use the median value and the figures to assess and compare the performance of the various methods, even for the source-detector problems where there are only 64 spatial elements.

As previously mentioned, since the challenge problems are simulated on a supercomputer, we expect the FOM data to have some variability that is not inherent in the methods themselves. Despite this, we identify some patterns in the FOM data that are consistent with the simpler problem simulated in the previous three chapters. Specifically, the median FOM data for the total neutron flux given in Table

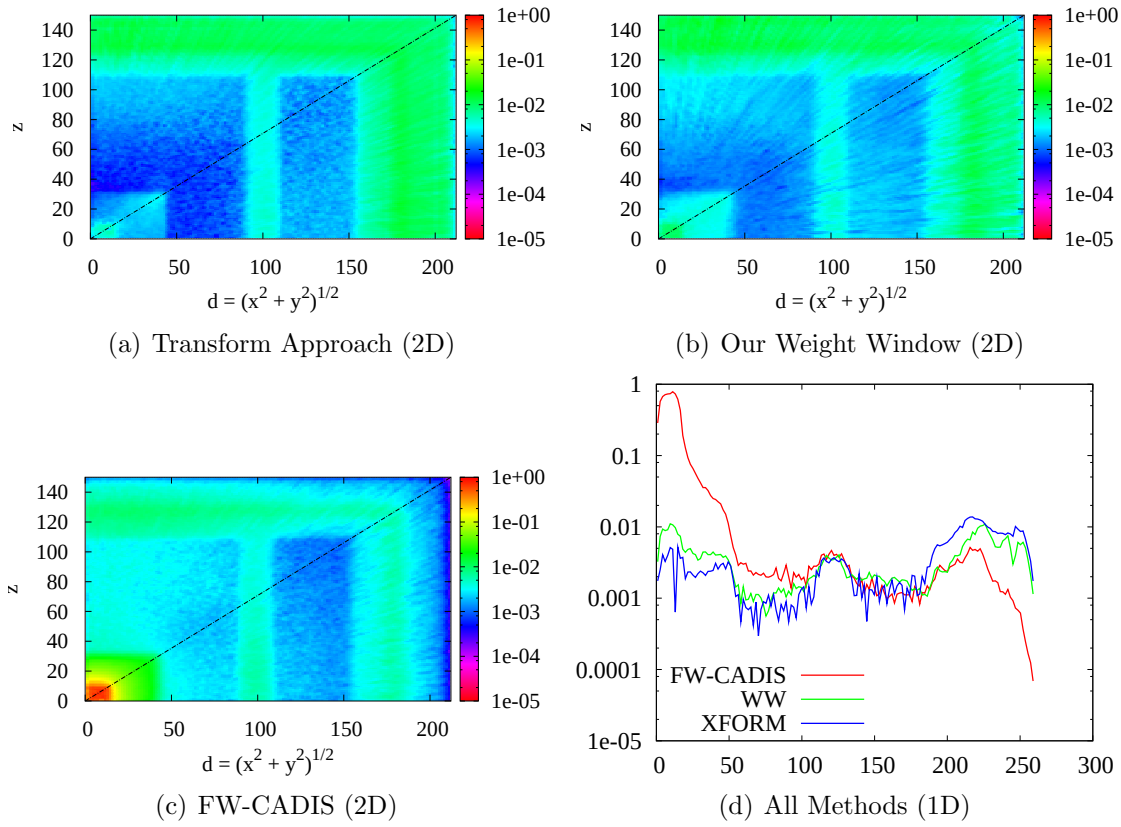

(a) Transform Approach (2D)

(b) Our Weight Window (2D)

(c) FW-CADIS (2D)

(d) All Methods (1D)

Figure 8.10: Total Flux FOM for Global Neutron Problem

8.2 indicates that the Transform approach generally outperforms the weight window methods, especially for the source-detector problem. The general trend, evidenced here and in previous chapters, is that the performance of the Transform approach generally degrades as the region of interest becomes larger. This means that as particles are allowed to spread out more in space, the benefits associated with the Transform approach (specifically the angularly biased scattering and angularly dependent distance-to-next collision) are not substantial enough to compensate for the additional computational cost associated with the method. This explains why the Transform approach's median FOM for the total photon flux given in Table 8.4 is comparable to the weight window approaches: since photons are not readily attenuated in the large water region, they readily spread out within the water region with no large gradients to drive them toward the "detector" region. (Recall that the gradient of the adjoint flux determines the strength of the angular biasing parameters in the Transform approach.) Thus, the source-detector and source region median FOMs for the photon flux are only comparable to the weigh window methods because the extra contributon physics implemented in the Transform approach have a small effect on

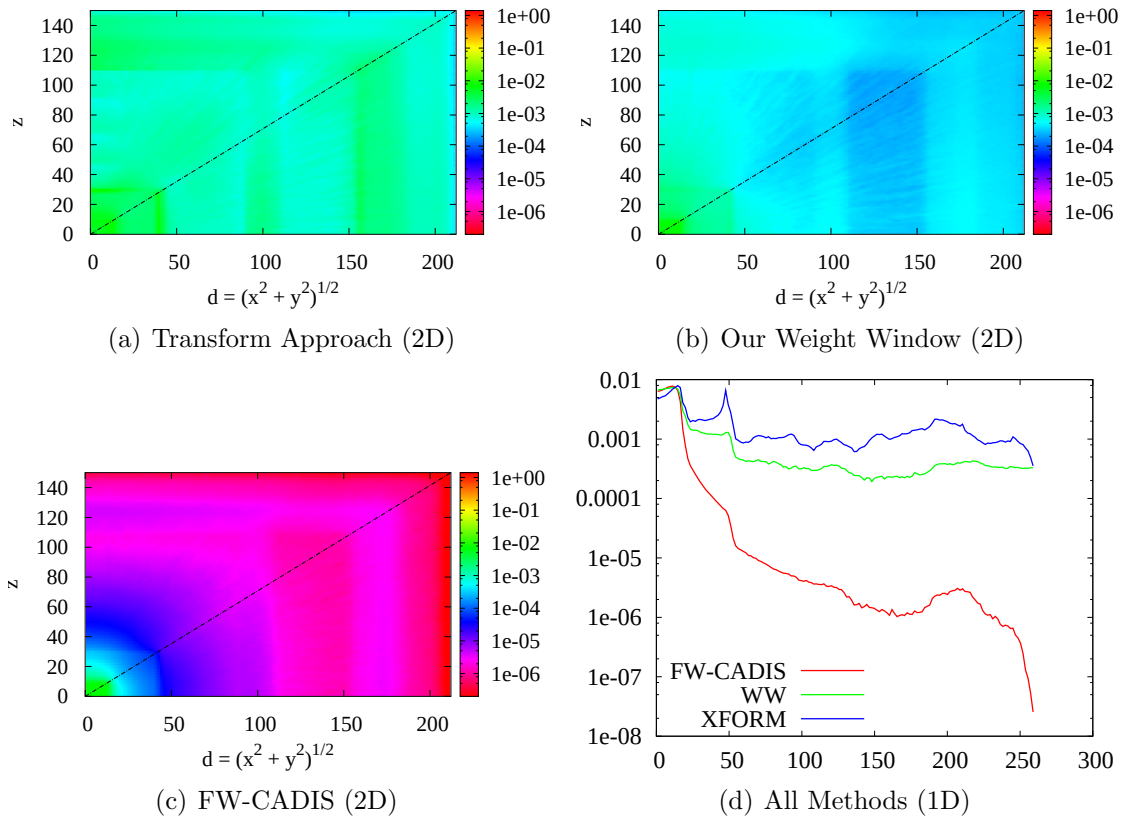

(a) Transform Approach (2D)

(b) Our Weight Window (2D)

(c) FW-CADIS (2D)

(d) All Methods (1D)

Figure 8.11: Total Simulated MC Particle Flux for Global Neutron Problem

guiding the particles toward the "detector" region. Figure 8.15 and 8.18 show the simulated Monte Carlo particle flux for the source-detector and source-region photon problems, respectively.

To decide whether to simulate a source-detector, source-region, or detector problem obviously depends on the application. The neutron FOM data in Table 8.2 shows that there can be a substantial benefit to simulating only the source-detector or source-region problem, with a median FOM that is over an order of magnitude larger than the median FOM for the global problem. The minimum FOM also shows that the median FOM is much more tightly bound for the source-detector problem than for the global problem. The photon FOM data in Table 8.4 indicates that the median FOM is larger for the global problem than for the source-detector problem. This result again occurs because photons readily fill the large water and concrete regions and produce good statistics there; whereas the detector region $\mathcal{V}_D$ exists behind several thick layers of lead. Thus, the median favors the global problem; however, the minimum FOM indicates that the median detector FOM is more tightly bound than the median global FOM. Figures 8.9 and 8.13 present the neutron FOM statistics

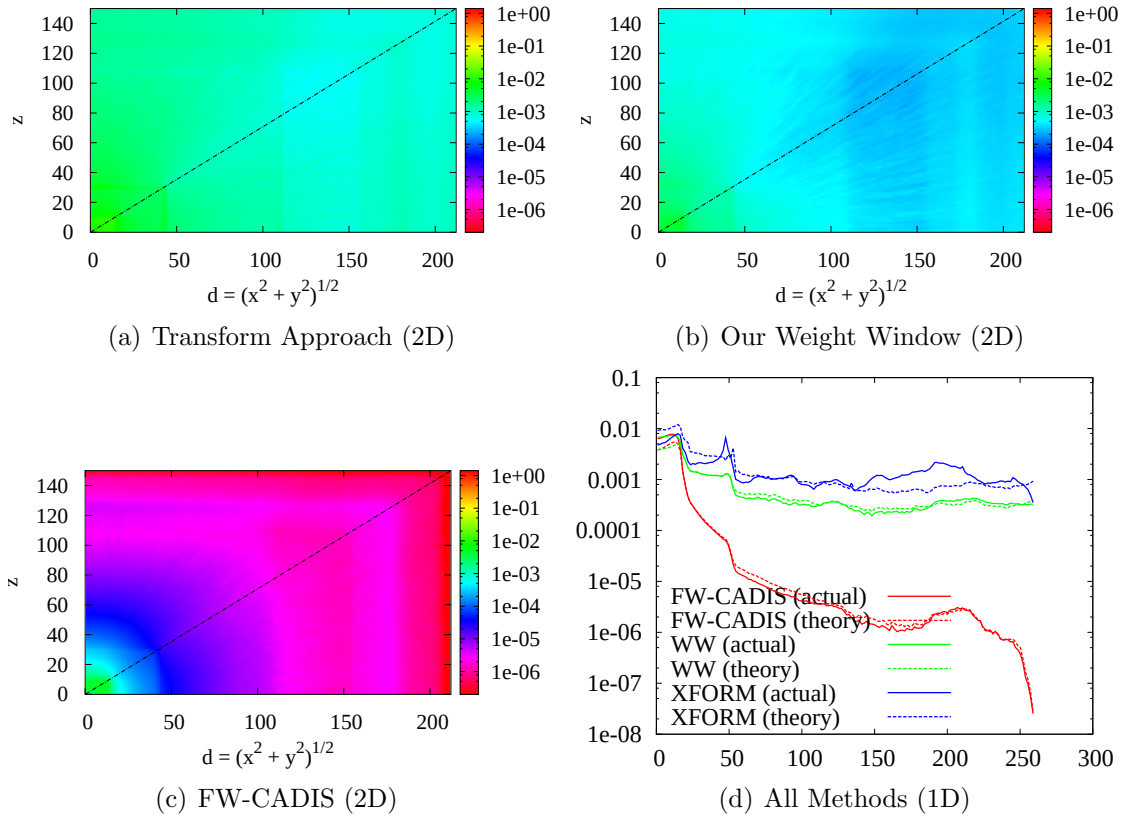

(a) Transform Approach (2D)

(b) Our Weight Window (2D)

(c) FW-CADIS (2D)

(d) All Methods (1D)

Figure 8.12: Total Predicted MC Particle Flux for Global Neutron Problem

for the source-region and global problem, respectively; specifically, they represent the number of spatial elements that correspond to a particular FOM. Figures 8.20 and 8.24 are the corresponding photon FOM data. This data indicates that for all the problems except the global neutron problem, the Transform approach and our weight window have a larger number of spatial elements at a higher FOM than the FW-CADIS method. In the global neutron problem, the methods are comparable.

The simulated Monte Carlo particle flux is depicted in Figures 8.4, 8.7, and 8.11 for the source-detector, source-region and global neutron response problem, respectively, and the corresponding predicted Monte Carlo particle flux is shown in Figures 8.5, 8.8, and 8.12. For the photon response, the simulated Monte Carlo particle flux is depicted in Figures 8.15, 8.18, and 8.22 for the source-detector, source-region and global problem, respectively, and the corresponding predicted Monte Carlo particle flux is shown in Figures 8.16, 8.19, and 8.23. The 1D Monte Carlo particle flux plots include both the simulated (actual) data and the predicted (theory) data, to better compare the accuracy of the theory. By comparing the 1D and 2D figures, we observe that there is good agreement between the simulated and predicted Monte Carlo par-

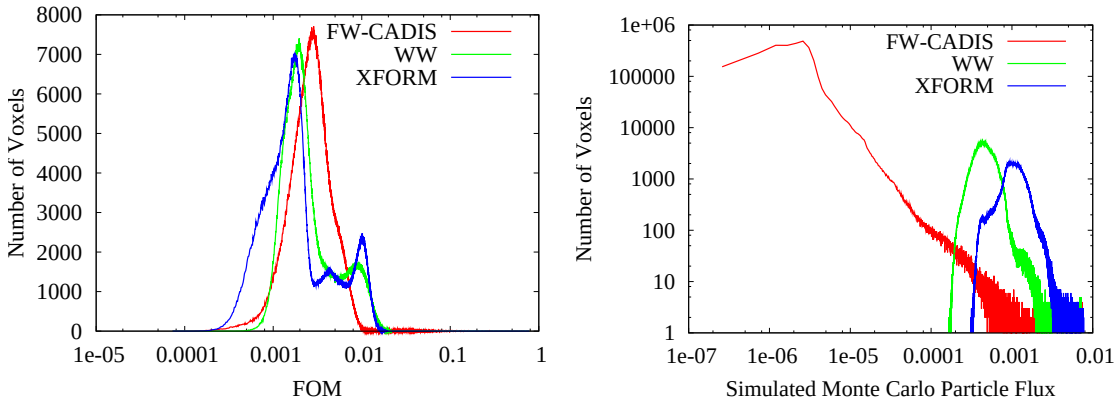

(a) Number of Voxels vs FOM

(b) Number of Voxels vs Simulated MC Flux

Figure 8.13: Statistics by Number of Voxels for Global Neutron Problem

ticle flux. The most significant deviation exists in the Transform approach, where the predicted Monte Carlo particle flux is only an approximation. Both weight window methods, however, show excellent agreement between the theoretical predictions and the simulated values.

As before, the challenge problem results indicate that a positive correlation exists between the FOM and the Monte Carlo particle flux since the shape of the curves is similar. However, comparing the 1D plots of the simulated Monte Carlo particle flux and the FOM demonstrates that there certainly is no obvious correlation since the particle flux data tends to be much smoother than the FOM data.

Finally, Table 8.6 provides data on the number of source-detector problems that could be run in the same time as one single global problem for the neutron and photon flux problems. This data is useful if the user does not need the solution everywhere but still in a large number of locations, perhaps along the boundary of the system. The data from the FW-CADIS method demonstrates that 105 source-detector neutron flux problems could be run before the a global problem makes sense while 45 source-detector photon flux problems could be simulated. This shows that, while FW-CADIS is well-suited for source-detector problems, it is less well-suited for global calculations. Our weight window demonstrates that 11 source-detector neutron flux problems could be run before a global calculation would make more sense while 3 source-detector photon flux problems could be simulated. This demonstrates how much better our weight window is than the FW-CADIS for obtaining good statistical results in the deep parts of the problem for global calculations. Finally, the data for the Transform approach shows that 23 source-detector neutron flux problems could be solved for the cost of one global calculation while only 3 could

be simulated for the photon flux problem before the computational cost exceeds one global calculation.

8.4 Summary

In this section, we have described a challenge problem to assess whether the methods presented in this thesis can adequately solve a more realistic shielding problem. The results indicate that all the methods are able to solve the source-detector, source-region, and global neutron and photon response problems by employing the methodology described in the previous three chapters. In addition, the challenge problem again validates the theory: for a given weight window or "transform" function, the Monte Carlo particle flux is correctly predicted by the theory. Finally, the results indicate that there is a positive correlation between the FOM and the Monte Carlo particle flux, but the figures here show that there may be less of a correlation than is suggested by the simpler 3-group problem.

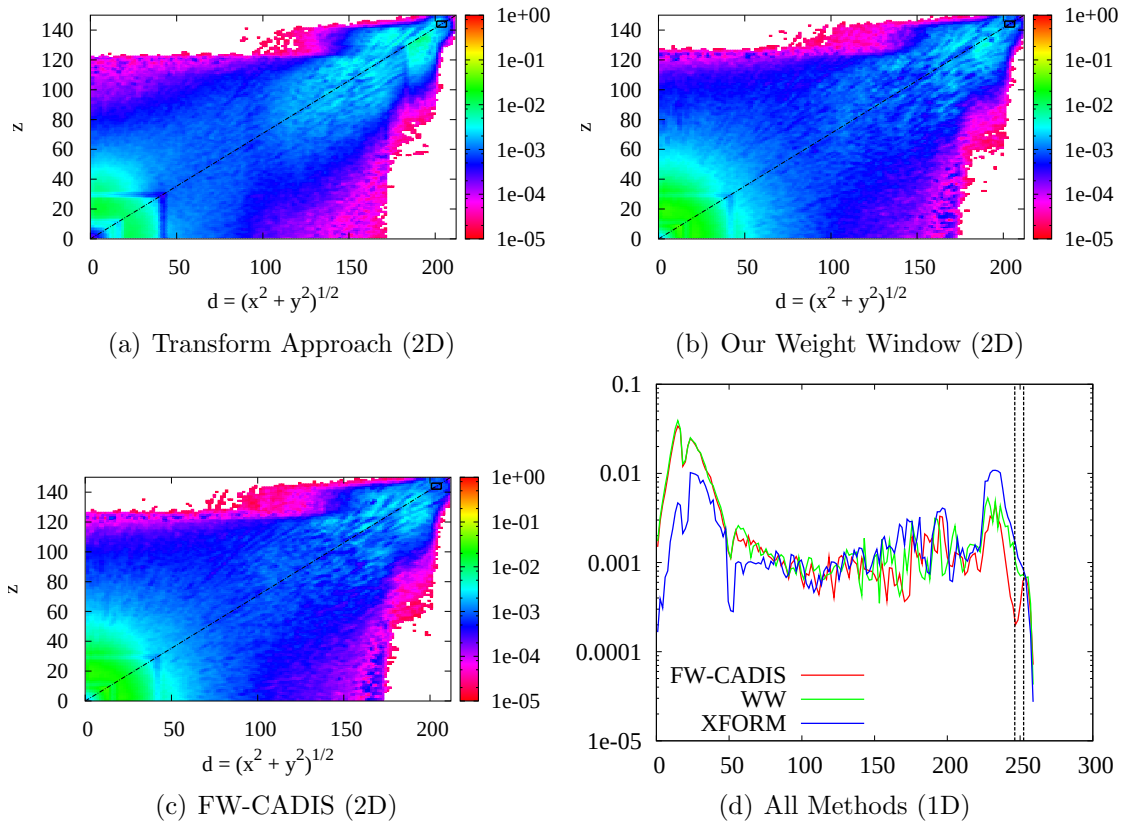

(a) Transform Approach (2D)

(b) Our Weight Window (2D)

(c) FW-CADIS (2D)

(d) All Methods (1D)

Figure 8.14: Total Flux FOM for Source-Detector (SD) Photon Problem

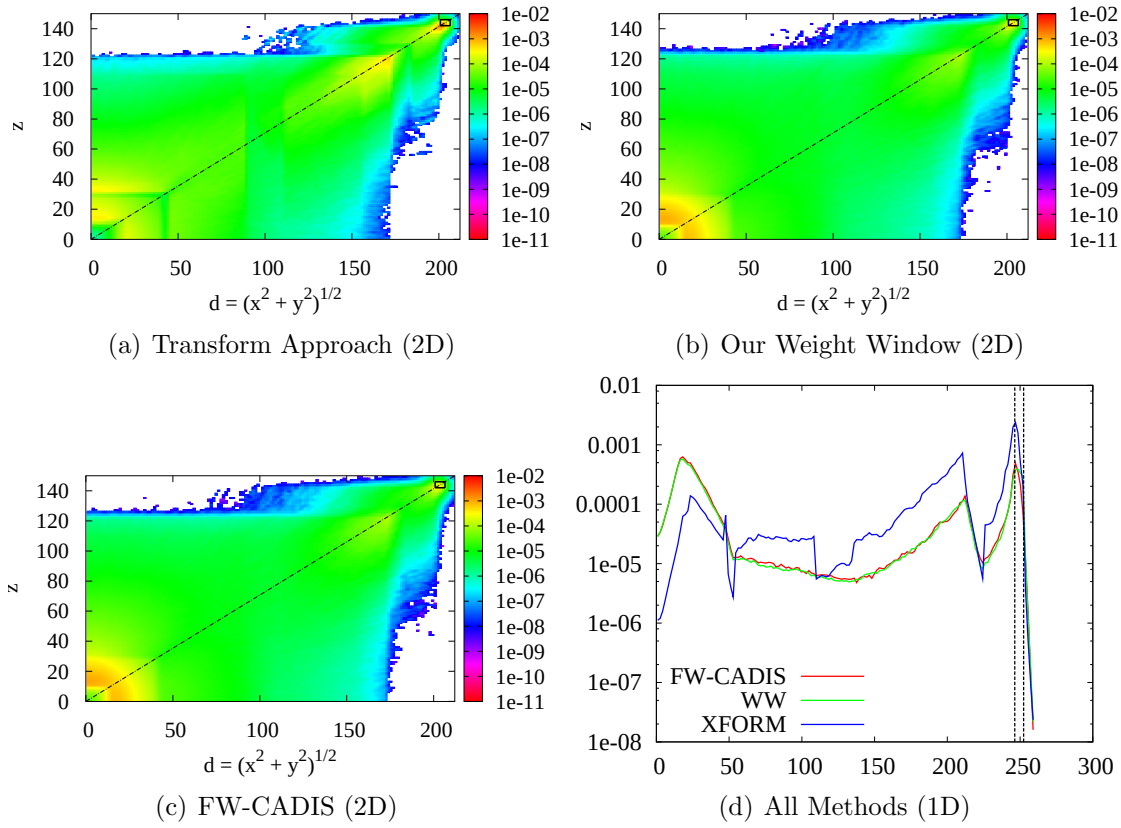

(a) Transform Approach (2D)

(b) Our Weight Window (2D)

(c) FW-CADIS (2D)

(d) All Methods (1D)

Figure 8.15: Total Simulated MC Particle Flux for SD Photon Problem

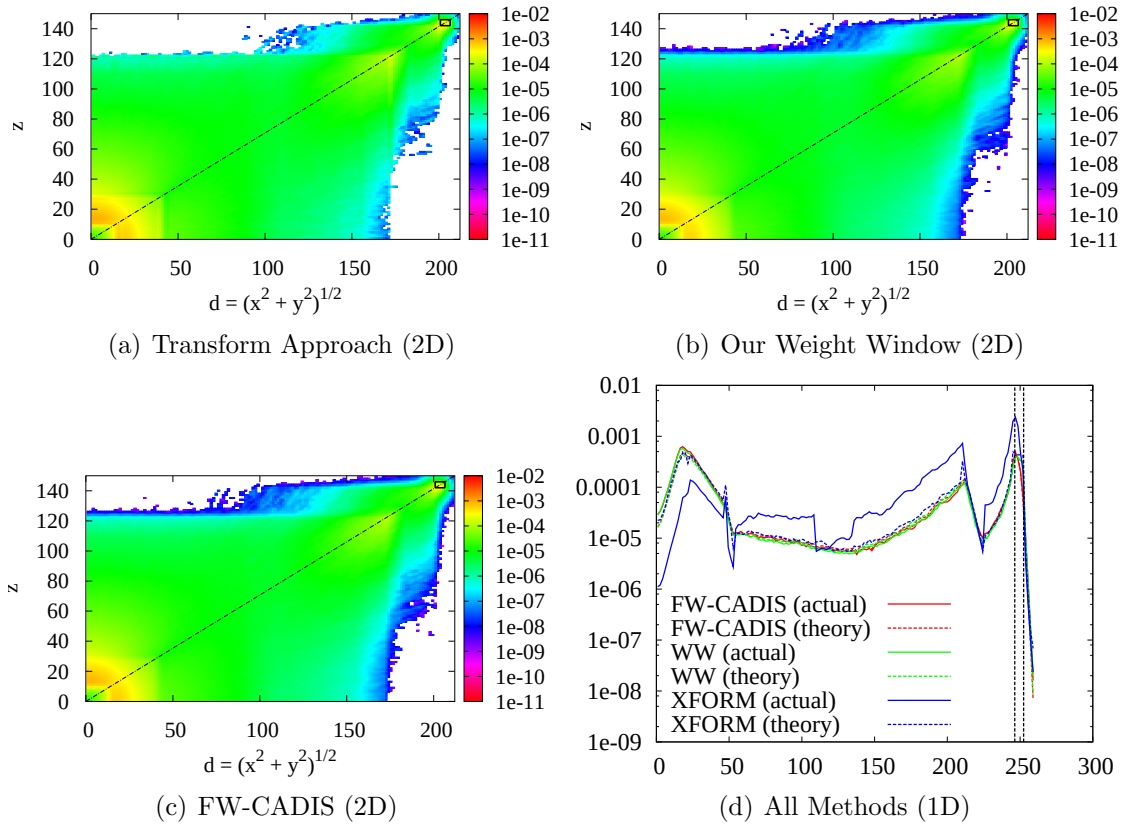

(a) Transform Approach (2D)

(b) Our Weight Window (2D)

(c) FW-CADIS (2D)

(d) All Methods (1D)

Figure 8.16: Total Predicted MC Particle Flux for SD Photon Problem

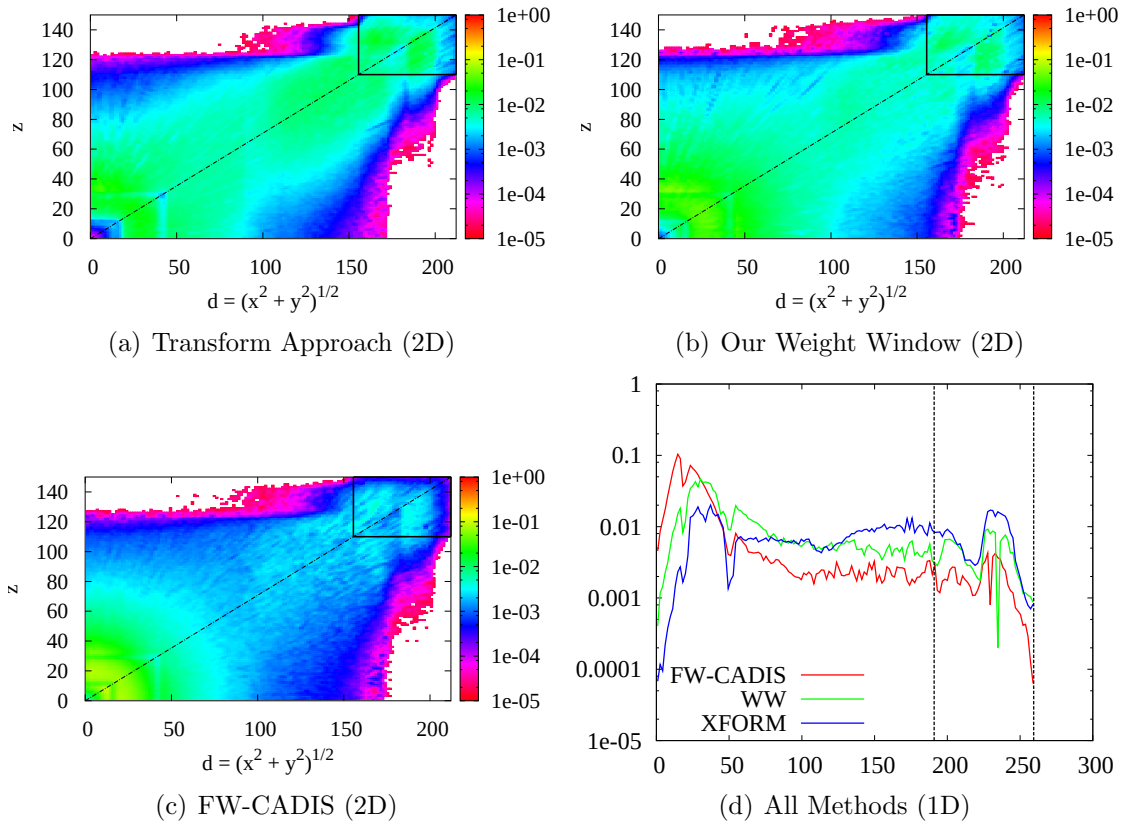

(a) Transform Approach (2D)

(b) Our Weight Window (2D)

(c) FW-CADIS (2D)

(d) All Methods (1D)

Figure 8.17: Total Flux FOM for Source-Region (SR) Photon Problem

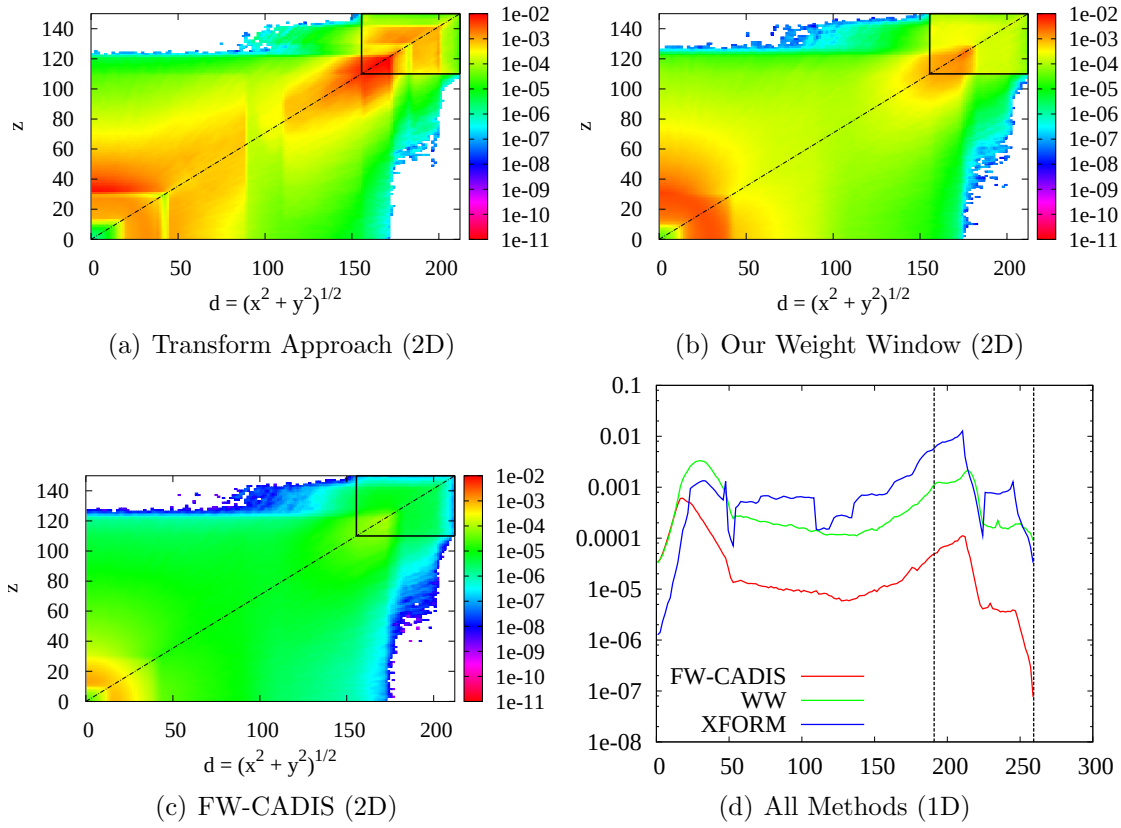

(a) Transform Approach (2D)

(b) Our Weight Window (2D)

(c) FW-CADIS (2D)

(d) All Methods (1D)

Figure 8.18: Total Simulated MC Particle Flux for SR Photon Problem

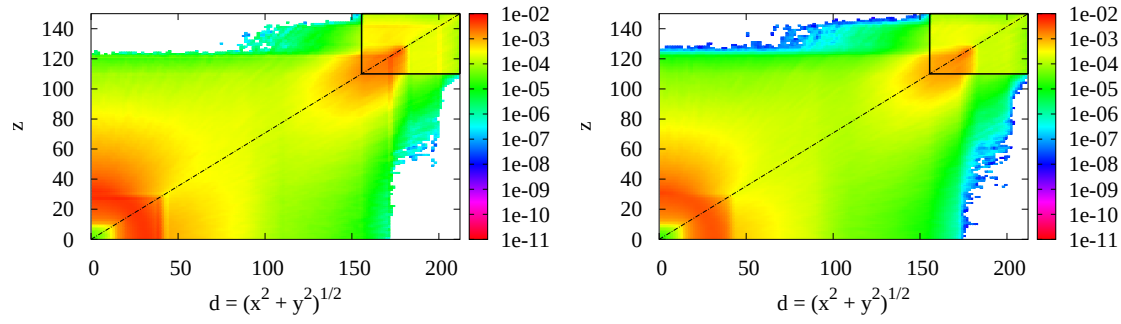

(a) Transform Approach (2D)

(b) Our Weight Window (2D)

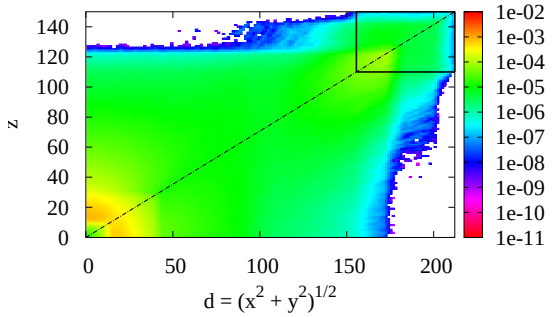

(c) FW-CADIS (2D)

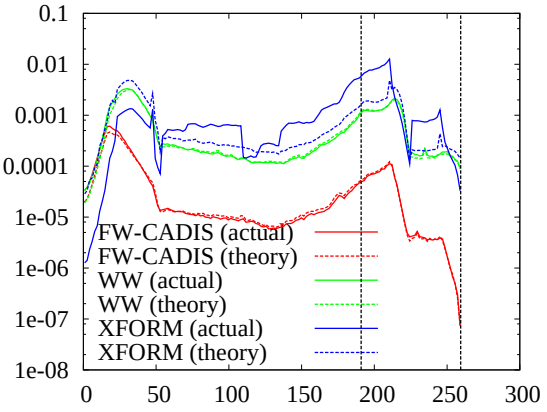

(d) All Methods (1D)

Figure 8.19: Total Predicted MC Particle Flux for SR Photon Problem

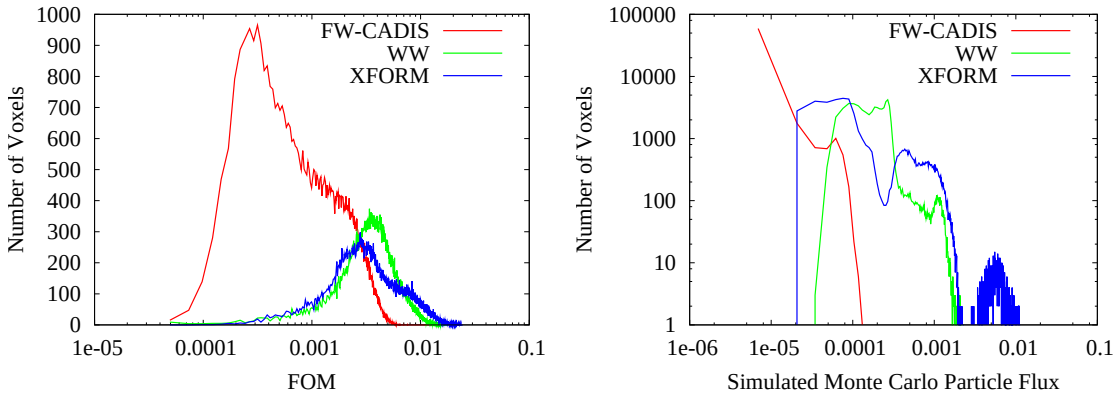

(a) Number of Voxels vs FOM

(b) Number of Voxels vs Simulated MC Flux

Figure 8.20: Statistics by Number of Voxels for SR Photon Problem

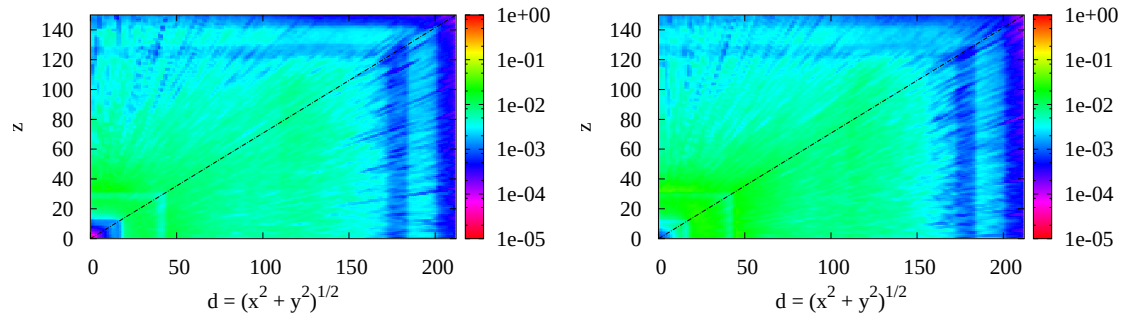

(a) Transform Approach (2D)

(b) Our Weight Window (2D)

(c) FW-CADIS (2D)

(d) All Methods (1D)

Figure 8.21: Total Flux FOM for Global Photon Problem

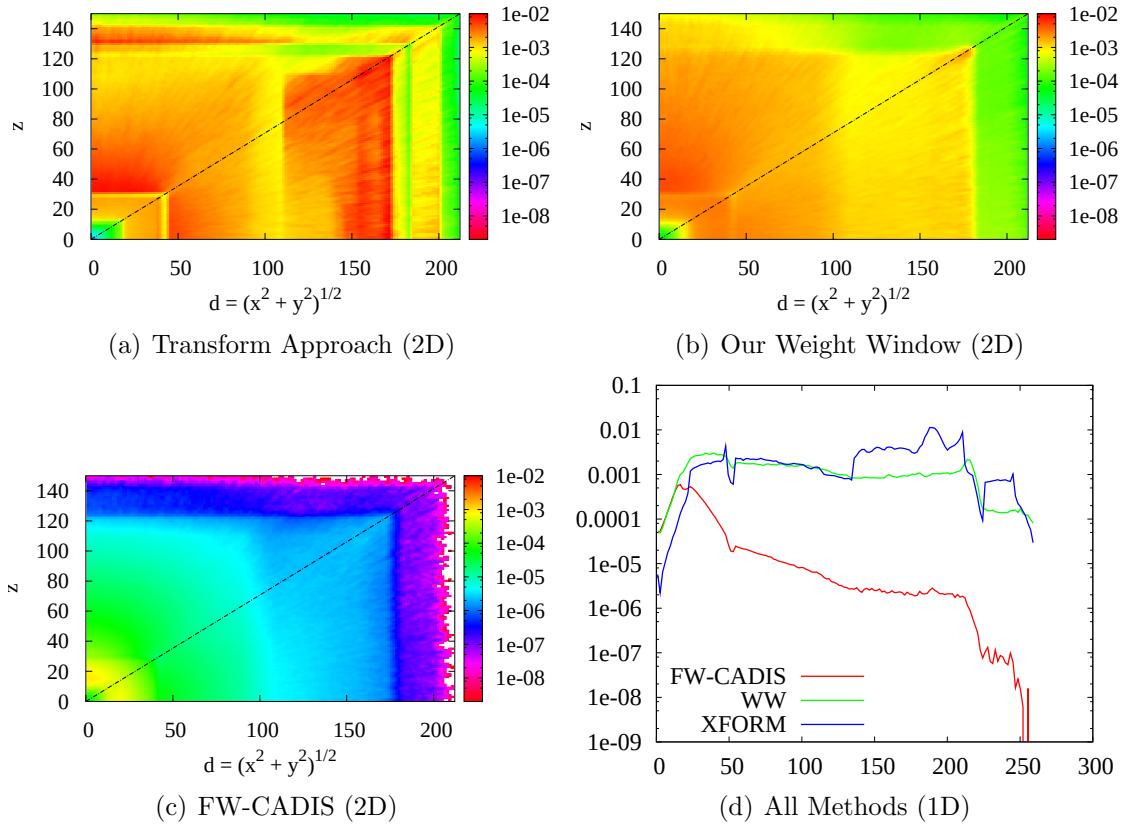

(a) Transform Approach (2D)

(b) Our Weight Window (2D)

(c) FW-CADIS (2D)

(d) All Methods (1D)

Figure 8.22: Total Simulated MC Particle Flux for Global Photon Problem

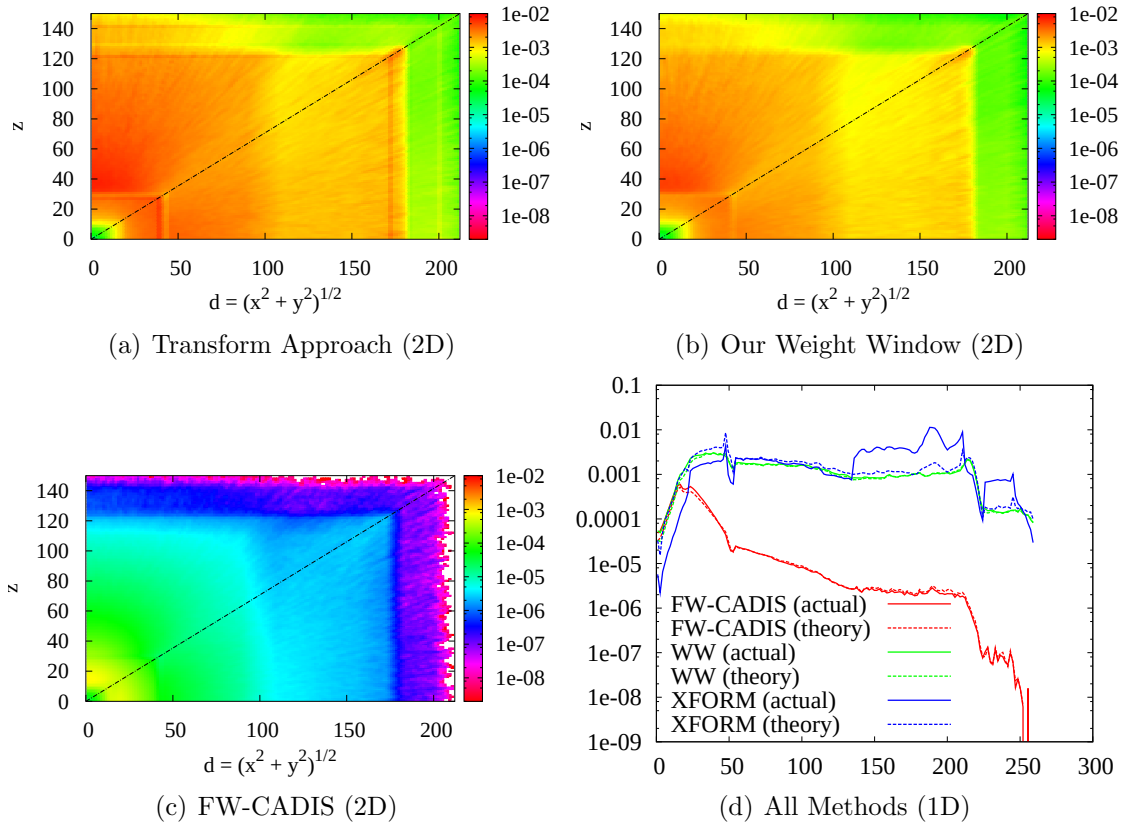

(a) Transform Approach (2D)

(b) Our Weight Window (2D)

(c) FW-CADIS (2D)

(d) All Methods (1D)

Figure 8.23: Total Predicted MC Particle Flux for Global Photon Problem

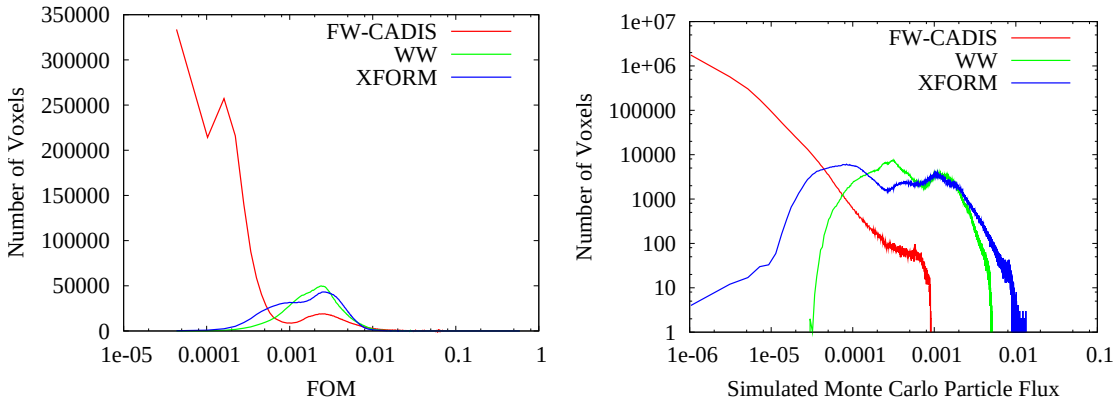

(a) Number of Voxels vs FOM

(b) Number of Voxels vs Simulated MC Flux

Figure 8.24: Statistics by Number of Voxels for Global Photon Problem

Chapter IX

Conclusions

In this thesis we have described in detail two methods – weight windows and the Transform approach – that allow Monte Carlo practitioners to disperse Monte Carlo particles throughout phase space according to a user-specified distribution. The weight window approach uses splitting and Russian roulette, resulting from a specific weight window, to achieved the user-specified distribution; it does not modify the underlying particle physics. This weight window is specified by a simple but useful theory that relates the Monte Carlo particle distribution to the weight window center. The Transform approach accomplishes the user-specified distribution by comprehensively modifying the underlying particle physics through the introduction of a specific transform into the neutron transport equation; the Monte Carlo method is then used to simulate this new equation with its modified particle physics. We derived an expression that relates the Monte Carlo particle distribution to a "transform" function that accomplishes the objectives of the Transform approach. The weight window and Transform approach are included within a more general framework for distributing particles, referred to as the General Transform approach.

The weight window and Transform approaches have been developed for and applied to three geometric classes of shielding problems: source-detector, source-region, and global problems. In the source-detector problem, a solution, such as the scalar flux or response, is desired in a single location in space – the detector; usually, the source and detector are separated by a non-trivial distance, the geometry is often complicated, and the solution experiences significant attenuation (by 10 or more orders of magnitude) from the source to the detector. (The classic source-detector problem is to obtain a single response in the detector.) In the source-region problem, a solution is desired throughout a significantly large "detector" region; it shares many similarities to the source-detector problem except that the region of interest is large

enough to exhibit significant attenuation within its domain. Finally, in the global problem, the solution is desired throughout the entire system; this problem is the most challenging, since good statistical results are required at all points in space. For each of these problems, two types of solution were considered – the energy-dependent scalar flux $\phi(\mathbf{x}, E)$ and a space-dependent response $\mathcal{R}(\mathbf{x})$. (For the source-detector problem, we sometimes considered a single-valued response, $\mathcal{R}_D$ since $\mathcal{R}(\mathbf{x}) \approx \mathcal{R}_D$ for a small detector.) The major difference between these two problems lies in how particles are distributed in the energy domain. For the flux problem, Monte Carlo particles should be distributed nearly uniformly in energy, since we require the scalar flux at every energy. For the response problem, Monte Carlo particles should be distributed in a way that more optimally resolves the space-dependent response.

To solve these problems, we implemented the Transform approach and two weight window techniques, the FW-CADIS weight window and our own weight window. For each technique, the Monte Carlo particles were distributed proportional to the contributon flux, or a modified form of the contributon flux, which estimates the relative importance of each phase-space element to the solution – flux or response. To obtain this particle distribution for each of the methods requires an estimate of the adjoint flux and sometimes the forward flux. However, since the adjoint problem is not inherently defined by the problem statement, we need to specify the correct adjoint source that corresponds to the type of solution we seek – flux or response – and the geometric class – source-detector, source-region, or global. This adjoint source can be defined for each problem type by identifying a suitable adjoint contributon source that corresponds to the desired solution; this is described in detail in Chapter V.

In Chapters V – VII, a test problem is solved indicating that all three methods are capable of obtaining the response and flux for the source-detector, source-region, and global problem. The Transform approach generally performed better than the weight window techniques; however, relative to the other methods, it performed much better for the source-detector problem than for the global problem. This indicates that the additional computational cost associated with simulating the contributon physics begins to undermine the gain for problems in which a solution is desired in an extended region of space. Our weight window generally performed better than the FW-CADIS method for the source-region and global problems; this can be attributed to modifying the Monte Carlo particle distribution in the "detector" region to be more uniform in space. This test problem also validated the theoretical expression relating the Monte Carlo particle distribution to the weight window center and the

"transform" function for the weight window techniques and Transform approach, respectively.

In addition to the test problem, a more realistic challenge problem was considered in Chapter VIII. All methods were able to obtain the total neutron and photon flux for each geometric class of problems — source-detector, source-region, and global problems. Although we did not make specific conclusions about the efficiency of each method due to the variability in the calculations obtained on the supercomputer, we did notice similar patterns seen in the test problem. Specifically, the Transform approach performed better than the weight window approaches when the "detector" region was small and the materials were optically thick to prevent particles from easily dispersing throughout the system. Again, the results for the weight window techniques validated the theoretical expressions relating the Monte Carlo particle distributions with the weight window center. Although the results for the Transform approach were only an approximation to the theoretical expression relating the Monte Carlo particle distribution and the "transform" function, they demonstrated reasonable agreement.

Overall, we have demonstrated in this thesis that weight window techniques and the Transform approach can be used to distribute Monte Carlo particles throughout phase space according to a user-specified distribution. Although we provided no theoretical expression that relates the Monte Carlo particle flux and the figure of merit, there seems to be a positive correlation between the two. Even without a theoretical link between the two, Monte Carlo particles exist within the system with some distribution; it seems better to have tools that allow the user to prescribe these distributions clearly.

We present here some ideas for future work:

1. The most obvious next step is to apply the weight window techniques and Transform approach to a continuous-energy Monte Carlo code. The weight window techniques would be simple to implement, since they are imposed on the system without altering the underlying particle physics. Most of the effort would be allocated toward determining an appropriate energy group structure for the deterministically-generated weight window. The Transform approach would be much more difficult to implement in a continuous-energy Monte Carlo code, since it requires adjusting the particle physics. This implicitly means sampling different probability distributions, which can be complicated for continuous-energy Monte Carlo calculations.

2. Another interesting pursuit would be to develop an algorithm, based on the methodology given in this thesis, that uses information obtained in the Monte Carlo simulation to generate the weight window and "transform" function parameters during run-time, or to at least adjust deterministically obtained parameters. The update would be performed at periodic intervals (e.g. every 100,000 particles) and would need to include some means to assess whether the data is statistically resolved enough to use. [Something similar to this is done now in MCNP to generate weight windows.]

3. Other forms of the General Transform approach, which include mixing weight windows with some modifications to the physics, should be investigated to determine whether they are more cost-effective than the full-blown Transform approach. Also, an angle-dependent weight window should be investigated based on the theory developed here.

4. If possible, a theory should be developed that clarifies the correlation between the Monte Carlo particle flux and metrics such as the FOM. This theoretical model would include deriving expressions that describe the effect of weight windows on the variance.

5. The work in this thesis has focused on distributing Monte Carlo particles according to the contributon flux; however, this is certainly not the only option. Other distributions may be better for specific types of problems; these should be investigated theoretically and experimentally.

6. A thorough comparison of source-detector and global problems should be performed to determine whether a correlation based on problem size and material properties can be developed to predict the number of source-detector problems that can be run before a global problem makes more sense, when using the weight window or Transform approaches.

Appendices

Appendix A

Atomic Composition of Materials

This appendix contains the atomic composition of each material used in the challenge problem in Chapter VIII: concrete, water, stainless steel 304, lead, and uranium dioxide.

Table A.1: Composition of concrete

Isotope/Element	Number Density (cm^{-3})	Atom Percent (%)
H-1(H20)	7.77e-3	10.4
C	1.15e-4	0.155
O-16	4.38e-2	58.9
Na-23	1.05e-3	1.41
Mg	1.48e-4	0.199
Al-27	2.39e-3	3.21
Si	1.58e-2	21.2
K	6.93e-4	0.932
Ca	2.29e-3	3.08
Fe-54	1.85e-5	0.0249
Fe-56	2.87e-4	0.386
Fe-57	6.57e-6	0.00883
Fe-58	8.76e-7	0.00118

Table A.2: Composition of water

Isotope/Element	Number Density (cm^{-3})	Atom Percent (%)
H-1(H20)	4.95e-2	66.7
O-16	2.48e-2	33.3

Table A.3: Composition of stainless steel 304

Isotope/Element	Number Density (cm^{-3})	Atom Percent (%)
C	2.37E-04	0.273
Si	8.93E-04	1.03
Cr-50	7.56E-04	0.870
Cr-52	1.46E-02	16.8
Cr-53	1.65E-03	1.90
Cr-54	4.12E-04	0.474
Mn-55	1.52E-03	1.75
Fe-54	3.44E-03	3.96
Fe-56	5.35E-02	61.5
Fe-57	1.22E-03	1.40
Fe-58	1.63E-04	0.188
Ni-58	5.84E-03	6.717
Ni-60	2.23E-03	2.56
Ni-61	9.66E-05	0.111
Ni-62	3.07E-04	0.353
Ni-64	7.78E-05	0.0895

Table A.4: Composition of lead

Isotope/Element	Number Density (cm^{-3})	Atom Percent (%)
Pb-206	7.94E-03	24.4
Pb-207	7.28E-03	22.4
Pb-208	1.73E-02	53.2

Table A.5: Composition of uranium dioxide

Isotope/Element	Number Density (cm^{-3})	Atom Percent (%)
U-235	4.96E-04	0.742
U-238	2.18E-02	32.582
O-16	4.46E-02	66.676

Appendix B

Multigroup Cross-Sections for Materials

This appendix contains the multigroup cross-sections for each material used in the challenge problem in Chapter VIII: concrete, water, stainless steel 304, lead, and uranium dioxide. These macroscopic cross-sections were obtained by weighting the isotopic/elemental microscopic cross-sections from the BUGLE-96 library [44] with the atomic compositions listed in Appendix A for each material and collapsing them to the 10-group structure given in Table 8.1 by arithmetically averaging over each energy group.

Table B.1: Concrete cross-sections for groups 1-5

Data \ g	1	2	3	4	5
$\Sigma_{t,g}\,(cm^{-1})$	1.13E-01	1.29E-01	2.23E-01	3.46E-01	3.63E-01
$\Sigma_{s,g\to1}\,(cm^{-1})$	4.21E-02	5.70E-03	5.70E-03	2.93E-03	6.12E-03
$\Sigma_{s,g\to2}\,(cm^{-1})$	0.0	5.13E-02	1.67E-02	9.96E-03	3.62E-03
$\Sigma_{s,g\to3}\,(cm^{-1})$	0.0	0.0	1.45E-01	6.55E-02	7.13E-03
$\Sigma_{s,g\to4}\,(cm^{-1})$	0.0	0.0	0.0	2.82E-01	4.58E-02
$\Sigma_{s,g\to5}\,(cm^{-1})$	0.0	0.0	0.0	0.0	2.85E-01
$\Sigma_{s,g\to6}\,(cm^{-1})$	0.0	0.0	0.0	0.0	0.0
$\Sigma_{s,g\to7}\,(cm^{-1})$	0.0	0.0	0.0	0.0	0.0
$\Sigma_{s,g\to8}\,(cm^{-1})$	0.0	0.0	0.0	0.0	0.0
$\Sigma_{s,g\to9}\,(cm^{-1})$	0.0	0.0	0.0	0.0	0.0
$\Sigma_{s,g\to10}\,(cm^{-1})$	0.0	0.0	0.0	0.0	0.0

Table B.2: Concrete cross-sections for groups 6-10

Data \ g	6	7	8	9	10
$\Sigma_{t,g}\,(cm^{-1})$	3.93E-01	4.48E-01	5.58E-02	7.62E-02	1.33E-01
$\Sigma_{s,g\to1}\,(cm^{-1})$	2.01E-03	1.25E-03	2.55E-04	3.39E-03	4.64E-03
$\Sigma_{s,g\to2}\,(cm^{-1})$	2.44E-03	1.19E-04	4.64E-05	1.28E-03	2.74E-03
$\Sigma_{s,g\to3}\,(cm^{-1})$	1.72E-03	6.31E-05	2.84E-04	1.44E-03	3.64E-04
$\Sigma_{s,g\to4}\,(cm^{-1})$	1.10E-02	9.21E-05	1.67E-03	3.85E-03	8.35E-04
$\Sigma_{s,g\to5}\,(cm^{-1})$	5.74E-02	4.29E-04	2.56E-03	9.64E-03	5.55E-03
$\Sigma_{s,g\to6}\,(cm^{-1})$	3.00E-01	1.04E-04	6.71E-04	8.19E-02	9.74E-03
$\Sigma_{s,g\to7}\,(cm^{-1})$	0.0	3.37E-01	1.56E-02	8.09E-02	1.12E-02
$\Sigma_{s,g\to8}\,(cm^{-1})$	0.0	0.0	1.80E-02	2.45E-02	1.24E-02
$\Sigma_{s,g\to9}\,(cm^{-1})$	0.0	0.0	0.0	3.70E-02	2.77E-02
$\Sigma_{s,g\to10}\,(cm^{-1})$	0.0	0.0	0.0	0.0	3.54E-02

Table B.3: Water cross-sections for groups 1-5

Data \ g	1	2	3	4	5
$\Sigma_{t,g}\,(cm^{-1})$	8.49E-02	1.47E-01	2.65E-01	5.94E-01	9.89E-01
$\Sigma_{s,g\to1}\,(cm^{-1})$	1.70E-02	2.72E-03	6.18E-03	8.60E-03	1.99E-02
$\Sigma_{s,g\to2}\,(cm^{-1})$	0.0	1.93E-02	2.82E-02	4.40E-02	2.27E-02
$\Sigma_{s,g\to3}\,(cm^{-1})$	0.0	0.0	7.70E-02	1.33E-01	4.32E-02
$\Sigma_{s,g\to4}\,(cm^{-1})$	0.0	0.0	0.0	2.86E-01	2.34E-01
$\Sigma_{s,g\to5}\,(cm^{-1})$	0.0	0.0	0.0	0.0	6.37E-01
$\Sigma_{s,g\to6}\,(cm^{-1})$	0.0	0.0	0.0	0.0	0.0
$\Sigma_{s,g\to7}\,(cm^{-1})$	0.0	0.0	0.0	0.0	0.0
$\Sigma_{s,g\to8}\,(cm^{-1})$	0.0	0.0	0.0	0.0	0.0
$\Sigma_{s,g\to9}\,(cm^{-1})$	0.0	0.0	0.0	0.0	0.0
$\Sigma_{s,g\to10}\,(cm^{-1})$	0.0	0.0	0.0	0.0	0.0

Table B.4: Water cross-sections for groups 6-10

Data \ g	6	7	8	9	10
$\Sigma_{t,g}\,(cm^{-1})$	1.10E+00	1.49E+00	1.79E-02	2.63E-02	4.74E-02
$\Sigma_{s,g\to1}\,(cm^{-1})$	1.03E-02	5.55E-03	3.71E-05	9.66E-04	1.55E-03
$\Sigma_{s,g\to2}\,(cm^{-1})$	1.56E-02	7.57E-04	0.00E+00	2.82E-03	9.94E-04
$\Sigma_{s,g\to3}\,(cm^{-1})$	1.05E-02	4.02E-04	0.00E+00	1.26E-03	7.02E-06
$\Sigma_{s,g\to4}\,(cm^{-1})$	6.98E-02	5.87E-04	0.00E+00	4.70E-03	1.70E-05
$\Sigma_{s,g\to5}\,(cm^{-1})$	3.15E-01	2.73E-03	0.00E+00	3.46E-02	2.49E-04
$\Sigma_{s,g\to6}\,(cm^{-1})$	6.05E-01	5.84E-05	0.00E+00	4.95E-01	4.53E-03
$\Sigma_{s,g\to7}\,(cm^{-1})$	0.0	9.51E-01	4.14E-02	4.88E-01	4.70E-03
$\Sigma_{s,g\to8}\,(cm^{-1})$	0.0	0.0	9.11E-03	6.41E-03	1.30E-09
$\Sigma_{s,g\to9}\,(cm^{-1})$	0.0	0.0	0.0	1.46E-02	2.86E-03
$\Sigma_{s,g\to10}\,(cm^{-1})$	0.0	0.0	0.0	0.0	6.61E-03

Table B.5: Stainless steel 304 cross-sections for groups 1-5

Data \ g	1	2	3	4	5
$\Sigma_{t,g}\,(cm^{-1})$	2.71E-01	2.91E-01	2.67E-01	3.71E-01	8.76E-01
$\Sigma_{s,g\to1}\,(cm^{-1})$	1.43E-01	9.54E-03	1.62E-02	2.93E-03	2.71E-03
$\Sigma_{s,g\to2}\,(cm^{-1})$	0.0	1.46E-01	2.77E-02	5.74E-03	1.86E-04
$\Sigma_{s,g\to3}\,(cm^{-1})$	0.0	0.0	2.13E-01	2.02E-02	5.09E-04
$\Sigma_{s,g\to4}\,(cm^{-1})$	0.0	0.0	0.0	3.51E-01	1.44E-03
$\Sigma_{s,g\to5}\,(cm^{-1})$	0.0	0.0	0.0	0.0	7.75E-01
$\Sigma_{s,g\to6}\,(cm^{-1})$	0.0	0.0	0.0	0.0	0.0
$\Sigma_{s,g\to7}\,(cm^{-1})$	0.0	0.0	0.0	0.0	0.0
$\Sigma_{s,g\to8}\,(cm^{-1})$	0.0	0.0	0.0	0.0	0.0
$\Sigma_{s,g\to9}\,(cm^{-1})$	0.0	0.0	0.0	0.0	0.0
$\Sigma_{s,g\to10}\,(cm^{-1})$	0.0	0.0	0.0	0.0	0.0

Table B.6: Stainless steel 304 cross-sections for groups 6-10

Data \ g	6	7	8	9	10
$\Sigma_{t,g}\,(cm^{-1})$	9.91E-01	9.62E-01	2.37E-01	2.72E-01	4.32E-01
$\Sigma_{s,g\to1}\,(cm^{-1})$	7.53E-04	9.94E-04	7.39E-03	1.02E-02	9.90E-03
$\Sigma_{s,g\to2}\,(cm^{-1})$	3.40E-08	9.27E-11	2.57E-03	6.23E-03	9.42E-03
$\Sigma_{s,g\to3}\,(cm^{-1})$	2.30E-05	2.71E-12	1.31E-03	2.21E-03	2.25E-03
$\Sigma_{s,g\to4}\,(cm^{-1})$	2.52E-05	2.35E-08	1.78E-03	2.37E-03	1.52E-03
$\Sigma_{s,g\to5}\,(cm^{-1})$	3.17E-03	5.02E-06	1.23E-02	1.78E-02	1.45E-02
$\Sigma_{s,g\to6}\,(cm^{-1})$	9.50E-01	6.53E-06	2.28E-03	3.78E-03	1.68E-02
$\Sigma_{s,g\to7}\,(cm^{-1})$	0.0	8.41E-01	1.47E-03	3.51E-03	3.74E-02
$\Sigma_{s,g\to8}\,(cm^{-1})$	0.0	0.0	1.46E-02	9.20E-02	1.25E-01
$\Sigma_{s,g\to9}\,(cm^{-1})$	0.0	0.0	0.0	5.77E-02	1.98E-01
$\Sigma_{s,g\to10}\,(cm^{-1})$	0.0	0.0	0.0	0.0	2.37E-01

Table B.7: Lead cross-sections for groups 1-5

Data \ g	1	2	3	4	5
$\Sigma_{t,g}\,(cm^{-1})$	1.86E-01	2.43E-01	1.79E-01	2.68E-01	3.40E-01
$\Sigma_{s,g\to1}\,(cm^{-1})$	1.06E-01	3.57E-03	2.56E-03	6.33E-04	5.14E-04
$\Sigma_{s,g\to2}\,(cm^{-1})$	0.0	1.80E-01	7.19E-03	1.27E-03	2.74E-05
$\Sigma_{s,g\to3}\,(cm^{-1})$	0.0	0.0	1.71E-01	7.45E-03	3.82E-05
$\Sigma_{s,g\to4}\,(cm^{-1})$	0.0	0.0	0.0	2.66E-01	1.39E-03
$\Sigma_{s,g\to5}\,(cm^{-1})$	0.0	0.0	0.0	0.0	3.31E-01
$\Sigma_{s,g\to6}\,(cm^{-1})$	0.0	0.0	0.0	0.0	0.0
$\Sigma_{s,g\to7}\,(cm^{-1})$	0.0	0.0	0.0	0.0	0.0
$\Sigma_{s,g\to8}\,(cm^{-1})$	0.0	0.0	0.0	0.0	0.0
$\Sigma_{s,g\to9}\,(cm^{-1})$	0.0	0.0	0.0	0.0	0.0
$\Sigma_{s,g\to10}\,(cm^{-1})$	0.0	0.0	0.0	0.0	0.0

Table B.8: Lead cross-sections for groups 6-10

Data \ g	6	7	8	9	10
$\Sigma_{t,g}\,(cm^{-1})$	3.60E-01	3.68E-01	5.28E-01	4.79E-01	7.01E-01
$\Sigma_{s,g\to1}\,(cm^{-1})$	1.05E-04	2.04E-04	5.45E-04	5.46E-03	8.41E-03
$\Sigma_{s,g\to2}\,(cm^{-1})$	3.08E-07	0.00E+00	3.61E-05	1.16E-05	7.92E-04
$\Sigma_{s,g\to3}\,(cm^{-1})$	7.15E-07	6.70E-12	9.30E-05	5.42E-05	5.03E-06
$\Sigma_{s,g\to4}\,(cm^{-1})$	4.06E-06	5.30E-12	2.70E-04	3.29E-04	1.62E-04
$\Sigma_{s,g\to5}\,(cm^{-1})$	2.64E-04	7.72E-10	8.82E-04	4.50E-03	2.91E-03
$\Sigma_{s,g\to6}\,(cm^{-1})$	3.56E-01	4.44E-07	2.28E-04	1.05E-03	1.64E-03
$\Sigma_{s,g\to7}\,(cm^{-1})$	0.0	3.59E-01	6.77E-04	3.73E-03	2.43E-03
$\Sigma_{s,g\to8}\,(cm^{-1})$	0.0	0.0	9.11E-03	3.08E-01	1.61E-01
$\Sigma_{s,g\to9}\,(cm^{-1})$	0.0	0.0	0.0	1.26E-01	1.81E-01
$\Sigma_{s,g\to10}\,(cm^{-1})$	0.0	0.0	0.0	0.0	1.96E-01

Table B.9: Uranium dioxide cross-sections and fixed source for groups 1-5

Data \ g	1	2	3	4	5
$\Sigma_{t,g}\,(cm^{-1})$	2.02E-01	2.22E-01	2.82E-01	4.25E-01	4.96E-01
$\Sigma_{s,g\to1}\,(cm^{-1})$	9.81E-02	4.38E-03	6.67E-03	2.72E-03	3.13E-03
$\Sigma_{s,g\to2}\,(cm^{-1})$	0.0	1.15E-01	7.05E-03	1.32E-03	7.90E-06
$\Sigma_{s,g\to3}\,(cm^{-1})$	0.0	0.0	1.92E-01	3.86E-02	2.46E-06
$\Sigma_{s,g\to4}\,(cm^{-1})$	0.0	0.0	0.0	3.94E-01	9.51E-03
$\Sigma_{s,g\to5}\,(cm^{-1})$	0.0	0.0	0.0	0.0	4.59E-01
$\Sigma_{s,g\to6}\,(cm^{-1})$	0.0	0.0	0.0	0.0	0.0
$\Sigma_{s,g\to7}\,(cm^{-1})$	0.0	0.0	0.0	0.0	0.0
$\Sigma_{s,g\to8}\,(cm^{-1})$	0.0	0.0	0.0	0.0	0.0
$\Sigma_{s,g\to9}\,(cm^{-1})$	0.0	0.0	0.0	0.0	0.0
$\Sigma_{s,g\to10}\,(cm^{-1})$	0.0	0.0	0.0	0.0	0.0
$Q_g\,(cm^{-3}s^{-1})$	2.61E+10	6.01E+11	1.43E+12	3.42E+11	4.85E+09

Table B.10: Uranium dioxide cross-sections and fixed source for groups 6-10

Data \ g	6	7	8	9	10
$\Sigma_{t,g}\,(cm^{-1})$	1.54E+00	1.16E+00	4.60E-01	4.33E-01	6.75E-01
$\Sigma_{s,g\to1}\,(cm^{-1})$	7.20E-04	3.83E-04	2.89E-04	4.94E-03	6.99E-03
$\Sigma_{s,g\to2}\,(cm^{-1})$	1.06E-06	8.14E-14	1.08E-06	2.17E-02	1.01E-02
$\Sigma_{s,g\to3}\,(cm^{-1})$	2.91E-08	2.18E-12	1.15E-07	2.27E-03	2.11E-02
$\Sigma_{s,g\to4}\,(cm^{-1})$	4.38E-08	8.60E-13	1.79E-07	3.68E-04	8.63E-04
$\Sigma_{s,g\to5}\,(cm^{-1})$	8.67E-03	4.21E-13	5.27E-06	1.24E-03	2.55E-03
$\Sigma_{s,g\to6}\,(cm^{-1})$	1.01E+00	1.05E-04	6.90E-05	9.44E-03	1.45E-02
$\Sigma_{s,g\to7}\,(cm^{-1})$	0.0	3.99E-01	9.70E-03	4.43E-03	9.49E-03
$\Sigma_{s,g\to8}\,(cm^{-1})$	0.0	0.0	2.04E-02	3.75E-02	9.43E-02
$\Sigma_{s,g\to9}\,(cm^{-1})$	0.0	0.0	0.0	6.94E-02	1.04E-01
$\Sigma_{s,g\to10}\,(cm^{-1})$	0.0	0.0	0.0	0.0	1.24E-01
$Q_g\,(cm^{-3}s^{-1})$	1.13E+08	2.03E+04	9.47E+09	7.37E+11	2.49E+12

Bibliography

Bibliography

[1] M.H. Kalos. "Importance Sampling in Monte Carlo Shielding Calculations". *Nuclear Science and Engineering*, 16:227, 1963.

[2] F. H. Clark. "The Exponential Transform as an Importance-Sampling Device – A Review". Technical Report ORNL-RISC-14, Oak Ridge National Laboratory, 1966.

[3] R.R. Coveyou, V.R. Cain, and K.J. Yost. "Adjoint and Importance in Monte Carlo Applications". *Nuclear Science and Engineering*, 27:219, 1967.

[4] V.R. Cain. "Application of S_N Adjoint Flux Calculations to Monte Carlo Biasing". *Transaction of the American Nuclear Society*, 10:399, 1967.

[5] G.E. Whitesides. "Adjoint Biasing in Monte Carlo Criticality Calculations". *Transaction of the American Nuclear Society*, 11:159, 1968.

[6] F.A.R. Schmidt, E.A. Straker, and V.R. Cain. "Applications of Adjoint Flux Calculations to Monte Carlo Biasing". Technical Report ORNL-TM-2454, Oak Ridge National Laboratory, 1968.

[7] S.N. Cramer. "Monte Carlo Graphite Benchmark Calculation using S_n Adjoint Biasing". *Transaction of the American Nuclear Society*, 12:947, 1969.

[8] C.E. Burgart and P.N. Stevens. "A General Method of Importance Sampling the Angle of Scattering in Monte Carlo Calculations". *Nuclear Science and Engineering*, 42:306, 1970.

[9] F.A.R. Schmidt. "Biased Angle Selection in Monte Carlo Shielding Calculations". *Nuclear Engineering and Design*, 15:209, 1971.

[10] J.S. Tang, T.J. Hoffman, and P.N. Stevens. "Angular Biasing of the Collision Process in Multigroup Monte Carlo Calculations". *Nuclear Science and Engineering*, 64:837, 1977.

[11] J.S. Hendricks and L.L. Carter. "Anisotropic Angle Biasing of Photons". *Nuclear Science and Engineering*, 89:118, 1985.

[12] J.C. Nimal and T. Vergnaud. "TRIPOLI: A General Monte Carlo Code, Present State and Future Prospects". *Progress in Nuclear Energy*, 24:195, 1990.

[13] J.P. Both, H. Derriennic, B. Morillon, and J.C. Nimal. "A Survey of TRIPOLI-4". In *Proceedings of the Eighth International Conference on Radiation Shielding*, volume 1, page 373, Arlington, Texas, April 24–28, 1994.

[14] F.X. Giffard, R. Jacqmin, J.C. Nimal, and Y. Peneliau. "Variance Reduction in 3-D Continuous-Energy Monte Carlo Simulations Using Importance Maps Generated by a Deterministic Code". In *Proceedings of the Mathematics and Computation, Reactor Physics and Environmental Analysis in Nuclear Applications*, page 273, Madrid, Spain, Sept. 27–30, 1999.

[15] S.N. Cramer. "Discrete Angle Biasing in Monte Carlo Radiation Transport". *Nuclear Science and Engineering*, 98:279, 1988.

[16] J.S. Tang and T.J. Hoffman. "Monte Carlo Shielding Analyses Using an Automated Biasing Procedure". *Nuclear Science and Engineering*, 99:329, 1988.

[17] J.S Tang. "SAS4: A Monte Carlo Cask Shielding Analysis Module Using an Automated Biasing Procedure, Sec. S4 of Scale: A Modular Code System for Performing Standardized Computer Analyses for Licensing Evaluations". Technical Report NUREG/CR-0200, Rev 6 (ORNL/NUREG/CSD-2/V2/R6), Oak Ridge National Laboratory, 1998.

[18] M.B. Emmett. "The MORSE Monte Carlo Radiation Transport Code System". Technical Report ORNL-4972, Oak Ridge National Laboratory, 1975.

[19] S.J. Chucas, I. Curl, T. Shuttleworth, and G. Morrell. "Preparing the Monte Carlo Code MCBEND for the 21st Century". In *Proceedings of the Eighth International Conference on Radiation Shielding*, volume 1, page 381, Arlington, Texas, April 24–28, 1994.

[20] S.J. Chucas and M.J. Grimstone. "The Accelerated Techniques used in the Monte Carlo Code MCBEND". In *Proceedings of the Eighth International Conference on Radiation Shielding*, volume 2, page 1126, Arlington, Texas, April 24–28, 1994.

[21] K.A. Van Riper, T.J. Urbatsch, P.D. Soran, D.K. Parsons, J.E. Morel, G.W. McKinney, S.R. Lee, L.A Crotzer, F.W. Brinkley, J.W. Anderson, and R.E. Alcouffe. "AVATAR – Automatic Variance Reduction in Monte Carlo Calculations". In *Proc. Joint Int. Conf. Math. Methods and Supercomputing in Nuclear Applications*, volume 1, page 661, Saratoga Springs, New York, October 6–10, 1997.

[22] S.A. Turner. "Automatic Variance Reduction for Monte Carlo Simulations via the Local Importance Function Transform". Technical Report LA-13119-T, Los Alamos National Laboratory, 1996.

[23] S.A. Turner and E.W. Larsen. "Automatic Variance Reduction for Three-Dimensional Monte Carlo Simulations by the Local Importance Function Transform". *Nuclear Science and Engineering*, 22:127, 1997.

[24] J.M. Depinay, M. Cailluad, and R. Sentis. "A New Automatic Biasing Technique for Transport Monte Carlo Methods". *Nuclear Science and Engineering*, 152:48, 2006.

[25] H.P. Smith and J.C. Wagner. "A Case Study in Manual and Automated Monte Carlo Variance Reduction with a Deep Penetration Reactor Shielding Problem". *Nuclear Science and Engineering*, 149:23–37, 2005.

[26] J.C. Wagner and A. Haghighat. "Automated Variance Reduction of Monte Carlo Shielding Calculations Using the Discrete Ordinates Adjoint Function". *Nuclear Science and Engineering*, 128:186, 1998.

[27] A. Haghighat and J. C. Wagner. "Monte Carlo Variance Reduction with Deterministic Importance Functions". *Progress in Nuclear Energy*, 42(1):25–53, 2003.

[28] M.A. Cooper and E.W. Larsen. "Automated Weight Windows for Global Monte Carlo Particle Transport Calculations". *Nuclear Science and Engineering*, 137:1, 2001.

[29] J.C. Wagner, E.D. Blakeman, and D.E. Peplow. "Forward-Weighted CADIS Method for Global Variance Reduction". *Transaction of the American Nuclear Society*, 97:630–633, 2007.

[30] D.E. Peplow, E.D. Blakeman, and J.C. Wagner. "Advanced Variance Reduction Strategies for Optimizing Mesh Tallies in MAVRIC". *Transaction of the American Nuclear Society*, 97:595–597, 2007.

[31] M.L. Williams. "The Concept of Spatial Channel Theory Applied to Reactor Shielding Analysis". *Nuclear Science and Engineering*, 62:220, 1977.

[32] M.L. Williams. "The Relations Between Various Contributon Variables Used in Spatial Channel Theory Applied to Reactor Shielding Analysis". *Nuclear Science and Engineering*, 63:220, 1977.

[33] M.L. Williams. "Generalized Contributon Response Theory". *Nuclear Science and Engineering*, 108:355–383, 1991.

[34] I.K. Abu-Shumays, M.A. Hunter, R.L. Martz, and J.M. Risner. "Generalization of Spatial Channel Theory to Three-Dimensional x-y-z Transport Computations". In *Proc. ANS Topical Meeting, Radiation Shielding and Protection Division*, Santa Fe, New Mexico, April 14-17 2002.

[35] J.W. Painter, S.A.W. Gerstl, and G.C. Pomraning. "The Theory of Contributon Transport". Technical Report LA-8536-MS, Los Alamos National Laboratory, 1980.

[36] S.A.W. Gerstl. "A New Concept for Deep-Penetration Transport Calculations and Two New Forms of the Neutron Transport Equation". Technical Report LA-6628-MS, Los Alamos National Laboratory, 1976.

[37] S.A.W. Gerstl and J.W. Painter. "Transport Equations for Contributons". *Nuclear Science and Engineering*, 69:129–131, 1979.

[38] T.E. Booth. "Automatic Importance Estimation in Forward Monte Carlo Calculations". *Transaction of the American Nuclear Society*, 41:308, 1982.

[39] T.E. Booth. "A Weight Window/Importance Generator for Monte Carlo Streaming Problems". In *Proceedings of the Sixth International Conference on Radiation Shielding*, page 210, Tokyo, Japan, May 16–20, 1983.

[40] T.E. Booth and J.S. Hendricks. "Importance Estimation in Forward Monte Carlo Calculations". *Nuclear Tecnology/Fusion*, 5:90, 1984.

[41] T.L. Becker, A.B. Wollaber, and E.W. Larsen. "A Hybrid Monte Carlo-Deterministic Method for Global Particle Transport Calculations". *Nuclear Science and Engineering*, 155:155–167, 2006.

[42] S.R. Dwivedi. "A New Importance Biasing Scheme For Deep-Penetration Monte Carlo". *Ann. Nucl. Energy*, 9:359–368, 1982.

[43] J.K. Shultis and R. E. Faw. *Radiation Shielding*. Prentice Hall PTR, New Jersey, 1996.

[44] "BUGLE-96, Coupled 47 Neutron, 20 Gamma-Ray Group Cross Section Library Derived from ENDF/B-VI for LWR Sheilding and Pressure Vessel Dosimetry Applications". Technical Report DLC-185, Oak Ridge National Laboratory, 1996.